UNIVERSIDADE ESTADUAL DE CAMPINAS

INSTITUTO DE FÍSICA "GLEB WATAGHIN"

LUIZ AUGUSTO STUANI PEREIRA

INVESTIGAÇÃO DE SINAIS DE MÚONS, RÁDIO E FLUORESCÊNCIA PROVENIENTES DE CHUVEIROS ATMOSFÉRICOS EXTENSOS DE ALTAS ENERGIAS PARA ANÁLISES DE COMPOSIÇÃO QUÍMICA

INVESTIGATION OF MUON, RADIO AND FLUORESCENCE SIGNALS FROM HIGH ENERGY EXTENSIVE AIR SHOWERS FOR CHEMICAL COMPOSITION ANALYSIS

CAMPINAS
2018

LUIZ AUGUSTO STUANI PEREIRA

INVESTIGAÇÃO DE SINAIS DE MÚONS, RÁDIO E FLUORESCÊNCIA PROVENIENTES DE CHUVEIROS ATMOSFÉRICOS EXTENSOS DE ALTAS ENERGIAS PARA ANÁLISES DE COMPOSIÇÃO QUÍMICA

INVESTIGATION OF MUON, RADIO AND FLUORESCENCE SIGNALS FROM HIGH ENERGY EXTENSIVE AIR SHOWERS FOR CHEMICAL COMPOSITION ANALYSIS

Tese apresentada ao Instituto de Física "Gleb Wataghin" da Universidade Estadual de Campinas como parte dos requisitos exigidos para a obtenção do título de Doutor em Ciências

Thesis presented to the Institute of Physics "Gleb Wataghin" of the University of Campinas in partial fulfillment of the requirements for the degree of Doctor in Science

Supervisor/Orientador Prof. Dr. Anderson Campos Fauth

ESTE TRABALHO CORRESPONDE À VERSÃO FINAL DA TESE DEFENDIDA PELO ALUNO LUIZ AUGUSTO STUANI PEREIRA, E ORIENTADA PELO PROF. DR. ANDERSON CAMPOS FAUTH.

CAMPINAS
2018

Agência(s) de fomento e nº(s) de processo(s): FAPESP, 2013/23074-0

Ficha catalográfica
Universidade Estadual de Campinas
Biblioteca do Instituto de Física Gleb Wataghin
Lucimeire de Oliveira Silva da Rocha - CRB 8/9174

P414i

Pereira, Luiz Augusto Stuani, 1989-
Investigation of muon, radio and fluorescence signals from high energy extensive air showers for chemical composition analyses / Luiz Augusto Stuani Pereira. – Campinas, SP : [s.n.], 2018.

Orientador: Anderson Campos Fauth.
Tese (doutorado) – Universidade Estadual de Campinas, Instituto de Física Gleb Wataghin.

1. Observatório Pierre Auger. 2. Raios cósmicos. 3. Múons. 4. Rádio. 5. Fluorescência. I. Fauth, Anderson Campos, 1957-. II. Universidade Estadual de Campinas. Instituto de Física Gleb Wataghin. III. Título.

Informações para Biblioteca Digital

Título em outro idioma: Investigação de sinais de múons, rádio e fluorescência provenientes de chuveiros atmosféricos extensos de altas energias para análises de composição química
Palavras-chave em inglês:
Pierre Auger Observatory
Cosmic rays
Muons
Radio
Fluorescence
Área de concentração: Física
Titulação: Doutor em Ciências
Banca examinadora:
Anderson Campos Fauth [Orientador]
Carola Dobrigkeit Chinellato
Edmilson José Tonelli Manganote
Helio Nogima
Marcelo Augusto Leigui de Oliveira
Data de defesa: 19-09-2018
Programa de Pós-Graduação: Física

MEMBROS DA COMISSÃO JULGADORA DA TESE DE DOUTORADO DE **LUIZ AUGUSTO STUANI PEREIRA** RA: **153926** APRESENTADA E APROVADA AO INSTITUTO DE FÍSICA “GLEB WATAGHIN”, DA UNIVERSIDADE ESTADUAL DE CAMPINAS, EM 19/09/2018.

COMISSÃO JULGADORA:

- Prof. Dr. Anderson Campos Fauth - (Orientador) - IFGW/UNICAMP
- Prof. Dr. Carola Dobrigkeit Chinellato - IFGW/UNICAMP
- Prof. Dr. Edmilson José Tonelli Manganote - IFGW/UNICAMP
- Prof. Dr. Helio Nogima - UNIVERSIDADE DO ESTADO DO RIO DE JANEIRO
- Prof. Dr. Marcelo Augusto Leigui de Oliveira- UNIVERSIDADE FEDERAL DO ABC

A Ata de Defesa, assinada pelos membros da Comissão Examinadora, consta no processo de vida acadêmica do aluno.

CAMPINAS
2018

"Never give up on what you really want to do. The person with big dreams is more powerful than the one with all the facts."

Albert Einstein

This Ph.D. thesis and all my academic achievements are dedicated to my family and friends for always supporting, helping and standing by me.

Acknowledgements

First and foremost, I would like to thank God, who has granted countless blessing, knowledge, strength, ability and opportunity, so that I have been able to undertake this research study and to persevere and accomplish it satisfactorily. Otherwise, this achievement would not have been possible.

I would like to express my sincere gratitude to my advisor Prof. Dr. Anderson Campos Fauth for the continuous support of my Ph.D. study and research, for his motivation and immense knowledge. His guidance helped me in all the time of research and writing of this thesis. Besides my advisor, I would like to thank Dr. Andreas Haungs (my supervisor at KIT (Karlsruhe Institute for Technology)) and all the radio and cosmic ray group especially Dr. Frank Schroeder and Dr. Ewa Holt for all the shared knowledge, teaching, technical support in the development of the research project. Their support, encouragement and credible ideas have been great contributors to the completion of the thesis. It was a wonderful and unique experience.

During my stay at KIT, I joined KSETA (Karlsruhe School of Elementary Particle and Astroparticle Physics), which is the Graduate School associated with the KIT Center Elementary Particle and Astroparticle Physics (KCETA), that bundles experimental and theoretical research and education at the interface between astronomy, astrophysics, elementary particle physics and cosmology. So I would like to heartily thank KSETA for all given opportunities (offered courses, talks and workshops). It was an amazing experience being a KSETA member and I am very glad of that. It definitely gave me a great experience and improvement in my cultural and professional life.

I have great pleasure in acknowledging my gratitude to my colleagues and fellow research (Paulo, Pedro, Gabriela, Monica, Bruno, Mary e Vanessa) in for the stimulating discussions, being there at times when I required motivation and for all the fun we have had in the last four years.

My acknowledgement would be incomplete without thanking the biggest source of my strength, my family: my parents (Luiz Antonio and Maria Regina) and my sister (Fernanda) for supporting me spiritually throughout writing this thesis and my life in general.

I would also like to thank FAPESP (process number 2013/23074-0) for financial support during the whole Ph.D. period in Brazil and FAPESP (process number 2015/22114-3) for the one-year research internship abroad and FAPESP's thematic project (process number 2010/07359-06).

Resumo

INVESTIGAÇÃO DE SINAIS DE MÚONS, RÁDIO E FLUORESCÊNCIA PROVENIENTES DE CHUVEIROS ATMOSFÉRICOS EXTENSOS DE ALTAS ENERGIAS PARA ANÁLISES DE COMPOSIÇÃO QUÍMICA

Na busca pela compreensão da formação e desenvolvimento do Universo a detecção de raios cósmicos possui um papel fundamental. Especialmente para altíssimas energias, sua origem é fracamente conhecida. A detecção de raios cósmicos ultra energéticos pode revelar uma natureza de forças ainda desconhecida no Universo. Múons de mais altas energias podem fornecer informações acerca dos processos ocorridos no desenvolvimento do chuveiro atmosférico extenso. Devido esta componente estar acoplada à componente hadrônica, logo fornece informações cruciais acerca das propriedades dos raios cósmicos primários. Assim, múons podem ser utilizados para se estudar a composição química das partículas primárias, pois sua multiplicidade depende do número atômico da primária. Nesta tese são estudadas medidas de composição química utilizando um arranjo de detectores híbridos composto pelos detectores de superfície (SD), detectores de múons (MD), detectores de fluorescência (FD) e detectores de rádio (RD) do Observatório Pierre Auger. É apresentado um estudo detalhado do poder de separação em massa dos raios cósmicos para chuveiros induzidos por próton e ferro utilizando a densidade muônica reconstruída em diferentes distâncias em relação ao eixo do chuveiro (300 - 1000 m). A separação em massa é analisada combinando-se a densidade muônica reconstruída com a energia de SD (energia primária medida com os detectores de superfície), energia de RD (energia de radiação emitida pela componente eletromagnética do chuveiro detectada pelas antenas de rádio) e a energia de FD (energia de fluorescência emitida pelas moléculas de nitrogênio na atmosfera). Estas análises são realizadas para investigar qual distância em relação ao eixo do chuveiro e qual estimador de energia oferece uma melhor separação em massa. Como resultado, temos que a razão entre a densidade muônica reconstruída a 500 m e a energia de FD oferece uma melhor separação para chuveiros induzidos por próton e ferro. Além do mais, a densidade muônica combinada com diferentes estimadores de energia fornece uma melhor separação em massa que o X_{max}, e esta separação aumenta com o aumento da energia primária. Finalmente, a medida dos observáveis sensíveis derivados da análise combinada do sinal de múons e diferentes estimadores de energia mostra uma composição compatível com as medidas do X_{max} para a região do espectro onde a transição entre raios cósmicos galácticos para extragalácticos ocorre.

Abstract

INVESTIGATION OF MUON, RADIO AND FLUORESCENCE SIGNALS FROM HIGH ENERGY EXTENSIVE AIR SHOWERS FOR CHEMICAL COMPOSITION ANALYSIS

In the search for understanding the formation and development of the Universe, the cosmic ray detection plays a key role. Especially at ultra-high energies, its origin is scarcely known. The detection of ultra high energy cosmic rays may reveal a still unknown nature of forces in the Universe. Higher energy muons can provide information about the processes involved in the development of extensive air showers. Since this component is coupled with the hadronic component, it immediately provides crucial information about the properties of the primary cosmic rays. Thus, muons can be used to study the chemical composition of primary particles as their multiplicity depends on the atomic number of the primary particle. In this thesis, the feasibility of cosmic ray mass composition measurements is studied using the hybrid detector array with surface detectors (SD), muon detectors (MD), fluorescence detectors (FD) and radio detectors (RD) of the Pierre Auger Observatory. A detailed study of the mass discrimination power for simulated showers induced by proton and iron is presented using the muon density reconstructed at different distances from the shower axis (300 - 1000 m). The mass separation power is analysed by combining the reconstructed muon density with the SD energy (primary energy measured with the surface detectors), the RD energy (radiation energy emitted by the electromagnetic component of the air shower which is detected by radio antennas) and the FD energy (fluorescence energy emitted by atmospheric nitrogen molecules). These analyses are performed to investigate which distance from the shower axis and which energy estimator gives the best mass separation. As a result, the ratio between the muon density reconstructed at 500 m and the FD energy features the best mass separation for proton and iron-induced showers. Moreover, the combined muon density with different energy estimators achieves a higher mass separation than X_{max} and it increases with increasing primary energy. Finally, the measurement of the mass sensitive observables derived from the combined analysis of the muon signal with different energy estimators shows a composition compatible with the measurements of the X_{max} for the spectrum region where the transition from Galactic to extragalactic cosmic ray occurs.

List of Figures

List of Tables

Contents

Introduction

Cosmic rays are fast-moving particles from space that hit the Earth from all directions. Although the first indications of their existence were obtained more than one hundred years ago by Victor Hess in 1912 [1], many of their properties remain mysterious. The largest earthbound cosmic ray experiment is the Pierre Auger Observatory. It started taking data in January 2004 and its construction was completed in 2008 [2]. The surface detector has accumulated more than three hundred thousand records of extensive air showers in the EeV regime.

The Pierre Auger Observatory is currently the most important experiment in ultra-high energy cosmic rays. The data taken at the site of the Observatory, located in Mendoza, Argentina, confirmed the energy spectrum suppression above 5.5×10^{19} eV [3, 4]. This suppression was predicted in 1966 by Greisen, Zatsepin and Kuzmin [5], right after the discovery of the cosmic microwave background by Penzias and Wilson in 1965 [6]. The hadron interactions with the background cosmic radiation imposes limits in the cosmic ray energy spectrum. One of the main efforts of the observatory is to improve the experiment and methods of data analyses to better measure the cosmic-ray composition at ultra-high energies and understand the production, propagation and interaction mechanisms of cosmic rays. Due to the low particle flux in the energy range from 10^{17} to 10^{19} eV the cosmic ray mass composition is observed through the differences in the shower development process in the atmosphere.

The current results of the Pierre Auger Observatory show a change in the chemical composition of the primary cosmic radiation at ultra-high energies indicating a transition from light to heavy elements with increasing energy [7], while the results from the experiments High-Resolution Fly's Eye (HiRes) [8] and Telescope Array (TA) [9] show a predominant composition of protons [10]. A better measure of the composition will lead to advances in our knowledge about anisotropy and will help to answer questions not yet understood about the origin of the flux suppression since this depends on the hadron mass.

The most sensitive parameters to cosmic-ray mass composition depend on our understanding of the hadronic interaction properties which are not very well known at ultra-high energy. The estimate of the primary-particle mass can only be made using sets of simulated reference showers, which have been generated with hadronic interaction models based on extrapolations of the results from particle accelerators. Thus, it is advisable to study different observables which are sensitive to both mass composition and hadronic interaction models to minimize the problem [11]. One of the most sensitive parameters to study cosmic ray mass composition

is the number of muons at the ground at a certain distance from the shower axis. Showers initiated by heavier primaries develop earlier and faster in the atmosphere and have a larger muon content than showers initiated by lighter primaries of the same energy. Moreover, the number of muons in a shower depends on many properties of hadronic interactions, including the multiplicity, the charge ratio and the baryon, and anti-baryon pair production [12, 13].

Several parameters taken with water-Cherenkov and fluorescence detectors carry, in principle, information about the identity of the primary particle and can be used to investigate the cosmic abundances at high energies. However, the situation regarding the mass composition of high-energy cosmic rays is not settled.

Radio emission from cosmic ray air showers offers the opportunity to use radio observations as an additional powerful observational technique in cosmic ray research. Similarly to the fluorescence technique, it allows a much more direct view into the shower development than particle measurements at the ground. The radio technique mainly measures quantities integrated over the full evolution of the shower. Radio signals complement the muon number measured by particle detector arrays as almost all muons generated in the shower development reach the ground [14].

In this thesis we perform multi-parametric analyses of sensitive observables to the chemical composition of primary cosmic rays using the *infill* array of the Observatory, which comprises the Surface Detectors (SD) for the detection of Cherenkov radiation emitted in the water by charged particles from the shower that reach the ground, the Fluorescence detectors (FD), the radio antennas of the AERA experiment (RD) and the muon detectors of the AMIGA array (MD). We present a detailed study of the mass discrimination power for simulated showers induced by proton and iron using the muon density reconstructed at different distances from the shower axis (300 - 1000 m). The mass separation power is analysed taking into account the SD energy (energy from the surface detectors), the RD energy (radiation energy emitted by the electromagnetic component of the air shower which is detected by AERA) and the FD energy (fluorescence energy emitted by atmospheric nitrogen). Those analyses were performed in order to investigate which distance from the shower axis and energy estimator feature the best mass separation of high-energy cosmic rays as the number of muons correlates well with the number of electrons in the shower. Moreover, those analyses are cross-checked with the maximum shower depth, X_{max}, to better determine the mass composition of high energy cosmic rays.

The scope of this thesis is described as following:

Chapter 2 gives an introduction about cosmic rays and their flux at the Earth's atmosphere. The principal topics are the origin, acceleration, and propagation of ultra-high energy cosmic rays as well as their possible accelerating astrophysical sources. Chapter 3 describes the phenomenon of extensive air showers. More specifically, the development of the air showers is addressed, which are qualitatively treated through detailed analytical calculations to obtain information about the properties of the primary cosmic rays that induced the air showers. These properties can be measured by analysing the characteristics of nuclear-electromagnetic

cascades induced by the cosmic ray interaction in the atmosphere. Hence the use of different Monte Carlo simulations is important to better understand the shower development. Many hadronic interaction models have been applied to study the air showers. Moreover, this chapter describes the different measurement techniques of ultra-high energy cosmic rays which covers a large area of detection. Chapter 4 gives details about the largest cosmic ray observatory, the Pierre Auger Observatory. Chapter 5 describes the shower parameters muon density at a reference distance from the shower axis reconstructed with AMIGA muon detectors and the different primary energy estimators measured with Surface and Fluorescence detectors and AERA. The air shower simulations used to investigate the mass separation sensitivity of the muon density combined with different energy estimators are shown in Chapter 6. For this, many simulation libraries were computed with CORSIKA and CoREAS simulation tools. For the analysis some quality cuts were applied to yield high-quality events. Finally, the mass-separation combined analysis was applied to measured events with AMIGA, in coincidence with AMIGA and AERA and AMIGA and Fluorescence detectors. The results are compared to the X_{max} measurement of the Fluorescence detectors and are described in Chapter 7.

High-Energy Cosmic Rays

The Earth is constantly bombarded by subatomic particles from outer space that can reach energies far higher than the largest accelerator machines, known as cosmic rays. The energies of these particles range from less than 1 GeV up to 10^{20} eV. Up to 10^{12} eV, these high energy particles are mainly protons (90%), alpha particle or nucleus of helium (9%) and heavier nuclei (1%), ranging up to the nuclei of lead atoms. Cosmic-ray particles travel at nearly the speed of light and some of them are the most energetic particles ever observed in nature. Although cosmic rays were discovered in 1912, their sources and propagation mechanisms are still subject of intense research. Therefore, this chapter provides a general overview of the properties of cosmic rays and describes common theories concerning their origin, propagation and acceleration mechanisms.

2.1 The origin of Cosmic Rays and Energy Spectrum

The cosmic-ray energy spectrum can be described by a power law $dN/dE \propto E^{-\alpha}$ over a wide energy range, indicating non-thermal acceleration processes [15]. The spectral index is $\alpha \approx 2.7$ below the *knee* region at 5×10^{15} eV, and $\alpha \simeq 3$ between the *knee* and the *ankle* at around 3×10^{18} eV. Above the *ankle* at 4×10^{18} eV, region where the spectrum is flattening, $\alpha \simeq 2.6$ followed by the flux suppression above $\sim$ 30 EeV. Figure 2.1 shows the experimental results of the differential energy spectra for several nuclei of the primary cosmic radiation for data taken from KASCADE-Grande, Hires 1 and 2, TA and the Pierre Auger Observatory. Understanding the origin of the characteristic features of the cosmic-ray flux is the key to identify their Galactic and extragalactic sources as well as the particle-acceleration processes and propagation mechanisms.

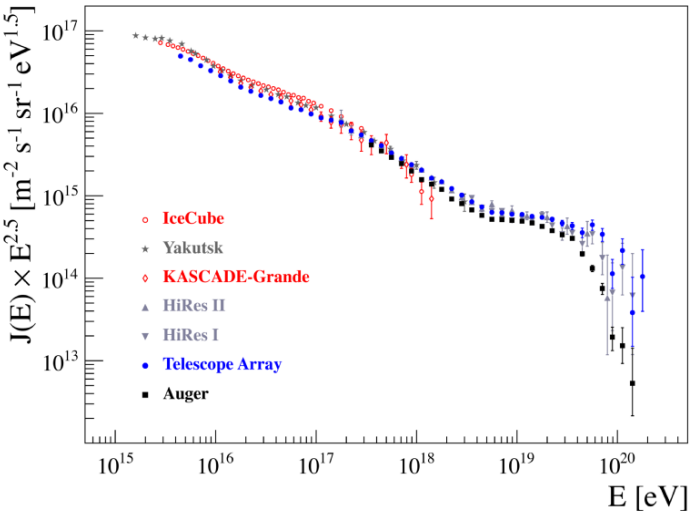

FIGURE 2.1: All particle spectrum of cosmic rays as a function of the energy per nucleon [16] measured by IceCube [17], Yakutsk [18], KASCADE-Grande [19], Hires 1 and 2 [20], TA [21] and Pierre Auger Observatory [22].

Up to the *knee* region of the energy spectrum, the particle flux is sufficiently high enabling a direct measurement of its elemental composition. Many researchers believe that cosmic rays with energy below the *knee* are Galactic, while higher energetic particles are extragalactic [16]. However, at energies from 10^{15} eV, the particle flux drops off dramatically to 1 m^{-2} yr^{-1}, disabling its direct detection. Thus, the energy spectrum can be determined indirectly through measurements of the properties of extensive air showers induced by the cosmic-ray particles in the Earth's atmosphere [23, 24]. The *knee* can be interpreted as the superposition of the energy spectra of different elements, that exhibit their cutoff at different energies.

Assuming that the cosmic-ray energy spectrum below 10^{18} eV is Galactic in origin, the *knee* region could reflect that most of the cosmic accelerators in the Galaxy have already reached their maximum energy. Some types of supernova remnants are considered as not able to accelerate protons above 10^{15} eV. Effects of propagation and confinement in the Galaxy [25] also need to be considered. The KASCADE-Grande experiment [26] and the Fly's Eye experiment [8] reported observations of a second *knee* at around 4×10^{17} eV.

Concerning the *ankle* region at about 10^{19} eV, a possible explanation for the flattening of the spectrum is the overlap of a population of high-energy particles over a low-energy one, i. e., an extragalactic flux begins to dominate over a Galactic particle flux [27]. Another possible explanation is the extragalactic proton interaction with the Cosmic Microwave Background (CMB) radiation, $p + \gamma_{\mathrm{CMB}} \longrightarrow e^+ + e^- + p$, at 2.7 K [28]. However, the origin of the *ankle* is not fully understood, and therefore it is an important issue to the research in cosmic rays.

If the cosmic-ray flux at high energies is cosmological in origin, there should be a suppression, a rapid steepening of the energy spectrum from 6×10^{19} eV predicted by the GZK cutoff (see next section for further details), resulting from

the inelastic interaction of Ultra High Energy Cosmic Rays (UHECR) with the CMB radiation.

2.2 Propagation and the GZK cutoff

The flux suppression of ultra-high energy cosmic rays was predicted by Zatsepin and Kuzmin [5, 29] in 1966 right after the discovery of the CMB radiation. In the rest frame of a proton with an energy of about 10^{20} eV, most incoming CMB photons have energies above 150 MeV, which is enough to produce the Δ^+ resonance that decays into a neutron and π^+ or into a proton and a π^0 as described below [7]

$$p + \gamma_{\mathrm{CMB}} \rightarrow \Delta(1232)^+ \rightarrow p + \pi^0, \tag{2.1}$$

$$p + \gamma_{\mathrm{CMB}} \rightarrow \Delta(1232)^+ \rightarrow n + \pi^+. \tag{2.2}$$

Assuming that the proton interaction cross-section is $\sigma \approx 10^{-28}$ cm^2 and that there are about 400 CMB photons per cubic centimeter, the mean free path becomes of the order of 10 Mpc. A proton loses on average 20% of its energy in each interaction, so after traveling 100 Mpc, its energy will decrease by one order of magnitude. The proton energy is attenuated by the electron-positron pair production and also due to the adiabatic expansion (*redshift*) of the Universe.

For primary cosmic rays with a mass number greater than 1 different interaction processes occur. Heavy nuclei lose energy via pair production and photo-disintegration processes due to the interaction with CMB and IR-UV intergalactic background light. Photo-disintegration involves the loss of one or more nucleons during propagation which happens when the center of mass energy exceeds the giant dipole resonance. The reactions corresponding to these processes are described as:

$$A + \gamma_{\mathrm{CMB,IR}} \rightarrow (A-1) + N, \tag{2.3}$$

$$A + \gamma_{\mathrm{CMB,IR}} \rightarrow (A-2) + 2N, \tag{2.4}$$

where N corresponds to a nucleon. The energy loss during the nucleon propagation cannot be calculated directly using the mean free path as for protons because the nucleus loses mass after the first photo-disintegration.

All species of cosmic rays with the exception of neutrinos interact with the CMB. Figure 2.2 shows a panorama of the various interaction processes.

The flux suppression can be understood in terms of an effective horizon within which a source can contribute significantly to the measured flux at Earth above a given energy threshold [7]. The horizon decreases for higher energy thresholds. As the effective volume within which the source can contribute shrinks, the flux is strongly suppressed at the highest energies. The "GZK horizon" is smaller

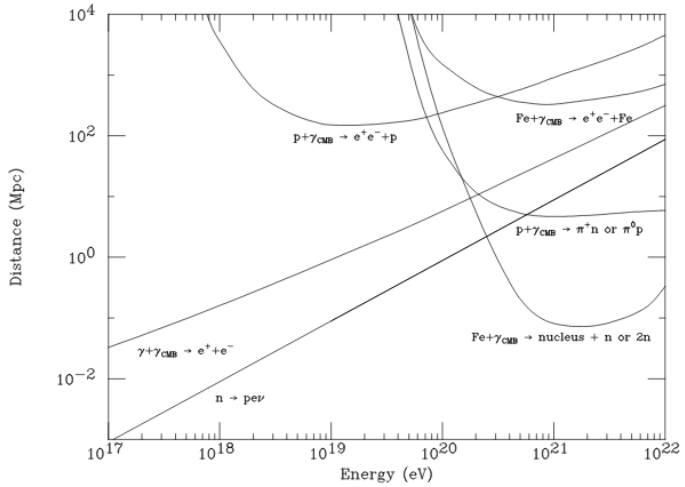

FIGURE 2.2: Panorama of the interactions of possible cosmic primaries with the CMB photons. Curves marked by "$p + \gamma_{\mathrm{CMB}} \rightarrow e^+e^- + p$" and "$Fe + \gamma_{\mathrm{CMB}} \rightarrow e^+e^- + p$" are energy-loss lengths (the distance for which the proton or Fe nucleus loses 1/e of its energy due to pair production). The curve marked by "$p + \gamma_{\mathrm{CMB}} \rightarrow \pi^+ n$ or $\pi^o p$" is the mean free path for photo-pion production of a proton on the CMB. The curve marked by "$Fe + \gamma_{\mathrm{CMB}} \rightarrow$ nucleus $+ n$ or $2n$" is the mean free path for a photo-nuclear reaction in which one or two nucleons are chipped off the nucleus. The curve marked "$\gamma + \gamma_{\mathrm{CMB}} \rightarrow e^+e^-$" is the mean free path for the interaction of a high-energy photon with the CMB. Added for reference is the mean decay length for a neutron indicated by "$n \rightarrow pe\nu$"[30].

for nuclei of intermediate mass, and is of comparable size for protons and iron nuclei (see Figure 2.3). From this figure, we can see that 90% of proton flux with energy greater than 6×10^{19} eV should come from distances smaller than 200 Mpc.

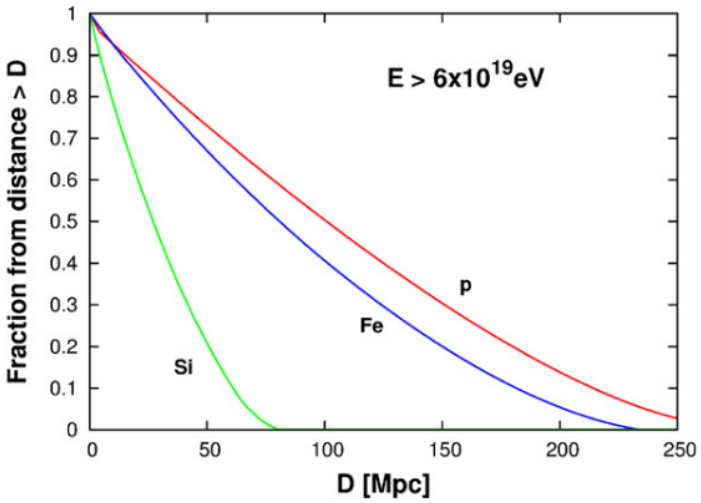

FIGURE 2.3: Fraction of cosmic rays that arrive at Earth with energy above 6 $\times 10^{19}$ eV for protons, silicon and iron from sources that are farther away than a distance D. The sources are assumed to be uniformly distributed with equal intrinsic luminosity and continuous energy loss [7].

The Hires experiment and the Pierre Auger Observatory measured a suppression of the cosmic-ray energy flux above 4×10^{19} eV forty-two years after the predictions of the GZK effect. The AGASA experiment gave unconfirmed evidence for trans-GZK particles [31]. Updated results from Pierre Auger Observatory show a flux suppression with significance of more than 20σ and that the flux at 4×10^{19} eV is half of what would be expected from a power-law extrapolation for smaller energies [32]. Telescope Array (TA) has also observed a flux suppression in the cosmic-ray energy spectrum [33]. The differential energy spectra measured by Auger and TA are compatible within their systematic uncertainties [34].

2.3 Anisotropy

2.3.1 Magnetic Field

Besides the cosmic-ray interaction with the CMB photons, there is also the interaction with cosmic magnetic fields that affect the cosmic ray direction and travel time. Charged particles are subject to the influence of magnetic fields in the source environment, in the intergalactic medium, and in the Galaxy, as shown in Figure 2.4. Thus, protons and heavier nuclei are deflected by the magnetic fields in the Galaxy and intergalactic medium. Very little is known about galactic and especially extragalactic magnetic fields.

A charged cosmic ray that travels a distance D in a regular magnetic field B is deflected with respect to its source by an angle $2.7^{\circ}\frac{6\times10^{19}\text{eV}}{E/Z}\left|\int_0^D \frac{d\mathbf{x}}{\text{kpc}}\times\frac{\mathbf{B}}{3\mu\text{G}}\right|$. Figure 2.5 shows trajectories of protons and iron nuclei in a conventional model for the galactic magnetic field. High energy protons at around 6×10^{19} eV are deflected by only a few degrees from a straight propagation in most parts of the sky, while for iron nuclei of the same energy there is no correlation between their arrival directions and their source positions.

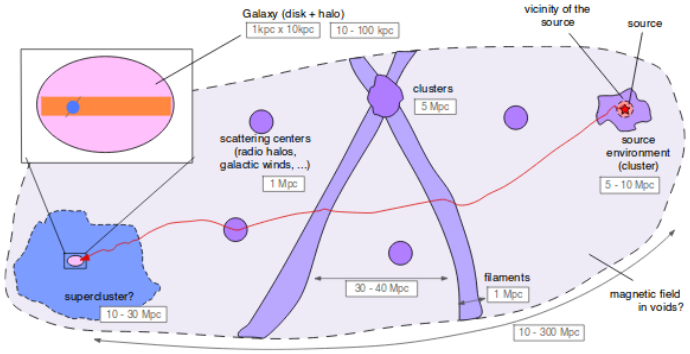

FIGURE 2.4: Representation of magnetized regions intervening in ultra-high energy cosmic ray propagation [35].

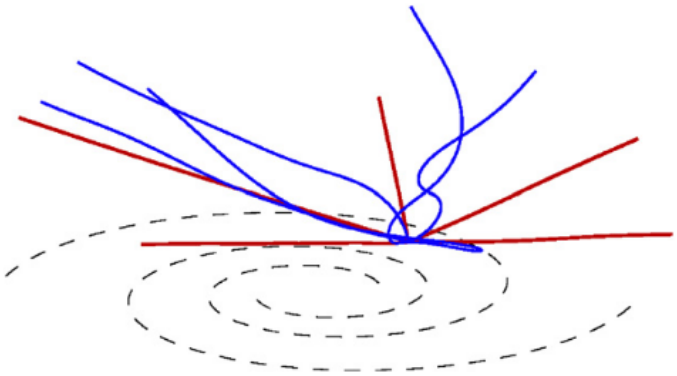

FIGURE 2.5: Trajectories of protons (red) and iron nuclei (blue) both with energy 6×10^{19} eV in a conventional model of the Galactic magnetic field and arrival direction at Earth [7].

Studies related to the Galactic magnetic field observations [36, 37, 38] concluded that the deflection for particles of charge Z and energy E should not exceed $\sim 10^{o}\ Z\ (40\ \mathrm{EeV}/E)$. Since Galactic magnetic fields are not uniform in the sky, angular deflections also depend on the observed direction [39, 40].

The intergalactic/extragalactic magnetic fields are not very well known [41]. The magnetic fields in clusters of galaxies can be estimated by measurements of Faraday rotation, that suggest these magnetic fields have typical strengths $\sim$ 1 - 40 μG. Some models set the origin of the extragalactic magnetic field in the primordial Universe [42]. On the other hand, other models set their origins through magnetic pollution from astrophysical sources such as galactic winds or jets from radio galaxies [43, 44, 45, 46]. The structure and strength of the extragalactic magnetic field can strongly affect the ultra-high energy cosmic-ray propagation.

The Galactic magnetic field is most likely unable to confine cosmic rays above 10^{18} eV. No significant excess of cosmic rays from the directions of the Galactic plane is observed at these energies. Therefore, a plausible origin for the highest energy cosmic rays is the acceleration at extragalactic astrophysical sites. In the following section the corresponding mechanisms for the acceleration of cosmic rays are described.

2.4 Acceleration Mechanisms

Charged particles are accelerated in the presence of electric fields. However, astrophysical plasmas destroy large-scale electric fields in the Universe. Particles can be accelerated by high-voltage drops found in regions of the magnetosphere or the wind of neutron stars, near black holes and their accretion disks. The space and time variations of the magnetic field of astrophysical objects generate transient electric fields which can accelerate cosmic rays. Cosmic rays with energy below 10^{17} eV can be accelerated by the Fermi mechanism of the first order. The Fermi acceleration mechanism was proposed by E. Fermi in 1949 [47]. The first-order Fermi process states that charged particles are accelerated at shock waves of magnetic plasmas and can gain energy as they bounce back and forth. This energy is proportional to the average velocity of the magnetic scattering center in units of c.

On the other hand, the astrophysical processes responsible for the acceleration of cosmic rays above 10^{18} eV are still unknown but there are theoretical models that seek to describe them. The models proposed to solve this question follow the *top-down* and *bottom-up* scenarios. The first one suggests that cosmic rays are produced as secondaries of the decay of very massive, long-lived particles, while in the *bottom-up* scenario, the energetic cosmic-ray proton and nuclei are accelerated in regions of intense magnetic field.

2.4.1 *Top-Down* Scenario

Since astrophysical acceleration up to 10^{20} eV and beyond is very difficult and unlikely, several models were proposed to explain the origin of UHECR. They were called *top-down* to distinguish from the *bottom-up* acceleration process. The *top-down*

model consists of an idea that cosmic-ray particles are originated from the physical process (decay of some supermassive X particles of mass $m_X \gg 10^{20}$ eV) in the early Universe. A detailed explanation of this scenario can be found in [48].

This model has different theories that involve the emission of X particles by topological defects, such as magnetic monopoles or cosmic strings, which are associated with the Grand Unification Theory [49]. On the other hand, these X particles can be remnants of the early Universe with a lifetime longer than the age of the Universe [50]. The *top-down* model generates mostly neutrinos, γ-rays and a small number of protons.

Although these scenarios are very interesting for creating new physics models, their predictions of high neutrinos and γ-rays fluxes are not consistent with the UHECR flux observed by the Pierre Auger Observatory, which reduces the possibility of these models being the emitting sources of UHECR. Moreover, cosmic rays generated by the decay of X particles present a relatively flat energy spectrum, close to a power law with spectral index equal to 1.5 [51], while the standard acceleration energy spectrum observed by HiRes, TA and Pierre Auger Observatory has spectral index exceeding 2.

2.4.2 *Bottom-Up* Scenario

The *bottom-up* model comprises the acceleration of charged particles from lower to higher energies in certain astrophysical environments [48]. In this scenario, the two main cosmic-ray acceleration mechanisms are the diffuse acceleration and Fermi acceleration, which are described in the following sub-sections.

Diffuse acceleration

When charged particles interact with regions of high magnetic field intensity they are accelerated in bursts. An illustration of this acceleration mechanism is shown in Figure 2.6. The energy losses in this regime are determined by the synchrotron limit that is given by [52],

$$-\frac{d\varepsilon^{(-)}}{dt} = \frac{2}{3}\frac{q^2}{R_{\rm L}^2}\left(\frac{\varepsilon}{m}\right)^4 = \frac{2}{3}\frac{q^4}{m^4}\varepsilon^2 B^2 \tag{2.5}$$

where B is the magnetic field strength, q and m are the charge and mass of the particle and ε is the maximal energy.

After each scattering off the flow, the particle travels along the Larmor orbit, radiates and slows down according to,

$$\int_{\varepsilon_0}^{\varepsilon}\frac{d\varepsilon}{\varepsilon^2} = -\frac{2q^4}{3m^4}\int_0^R B^2(x)dx. \tag{2.6}$$

Thus,

$$\frac{1}{\varepsilon} = \frac{1}{\varepsilon_0} + \frac{2q^4}{3m^4}\int_0^R B^2(x)dx. \tag{2.7}$$

The maximum acceleration energy ($\varepsilon = \varepsilon_{CR}$) is determined considering synchrotron energy loss, by setting $\varepsilon_0 \to 0$, as

$$\frac{1}{\varepsilon_{CR}} = \frac{2q^4}{3m^4}\int_0^R B^2(x)dx \simeq \frac{2q^4}{3m^4}B^2R, \tag{2.8}$$

and then we obtain,

$$\varepsilon_{\mathrm{CR}} = \frac{3}{2}\frac{m^4}{q^4}B^{-2}R^{-1}. \tag{2.9}$$

Eq. 2.9 gives an upper limit for the maximum acceleration energy and does not refer to a particular acceleration mechanism.

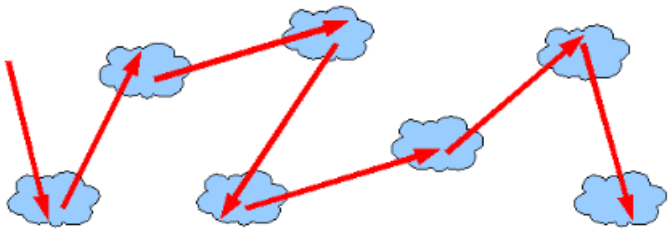

FIGURE 2.6: Schematic illustration of the cosmic-ray diffuse acceleration [53].

Fermi acceleration

Second order Fermi acceleration

In 1949, Enrico Fermi proposed a model to explain the acceleration of relativistic charged particles by means of their interaction with the clouds of the interstellar medium. The particles gain energy after being repeatedly scattered by the interstellar clouds. These clouds act as magnetic mirrors reflecting the particles. A schematic illustration of the scattering process is shown in Figure 2.7.

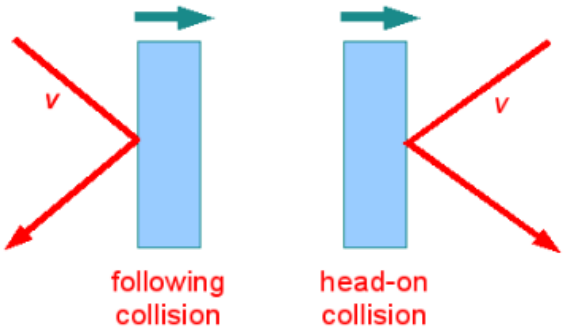

FIGURE 2.7: Second order Fermi acceleration mechanism [53].

The average energy gain of the particle after one collision is given by [53]

$$\left\langle \frac{\Delta E}{E} \right\rangle = \frac{8}{3}\left(\frac{V}{c}\right)^2, \tag{2.10}$$

where V the cloud speed and the particle moves with a relativistic speed, $v \approx c$, respectively. This acceleration process is known as the second order Fermi acceleration as the energy gain depends on the velocity squared of the magnetized cloud, $(V/c)^2$.

From Eq. 2.10 we can derive the energy rate by calculating the average time between particle collisions as

$$\frac{dE}{dt} = \frac{4}{3}\left(\frac{v^2}{cL}\right)E = \alpha E, \tag{2.11}$$

being L the mean free path between the clouds. Solving a diffuse-loss equation in the steady state and taking into account this energy rate, we can find the energy spectrum $N(E)$ as

$$N(E)dE = \text{const.} \times E^{-(1+1/\alpha\tau_{esc})}dE, \tag{2.12}$$

where τ_{esc} is the characteristic time for a particle to stay in the accelerating region.

Although the second-order Fermi acceleration mechanism succeeds in generating a power-law energy spectrum, it is inefficient to accelerate charged particles at ultra-high energies. Moreover, this acceleration mechanism fails to explain the spectral index of 2.7 in the power-law spectrum. The index is obtained by the uncertainty in the combination of $\alpha\tau_{\text{esc}}$ [53]. Thus, this model was modified in 1970 [54] to describe acceleration processes with high efficiency, which is known as the first-order Fermi acceleration mechanism.

First order Fermi acceleration

In the first-order acceleration mechanism the average particle energy gain after each collision is linear in (V/c), making the acceleration process more efficient, mainly at relatively high values of V. When a high-energy particle collides with the shock wave from downstream to upstream or from upstream to downstream there is a strong symmetry due to the isotropic particle velocity distribution in the reference frame where the interstellar cloud is at rest in both sides of the shock wave (see Figure 2.8).

The average particle energy gain in both ways of crossing the shock waves is given by [53]

$$\left\langle \frac{\Delta E}{E} \right\rangle = \frac{4}{3}\left(\frac{V}{c}\right). \tag{2.13}$$

The particle energy after one collision is defined as $E = \beta E_0$, with $\beta = V/c$ and E_0 the initial particle energy. Considering P_{esc} the probability that the particle escapes from the acceleration region (the interstellar cloud) after one collision

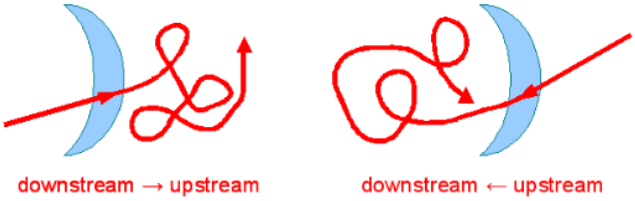

FIGURE 2.8: First-order Fermi acceleration mechanism [53].

and $(1 - P_{esc})$ the probability that the particle remains inside the acceleration region. Using kinetic theory we have

$$P_{esc} = \frac{4}{3}\left(\frac{v}{c}\right). \tag{2.14}$$

The energy spectrum can be obtained as

$$N(E)dE = const. \times E^{-1+\frac{\ln P_{\rm esc}}{\ln \beta}} dE. \tag{2.15}$$

Replacing Eqs. 2.13 and 2.14 in Eq. 2.15, we have

$$N(E)dE = \text{const.} \times E^{-2}dE. \tag{2.16}$$

The first-order acceleration mechanism is very effective and promising since it is based on charged-particle collisions with shock waves, which are present in distinct astrophysical environments. Although the obtained spectral index is different from the observed one (2.7), it is a fixed numerical value and not an expression as in the second-order Fermi mechanism.

Possible accelerating astrophysical sources for the *bottom-up* scenario are Gamma Ray Bursts (GRB) and Galactic Active Nuclei (AGN). These sources and other possible candidate sources of UHECR are discussed in the next section.

2.5 Candidate Sources and Cosmic Ray Accelerators

The motivation to search for UHECR sources is based on the fact that as the Larmor radius (radius of gyration of a particle) in the magnetic field is larger than the thickness of the Galactic disk, the UHECR is not confined in the galaxy. Moreover, astrophysical objects and the magnetic-field strength should be large and strong to accelerate particles up to 10^{20} eV. The Larmor radius r_L increases with the particle energy E according to [55]

$$r_L = \frac{1.1}{Z}\left(\frac{E}{10^{18}\text{eV}}\right)\left(\frac{B}{\mu\text{G}}\right)^{-1} \text{kpc}. \tag{2.17}$$

The energy of a cosmic-ray particle with charge Ze is naturally limited by the Hillas criterium, which postulates that the Larmor radius of the particle cannot

be larger than the size of the source (R_{source}). Thus, the maximum energy a particle can reach is given by

$$E_{\text{max}} \simeq Z \left(\frac{B}{\mu\text{G}}\right) \left(\frac{R_{\text{source}}}{\text{kpc}}\right) \times 10^{18}\text{eV}. \tag{2.18}$$

Figure 2.9 shows the Hillas plot [56] in which this particle-energy limitation can be seen. This diagram aims to classify some UHECR accelerators by means of the characteristic magnetic-field strength B and its size R. From this figure, for UHECR around 10^{12} GeV the number of sources is very sparse. For protons, the plausible candidate sources are radio galaxy lobes and clusters of galaxies. For nuclei, the potential candidate sources are terminal shocks of galactic superwinds which originate in the metally-rich starburst galaxies.

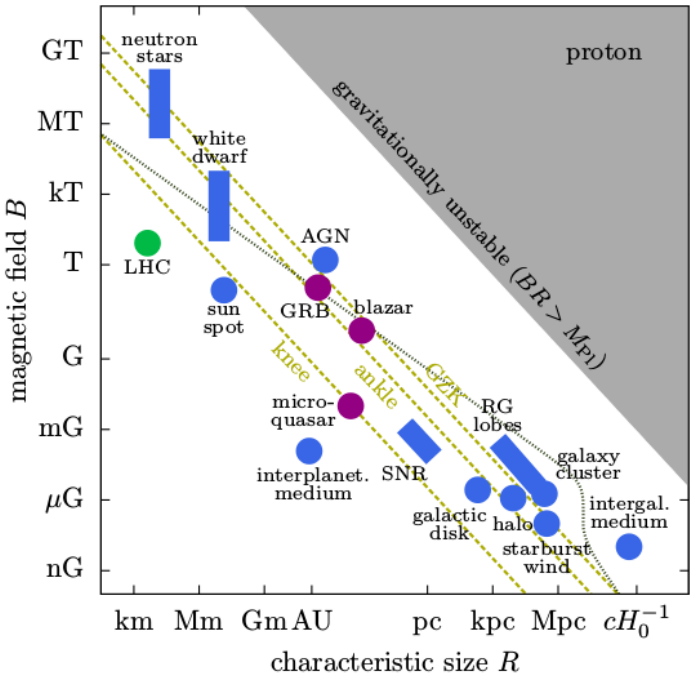

FIGURE 2.9: The Hillas plot for various cosmic-ray candidate sources in blue. The jet-frame parameters for blazars, gamma-ray bursts and microquasars are shown in purple. The golden dashed lines correspond to the lower limit for proton accelerator at the *knee* ($\sim 10^{14.5}$ eV), *ankle* ($\sim 10^{18.5}$ eV) and GZK suppression region ($\sim 10^{19.6}$ eV). The dotted gray lines are the upper limits for proton interaction with the CMB photons and synchrotron loss [57].

2.5.1 General constraints from geometry and radiation

Astrophysical objects have to fulfill several general constraints to be considered as possible sources of UHECR [52]. These criteria are summarized below:

• **geometry** - the accelerated particle should be inside the astrophysical source while it is accelerated;

• **power** - the source should have the sufficient amount of energy to give to the accelerated particle;

• **radiation losses** - the energy lost for radiation by a particle should not exceed the energy gain in the accelerating field;

• **interaction losses** - the energy lost in interactions by a particle with other particles should not exceed the energy gain;

• **emissivity** - the total density and power of sources must be able to account for the observed UHECR flux;

• **accompanying radiation** of photons, neutrinos and cosmic rays of low energies should not be greater than the observed fluxes. This constraint should be satisfied for a given source and for the diffusive background.

2.5.2 Active Galactic Nuclei (AGNs)

AGNs are galaxies composed of an accretion disk around a central super-massive black hole and are sometimes associated with jets terminating in lobes that can be detected in radio [57]. These galaxies have an unusual luminosity, which is much higher than the normal luminosity in almost all the electromagnetic spectrum. The emission excess was observed in radio, microwave, infrared, optical, ultraviolet, X-ray and gamma-ray frequency bands. A great fraction of the AGN luminosity is from the non-thermal emission of the galactic nuclei. The AGNs are the most luminous sources of electromagnetic radiation in the Universe.

The AGNs can be classified in radio-quiet and radio-loud categories. The first one comprises objects that have no prominent radio emission or jets, and the second one objects presenting jets.

Radio-quiet AGN

• **Seyfert galaxies**

The Seyfert are spiral galaxies with bright emission line nuclei. These galaxies often have starburst activity and do not have relativistic jets in large scale [52]. They were first observed in 1943 and are the most common astrophysical objects in the Universe. They are divided into two types Seyfert I and II. A Seyfert I galaxy is characterized by the broad emission lines and is likely to show strong X-ray emission of low energy. On the other hand, Seyfert II has narrow emission lines.

• **Quasars**

Quasars are distant objects and are defined by their optical properties. They are first identified as radio emission sources and in photographic images, they appear as point sources indistinguishable from stars, that is why they are called quasars (quasi-stellar radio source). They emit energy across the electromagnetic spectrum, from X-rays to the far infrared. Some quasars are the very strong emitter of radio waves and gamma-rays.

Radio-loud AGN

• Radio galaxies

Radio galaxies are radio-loud elliptical galaxies with relativistic jets [58]. They can be classified into two luminosity classes, the Fanaroff-Riley I (FRI) and Fanaroff-Riley II (FRII). In FRI type the radio emission is less powerful and the jet is brighter towards the core. On the other hand, for FRII type the radio emission is more powerful and the jets are brighter at the hot spots at their endpoints [52].

• Blazars

Blazars are point-like objects with non-thermal energy spectrum. They can be associated with radio galaxies whose jets are pointed towards the observer. Moreover, they may be classified into two types of objects: i) the BL Lac type objects which are possible counter-parts of FRI radio galaxies with no emission lines, and ii) optically strongly variable quasars which are possible counterparts of FRII with very powerful emission [52].

The unification scheme of AGNs is summarized in Figure 2.10. The two main parameters are i) the orientation of the AGN with respect to the line of sight, which determines the detectability of the central engine and the broad line region in the optical domain and ii) the radio loudness, which indicates whether or not the AGN produces a significant jet [59].

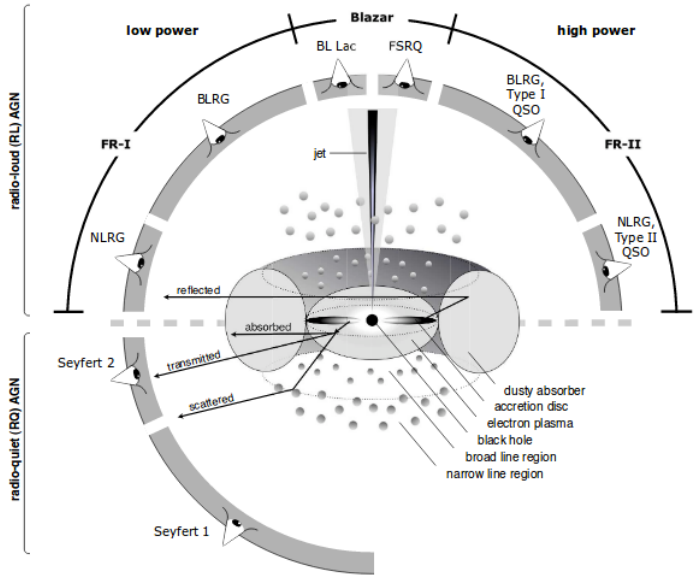

FIGURE 2.10: Schematic representation of the AGN classification. Radio-loud objects are generally thought to display symmetric jet emission [59].

2.5.3 Gamma-Ray Bursts (GRB)

The GRB explosion leads to the formation of multiple shock regions which are potential acceleration zones for UHECR [35]. The origin of GRB up to GeV could be explained by merges of black holes or neutron stars and the collapse of massive stars. Acceleration of electrons to relativistic velocities generates gamma-ray emission via synchrotron radiation and inverse Compton scattering process. Electrons and protons are accelerated through the first-order Fermi acceleration mechanism, i. e., the acceleration mechanism of UHECR in GRB is diffuse. The GRB average energy emission rate is consistent with the luminosity required for cosmic rays with energy above 10^{19} eV. This makes GRB possible emitting sources of cosmic rays.

2.5.4 Neutron Stars

Neutron stars are the smallest and the densest stars ever known [60]. According to Hillas plot (Figure 2.9), the neutron stars are the most favorable candidate sources for the acceleration of UHECR, however, they are scarcely discussed in the literature. They host the highest known magnetic fields in the Universe. Magnetars are neutron stars with strong magnetic fields of the order 10^{15} G [35], while normal neutron stars have $\sim 10^{12}$ G [52]. The magnetars are also good cosmic-ray accelerator candidates.

Detection of High Energy Cosmic Rays

The phenomenology of air showers induced in the atmosphere by cosmic-ray particles and the different detection methods used to measure the shower properties are described in this chapter. Moreover, a mass composition review using different shower observables is also presented.

3.1 Extensive Air Showers

When the primary cosmic ray enters the top of the Earth's atmosphere at a typical height of 15 km, it interacts with the atmospheric nuclei, mainly Oxygen, Nitrogen and Argon, producing secondary particles as hadrons (mainly charged and neutral pions, kaons and baryons), which depending on their energy decay or interact with other atoms of the atmosphere producing tertiary particles and so on. This particle cascade is called Extensive Air Shower (EAS). The number of particles in an EAS starts rapidly to increase as the shower evolves down in the atmosphere, then reaches a maximum and attenuates as particles fall below the threshold for further particle production [61]. A schematic illustration of the shower development can be seen in Figure 3.1.

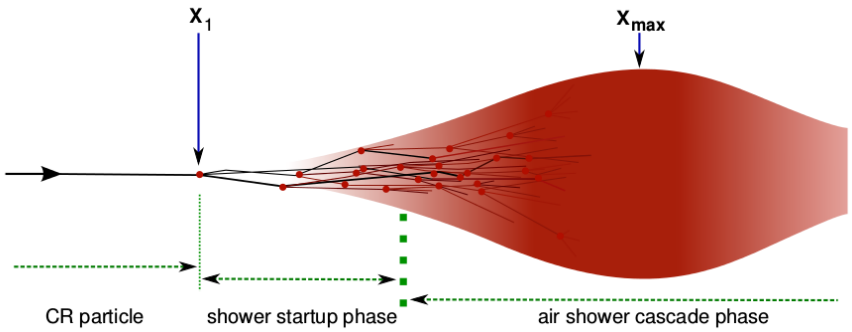

FIGURE 3.1: Simple description of an EAS development [62].

The secondary particles created in an EAS can be grouped into hadronic, muonic and electromagnetic component. Figure 3.2 illustrates the three air shower components. The size of the EAS at sea level depends on the energy, type, and arrival direction of the primary particle. For shower energy of 10^{18} eV the footprint of secondary particles on the ground is usually $\sim$1 km^2 and increases with energy [63]. Moreover, the shower content at sea level is composed of 90% of the electromagnetic

component, 9% of the muonic component and only 1% of the hadronic component. A better description and understanding of the cosmic-ray air shower components is discussed in the following section.

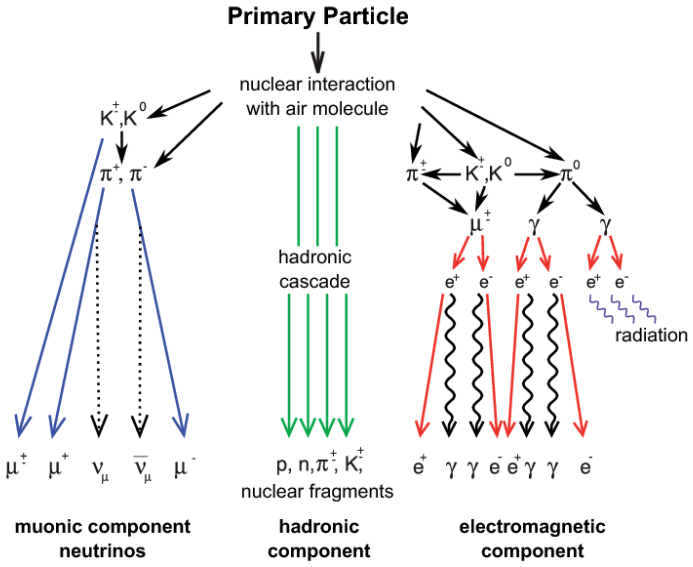

FIGURE 3.2: Schematic illustration of the EAS development with the hadronic, muonic and electromagnetic component respectively [64].

3.1.1 Hadronic Component

The shower core is composed of high-energy hadrons which are responsible for the energy transport and supply in the shower development. The hadronic component reveals intrinsic information about the energy and mass of the primary cosmic-ray particle.

The hadron component is composed mainly of mesons and some baryons produced in rare cases. The most frequent hadrons are pions (90%) followed by kaons (10%). Since pions and kaons are unstable particles, they decay producing stable particles, such as photons from $\pi^0 \rightarrow \gamma\gamma$, feeding the electromagnetic cascade, and muons and neutrinos from $\pi^+ \rightarrow \mu^+ + \nu_\mu$ and $\pi^- \rightarrow \mu^- + \nu_\mu$, forming the muonic component. Moreover, kaons also decay via process $K^{+/-} \rightarrow \mu^{+/-} + \nu_\mu$, producing muons and via decay mode $K^{+/-} \rightarrow \pi^{+/-} + \pi^0$, producing neutral and charged pions.

The hadronic cascade comes to an end when the decay probability of the charged pions is larger than the probability that they interact. The critical energy of the charged pion marks the energy at which most pions decay and its value depends on the zenith angle of the primary cosmic ray, ranging from 10 GeV to beyond 100 GeV [62].

3.1.2 Muonic Component

As described above, muons are generated via positive and negatively charged pion decay. The number of muons in an air shower depends on the pion decay probability before interacting with the atmospheric nucleus. Moreover, the muonic content is sensitive to the initial baryonic content of the primary particle, as well as its energy and local air density. For an air shower initiated by a vertical proton with energy 10^{20} eV, there are about 5×10^8 muons at sea level with energy above 10 MeV [65]. Muons have a smaller cross section for radiation and pair production than electrons and, therefore, this component develops differently in the atmosphere than the electromagnetic one. Thus, as muons interact weakly with matter they suffer small multiple scattering during their propagation in the atmosphere and, therefore, they arrive at earlier times at ground level than does the electromagnetic component. Most muons are produced at a height of about 15 km and they propagate with an average velocity of about $0.9998c$ (c is the speed of light). This high speed dilates the muon lifetime in the laboratory frame, allowing that most muons arrive at the ground. On the other hand, only a few low energy muons (with a lifetime of 2.19703 $\pm$ 0.00004 μs) decay before reaching the ground via the process

$$\mu^{\pm} \rightarrow e^{\pm} + \nu_e(\bar{\nu}_e) + \nu_\mu(\bar{\nu}_\mu), \tag{3.1}$$

and, therefore, contribute to the electromagnetic component.

High-energy muons can be detected at sea level and they can provide information about the process involved in the shower development as the muonic component is coupled with the hadronic one. Thus, muons can be used to study cosmic-ray mass composition as their multiplicity depends on the atomic number of the primary particle.

3.1.3 Electromagnetic Component

The electromagnetic component consists of electrons, positrons and photons produced by charged and neutral meson decay. At sea level, the muon decay is the dominant source of low energy electrons. Moreover, photon-induced showers are even more dominated by the electromagnetic channel. Photons are produced via neutral pion decay high in the atmosphere. When a photon interacts with an air nucleus X, an electron-positron pair is produced according to the following reaction

$$\gamma + X \rightarrow e^+ + e^- + X. \tag{3.2}$$

Electrons and positrons are produced in the neighborhood of a nucleus via *bremsstrahlung* process

$$e^{\pm} + X \rightarrow e^{\pm} + \gamma + X. \tag{3.3}$$

Due to the small radiation length X_0 in the air (≈ 37 g/cm^2) and the low critical energy ≈ 84 MeV, the number of electrons rapidly increases, reaching its

maximum as electrons and positrons get close to the critical energy. Below this energy, the particles lose energy by ionization, decreasing exponentially after reaching the shower maximum. The integrated vertical intensity of electrons and positrons is about 30, 6 and 0.2 m^{-2} s^{-1} sr^{-1} above 10, 100 and 1000 MeV respectively [66, 67]. The ratio between the number of photons and electrons plus positrons is about 1.3 above 1 GeV and 1.7 below the critical energy. The electromagnetic cascade dissipates about 90% of the energy of the primary particle, so the total number of electromagnetic particles in a shower is nearly proportional to the shower energy.

For a vertical proton induced air shower with energy 10^{20} eV, there are about 10^{11} secondary particles that reach the ground level with energy above 90 keV. Of these, 90% are photons, electrons, and positrons with a mean energy of about 10 MeV. These particles are distributed all over a region that extends from 8 m to 8 km from the shower core [65].

It is worth saying that the electromagnetic component at the ground changes dramatically according to the zenith angle of the primary particle. For very inclined air showers ($\theta > 70^{o}$) the electromagnetic component is exponentially attenuated with atmospheric depth and is almost completely absorbed before reaching the ground [65].

The electromagnetic cascade comes to an end when electrons lose more energy in collisions than in radiative process and get absorbed by the atmosphere. Part of the electron energy is released in the atmosphere as fluorescence light. Electrons and muons moving at relativistic speeds emit Cherenkov light which is emitted in the forward direction [62].

3.1.4 Heitler Model for Air Showers

A qualitative treatment of the extensive air shower through detailed analytical calculation is necessary to infer information about the properties of the primary cosmic ray that induced those showers. The development of an air shower is a combination of hadronic and electromagnetic cascades.

Before the era of high-speed computing, Heitler presented a model for the electromagnetic cascade development. Later, he and others developed more sophisticated tools to better analyse the physical effects in the shower development (see ref. [61] for further details).

Electromagnetic Showers

An electron after travelling a distance $d = \lambda_r \ln 2$, with λ_r as the radiation length in air ($\lambda_r \approx 37$ g/cm^2), radiates a single photon, losing half of its energy. The photon produces an electron-positron pair after traveling the same distance as the electron. In this model, any interaction of a particle (electron or photon) with energy E leads to two new particles (electron, positron, or photon) with energy $E/2$. After n consecutive interactions, the number of particles at a given depth, $X = n\lambda_r \ln 2$, is given by $N(X) = 2^n = e^{x/\lambda_r}$ and the particle energy is given by $E(X) = E_0/2^{X/\lambda_r}$ (E_0 is the primary particle energy) [68] (see Figure 3.3). When the particle (electron or

photon) energy is too low for pair production or *bremsstrahlung* there is no more particle production. This energy is referred as the particle critical energy E_c, which in the air is equal to 85 MeV [69].

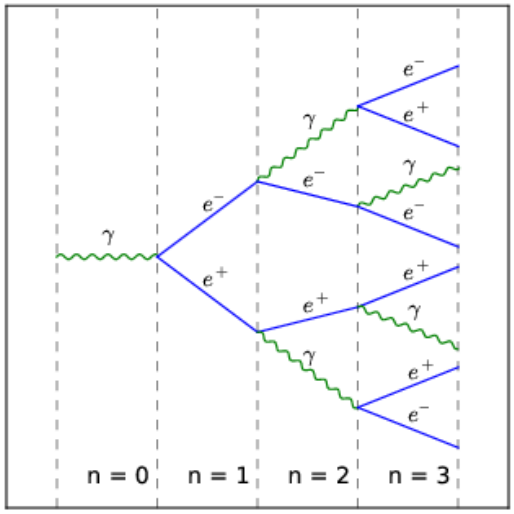

FIGURE 3.3: Schematic illustration of the electromagnetic cascade in Heitler model [70].

The number of particles in the cascade reaches a maximum $N(X) = N_{max}$ when all particle energies are $E = E_c$, so that,

$$N_{max} = \frac{E_0}{E_c}. \tag{3.4}$$

The depth at which the number of particles is maximum, X_{max}, is obtained by calculating the required number of particle interactions n_c, so that the energy per particle is reduced to the critical energy E_c. Thus, considering $N_{max} = 2^{n_c}$, we have from Eq. 3.4, $n_c = \ln(E_0/E_c)/\ln 2$. Then the depth of the shower maximum for pure electromagnetic cascade X_{max}^{EM} is given by [69]

$$X_{max}^{EM} = n_c \lambda_r \ln 2 = \lambda_r \ln\left(\frac{E_0}{E_c}\right). \tag{3.5}$$

From the expressions above, the number of particles at shower maximum is proportional to the energy of the primary particle E_0 and the depth of the shower maximum X_{max}^{EM} depends logarithmically on E_0. These results are in good agreement with detailed simulations and experiments, showing that the Heitler model reproduces very well the two basic features of the electromagnetic cascade [68].

Hadronic Showers

It is possible to extend the Heitler model for hadron-induced showers by writing a set of cascade equations. The hadronic particle interacts with an air nucleus after

traversing one atmospheric layer with thickness $\lambda_I \ln 2$ (λ_I is the interaction length and has a constant value) producing N_{ch} charged pions and $\frac{1}{2}N_{ch}$ neutral pions (see Figure 3.4). For pions in air we have $\lambda_I \approx 120$ g/cm^2 [61]. The neutral pions almost immediately decay into two photons and the charged pions interact with the air nuclei after travelling through another layer. Once the charged pion energy is below the critical energy E_c^π, these particles decay yielding muons.

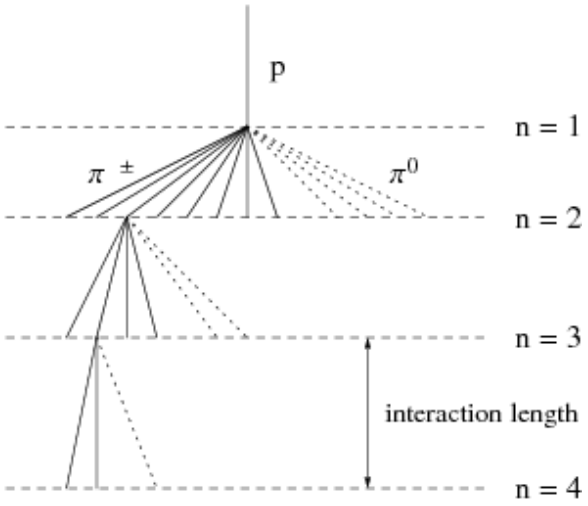

FIGURE 3.4: Schematic illustration of the hadronic cascade. The dashed lines correspond to the neutral pions, while the solid lines represent the charged pions. The neutral pions quickly decay producing electromagnetic sub-showers which are not shown in the diagram. After the second level (n=2) the pion lines are not shown [71].

Firstly the hadronic cascade model is treated for proton-induced air shower, and later the results can be extended to heavier nuclei as primary particles.

Assuming that a cosmic-ray proton enters the atmosphere with energy E_0, after n interactions with air nuclei there are $N_\pi = (N_{ch})^n$ charged pions. In each interaction two-thirds of the initial energy is transferred to the charged pions, so after n atmospheric layers, these pions have a total energy of $\left(\frac{2}{3}\right)^n E_0$. The one-third left of the primary energy is transferred to the electromagnetic component via neutral pion decay. Each charged pion has an energy at each atmospheric layer n given by [69]

$$E_\pi = \frac{E_0}{\left(\frac{2}{3}N_{ch}\right)^n}. \tag{3.6}$$

After a considerable number of interactions, E_π becomes smaller than E_c^π.

The required number of interactions to have $E_\pi = E_c^\pi$, using Eq. 3.6, is given by [69]

$$n_c = \frac{\ln\left(\frac{E_0}{E_c^\pi}\right)}{\ln\left(\frac{3}{2}N_{ch}\right)} = 0.85\log_{10}\left(\frac{E_0}{E_c^\pi}\right) \tag{3.7}$$

Muon and Electron sizes

The number of muons in the shower is obtained assuming that all pions decay, i. e., using $N_\mu = N_\pi = (N_{ch})^{n_c}$. The energy dependence of the muon size is derived from applying Eq. 3.7. Then, we have

$$\ln N_\mu = n_c \ln N_{ch} = \beta \ln\left(\frac{E_0}{E_c^\pi}\right) \tag{3.8}$$

,
with

$$\beta = \frac{\ln(N_{ch})}{\ln\left(\frac{3}{2}N_{ch}\right)} = 0.85. \tag{3.9}$$

However, during the shower development the parameter N_{ch} changes and β depends only on the logarithm of its value.

Thus, the muon size in a proton-induced air shower in the Heitler-Matthews model is given by

$$N_\mu = \left(\frac{E_0}{E_c^\pi}\right)^\beta \approx 10^4 \left(\frac{E_0}{1\,\mathrm{PeV}}\right)^{0.85}. \tag{3.10}$$

Several EAS Monte Carlo simulation studies reported β values ranging from 0.85 to 0.92 [72].

From the above expression, we can see that the muon number in an air shower depends on the primary cosmic-ray energy, the air density, and the charged-particle multiplicities of hadronic interactions, as already mentioned in section 3.1.2.

The electron size is estimated considering the conservation energy principle which implies that the primary cosmic-ray energy is split into hadronic and electromagnetic components ($E_0 = E_h + E_{em}$). The hadronic energy appears in the muon component as $E_h = N_\mu E_c^\pi$. Thus, the energy fraction going into the electromagnetic component can be written as

$$\frac{E_{em}}{E_0} = \frac{E_0 - N_\mu E_c^\pi}{E_0} = 1 - \left(\frac{E_0}{E_c^\pi}\right)^{\beta-1}, \tag{3.11}$$

with β from Eq. 3.9. For a primary proton with $E_0 = 10^{14}$ eV, after four interactions the individual pion energy is 30 GeV, using N_{ch}=10, while for $E_0 = 10^{17}$ eV, the pion energy is 10 GeV. Thus, the pion critical energy slowly decreases with increasing

primary energy. For $E_0 = 10^{14}$ eV the electromagnetic fraction is 79% and 91% at $E_0 = 10^{17}$ eV.

Approximating Eq. 3.11 by a power-law function, we have

$$\frac{E_{\rm em}}{E_0} \approx \left(\frac{E_0}{E_{\rm c}^{\pi}}\right)^{\alpha}. \tag{3.12}$$

After comparing series expansions near $E_0 = 10^5 E_{\rm c}^{\pi}$, the electron size as a function of the energy is given by

$$N_{\rm e} = \frac{1}{\rm g}\frac{E_{\rm em}}{E_{\rm c}^{\rm e}} \approx 10^6 \left(\frac{E_0}{1\,\rm PeV}\right)^{\alpha}, \tag{3.13}$$

with g as a constant equal to 10. The value of g can vary when comparing the electron size with experimental measurements.

In Eq. 3.13, $\alpha = 1 + \dfrac{1-\beta}{10^{5(1-\beta)}-1} \approx 1.03$.

From Eq. 3.13 the number of electrons increases with the primary energy slightly faster than exactly linear. It is worth saying that in this model the absorption in the atmosphere is not taken into account, so the estimated number of electrons is valid at shower maximum.

Depth of shower maximum

The atmospheric depth at which the air-shower electrons and photons reach their maximum number is called $X_{\rm max}$. As previously mentioned, the electromagnetic component is generated via neutral pion decays. In the hadronic interaction one-third of the initial energy ($1/3E_0$) goes to the electromagnetic component. For a simple estimation of the $X_{\rm max}$ only the first generation of electromagnetic showers will be used. This method underestimates the evaluation of $X_{\rm max}$ because it neglects all the additional showers from each subsequent interaction point.

The primary particle interaction cross-section and the particle multiplicity from the first interaction depend on the primary energy. In fact, the higher the primary energy, the higher is the interaction cross-section, causing the shower to start higher in the atmosphere.

The first hadronic interaction occurs at an atmospheric depth $X_0 = \lambda_i \ln 2$, with λ_i as the interaction length of the primary proton. Approximating λ_i using the inelastic cross-section for proton-air interactions we obtain

$$X_0 = \lambda_i \ln 2 = (61\,{\rm g/cm^2}) \left(1.0 - 0.1 \left(\frac{E_0}{1\rm PeV}\right) \ln 2\right). \tag{3.14}$$

In the first interaction, half of the $N_{\rm ch}$ neutral pions are produced, yielding $N_{\rm ch}$ photons. Each photon starts an electromagnetic shower with energy $E_0/(3N_{\rm ch})$, which develops in parallel with the others. The charged-particle production in the first interaction can be parametrized for energies around 1 PeV as

$$N_{ch} = 41.2 \left(\frac{E_0}{1\,\mathrm{PeV}} \right)^{1/5} \tag{3.15}$$

In an analogous way to the determination of X_{max} for a pure electromagnetic shower (Eq. 3.5), the shower maximum for hadronic interaction is obtained considering an electromagnetic shower of energy $E_0/(3N_{ch})$ starting after the first interaction at depth X_0. Then, we have

$$X^{p}_{max} = X_0 + \lambda_r \ln \left(\frac{E_0}{(3N_{ch}E^{EM}_c} \right). \tag{3.16}$$

Using Eqs. 3.14 and 3.15 in Eq. 3.16, we obtain

$$X^{p}_{max} = \left(470 + 58 \log_{10} \left(\frac{E_0}{1\,\mathrm{PeV}} \right) \right) \mathrm{g/cm^2}. \tag{3.17}$$

The values of the obtained X^{p}_{max} are lower when compared to simulations by a factor of 110 $\mathrm{g/cm^2}$ or a bit less than $2\lambda_r$. This is because of neglecting the contributions of the next one or two generations of neutral pion production.

An important aspect of the hadronic interaction was not taken into account in the hadronic cascade model described above. When there is an interaction between two hadrons only a fraction of the total energy is available for secondary particle production (both $\pi^{\pm}$ and π^0, which is characterized by an *inelasticity* parameter κ). The remaining energy fraction is carried away by a single 'leading' particle. The value of κ is about 0.5, but it is not well understood at high energy. In the model described above it was considered κ = 1.0. So, considering κ = 0.5 in Eq. 3.17, X^{p}_{max} will systematically raise by $\sim 58\log_{10}(2)$ = 17 $\mathrm{g/cm^2}$.

Heavier primaries

In the simplified shower model shown above only proton-induced air showers were considered. In order to extend this approach to an air shower induced by a heavy nucleus, the *superposition model* is used [69]. A heavy cosmic ray with atomic number A and energy E_0 is taken as A single nucleons like proton showers, each with energy E_0/A, starting at the same point, each nucleon acting independently.

It is possible to derive generalized expressions for the shower observable features for a heavy cosmic ray by substituting E_0 by E_0/A and summing A such showers where appropriate in the formulas previously described for the proton interaction model. Therefore, the resulting shower properties for nuclei-induced showers are expressed in terms of the corresponding quantities of a proton with the same energy E_0.

The number of muons in heavy-nuclei showers, using Eq. 3.13, is given by

$$N_{\mu}^{A} = A\left(\frac{E_0}{(AE_c^{\pi})}\right)^{\beta} = \left(\frac{E_0}{E_{\pi}^{c}}\right)^{\beta} A^{(1-\beta)} \approx 1.69 \times 10^4 \cdot A^{0.07}\left(\frac{E_0}{1\,\mathrm{PeV}}\right)^{0.93}. \quad (3.18)$$

From Eq. 3.18 we can see that the number of muons increases almost linearly as a function of the primary energy E_0 and increases with the mass of the primary by a factor proportional to $A^{0.07}$. Therefore, an iron-induced air shower has about $(56)^{0.15}$ = 1.8 more muons than a proton shower of the same energy.

The number of electrons is given by

$$N_{e}^{A} = \frac{1}{g}\frac{E_{em}}{E_c} \approx 10^6 \cdot A^{1-\alpha} \cdot \left(\frac{E_0}{1\,\mathrm{PeV}}\right)^{\alpha} \approx 10^6 \cdot A^{-0.03} \cdot \left(\frac{E_0}{1\,\mathrm{PeV}}\right)^{1.03}. \quad (3.19)$$

The number of electrons in an air shower induced by a heavy nucleus increases slightly faster with increasing energy but decreases with increasing mass number. So, a shower induced by a heavier nucleus has a smaller electron number than showers induced by lighter primaries of the same energy.

The depth of shower maximum, using Eq. 3.16, is given by

$$X_{max}^{A} = X_{max}^{p} - \lambda_r \ln A. \quad (3.20)$$

From Eq. 3.20 we can see that an air shower induced by a heavy nucleus has a shower maximum higher in the atmosphere than lighter primaries. In general, an iron shower has an X_{max} shallower by $\lambda_r \ln(56)$ = 150 g/cm^2 at all energies compared to a proton shower.

Since muons are mainly produced in hadronic interactions in the atmosphere, their number can be used as mass-composition sensitive parameter of primary cosmic rays. Figure 3.5 shows the distributions of the muon number as a function of the electron number for vertical showers induced by proton, iron and gamma-ray with different energies. These showers were simulated with different hadronic interaction models (QGSJET 01, QGSJET II-3 and Sibyll 2.1). The distributions are in good agreement with the expectations of the *superposition model*. Due to the limited knowledge about the hadronic multiparticle production at high energies, the discrimination power of electron-muon number has large systematic uncertainties [73]. The used hadronic interaction models are described in the following section.

Hadronic Interaction Models

UHECR are studied using different EAS experimental techniques. The properties of the cosmic-ray particles are measured analyzing the characteristics of nuclear-electromagnetic cascades induced by the cosmic-ray interaction in the atmosphere [74]. So the use of Monte Carlo simulations is of great importance, particularly, for

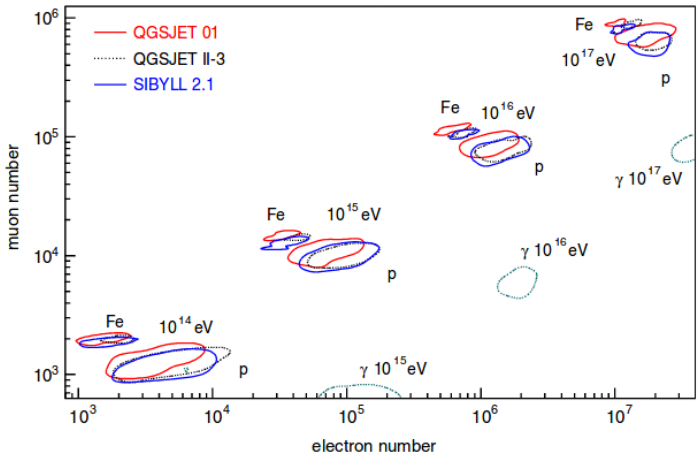

FIGURE 3.5: Expected number of muons and electrons for vertical showers induced by protons, iron and gamma-rays of different energies as primaries. The curves represent the Full Width at Half Maximum (FWHM) of the particle distributions for three different hadronic interaction models (QGSJET 01, QGSJET II-3 and Sibyll 2.1) [73].

the different nuclear interaction process. The success of the very different experimental studies is deeply related to the validity of the different hadronic interaction models used in the analyses.

Cosmic-ray observables used to determine the primary cosmic-ray particle depend on the hadronic interaction process. The muon number N_μ at the ground depends on the properties of the pion interaction with the air nuclei and the multiplicity of the charged hadrons produced, as well as their spectral shape. The depth of shower maximum X_{max} depends on the interaction of the primary particle with the air nuclei, the inelastic cross section and produced secondary hadron spectra.

Several hadronic interaction models at high energies have been applied to study the cosmic-ray air showers. They are based on the extrapolation of the results from the Large Hadron Collider (LHC) data to higher energies combined with different theories of physics. The most common high-energy models used are QGSJETII [75, 76], EPOS [77, 78] and Sibyll [79].

QGSJET and EPOS employ the semihard Pomeron model, treating both contributions within the Reggeon Field Theory framework. On the other hand, Sibyll is based on the minijet model. Recently, a new version of Sibyll was released that describes better the multiparticle production aiming more accurate and reliable predictions of the EAS development and the calculations of the lepton flux.

Figures 3.6 and 3.7 show the predictions for the number of muons and X_{max} for air showers simulated with QGSJETII-04, EPOS-LHC, Sibyll 2.1 and Sibyll 2.3rc3b. The muon-number predicted with Sibyll model has increased and is very similar to QGSJETII-04. Moreover, showers simulated with Sibyll 2.3rc3b develop deeper in the atmosphere and the obtained values for the X_{max} show a heavier mass composition than before with Sibyll version 2.1.

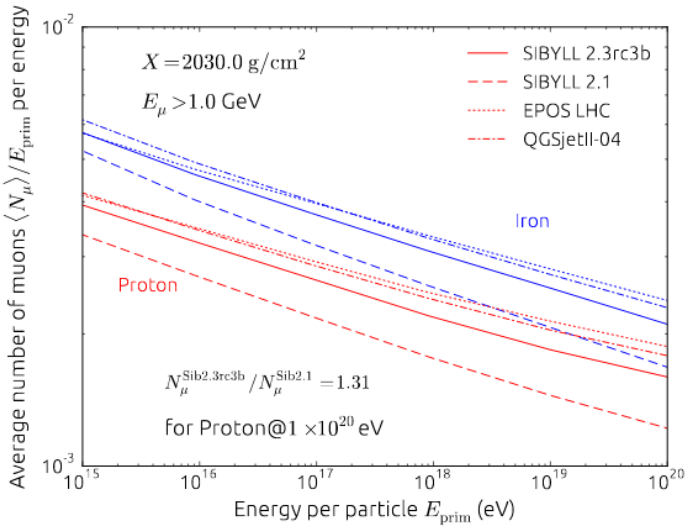

FIGURE 3.6: Comparison of predictions of hadronic interaction models of the mean number of muons at a shower depth of 1000 g/cm^2 [79].

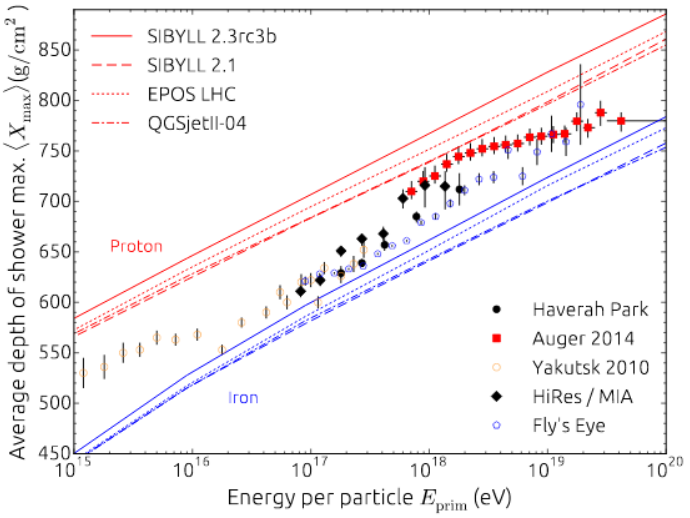

FIGURE 3.7: Comparison of predictions of hadronic interaction models for the shower maximum X_{max} [79]. The results of the models are plotted together with the measurements of different cosmic-ray experiments [11, 80].

3.2 Detection Techniques

Cosmic rays with energy below 10^{13} eV are plentiful and can be directly measured above the Earth's atmosphere with balloon-borne or satellite experiments. On the other hand, for higher energy cosmic rays ($E > 10^{14}$ eV) the flux becomes so low that they cannot be directly detected [55], otherwise we would need to lift a detector big enough above the atmosphere to detect a significant amount of cosmic ray particles. For energies above 10^{18} eV, the cosmic ray flux is of one particle per week per square kilometer. Above 10^{20} eV, the flux drops to one particle per square kilometer per century. Higher energy cosmic rays have enough energy to develop a particle cascade in the atmosphere. Those air showers contain millions of secondary particles that reach the Earth's surface over a large area of square kilometers. Therefore a big array of ground-based detectors is needed to detect those secondary particles in order to determine the primary cosmic-ray particle.

Classical and very successful measurement techniques of high energy cosmic rays rely either on arrays of several particle detectors (such as scintillators and water-Cherenkov detectors) covering a large area, or optical detectors which consist of fluorescence telescopes that detect the particle ionization loss in the atmosphere in the form of visible light. Another EAS detection method, with a higher duty cycle which is very promising comprises the detection of radio pulses emitted by the electromagnetic component of the air shower. Figure 3.8 shows a schematic illustration of the possible detection techniques for cosmic-ray air showers. All these techniques are better described in the following sections.

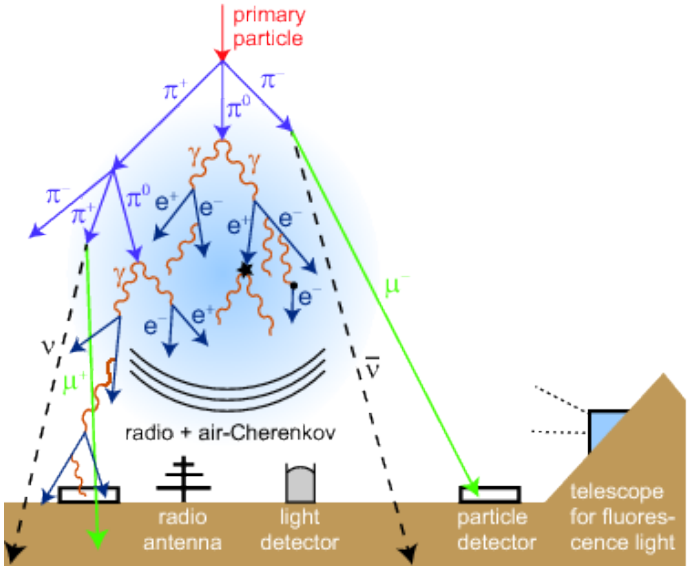

FIGURE 3.8: Simplified schematic illustration of the possible techniques used for the detection of secondary cosmic ray particles. Most detection techniques such as fluorescence light, radio and air-Cherenkov are only sensitive to electrons and positrons. Moreover, particle detectors also measure muons that can reach deeper regions than the electromagnetic component of the shower [81].

Examples of array detectors used to detect cosmic-ray particles with energy from 10^{13} to 10^{16} eV around the *knee* region of the energy spectrum are the EAS-TOP experiment [82], where 37 modules of scintillators 10 m^2 each, distributed over an area of 10^5 m^2, located at Campo Imperatore at 2000 m a.s.l., above Gran Sasso national underground laboratories, and the KASCADE (Karlsruhe Shower Core and Array DEtector) experiment [83], which was composed of 252 detectors placed on a rectangular 13 m grid over an area of 200 $\times$ 200 m^2 in the Forschungszentrum Karlsruhe at 110 m a.s.l. (above seal level). Moreover, there was a further extension of the KASCADE experiment, named KASCADE Grande [84], which was formed by reassembling 37 detector stations of the EAS-TOP experiment on the site of KASCADE. One of the main results obtained by these last two experiments is regarding a heavier mass composition for cosmic rays above the *knee* region which is caused by a break in the spectrum of the light elements.

For studying the origin of UHECR there was the AGASA (Akeno Giant Air Shower) experiment [85] composed of 111 Cherenkov detectors and 27 muon counters covering an area of 100 km^2. The results from the AGASA experiment helped to calculate the energy spectrum and anisotropy in the arrival direction of cosmic rays, as well as confirm the existence of cosmic rays with energy above 5 $\times$ 10^{19} eV. Furthermore, there was HiRes (High-Resolution Fly's Eye) experiment [86] which was composed of two sites separated by 12.6 km in the western Utah desert, named HiRes-I and HiRes-II. This experiment was composed of atmospheric fluorescence detectors with elevation from 3 to 17 degrees in the site of HiRes-I and from 3 to 31 degrees in HiRes-II. Both observatory sites had full azimuthal coverage and operated in moonless, clear nights with a duty cycle of 10%. HiRes was the first experiment to observe the GZK-cutoff in the cosmic-ray energy spectrum. Following-on experiments are the Telescope Array (TA) [87] and the Pierre Auger Observatory [88], which are currently operating and consist of surface and fluorescence detectors spread over an area of hundreds to thousands of square kilometers. These hybrid experiments take data simultaneously with the two detection systems. Although the acquired data have high quality they are limited by the low duty cycle ($\sim$ 10%) of the fluorescence telescopes.

The TA is composed of 507 scintillation surface detectors (SSD) and three fluorescence telescopes, around the SSD array, distributed over an area of about 762 km^2 in the high desert in Millard County, Utah, at about 1400 m a.s.l. The SSD are spaced 1.2 km from each other and each one is composed of two layers of scintillation detectors, which are made of extruded plastic scintillator of 3 m^2 surface area and 1.2 cm thickness, and electronics. The fluorescence telescopes cover an elevation from 3 to 33 degrees and 108 degrees in azimuth. The TA experiment started acquiring data in 2007, three years after the Pierre Auger Observatory started its data acquisition. Moreover, TA has four times smaller detection area than Auger. The latter is explained in detail in the next chapter.

3.2.1 Water-Cherenkov Detectors

The water-Cherenkov Detectors (WCDs) measure charged particles from the electromagnetic and muonic components of the air showers. These detectors have an area of typically 10 m^2 and, therefore, are very useful for the measurement of horizontal air showers which can be used to detect high-energy neutrinos. The primary particle arrival direction can be estimated from the relative arrival times of the particles at a minimum of three non-collinear WCDs [55]. The primary energy can be estimated from the measurement of the secondary lepton density at a large distance from the shower core. Since muons are heavier and more energetic than electrons of the electromagnetic component of the shower, they lose less energy and are less scattered. Thus, the muonic component arrives earlier and over a shorter period of time in the WCDs than the electromagnetic one. So it is possible to distinguish the signal from muons and electrons and gammas in the WCDs being useful to estimate the composition of the primary cosmic ray. Nevertheless, due to shower-to-shower fluctuations and the extrapolation of the hadronic interaction models to higher energies there is relatively large uncertainty in the determination of the primary composition. Moreover, the WCDs have a duty cycle close to 100%.

3.2.2 Fluorescence Detectors

The longitudinal development of the particle cascade in the atmosphere can also be measured to determine the primary composition. Fluorescence telescope observe the fluorescence light in the 300 - 400 nm ultraviolet range emitted by the air nitrogen molecules when excited by the charged particles of the shower at energies above approximately 10^{17} eV. The fluorescence observations can only be made in clear moonless nights, yielding a duty cycle of approximately 10%. The intensity of the emitted fluorescence light is proportional to the amount of charged particles in the shower and consequently to the primary energy within small uncertainties. Furthermore, measuring the shower profile, the position of the shower maximum $X_{\max}$ can be obtained (with $\Delta X_{\max} \sim 20$ g/cm^2) [81]. In general, similarly to the radio emission and air-Cherenkov light, the fluorescence light is hardly sensitive to the poorly understood muonic component and very sensitive to the well understood electromagnetic component of the air shower.

3.2.3 Measurement of radio emission

The detection of radio emission induced by high-energy and ultra-high-energy cosmic rays hitting the Earth's atmosphere is possible because of the coherent radiation from the EAS at radio frequencies. This radiation, which is emitted by secondary particles in the air shower, can be measured with simple radio antennas. The main features about the radio emission from air showers was theoretically predicted by Askaryan in 1961 [89] and in 1965 by Kahn and Lerche [90], and then detected more than 60 years ago, in 1965, by Jelly et al. at a frequency of 44 MHz [91]. In the following sections, a brief description of the radio-emission physics is shown.

Geomagnetic emission

The main emission mechanism of radio pulses from cosmic-ray particles in an air-shower development is related to the geomagnetic field. This emission occurs when secondary positrons and electrons in the shower front are accelerated in the magnetic field. In the equilibrium of acceleration by the magnetic field and deceleration in interactions with air molecules, a net drift of the electrons and positrons arises in opposite directions because of the Lorentz force ($\propto \vec{v} \times \vec{B}$) [14]. Thus, the polarization of this emitted radiation is linear with the electric field aligned to the Lorentz force (see Figure 3.9 - left panel). For particles moving along the shower axis, the resulting current is perpendicular to the shower axis, which is referred as transverse current. Muons are also deflected by the magnetic field, but due to the low charge-mass ratio they do not contribute significantly to the radio emission. As long as the air shower develops in the atmosphere, the number of secondary particles increases until the shower maximum is reached, varying those transverse currents. It is the time variation of the transverse currents which leads to the electromagnetic emission.

Charge excess

In addition to the geomagnetic emission, there is a secondary sub-dominant effect in an air-shower development called charge-excess emission or Askaryan effect which corresponds to a negative charge excess of $\approx$ 10-20%. The ionization of the air molecules by the air-shower particles leads to swept ionized electrons with the cascade, while the much heavier positive ions stay behind. As long as the shower evolves, the negative charge in the cascade grows until the shower reaches a maximum and decreases when the shower dies out. Thus, as described above there is a time-varying charge excess, which leads to the radiation of electromagnetic pulses [14].

The polarization of this radiation is also linear, but the electric-field vector is oriented radially with respect to the shower axis. A schematic illustration of the polarization of the radiation by the charge excess is shown in Figure 3.9 (right panel).

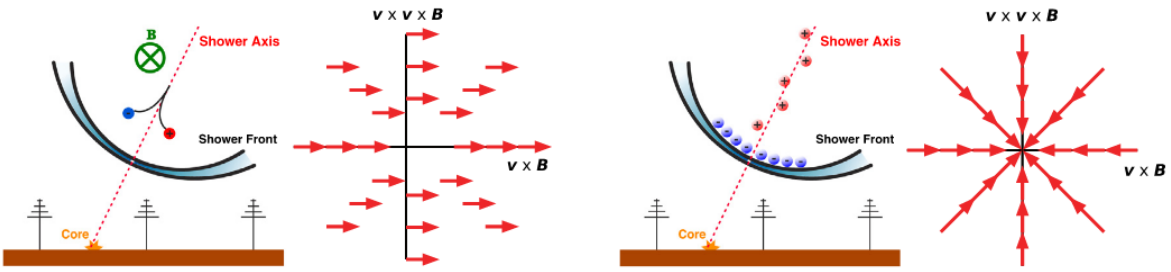

FIGURE 3.9: Left panel: Illustration of the geomagnetic emission mechanism [92]. The arrows denote the direction of linear polarization in the plane perpendicular to the shower axis. Right panel: Illustration of the charge-excess emission. The arrows illustrate the linear polarization with electric-field vectors oriented radially with respect to the shower axis [93, 94].

By acquiring detailed information about the polarization of the radio pulses [95], an understanding of the two fundamental emission mechanisms, geomagnetic and charge excess emission, has been established. Together with the convergence between predictions of Monte Carlo simulation codes and the radio measurements [96], significant improvements were achieved in the parametrization of the lateral energy density distribution [97, 98]. The shape of the radio-wave front has been found to be hyperbolic [99, 100] and the shape of the measured pulses is also the subject of intense research [101]. With these developments, parameters which are sensitive to the air-shower development (often characterized by the atmospheric depth of maximum shower development, $X_{\max}$) and to the properties of the initial cosmic ray have been identified [102].

Radio Detectors

Radio detectors provide the cosmic-ray observation via electromagnetic radiation emitted in the radio band. It was only after the development of digital radio-antenna arrays that the interest in the radio technique to detect cosmic rays with energies above 10^{17} eV increased. Charged particles, mainly electrons and positrons, in an air shower can be deflected by the Earth's magnetic field emitting radio pulses. The amplitude of the radio emission is proportional to the number of particles in the electromagnetic cascade and roughly to the primary energy. Radio detection provides a calorimetric measurement of the shower as well as the fluorescence detectors. Thus, radio detectors are sensitive to the shower development, being able to provide information about the $X_{\max}$, and therefore, determine the primary mass composition. The $X_{\max}$ is not directly visible but it can be reconstructed using the properties of the measured signal [81]. Measuring the pulse arrival times it is possible to determine the cosmic-ray arrival direction. Moreover, radio detectors have a duty cycle close to 100%, being only disturbed by thunderstorms and high-atmospheric electric fields. In general, radio detectors provide an alternative detection technique to the established optical and particle detectors.

In the 1990's, the first digital radio measurements at frequencies up to a few MHz was performed by the AGASA and EAS-TOP experiments [103]. Moreover, the RICE (Radio Ice Cherenkov Experiment) experiment [104, 105, 106] made some numerical calculations for the coherent radio pulse generated by the excess charge in a high-energy electron cascade in matter [107]. This experiment consisted of an array of 16 - 20 radio antennas deployed at depths of 100 - 300 m near the South Pole. It was designed to intercept the Cherenkov cone of coherent radiation in the radio frequency by a neutrino-induced shower in the Antarctic ice cap [108]. In the early 2000's, the microwave Cherenkov radiation from the Askaryan effect was observed by measurements made at the Stanford Linear Accelerator Center (SLAC) using bremsstrahlung photons from picosecond pulses of 28.5 GeV electrons directed into a 3.5-ton silica sand target, producing electromagnetic showers several meters long [109]. This observation served as motivation for the ANITA (Antarctic Impulsive Transient Antenna) experiment to look for radio emission from induced neutrino showers in the Antarctic ice [110].

Furthermore, larger digital radio-detector arrays were employed in order to complement the measurements of UHECR. In particular, the LOPES (LOfar PrototypE Station) experiment [111] successfully implemented the interferometric technique to measure the radio emission from electromagnetically charged particles of the air shower. LOPES was located at the site of the KASCADE-Grande experiment and consisted of an array of 30 dipole antennas with digital readout in the frequency range from 40 to 80 MHz. Results from LOPES confirmed that the radio emission is coherent and has a geomagnetic origin, as expected by the geosynchrotron mechanism [112]. At almost the same time there was the CODALEMA (COsmic ray Detection Array with Logarithmic ElectroMagnetic Antennas) experiment [113] which was dedicated to the measurement of the radio transients coming from the EAS. CODALEMA was set-up at the Nançay Observatory in France. Its results revealed a north-south asymmetry in the arrival directions of the radio-detected cosmic rays. Moreover, it revealed that the intensity of the charged-particle deflection in the atmosphere due to the Lorentz force depends on the geomagnetic angle, which comprises the angle between the shower axis and the Earth's magnetic field. The experiment made great progress in the understanding of the electric field transients generated by the EAS [114].

A second generation of digital radio-detector arrays, AERA (Auger Engineering Radio Array), is successfully operating and detecting cosmic-ray air showers thanks to the combined experiences and advantages of both experiments LOPES and CODALEMA. AERA is a new antenna system that measures radio signals in the MHz frequency band and is located at the Pierre Auger Observatory in Argentina. It consists of an array of 153 autonomous antennas, with different spacings, over an area of about 17 km^2, and a signal-processing electronics developed for this purpose [115] (see next chapter for further details). Additionally, there is the TUNKA experiment, which is now named TAIGA (Tunka Advanced Instrument for cosmic ray physics and Gamma Astronomy) and is located in Siberia near Lake Baikal. Nowadays, it is the only running EAS Cherenkov experiment working around the *knee* region of the cosmic-ray energy spectrum [116]. Tunka-REX, a radio extension of the TUNKA experiment, is an array of 63 radio antennas. The radio antennas are connected directly to the TUNKA main detector, which observes the EAS Cherenkov light in dark and clear nights using non-imaging photomultipliers. Thus, it is possible to cross-calibrate the radio signal with the air-Cherenkov signal of the same showers, with respect to the energy and shower maximum, and, therefore, enhancing the duty cycle of the experiment as the radio measurements are done during day and night [117].

In summary, cosmic-ray detection using radio-detector arrays has been a very reliable technique with a competitive resolution to determine the cosmic-ray parameters such as the arrival direction, primary energy, and the shower maximum which is sensitive to the primary mass. On the other hand, in dense media, the radio emission occurs via neutrino-induced showers [118]. The shower size is smaller than in air and the main contribution for the radio emission is caused by charge excess [109]. The use of the radio-detection technique to look for neutrino in dense

media seems to be one of the most promising techniques to reach very huge detection volumes required to measure neutrinos at energies beyond the PeV-scale flux established by IceCube [118].

3.3 Mass-Composition Measurements

The mass-composition of cosmic rays with energy up to approximately 100 TeV can be directly measured with space-based experiments [119] with non-significant disturbing effects from the interaction of cosmic rays in the atmosphere. On the other hand, as higher energy cosmic rays are indirectly measured by ground-based arrays, their chemical abundance can be inferred by the observed development and particle content of the EAS. The primary mass composition is estimated by comparing the experimental mass-sensitive observables with shower simulations, which are subject to the uncertainties in hadronic interaction models at ultra-high energies, as the energy of the center of mass of the first air-nucleus interaction is beyond accelerator energies and the estimates rely only on extrapolations of the models. This makes those parameters the most difficult ones to be measured amongst all EAS measurements. Thus, identifying different mass-sensitive EAS observables is of great importance to determine consistent conclusions about the primary cosmic-ray properties. Therefore, in what follows, some mass sensitive observables from particle and optical detectors are introduced.

3.3.1 Observables from Particle Detectors

N_e-N_μ Method

The combined electron and muon number, as well as their uncertainties, is a common method used to determine the primary mass composition of cosmic rays. The sum of electron and muon number is related to the primary energy while their ratio is related to the primary mass. Several experiments, such as EAS-TOP [82], KASCADE [83], KASCADE-Grande [26], GAMMA [120] and Yakutsk [121], worked on the discrimination of electron and muon number at ground level by employing a combination of shielded and unshielded scintillation detectors mainly focused on the energy range from 10^{16} to 10^{18} eV. The WCD of the Pierre Auger Observatory enables the discrimination between the electromagnetic and muonic component of the EAS by measuring their relative Cherenkov pulses. At detector level, the electromagnetic particles are more numerous than muons and have an energy of some 10 MeV, while muons have an energy of around 4 GeV [11]. Combinations of surface and underground detectors have been used by different experiments such as EAS-TOP and MACRO at the Gran Sasso to measure the electromagnetic and muonic content of the shower. Nowadays, with the enhancement of the Auger Observatory, this method is also available, in which underground scintillation counters are employed to measure the muon number at the ground. The importance of taking

into account the air-shower fluctuations in the analysis has already been emphasized. The numbers of muons and electrons do not fluctuate independently on an event-by-event basis but are mutually correlated.

The KASCADE experiment reconstructed the energy spectra for five different elemental groups (H, He, CNO, Si, Fe), representing the chemical composition of cosmic rays, using the measured number of electrons and muons ($E_\mu > 230$ MeV) with a scintillator array of 252 detector stations arranged on a square grid of 200×200 m^2 with spacing of 13 m [122]. The observable parameters were the total electron number N_e and the number of muons at distances between 40 and 200 m from the shower core, the so-called truncated muon number N_μ^{tr}. The analyses were performed using air showers simulated with the hadronic interaction models QGSJET I and Sibyll 2.1. Unfolding methods to derive the energy spectra of the five elemental groups were applied. Details and procedures for the analysis, as well as the unfolding algorithms, can be found in [122]. The obtained results are within systematic uncertainties and are consistent with the results from other experiments. In all particle spectra, there is a *knee* at about 4 PeV. The appearance of knee-like features in the light element spectra is independent of the used hadronic interaction model. The higher the element number, the more shifted is the position of the *knee* towards higher energies. Unfortunately, none of the used interaction models is able to consistently describe the measured data. The analysis deviates at low energies for QGSJET model and for high energies for Sibyll. In summary, in all particle energy spectra, the *knee* is due to the decrease of light elements, implying in a heavier cosmic ray composition above the *knee* region.

Similarly to KASCADE, the CASA-MIA experiment [123] also observed a heavier primary chemical composition crossing the *knee* region by analyzing the average number of muons as a function of the number of electrons. Moreover, the EAS-TOP experiment [82] and the EAS-TOP and MACRO [124] collaborations observed this knee-like feature by fitting the muon-number distributions in bins of the electron number [125]. The KASCADE-Grande experiment performed unfolding analyses with enough statistics for energies close to 10^{18} eV, but limited to only three elemental mass groups, indicating a heavy composition at about 10^{17} eV, confirming the previous results from KASCADE.

Muon Tracking and Time

The interest in using the mean Muon Production Depth (MPD) in EAS started in the 1960's, but unfortunately, the inappropriate angular resolution of the detector array and the accuracy of the shower simulations disabled the use of this parameter to investigate the primary mass composition. In the 1990's, this technique was reviewed and used by the Muon Tracking Detector at KASCADE [126] and GRAPES [127]. In these detectors, the orientation of the muon track is measured according to the shower axis and then the muon production height is reconstructed by means of triangulation [11]. Measurements performed by the KASCADE-Grande [128] experiment of the muon production height are compatible with a transition from light to

heavy composition with increasing shower energy around the *knee* of the cosmic-ray energy spectrum.

An alternative way of determining the mean MPD is to measure the time delay of muons in each detector station at ground level with respect to the shower front. Since muons are produced close to the shower axis, those produced at high altitude can reach a detector at a certain distance from the shower core at a smaller average path length than muons produced deeper in the atmosphere [11]. Thus, the measurement of the time signals produced by muons in the detectors corresponds to the mean MPD in the atmosphere. This method was first applied to real data by the Pierre Auger Collaboration [129], considering events with energy above 2 $\times$ 10^{19} eV, zenith angles between 55 and 65 degrees, and stations distant more than 1700 m from the shower core. The shape of the MPD distributions contains information about the development of the hadronic cascade and the first interaction point. The MPD profile is fitted using a Gaisser-Hillas function and a new observable is defined, the X^{μ}_{max}. The X^{μ}_{max} corresponds to the depth where the production of muons reaches the maximum along the cascade development [130]. Recent results from Auger [131] reported analysis performed with a new method to reconstruct the MPD [132] considering events with energies greater than 1.5 $\times$ 10^{19} eV, zenith angles between 45 and 65 degrees and muons arriving at radial distance farther than 1200 m from the shower core. The new reconstruction method of the MPD combines different ingredients [133] which are summarized as follows: *i)* the electromagnetic component of the shower must be removed in order to have only the muonic signal in the FADC trace registered by the surface detectors; *ii)* the production depth X (corresponding to the muonic longitudinal profile) is evaluated after the muonic signal has been extracted; *iii)* the MPD profile for each event is fitted with a Universal Shower Profile (USP) function [134] and *iv)* a set of quality cuts were applied to have only high-quality reconstructed events. These cuts can be found in [131]. The results of the analysis show a heavier composition for the registered events with energy above 1.5 $\times$ 10^{19} eV. But taking into account the mass estimated with fluorescence detectors, the simulated data do not reproduce the measured data in a consistent way. So it is difficult to estimate the primary cosmic-ray composition with the MPD. However, the performed measurements have great potential to contribute to the understanding of the hadronic interaction models and how to reduce their systematic uncertainties in the determination of the primary composition.

Rise-Time

Another parameter used to infer information about the primary mass composition is the time profile of the electrical detector pulse of the shower particles. This parameter uses the idea that most muons are detected close to the shower front and electrons are stronger attenuated in the atmosphere than muons. This method requires the state-of-the-art of the FADC electronics for full exploitation. Furthermore, the signals from inclined air showers in WCD located upstream exhibit faster rise-time than the detectors situated downstream, thus, there is a rise-time asymmetry

in the signal [135]. The rise-time is understood as the time it takes to increase the integral signal from 10 to 50% of its value [11].

For vertical air showers, there is no rise-time asymmetry because there is no difference in the path traveled by the electromagnetic particles to reach the detector level. On the other hand, the difference in the attenuation of the electromagnetic component due to the different traveled paths increases as the zenith angle increases and, therefore, rise-time asymmetries start to appear. For very inclined showers only a small rise-time asymmetry is found because of the dominance of the muonic over the electromagnetic component, being the latter almost completely absorbed by the atmosphere. The asymmetry decreases with θ and so the larger is the angle, the lower is the contribution of the electromagnetic component. The muonic component is basically free of asymmetry. Therefore, as the asymmetry depends on the zenith angle, it provides information about the stage of the shower evolution and thereby sensitiveness to the mass composition [135]. The application of the method to data [136] indicates a transition from a light to a heavy composition for the energy range between 3×10^{18} eV and 4×10^{19} eV. The results are presented in units of $(\sec\theta)_{\max}$ (see Figure 3.10), which corresponds to the azimuthal asymmetry in the rise-time of the surface-detector signals of the Pierre Auger Observatory. The magnitude of the asymmetry depends on the zenith angle and the state of development of the shower.

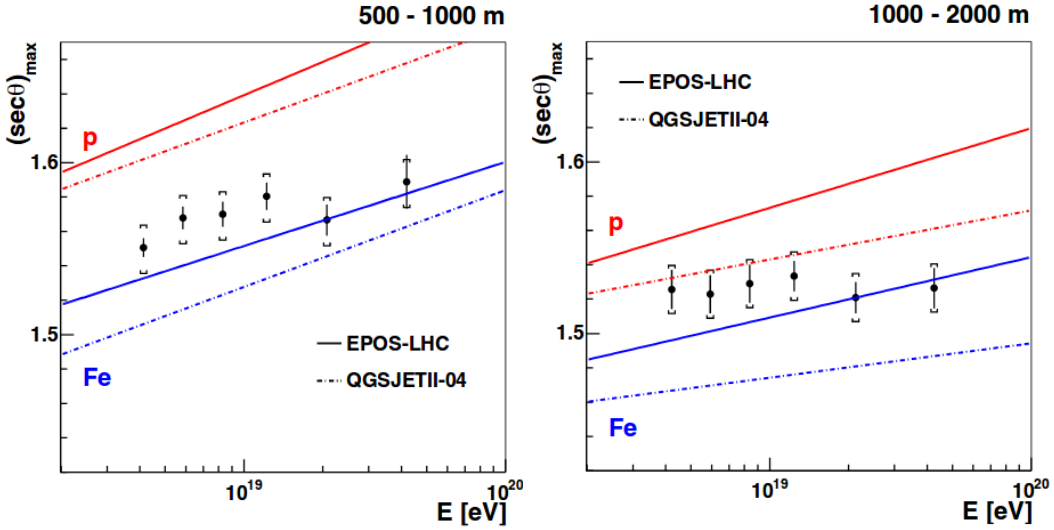

FIGURE 3.10: Comparison of the energy dependence of the measured $(\sec\theta)_{\max}$ with predictions for proton (red) and iron (blue) primaries simulated with hadronic interaction models QGSJETII-04 (dashed lines) and EPOS-LHC (solid lines) in the 500 - 1000 m interval (left panel) and in the 1000 - 2000 m interval (right panel) [136].

3.3.2 Non-imaging Cherenkov Detectors

The particle measurements at the ground can be complemented by observations of Cherenkov and fluorescence light emitted by the EAS. A non-imaging technique of

EAS observations was first applied successfully at energies around the *knee* region of the energy spectrum by the HEGRA [137] array experiment and CASA-BLANCA [138] in Utah. CASA measured the charged-particle distribution of air showers, while BLANCA measured the lateral distribution of Cherenkov light emitted by air showers with energies between 3×10^{14} eV and 3×10^{16} eV. Later experiments like Tunka [139, 140] and Yakutsk [141] extended the measurements to ultra-high energies.

The measurements of the average shower maximum from BLANCA, Tunka and Yakutsk show a small elongation rate [1] at energies above 5×10^{15} eV indicating a change from light to a heavier composition. Moreover, Tunka-133 [143] provides measurements of the $\langle X_{\mathrm{max}} \rangle$ with an accuracy of 30 g/cm^2, indicating a heavier composition in the energy range from 10^{16} eV to 3×10^{16} eV and a lighter one in the range from 10^{17} eV to 10^{18} eV. The Yakutsk collaboration analyzed the Cherenkov component from EAS, by reconstructing the air-shower development using an LDF (Lateral Distribution Function) in the energy region between 10^{16} eV and 10^{20} eV and zenith angles between 0 and 55 degrees. The comparison between experimental data and Monte Carlo simulations show qualitatively that: *i)* in the lower energy region there are more nuclei with an atomic weight between 4 and 56; *ii)* in the range of 10^{17}-10^{18} eV the proton fraction reaches a maximum between 60 and 80%, and *iii)* this fraction decreases gradually in the energy range of 10^{19}-10^{20} eV, indicating a composition of helium nuclei, CNO and heavier elements.

The measured values of $\langle X_{\mathrm{max}} \rangle$ as a function of the primary cosmic-ray energy from different experiments are shown in Figure 3.11. The measurements for energies below 1×10^{17} eV are from non-imaging Cherenkov telescopes, while for higher energies the measurements are from fluorescence telescopes. At energies below 10^{16} eV, the Yakutsk and Tunka measurements disagree by up to 40 g/cm^2. The average shower maximum from Tunka and Yakutsk measurements for energies around 10^{17} eV approach the values for heavy primaries and beyond it increases towards light primaries. At higher energies, only Yakutsk measured the shower maximum with non-imaging Cherenkov detectors. The results will be discussed in the following section with the fluorescence telescope measurements.

3.3.3 Fluorescence Telescopes

The Fly's Eye [145] experiment and its successor HiRes [86] were one of the pioneers to measure the longitudinal profile of air showers using fluorescence telescopes and studying the shower maximum as a function of the energy [146, 147]. Currently, as mentioned in section 3.2, there are only the Telescope Array and Auger Observatory in operation that make use of the fluorescence technique to determine the energy scale and mass composition of cosmic rays. Since the fluorescence-light yields are proportional to the energy deposited in the atmosphere, it is possible to reconstruct the shower development in the atmosphere as a function of the slant depth.

[1] The elongation rate denotes the rate of change location of the depth of the shower maximum, X_{max}, per decade of primary energy or shower size [142].

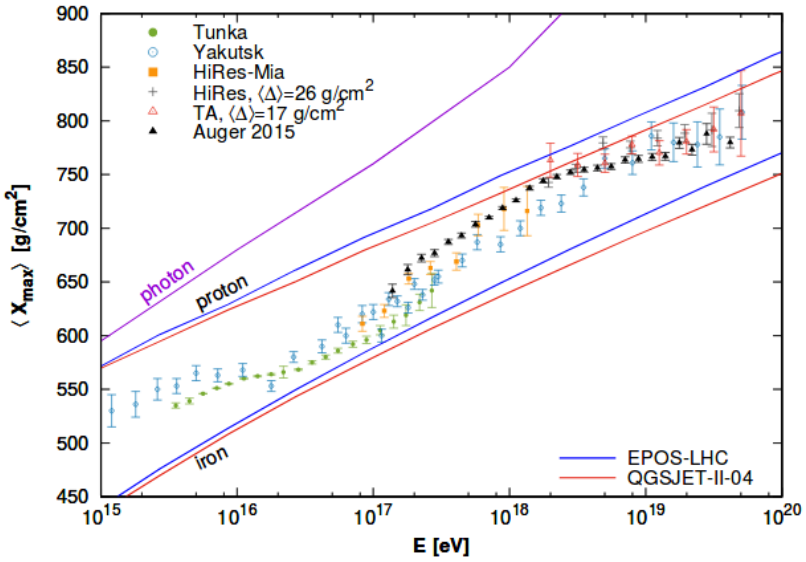

FIGURE 3.11: Measurements of $\langle X_{\max} \rangle$ as a function of the primary energy for different experiments. The predictions for proton, iron and photon-induced showers simulated with QGSJETII-04 and EPOS-LHC are shown for comparison. The $\langle X_{\max} \rangle$ measured by TA and HiRes is shifted by the amount $\langle \Delta \rangle$ indicated in each case due to experimental data correction for detector effects [144].

The observed longitudinal profile can be fitted with a Gaisser-Hillas function [148], like the one used by the Auger collaboration [149], or a Gaussian in shower age [150], as used in the final analysis of the HiRes experiment. The measurement of the longitudinal shower development provides a direct measurement of the depth of shower maximum in units of g/cm^2. On a shower-by-shower basis, it is roughly possible to discriminate between light and heavy primary cosmic ray by comparing the $X_{\max}$ position. The dominant contribution to fluorescence-light emission is due to the energy loss of the EAS electromagnetic component. Since the production and energy-loss mechanisms of the electromagnetic component are less dependent on the hadronic interaction model used in the shower simulation, the $X_{\max}$ parameter depends less on simulations than other techniques used to estimate the primary mass composition [151].

Showers initiated by heavier particles develop earlier and faster in the atmosphere due to their higher nuclear cross section than showers initiated by lighter primaries of the same energy, as can be seen in Figure 3.7. Proton showers fluctuate more about $\langle X_{\max} \rangle$ providing another composition measurement, which is the Root Mean Square (RMS) fluctuation about $\langle X_{\max} \rangle$, defined as $\sigma(X_{\max})$ [35].

The observations of the Fly's Eye [152] experiment in 1993 gave the first indication of a mass composition change at very high energies which are correlated with the features in the all-particle energy spectrum. The transition is from an iron dominated composition at about 10^{17} eV to a proton dominated one at $10^{19.3}$ eV. This transition occurs close to $10^{18.5}$ eV. In contrast to the old measurements of the

Fly's Eye experiment, HiRes/MIA and Auger data confirm the trend observed by the non-imaging Cherenkov detectors of the Yakutsk experiment, the large elongation rate indicating a transition from heavy to light dominated composition at around 10^{18} eV that is qualitatively consistent with a transition from a heavy Galactic composition to a light extragalactic composition. At higher energies, Auger has observed a gradual increase of the average mass of cosmic rays, with the exact relative position of the $\langle X_{\mathrm{max}} \rangle$ depending on the hadronic interaction model used in the analysis [153].

An interpretation of the full X_{max} distribution in each energy bin is achieved by fitting a superposition of X_{max}-templates obtained from simulations of proton, helium, nitrogen and iron-induced air showers to the data [153] (see Figure 3.12). At high energies, the mass fractions show a composition dominated by a single elemental group starting from protons below the *ankle* region and going through helium to nitrogen with increasing energy. Moreover, a small proton fraction may persist up to ultra-high energies and there might be an iron contribution emerging above $10^{19.4}$ eV depending on the hadronic interaction model.

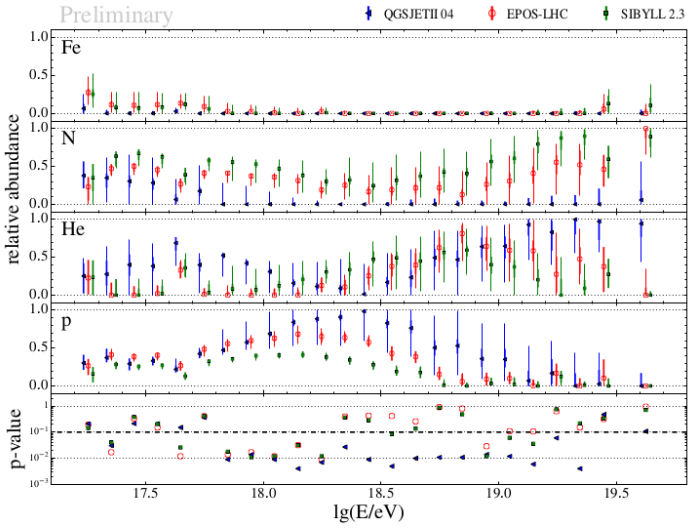

FIGURE 3.12: Results from a fit of the X_{max} distributions with a superposition of proton, helium, nitrogen and iron-induced air showers. The upper four panels show the best-fit mass fractions and the goodness of fit is displayed in the lowest panel. Thick error bars denote the statistical uncertainties, thin error bars the systematic ones [153].

Average logarithmic mass

The composition can also be estimated by an often-used quantity which is the mean logarithmic mass, defined as $\langle \ln A \rangle = \Sigma_i f_i \ln A_i$, with f_i as the relative fraction of nuclei of mass A_i. The $\langle \ln A \rangle$ parameter can be obtained using two different shower quantities that are sensitive to the mass of the primary particle: *i)* it is proportional to the electron-muon ratio measured at ground level, $\langle \ln A \rangle \propto \log_{10}(N_e/N_\mu)$ and *ii)* it

is proportional to the shower maximum according to $\langle X^{A}_{max} \rangle = \langle X^{p}_{max} \rangle - D_p \langle \ln A \rangle$, with D_p as a constant dependent on the characteristics of hadronic interactions [11].

Since we know the shower maximum for simulated iron and proton-induced showers, we can determine the mean logarithmic mass from the measured data X^{data}_{max} values using the relation

$$\langle \ln A \rangle = \left(\frac{X^{data}_{max} - X^{p}_{max}}{X^{Fe}_{max} - X^{p}_{max}} \right) \cdot \ln A_{Fe}. \tag{3.21}$$

The corresponding $\langle \ln A \rangle$ values as a function of the energy derived from X_{max} measurements with optical detectors for different hadronic interaction models are shown in Figure 3.13.

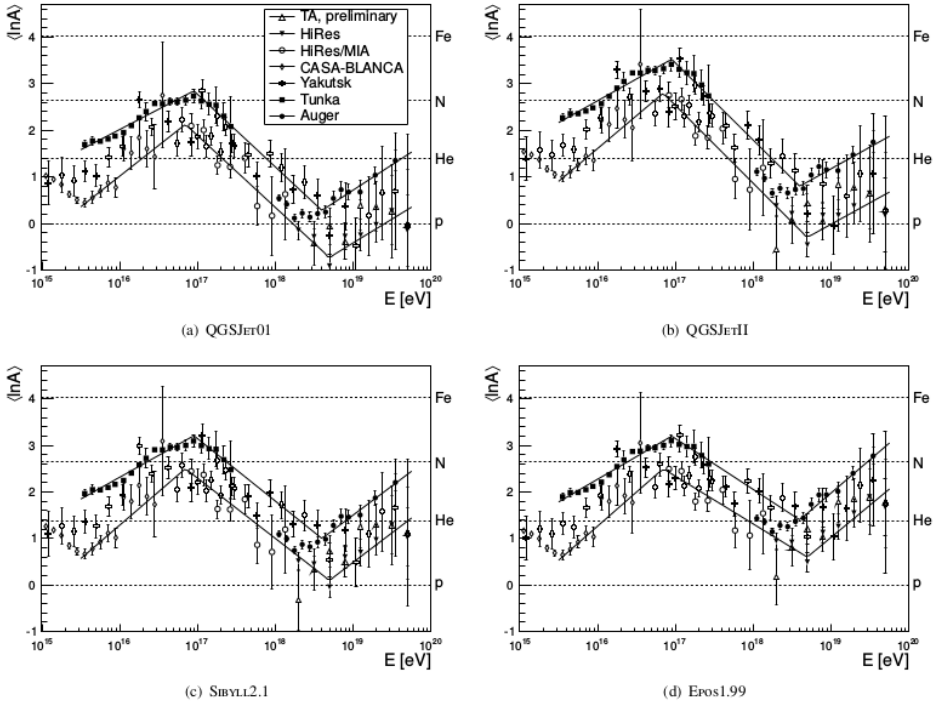

FIGURE 3.13: Average logarithmic mass, $\langle \ln A \rangle$, of cosmic rays as a function of energy derived from X_{max} measurements with optical detectors for different hadronic interaction models (QGSJETI, QGSJETII, Sibyll 2.1 and EPOS 1.99). The dashed lines correspond to the experimental systematics, i.e. upper and lower boundaries of the different experimental data with non-imaging Cherenkov detectors (Tunka [139], Yakutsk [154, 155] and CASA-BLANCA [138]) and fluorescence telescopes (HiRes/MIA [156], HiRes [157], Auger [129] and TA [158]) [11].

According to this figure all the used hadronic interaction models indicate a gradual increase of $\langle X_{\mathrm{max}} \rangle$ for energies between 10^{15} eV and 10^{17} eV, followed by a transition to a lighter mass composition for energies up to about $10^{18.4}$ eV. The Tunka data interpreted with the QGSJETII hadronic interaction model presents the heaviest composition with $\langle \ln A \rangle \approx 3.5$ at about 10^{17} eV. Results from TA and HiRes at very high energies are compatible with pure proton composition for both QGSJET01 and QGSJETII. On the other hand, Auger data shows a trend towards a heavier composition for all hadronic interaction models and the same result is expected for HiRes and TA data using EPOS and Sibyll models.

Measurements from particle detectors such as the average muon production depth and the rise-time asymmetries correlate well with the shower maximum, thus it can be assumed that they have a linear dependence on $\langle \ln A \rangle$. Therefore, we can quantify the inconsistencies in the modeling of air showers by converting these average properties of the ground signal measured by the particle detectors to $\langle \ln A \rangle$ to have a common scale between these observables and the X_{max} measurements by the optical detectors [153]. Figure 3.14 shows the $\langle \ln A \rangle$ as a function of the energy derived from particle detector measurements for different hadronic interaction models (QGSJET01, Sibyll 2.1 and QGSJETII). The upper and lower limits from measurements with the optical detectors in Figure 3.13 are indicated by the superimposed lines. When comparing the results from the particle and optical detector measurements there are some systematic differences at low energies, although all experiments report an increase of the mean logarithmic mass below 10^{17} eV. At ultra-high energies above 10^{19} eV, the interpretation of the Auger data with the QGSJETII and Sibyll 2.1 models indicate an increase of $\langle \ln A \rangle$.

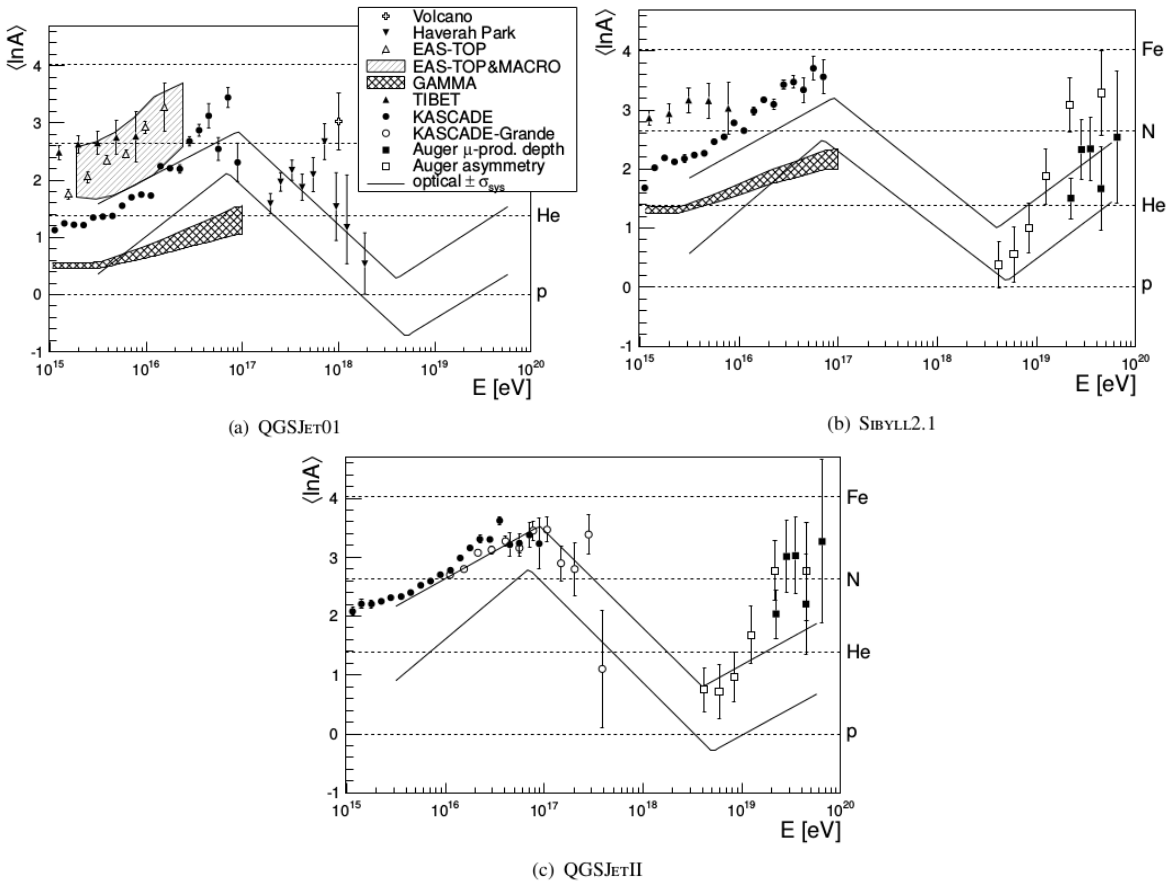

(a) QGSJET01 (b) SIBYLL2.1

(c) QGSJETII

FIGURE 3.14: Average logarithmic mass, $\langle \ln A \rangle$, of cosmic rays as a function of energy derived from measurements with particle detectors (EAS-TOP [82], MACRO [124], GAMMA [120], TIBET [159], KASCADE [83], KASCADE-Grande [26], and Auger [88]) for different hadronic interaction models (a) QGSJETI, (b) Sibyll 2.1 and (c) QGSJETII. The dashed lines correspond to the lower and upper edges from the optical technique measurements (see Figure 3.13) [11].

Pierre Auger Observatory

In this chapter the Pierre Auger Observatory is introduced, which is the largest cosmic ray observatory ever built. The Observatory allows the hybrid detection of air showers detected simultaneously by several detection techniques. The reconstruction methods of air showers employed in the Observatory and also for the analyses in this thesis are described in the following sections.

The Pierre Auger Observatory completed the installation of its detectors in the Mendoza region of Argentina in 2008. The instrument aims the study of cosmic rays with energies above 10^{18} eV. These are the particles with the highest known energy, surpassing the energies reached at man-made accelerators in thousand times. The study of these particles allows us to look for the cosmic ray origin(s) and study the acceleration, propagation and interaction mechanisms of these particles.

The Observatory is a hybrid detector which employs two main distinct and independent methods for the observation of UHECR [2]. One is the measurement of the Cherenkov radiation in large water tanks emitted by charged particles that propagate at relativistic velocities, with $v > c/n$ (n = refractive index), in the medium. The other technique detects the fluorescence radiation emitted by atmospheric Nitrogen molecules due to cosmic ray interaction. The hybrid nature of the Observatory comprises an array of surface detectors and a set of fluorescence telescopes. A better description of these detector arrays is explained in the following sections.

4.1 Surface Detectors

The Surface Detector Array (SD) consists of 1660 WCDs filled with ultra-pure water in a hermetic bag, the liner, whose internal surface diffusely reflects the photons produced by the Cherenkov effect in water. These detectors are located in an area of approximately 3000 km^2. Each detector consists of a 3.6 m diameter cylindrical water tank filled with twelve tons of ultra pure-water [2]. On the inner top of the liner, three photomultiplier tubes are installed. The Pierre Auger Observatory comprises WCDs arranged as an array on a triangular grid with 1500 m and 750 m spacing, each detector having a solar panel, batteries, GPS antenna, communication antenna and electronic signal digitizer. Figure 4.1 shows a schematic illustration of one of the WCD (left panel) and an image of its installation in the Observatory (right panel). Each detector works autonomously and communicates with the Central Data Acquisition System (CDAS) via a wireless network.

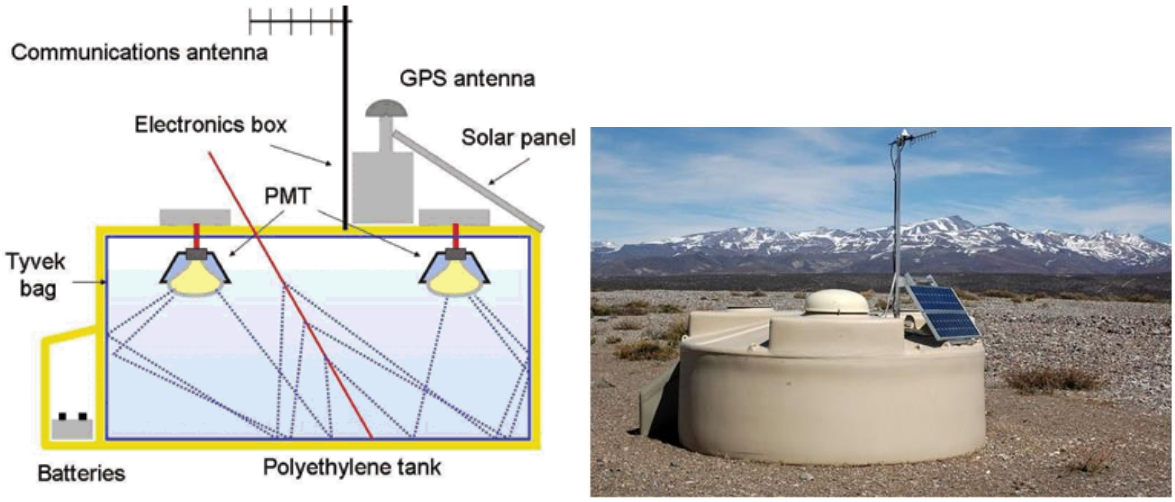

FIGURE 4.1: Left: Schematic illustration of a water-Cherenkov Detector [160]. Right: Image of a WCD installed at the observatory.

The energetic particles from EAS travel at relativistic velocities higher than the light speed in water. Therefore, when they reach the detector they produce Cherenkov light. This radiation can be measured by the photomultiplier tubes installed on the inner surface of the WCD. The EAS has around billions of secondary particles that can produce light signals in more than five WCD. Thus, the primary cosmic ray energy can be estimated based on the quantity of light detected in the WCD which is produced by the secondary particles. Moreover, the WCD height of 1.2 m makes it also sensitive to high energy photons, which are converted into an electron-positron pair in the water volume [2].

4.2 Fluorescence Detectors

During the air shower development the secondary particles, predominantly electrons and positrons, deposit their energy in the atmosphere by exciting or ionizing atmospheric nitrogen which afterwards deexcitate by emitting ultraviolet light (300 - 400 nm) via a process called fluorescence. Figure 4.2 shows the various emission bands of nitrogen in the dry air. This light is invisible to the human eye but not to the Observatory's optical telescopes.

The Fluorescence Detector (FD) consists of 24 fluorescence telescopes grouped in units of six at four locations on the periphery of the SD (see Figure 4.3). The names of the FD buildings in the clockwise sequence are Los Leones, Coihueco, Loma Amarilla and Los Morados, starting withfrom the most southern building. The Field Of View (FOV) of a single camera of the telescope comprises an angular area of $30^o \times 30^o$ in azimuth and elevation so that each telescope building covers a region of 180^o in azimuth and 30^o in elevation starting at the horizon. The minimum elevation above the horizon is 1.5^o. The four FD sites allow for the observation of the atmosphere above the SD.

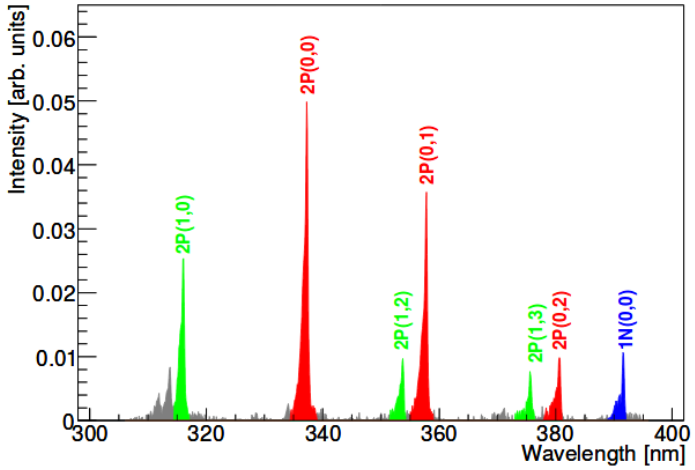

FIGURE 4.2: Nitrogen fluorescence spectrum between 300 nm and 400 nm in the dry air at 1013 hPa [161].

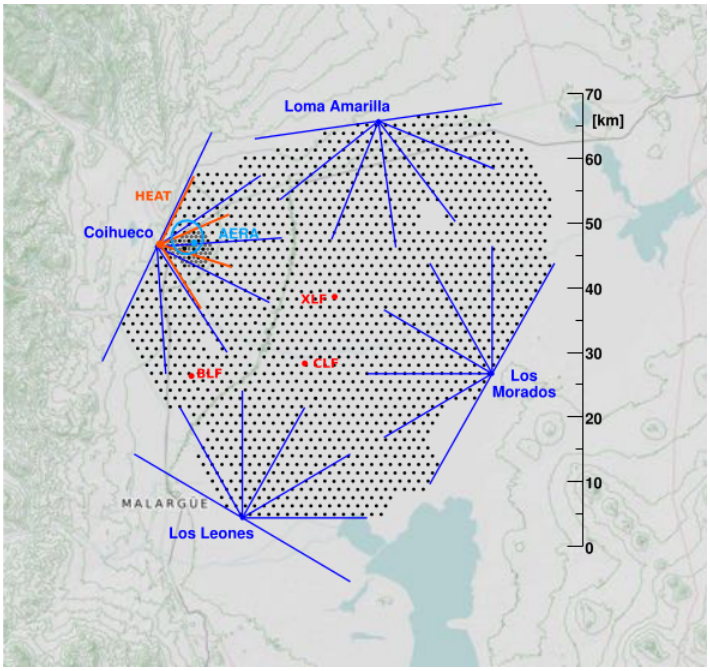

FIGURE 4.3: Geographical map showing the southern site of the Pierre Auger Observatory located close to the city of Malargüe in Argentina. The positions of the detectors are indicated by black dots while the locations and the FOVs of the FD cameras are displayed by blue lines. Starting with the lower left and going anticlockwise their names are Los Leones, Los Morados, Loma Amarilla and Coihueco. At the Coihueco site, the HEAT extension is installed (the orange lines show the FOV). The grey dots and light blue circle indicate the position of the AMIGA and AERA detectors (see next sections for further details). The atmospheric monitoring sites, CLF (Central Laser Facility), XLF (eXtreme Laser Facility) and BLF (Balloon Launching Facility), are shown as red dots [162].

The fluorescence telescopes observe the trail of nitrogen fluorescence and track the development of air showers by measuring the brightness of the emitted light, allowing the observation of the longitudinal development of the EAS and a calorimetric determination of the primary cosmic-ray energy. The production of photons by the secondary particles is at around five photons per meter and these are emitted isotropically. Moreover, using a grid of focusing mirrors to collect the light, cameras can view the air shower up to 15 kilometers away. A detailed description of the FD can be found in the paper 'The fluorescence detector of the Pierre Auger Observatory' [163].

Figure 4.4 shows the arrangement of the FD building with six telescopes (left panel) and a schematic illustration of the different components of the fluorescence telescope (right panel). The optical system of the telescopes consists of a filter, a Schmidt optics corrector ring, a spherical mirror and the PMT camera. The light enters through a circular diaphragm containing a filter of 1.10 m in diameter that allows the passage of wavelengths between 300 and 400 nm. The filter reduces the number of background photons which disturb the detection of the fluorescence light. The background photons are outside of the fluorescence wavelength range. The light reflected by the mirror arrives at an array of 440 photomultiplier tubes (PMTs), being each one a pixel of the telescope. The pixels are arranged in a geometric matrix (22×20) at the focal plane of the telescope. The pixel FOV corresponds to an angular size of 1.5^{o}.

Automatic shutters protect the telescopes against daylight, rain and wind. Moreover, there is a fail-safe curtain positioned behind the diaphragm to protect the camera from daylight illumination in case the shutter is malfunctioning.

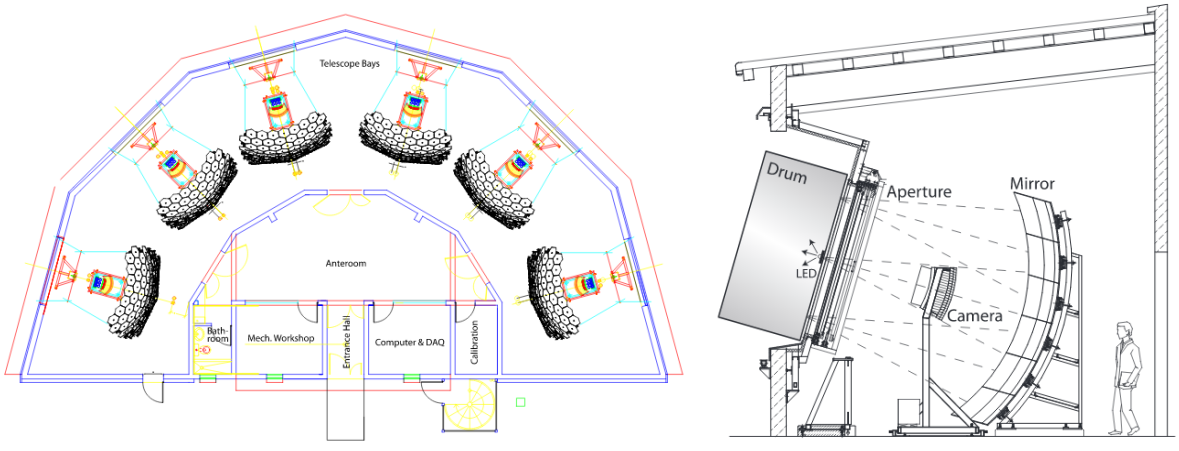

(A) (B)

FIGURE 4.4: Left: Schematic layout of the fluorescence building with six telescopes. Right: Schematic view of a fluorescence telescope with its different components [163].

Since 2006 several proposals have been developed in the Pierre Auger Collaboration to add improvements to the initial project. One of the aims was to extend the cosmic ray observation to lower energies, up to 10^{17} eV, and to study the transition from Galactic (lower energy) to extragalactic (higher energy) cosmic rays. In addition to this, another objective comprised the determination of the shower muon content at energies around 10^{18} eV through measurements independent of the surface detectors and telescopes, as well as testing and improving the hadronic interaction models at high energies. Techniques related to the detection of radiation from air showers in the MHz or GHz range were also proposed. The low energy enhancements of the Observatory are explained in the following sections.

4.3 Enhancements of the Observatory

4.3.1 Auger Muon Infill for the Grand Array (AMIGA)

AMIGA comprises two improvements of the Observatory, which are the *infill* array and the muon counters. The *infill* array minimizes the energy threshold of the SD for a maximum trigger efficiency. The trigger system of the *infill* array is adapted from the regular Auger array. An event is accepted when at least three surface detectors forming a triangle satisfy a local trigger of the type Time-over-Threshold (3ToT event) [164]. The trigger efficiency as a function of the cosmic ray energy for 3ToT events with zenith angles below 55º is illustrated in Figure 4.5. On the other hand, the muon counters aim to improve the measurement of the chemical composition of the primary cosmic rays as they are purely sensitive to the muon content of the shower. The AMIGA muon counters will enrich the physics investigations in the *ankle* region of the energy spectrum.

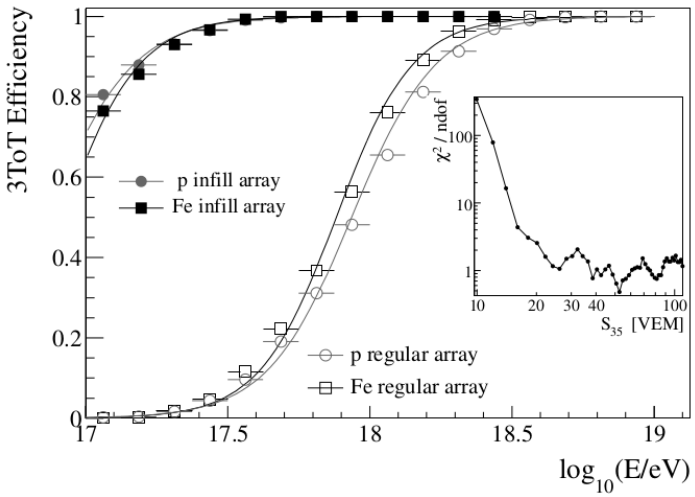

FIGURE 4.5: 3ToT trigger efficiency for the *infill* and regular array obtained from simulations of iron and proton-sinduced air showers [129].

The *infill* array of the AMIGA project consists of 61 pairs of detectors, each composed of a WCD and a muon counter. The WCD use the same modular system as the surface detectors of the regular array and are arranged in an hexagonal grid spaced 750 m apart from each other, instrumenting a total area of 23.5 km^2, to directly measure the air showers with primary energies $\geq 3 \times 10^{17}$ eV (see Figure 4.6). The muon counters are composed of 30 m^2 scintillation detectors buried at a depth of 2.3 m (equivalent to an atmospheric depth of 540 g/cm^2), which sufficient decreases the electromagnetic punch-through to a negligible level at core distances of interest [165]. Muons propagating in the soil with energy higher than or equal to 1 GeV are capable of reaching the muon detector which is located near the WCDs.

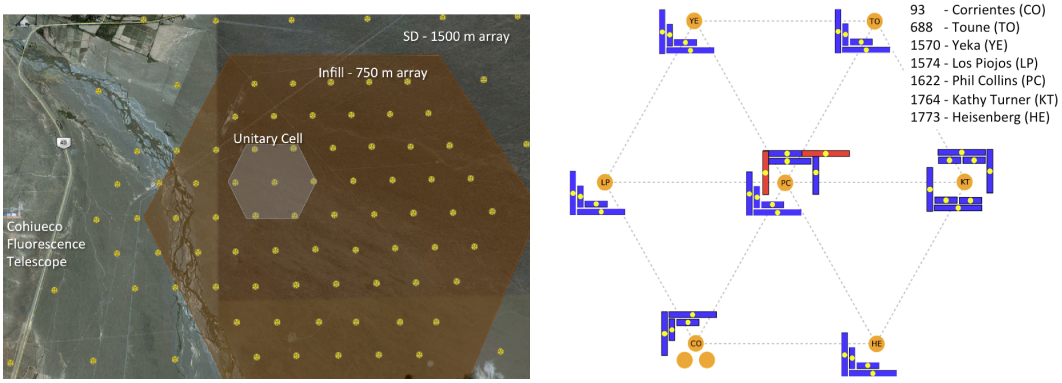

FIGURE 4.6: Left: Map of the AMIGA array with a brown background. The engineering array positions, where muon counters are already deployed, can be seen highlighted in gray (also called the Unitary Cell) [92]. Right: AMIGA Unitary Cell layout showing the locations of the muon counters and corresponding WCDs installed since February 2015. Two of the Unitary Cell positions have twin muon detectors, which consist of two 30 m^2 muon counters separated by $\sim$ 10 m. The purpose of these detectors is to study counting fluctuations [166].

The muon detectors count muons from air showers which are reconstructed by the SD and FD. Each muon counter has a modular design in which the 30 m^2 detection area is divided into two modules with 5 m^2 and two with 10 m^2 detection area for pile-up and signal attenuation cross comparison tests [165]. Each of the detector modules has its own acquisition system triggered by the surface detectors (see Figure 4.7).

Scintillator modules

Every scintillator module comprises 64 scintillation bars, each of dimensions 40 mm $\times$ 10 mm $\times$ 4 m, with a 1.2 mm diameter wavelength-shifting (WLS) optical fiber glued into a lengthwise groove of the bar. The light produced in the scintillation bars is collected and propagated along the WLS fibers, which then couple to multi-pixel PMTs (photomultiplier tubes). The 64 scintillators and optical fibers are lodged within a PVC (Polyvinyl Chloride) casing and, together with the electronics kit, form the detector module (see Figure 4.8).

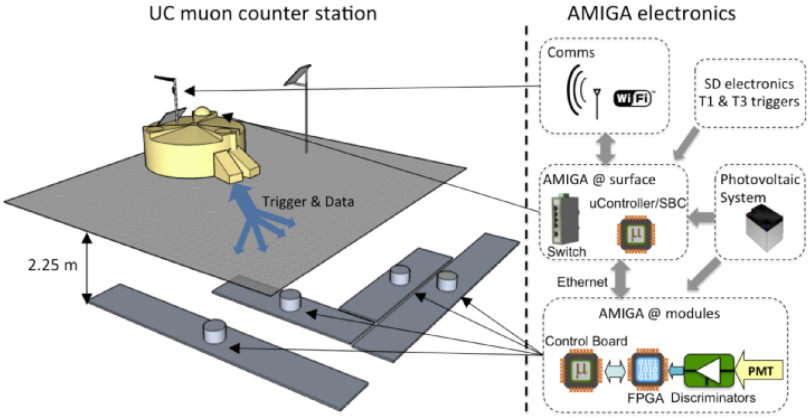

FIGURE 4.7: Schematic illustration of one of the AMIGA detectors in the Unitary Cell together with the electronic system [165].

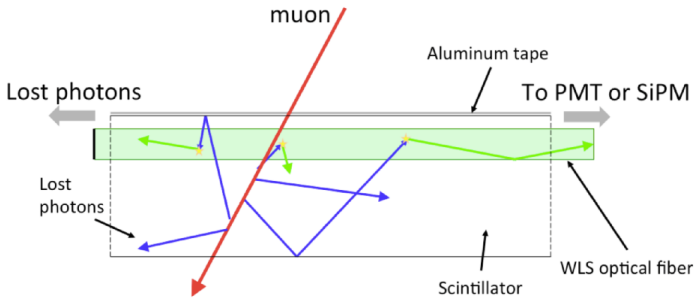

FIGURE 4.8: Illustration of a scintillator bar excited by a muon. Highlighted are the trajectories of the incident particle (in red), the photons produced within the bar (in blue) and within the fiber (in green) [165].

The scintillation bars are made of plastic and were produced and quality-controlled at Fermilab. They are 4 m long extruded bars (for the 10 m^2 modules) of polystyrene doped with fluor and co-extruded with TiO_2 as an outer layer for reflectivity.

As the AMIGA modules are buried, their mechanical design provides an access tube for both the electronics and the PMT for maintenance purposes. The access tube is filled with large bags of local soil to ensure uniform shielding (Figure 4.9). Furthermore, in order to resist sun exposure, large animals and high-speed winds the access tube is covered with a lid designed for this purpose [165].

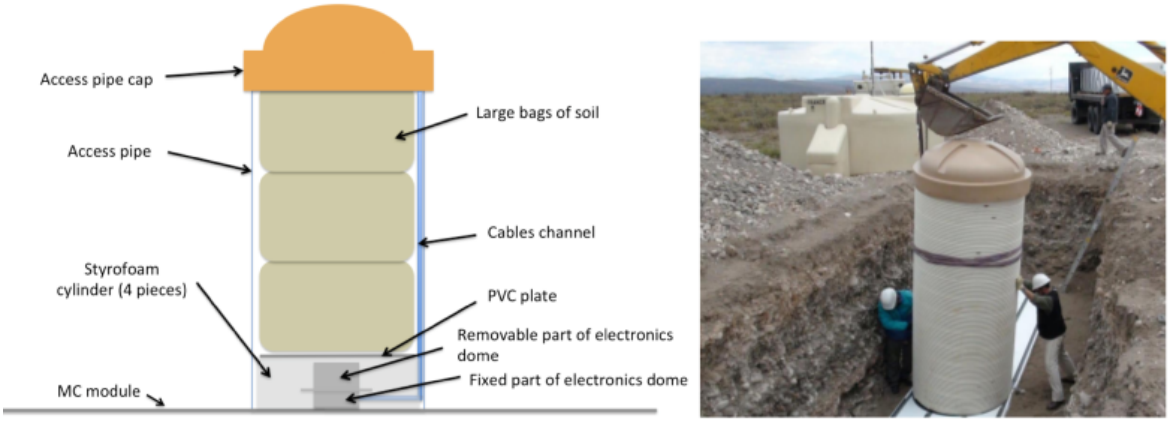

FIGURE 4.9: Left: Schematic illustration of the module-access tube used for electronics maintenance. Right: Installation of an access tube, which is sealed to the module for water tightness [165].

Layout

The four modules of each muon counter of the Unitary Cell are arranged in an 'L' shape (see Figure 4.10) in order to minimize possible systematics arising from highly-inclined muons. Moreover, to improve the shielding uniformity independently of the shower arrival direction the modules are deployed with a 5 m horizontal separation from the surface detectors.

4.3.2 High Elevation Auger Telescopes (HEAT)

The telescopes of the Observatory measure the longitudinal profile of the air shower development in the atmosphere with high accuracy. The telescopes have a FOV between 1 and 30 degrees above the horizon. Showers with lower energy than 10^{18} eV have their maximum development above the telescope FOV, and therefore, the detection efficiency is lower and the X_{max} measurement is biased by the quality cuts of the FOV. To avoid any bias in the determination of X_{max}, three additional fluorescence telescopes with higher elevation, called HEAT, were installed in the north-east side of the Coihueco FD building in the same region where the AMIGA *infill* array is located (Figure 4.11).

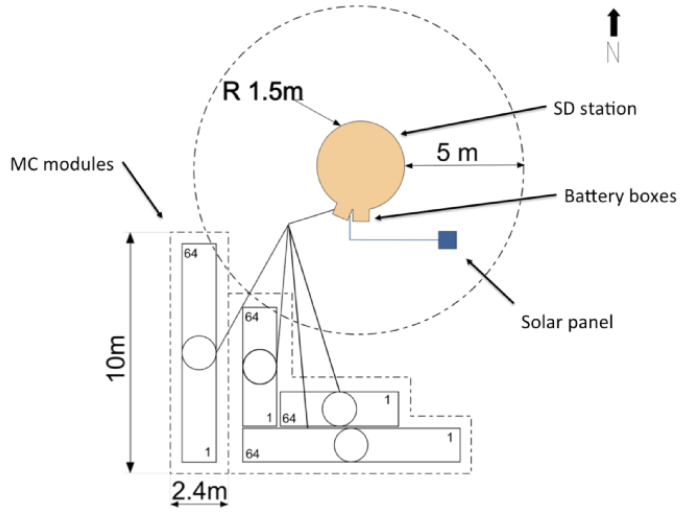

FIGURE 4.10: Layout of the modules of a muon counter in the AMIGA Unitary Cell. To improve the shielding uniformity there is a horizontal separation between the modules the surface detector of approximately 5 m [165].

FIGURE 4.11: Photo of the three HEAT telescopes titled upward, end of January 2009 [167].

The design of the HEAT telescopes is very similar to the original FD system [163]. A large FOV of about $30^o \times 30^o$ is obtained using Schmidt optics. Fluorescence light entering the aperture is focused by a spherical mirror onto a camera containing 440 hexagonal PMTs. A UV transmitting filter mounted at the entrance window reduces background light from stars effectively. An angular corrector ring assures a spot size of about 0.6^o despite the large effective aperture of 3 m^2. All optical components are connected to a heavy-weight ground plate to avoid wind-induced vibrations and to keep the geometry fixed.

Like the conventional FD electronics, the Data Acquisition System (DAQ) of HEAT contains 20 Analog Boards (AB) for analog signal processing, 20 First Level Trigger (FLT) boards for signal digitizing and storage, and one Second Level Trigger (SLT) board for the recognition of fluorescence light tracks and the initiation of data readout.

The air showers can be measured by HEAT in 'downward' and 'upward' positions, as shown in Figure 4.12. The FOV of the existing Coihueco telescopes overlaps with HEAT in 'downward' mode, so the events can be detected simultaneously by both telescopes and compared for systematic studies [167]. By comparing the reconstruction results from both installations one can directly determine the telescope resolution in energy and X_{max}.

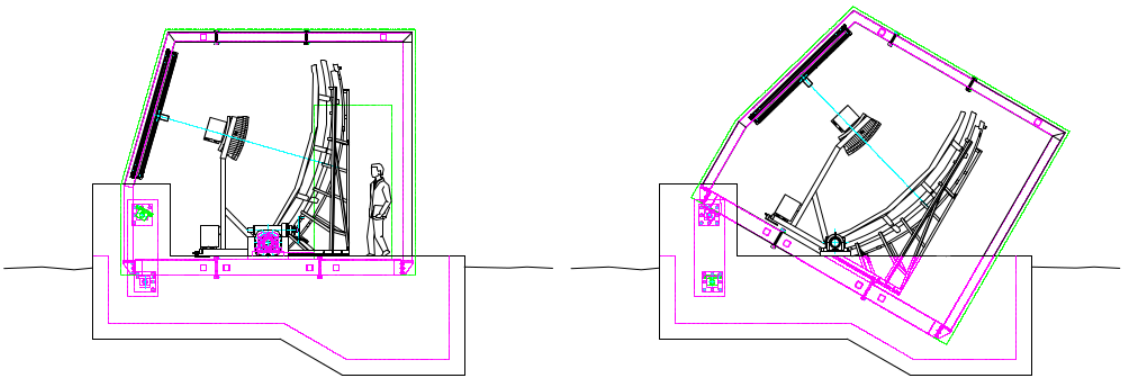

FIGURE 4.12: HEAT in 'upward' (left panel) and 'downward' (right panel) measurement modes [162, 167].

Lower energy cosmic rays come from our own Galaxy, the Milky Way, while the highest energy cosmic rays are probably extragalactic in origin. Expanding the range of energies with HEAT and studying the mass composition of primary cosmic rays will enable the deduction at what energy levels the transition between Galactic and extragalactic cosmic rays occurs.

4.3.3 Auger Engineering Radio Array (AERA)

AERA is a new antenna system designed to measure short radio pulses emitted by the highest energy cosmic ray air showers. It consists of an array of dozens of antennas sensitive to a frequency range from 30 to 80 MHz with signal processing and electronics developed specifically for this purpose.

The AERA project was carried out in three phases [102]. AERA24 was deployed in September 2010 and consisted of an array of 24 stations equipped with Logarithmic-Periodic Dipole Antenna (LPDA) antennas [168] on a grid with 150 m antenna separation. The LPDA antennas are oriented in magnetic North-South and East-West directions. The signals are amplified and filtered before they are introduced into a filter-amplifier and digitization chain. There they are bandpass filtered between 30-80 MHz, digitized and further processed by a Field Programmable Gate Array (FPGA) and a Central Processing Unit (CPU). Later, 100 stations using butterfly antennas [169] were deployed in May 2013 featuring the second phase of the AERA project, AERA124. The 100 new radio stations in AERA124 are spaced 250 m or 375 m apart from each other. The butterfly antenna is highly sensitive towards the ground which enhances the antenna gain. The general layout of the digitizing chain is similar to the one used in AERA24. Additional antenna prototypes were installed with the goal of measuring the three-dimensional electric field vector. In the third stage, 25 more antenna stations were deployed on a grid with up to 750 m antenna separation in Spring 2015, allowing improved studies of horizontal air showers (zenith angle higher than 60^{o}) with large-scale radio footprints. This last stage features AERA153 which covers an area of about 17 km^2. In total, 89 butterfly antennas are equipped with deeply buffering hardware and 40 butterfly antennas are employing internal triggering only. This internal trigger is based on radio self-triggering and small scintillation counters in the electronics compartment of the radio station itself. Due to the increased size of the array, wireless links were introduced for the new stations. All 153 stations operate autonomously employing solar power systems. Figure 4.13 shows the LPDA and butterfly station designs deployed at AERA site.

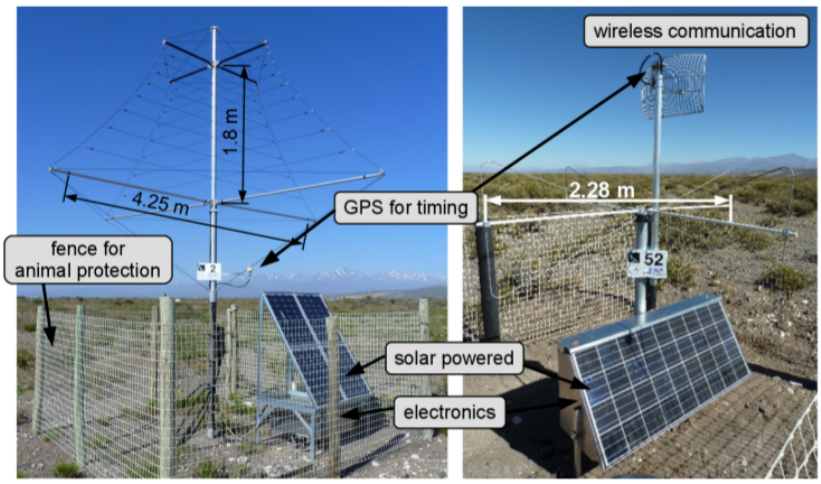

FIGURE 4.13: Photos of the radio station LPDA (left) and butterfly (right) design [115].

AERA regularly detects cosmic rays in coincidence with surface and fluorescence detectors, allowing the cross-calibration of its measurements with the established baseline detectors of the Observatory. Initial analyses have already led to significant first results, in particular confirming the theoretical predictions of the emission mechanism of radiation in the radio frequency.

It is worth saying that AERA is sensitive to the three main properties of a cosmic ray which are the arrival direction, energy and particle type [102]. The primary energy can be reconstructed from the radiation energy emitted by the electromagnetic shower component in the radio frequency. Therefore, the electric field traces are converted into the energy fluence, i. e., the energy deposit per area, of the electromagnetic wave via the Poynting vector. The measured energy density at all positions of the signal stations is fitted with a two-dimensional lateral distribution function [97, 102].

The radiation energy is subject of ongoing work as it can be predicted by Monte Carlo simulations without being strongly influenced by the uncertainties of the hadronic interaction models [170]. Therefore the energy scale of cosmic rays can be studied based on classical electrodynamics. Since the radio emission contains information about the shower development, in particular, the shower maximum, the X_{max} can be reconstructed from radio emission [171] using the shape parameters of the hyperbolic radio wavefront [172], the width of the radio footprint in the shower plane [173] or the slope of the frequency spectrum in single radio antennas [101]. In addition to the X_{max} reconstruction from radio data, the AERA measurement can be combined with underground particle detectors, which measure the muonic component of the shower, to estimate the primary particle type [170].

4.4 Upgrade of the Observatory

The upgrade of the Auger Observatory, known as AugerPrime, will allow us to estimate the primary mass of the highest-energy cosmic rays on a shower-by-shower basis [174]. The upgrade will search for light primaries at the highest energies, aiming to reach a sensitivity as small as 10% in the flux contribution of protons in the suppression region of the cosmic-ray energy spectrum [175]. Moreover, it will perform composition-selected anisotropy studies as well as search for new phenomena including unexpected changes in hadronic interactions [174]. The upgrade consists of the installation of a new detector above each of the 1660 existing WCD. The detectors are plane plastic scintillators, named Surface Scintillator Detector (SSD), and they will be triggered by the WCD below it. The shower particles will be sampled with two detectors having different responses to muons and electromagnetic particles, providing a complementary measurement of the shower particles. An SSD unit consists of a box of 3.8 m $\times$ 1.3 m containing two scintillator modules. The modules are composed of 24 scintillation bars produced at the Fermi National Accelerator Laboratory with dimensions of about 1.6 m length, 5 cm width and 1 cm thickness [175]. The scintillators are mounted on the top of the existing WCD (see Figure 4.14) and are read out by wavelength-shifting fibers which guide the light of the two modules to a PMT (model Hamamatsu R9420) [174].

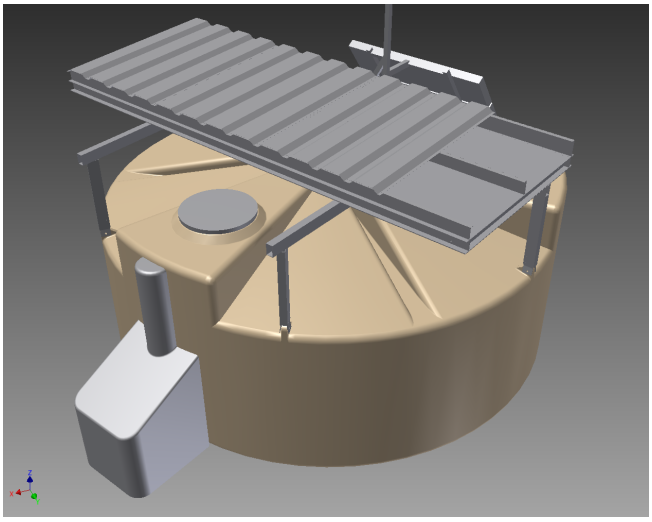

FIGURE 4.14: 3D view of an SSD mounted on a WCD. A double roof, with the upper layer being corrugated aluminum (here shown partially cut away for clarity), is used to reduce the temperature variations [174].

Another important improvement of the Observatory is the upgrade of the electronics of the WCD that will process both WCD and SSD signals [175, 176]. This upgrade will increase the data quality due to a better timing accuracy and a faster sampling for Analog-to-Digital Converter (ADC) traces, as well as to improve the capabilities of the surface-detector calibration and monitoring. Since the Auger-Prime design aims to measure the properties of air showers at energies above 6×10^{19} eV at distances close to 250 m from the shower core, the WCD is equipped with an additional small PMT (1 inch Hamamatsu R8619 PMT) which is dedicated to the unsaturated measurement of large signals. The large-PMT signals are calibrated with background muons, while for the cross-calibration between the large and small PMTs either small shower events are used or else the existing LED flasher system which is adapted for brighter light pulses [176].

The Engineering Array of the upgrade has already been started since September 2016 with the deployment of the first twelve stations of AugerPrime. About the location of the Engineering Array, nine detectors are located in the array where the surface-detector separation is 1500 m and three detectors in the 750 m spaced array. They have been taking data since the beginning of October 2016 and have already permitted the reconstruction of more than 3000 cosmic-ray events [175].

The Auger upgrade promises high-quality future data from 2018 until 2024. The event statistics collected with the upgraded detectors will be comparable to the existing Auger data set, with the critical added advantage that every event will now have mass information. This will allow us to better understand the origin of the flux suppression, the prospects of light-particle astronomy and secondary particle fluxes, and the possibility of new particle physics at extreme energies.

Reconstruction of air-shower properties

This Chapter describes the reconstruction methods of air-shower observables used in this thesis which are the muon densities reconstructed with AMIGA at different reference distances from the shower axis combined with the primary energy measured by the surface, fluorescence and radio detectors. The goal of the air shower reconstruction is to reconstruct the energy, the particle type and the arrival direction of the primary cosmic ray that produced the air shower measured by the Pierre Auger Observatory. The reconstruction methods described in this chapter are the same for simulations (Chapter 6) and real data (Chapter 7). For simulated showers, the reconstruction is applied after the air shower simulation and the simulation of the detector response.

The data recorded by the surface (SD), fluorescence (FD), radio (RD) and muon (MD) detectors are analysed with the software framework $\overline{\text{Off}}\underline{\text{line}}$ [177] of the Pierre Auger Collaboration. The $\overline{\text{Off}}\underline{\text{line}}$ framework has a clear structure to allow for easy maintenance and ongoing shared development over the whole life-time of the Pierre Auger Observatory. The internal representations of the *Detector* and the *Event* in $\overline{\text{Off}}\underline{\text{line}}$ are clearly separated. The *Detector* provides access to all the relevant detector information such as the positions of detectors in the field, the hardware associated with these detectors, etc [178]. On the other hand, the *Event* data structures hold all the data applying to a specific event, such as ADC traces, as well as reconstructed quantities such as the event geometry. These two structures are not directly connected, but there is an analysis *Modules* which combines their defined interfaces to carry out their specific analysis tasks. The muon detectors which consist of an array of counters are implemented in a class named *MDetector*. The counter positions are acquired from the associated WCD.

The radio analysis functionality had to be implemented. Similarly to the hierarchy of *Detectors* and *PMTs* in the SD functionality, the radio-data structures were divided into *Detectors* and *Channels*. The radio functionality provides features that facilitate an advanced radio-data analysis [178]. For the AMIGA detectors, the *infill* component was easily integrated in the official $\overline{\text{Off}}\underline{\text{line}}$ code, given the flexibility of this code. However the implementation of the scintillator channel took a big effort in order to achieve a realistic description of the device.

The cosmic-ray event simulation and the reconstruction are performed by running several software modules in a specified order. For each module, there

are different aspects of the reconstruction. Hence, the analysis can be adjusted individually. The module sequences for the simulation and reconstruction consist of different combinations of the hybrid detectors for radio and muon analysis, which were optimized for an efficient hybrid muon-radio event reconstruction.

For the Offline output data analysis the toolkit ROOT is used [179]. This toolkit, beyond other features, allows the organization of raw data into events and the study of correlations among event variables, by applying filters, performing projections and function settings, thus optimizing the handling of large amounts of raw data that are used.

5.1 Geometry and Primary Energy Reconstruction

The signal detected by the surface detectors provides information about the cosmic-ray arrival direction, the shower core and the primary energy [2]. The shower event reconstruction starts with reconstructing the arrival direction which is determined by fitting the arrival time of the primary particle in each surface detector to a shower front model. Firstly, the shape of the shower front model is assumed to be planar moving at the speed of light to estimate the shower incoming direction. Later, the shower direction reconstruction is improved by using a spherical-front approximation. The shower core is determined by calculating the barycentre of the signals in the detectors, which is the shower impact point on the ground. The shower axis corresponds to the unitary vector at the impact point and is perpendicular to the shower plane pointing back to the particle source. Figure 5.1 shows a schematic illustration of the shower direction reconstruction based on the arrival time of the shower front at the detector. The left panel shows a first estimation of the shower incoming direction by assuming a planar-front approximation and the right panel shows the improved shower direction reconstruction using a spherical-front approximation.

Once the shower axis is estimated, the lateral distribution of the measured signals in the surface detectors is determined in the shower plane perpendicular to the shower axis. The chosen lateral distribution function (LDF) to fit the signal as a function of the distance to the shower axis is the NKGBetaOnly, which is a modified version of the Nishimura-Kamata-Greisen (NKG)-type function [181]. This function is performed via a maximum-likelihood method, which takes into account zero-signals and saturated detectors as well as a model for the signal fluctuations. The modified NKG function is given by

$$S(r) = S(r_{\mathrm{opt}}) \cdot f_{\mathrm{LDF}}(r) = S(r_{\mathrm{opt}}) \cdot \left(\frac{r}{r_{\mathrm{otp}}}\right)^{\beta} \left(\frac{r + r_{\mathrm{opt}}}{r_{\mathrm{scale}} + r_{\mathrm{opt}}}\right)^{\beta}, \tag{5.1}$$

where $f_{\mathrm{LDF}}(r_{\mathrm{opt}}) = 1$, β is the LDF slope, r_{opt} is the distance on the shower plane where the changes in β due to shower-to-shower fluctuations and statistical uncertainties in the number of particles minimally influence the signal model. This parameter depends on the geometry of the array. This parameter is fixed to 270 m

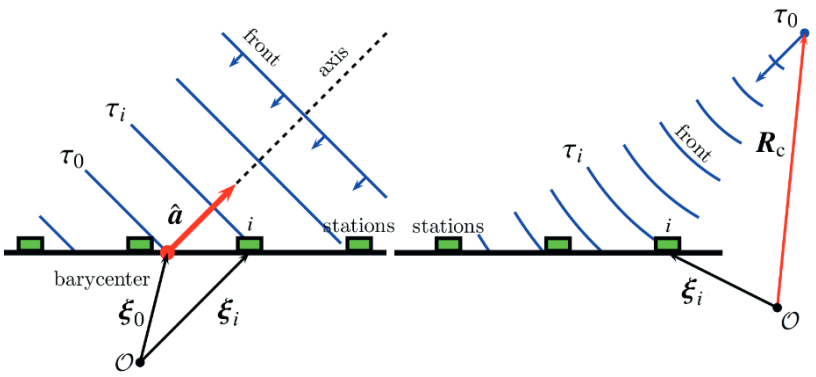

FIGURE 5.1: Left panel: Schematic illustration of the shower direction reconstruction assuming a planar shower front model moving at the speed of light. The planar shower-front comes from the direction (unitary vector) and arrives at a time τ at a particular detector position $\xi(\tau)$ with respect to the barycenter $\xi_0(\tau_0)$. Right panel: Schematic illustration of the improved direction reconstruction using a spherical shower front approximation. The incoming direction is estimated by approximating the curvature of the shower front by a spherical surface expanding at the speed of light, starting at time τ_0 and at the position R_c [180].

for the AERAlet array, while for the *infill* array it is 450 m and for the regular array it is 1000 m. The parameter r_{scale} influences the signal only for larger distances and is strongly correlated to β. Its value is hard-coded to 700 m.

The slope β parameter is free, but if the number of detectors that measured the event is less than five the slope is fixed to

$$\beta(\log_{10}S_{r_{\text{opt}}}, \theta) = a + b \cdot \log_{10}S_{r_{\text{opt}}} + (c + d \cdot \log_{10}S_{r_{\text{opt}}})\text{sec}\theta + (e + f \cdot \log_{10}S_{r_{\text{opt}}}) \cdot sec^2\theta \tag{5.2}$$

where θ is the zenith angle of the incoming shower and $S_{r_{\text{opt}}} \equiv S(r_{\text{opt}})$. The parameters from a to f depend on the geometry of the array.

The signal $S(r_{\text{opt}})$ is used to estimate the primary cosmic ray energy and depends on the zenith angle due to the atmospheric attenuation of the shower particle. This effect can be corrected by means of the Constant Intensity Cut (CIC) method. Assuming that the cosmic-ray flux is isotropic and uniformly distributed over $\cos^2\theta$, $S(r_{\text{opt}})$ is converted into a reference signal size $S(\theta_{\text{ref}})$, in which θ_{ref} depends on the trigger-threshold energy of the array. The energy scale is calibrated against the fluorescence light detected by the telescopes from measurements of hybrid events.

An example of an event reconstructed with the surface detectors is shown in Figure 5.2.

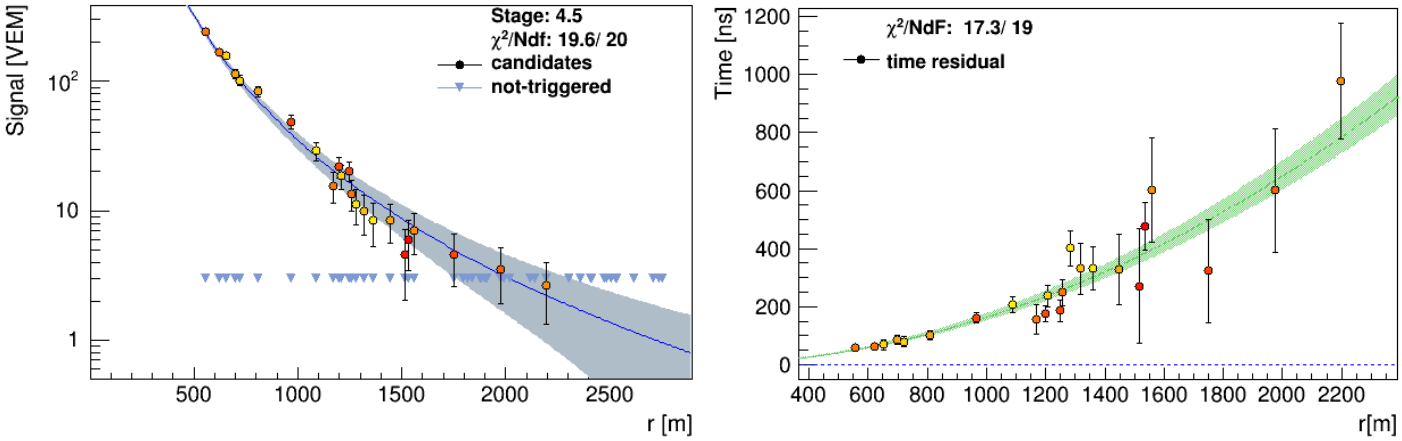

FIGURE 5.2: SD energy reconstruction for a proton-induced air shower with reconstructed energy of E = $(6.78 \pm 0.19 \pm 0.34) \times 10^{18}$ eV based on S(450) = $447 \pm 13 \pm 22$ VEM with zenith angle of 37.9 ± 0.2^{o} and azimuth of 148 ± 0.3^{o}. Left: Lateral distribution function fitted to the signal sizes registered at different distances from the shower axis. Right: Time residuals with respect to the spherical-front model.

5.2 Muon density reconstruction

The AMIGA muon detector (MD) reconstruction for a simulated or for real event needs the geometry and energy reconstruction of the induced air shower, which are calculated by means of the SD reconstruction. The counting strategies for the MD reconstruction at the level of each individual strip are implemented and an LDF is fitted.

The muon numbers registered by the muon counters can be studied using a Muon Lateral Distribution Function (MLDF). One of the first MLDF parametrizations was introduced by K. Greisen [5]. Later other groups proposed different functional expressions for the MLDF. Although all these formulas describe very accurately the MLDF in the range of short and intermediate distances from the shower axis, they are not so good for large distances and for higher energy showers. A new MLDF parametrization was proposed by the KASCADE-Grande Collaboration which is a modification of the Greisen formula [182], as

$$\rho_{\mu}(r) = \rho_{\mu}(r_{\mathrm{ref}}) \left(\frac{r}{r_0}\right)^{-\alpha} \left(1 + \frac{r}{r_0}\right)^{-\beta_{\mu}} \left(1 + \left(\frac{r}{10 r_0}\right)^{2}\right)^{-\gamma}, \tag{5.3}$$

where $\rho_{\mu}(r_{\mathrm{ref}})$, r_0, α, β_{μ} and γ are parameters which define the shape and size of the MLDF.

The parameters α=1, γ=1.85, r_0=150 m are fixed and β_{μ} and $\rho_{\mu}(r_{\mathrm{ref}})$ are fitted to measured muon densities. Since the muon density is a parameter sensitive to the primary mass, we reconstructed the muon density at different reference distances from the shower axis (r_{ref} =300, 350, 400, 450, 500, 550, 600, 650, 700, 750,

800, 850, 900, 950 and 1000 m) to investigate the distance which could provide the best mass separation for showers induced by proton and iron as primary particles. β corresponds to the slope of the lateral distribution function and if the number of muon counters with a signal is less than four it is a fixed parameter given by

$$\beta(\theta) = 3 - \sec\theta \tag{5.4}$$

otherwise it is a free parameter.

Figure 5.3 shows a MLDF fit for a single iron shower with E=8.65$\times 10^{18}$eV, θ = 38^{o} and ϕ = 122^{o}.

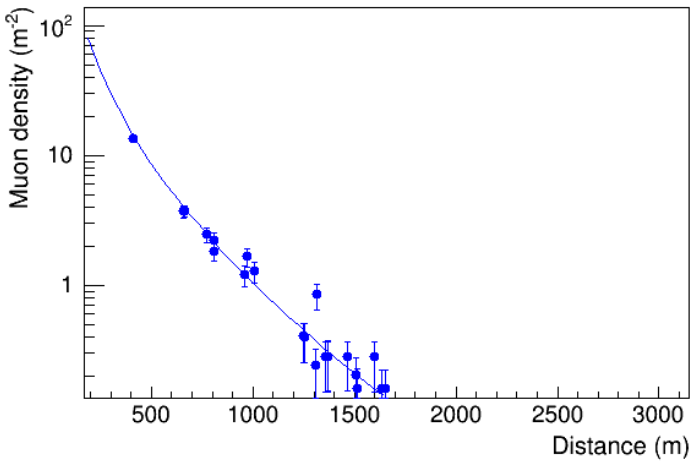

FIGURE 5.3: Example of a MLDF fit for a shower initiated by an iron nucleus with $E = 8.65 \times 10^{18}$ eV, $\theta = 38^{o}$ and $\phi = 122^{o}$.

5.3 Radiation Energy Reconstruction

The exact amount of observed electromagnetic radiation in the radio frequency strongly depends on the coherence effects [183] and the position of the observer relative to the shower axis. However, the radio emission occurs through the charged particle acceleration and is described by the classical electrodynamics.

The total amount of radiation emitted by an extensive air shower can be quantified by using the radiation energy concept [184, 185, 186], which corresponds to the energy emitted in radio waves by a shower. In most experiments the radio frequency band between 30 and 80 MHz is used. Below 30 MHz, there are atmospheric noise and small short-wave transmitters which impair the measurement of the electromagnetic emission, and above 80 MHz there is the FM band that also interferes in the measurements.

Experimentally the radiation energy can be calculated by means of interpolation and integral of the energy fluence measured at ground level. As soon as the shower has emitted all the radiation energy, the radiation energy emitted keeps constant with increasing atmospheric depth as the atmosphere is essentially transparent to the radio emission. Moreover, the radiation energy is independent of the

radio signal distribution at the ground, just varying with the incidence angle of the primary cosmic ray.

In the radio reconstruction with Offline, a Geomagnetic and Charge-excess Lateral Distribution Function (GeoCeLDF) is fitted to obtain an absolute energy estimator. This LDF corresponds to the energy density of the electromagnetic field at ground level in shower coordinates in units of eV/m^2. It takes into account the signal asymmetries due to constructive and destructive interference between the geomagnetic and charge-excess components, as well as Cherenkov time-compression effects [187].

Figure 5.4 shows the distribution of the energy fluence in the $\vec{v} \times \vec{B} - \vec{v} \times (\vec{v} \times \vec{B})$ coordinate system of an iron-induced air shower with 38° zenith angle and energy of 2.50×10^{18} eV. On the $\vec{v} \times (\vec{v} \times \vec{B})$ axis, the polarizations of the radio pulses from the geomagnetic and charge-excess emission mechanisms are orthogonal. The electric field component in the $\vec{v} \times \vec{B}$ direction ($\vec{E}_{\vec{v}\times\vec{B}}$) originates only from the geomagnetic emission, whereas the component in the $\vec{v} \times (\vec{v} \times \vec{B})$ direction ($\vec{E}_{\vec{v}\times(\vec{v}\times\vec{B})}$) originates from the charge-excess emission. Thus, the energy fluences $f_{\vec{v}\times\vec{B}}$ and $f_{\vec{v}\times(\vec{v}\times\vec{B})}$ are calculated from both electric field components.

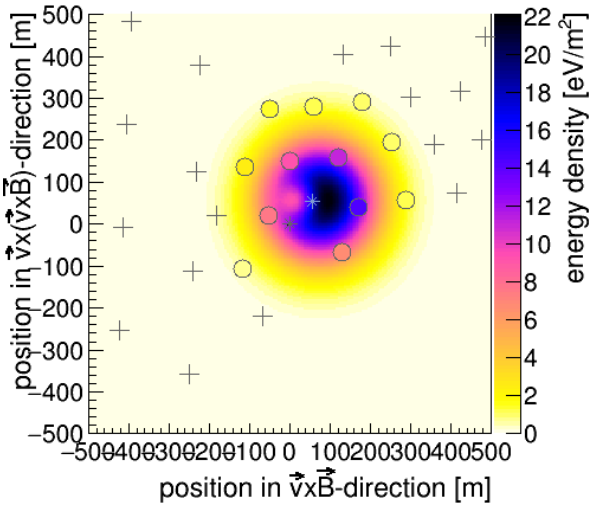

FIGURE 5.4: Distribution of the combined energy fluence of the geomagnetic and charge-excess emission of an iron-induced air shower with 38° zenith angle and energy of 4.39×10^{17} eV.

The energy fluence, which is the energy deposit per area, is the time-integral over the Poynting flux of the radio pulse and is calculated using the following equation [188]

$$f = f_{\vec{v}\times\vec{B}} + f_{\vec{v}\times(\vec{v}\times\vec{B})} \tag{5.5}$$

with the two components given by

$$f_{\vec{v}\times\vec{B}}(\vec{r}) = \varepsilon_0 c \Delta t \sum_i E^2_{\vec{v}\times\vec{B}}(\vec{r}, t_i), \tag{5.6}$$

$$f_{\vec{v}\times(\vec{v}\times\vec{B})}(\vec{r}) = \varepsilon_0 c \Delta t \sum_i E^2_{\vec{v}\times(\vec{v}\times\vec{B})}(\vec{r}, t_i), \tag{5.7}$$

where ε_0 is the vacuum permittivity, c is the speed of light in vacuum, and Δt is the sampling interval of the electric field $\vec{E}(\vec{r}, t)$ which depends on the position $\vec{r}$ and time t.

The electric field components can be written as

$$\vec{E}_{\vec{v}\times\vec{B}}(\vec{r}, t) = E_{\text{geo}}(\vec{r}, t) + \cos\phi E_{\text{ce}}(\vec{r}, t) \tag{5.8}$$

$$\vec{E}_{\vec{v}\times(\vec{v}\times\vec{B})}(\vec{r}, t) = \sin\phi E_{\text{ce}}(\vec{r}, t), \tag{5.9}$$

where E_{geo} and E_{ce} are the modulus of the electric field from the geomagnetic and charge-excess emission respectively.

Thus, using the relations 5.6 and 5.7, Eqs. 5.8 and 5.9 can be rewritten as

$$f_{\vec{v}\times\vec{B}}(\vec{r}) = \left(\sqrt{f_{\text{geo}}(r)} + \cos\phi\sqrt{f_{\text{ce}}(r)}\right)^2 \tag{5.10}$$

and

$$f_{\vec{v}\times(\vec{v}\times\vec{B})}(\vec{r}) = \sin^2\phi f_{\text{ce}}(r). \tag{5.11}$$

The energy fluence of the geomagnetic emission ($f_{\vec{v}\times(\vec{v}\times\vec{B})} = f_{\text{geo}}$) can be parametrized as

$$f_{\text{geo}} = \begin{cases} \dfrac{1}{N_{R_-}} E'_{\text{geo}} \exp\left(-\left(\dfrac{r - R_{\text{geo}}}{\sqrt{2}\sigma_{\text{geo}}}\right)^{p(r)}\right), & \text{if } R_{\text{geo}} < 0. \\ \dfrac{1}{N_{R_+}}\left[\exp\left(-\dfrac{r - R_{\text{geo}}}{\sqrt{2}\sigma_{\text{geo}}}\right)^{p(r)} + \exp\left(-\left(\dfrac{r + R_{\text{geo}}}{\sqrt{2}\sigma_{\text{geo}}}\right)^{p(r)}\right)\right], & \text{if } R_{\text{geo}} \geq 0. \end{cases} \tag{5.12}$$

where R_{geo} is the radius of the Cherenkov ring, σ_{geo} describes the width of the function, $p(r)$ is a small correction to an exponent of 2 (this means the two-dimensional

integral over the function can be calculated analytically), N_{R_-} and N_{R_+} are constants chosen so that E'_{geo} is the geomagnetic radiation energy for $p(r) = 2$.

The energy fluence of the charge-excess emission ($f_{\vec{v}\times\vec{B}} = f_{\text{ce}}$) can be parametrized with a modification of the Gamma distribution

$$f_{\text{ce}}(r) = \frac{1}{N_{\text{ce}}} E'_{\text{ce}} r^k \exp\left(\frac{-r^{p(r)}(k+1)}{p(r)\sigma_{\text{ce}}^{p(r)}}\right), \tag{5.13}$$

where $k \geq 0$. For $k = 0$ and $p(r) = 2$, the function is a Gaussian with mean zero. For $k > 0$, the function has the property to be zero at $r = 0$. The function has its maximum for $r_{\text{ce}} = \sigma_{\text{ce}}\sqrt{k}/\sqrt{k+1}$. N_{ce} is chosen so that the two-dimensional integral over f_{ce} is E_{ce} for $p(r) = 2$ and E'_{ce} corresponds to the radiation energy of the charge-excess emission E_{ce}.

The spatial integral of the LDF [189] gives the amount of energy radiated by the electromagnetic component of the air shower in the AERA frequency band (30 - 80 MHz) as

$$E_{\text{rad}} = \int_0^{2\pi} d\phi \int_0^{\infty} dr r f(r,\phi), \tag{5.14}$$

where $f = f_{\vec{v}\times\vec{B}} + f_{\vec{v}\times(\vec{v}\times\vec{B})}$.

5.4 Fluorescence Energy and Shower Profile Reconstruction

The cosmic-ray interactions with the Earth's atmosphere generate fluorescence light and Cherenkov radiation. The Cherenkov radiation is much more intense, but emitted only along the shower axis, while the fluorescence light is emitted isotropically. A significant amount of Cherenkov radiation can be detected by the fluorescence detectors of the Observatory if the shower axis is pointed directly to the telescope, or when the atmospheric constituents (molecules, aerosols or clouds) scatter part of the light beam in the telescope direction [190].

The optical bandpass of the telescopes is restricted (by optical filters) to the range from 300 to 400 nm, which corresponds to the band of the nitrogen spectrum and minimizes the contribution of the background radiation of the sky. For this band there is no radiation absorption by the atmospheric molecules and the light attenuation is due to the Rayleigh scattering by molecules and Mie scattering by aerosols.

The optical signal measured at the fluorescence detectors consists of fluorescence and Cherenkov light (the latter is composed of direct and scattered light). The energy emitted as fluorescence light is a known fraction of the total energy deposited by the shower. Hence the measurement yields the dE/dX as a function of the atmospheric depth, which is called the energy-deposit profile. The shower profile is obtained analytically by a linear least-square minimization of a Gaisser-Hillas function [148] f_{GH} with four parameters, which is given by

$$f_{GH}(X) = \left(\frac{dE}{dX}\right)\left(\frac{X - X_0}{X_{max} - X_0}\right)^{\frac{X_{max} - X_0}{\lambda_r}} e^{\frac{X_{max} - X}{\lambda_r}} \tag{5.15}$$

where X_{max} is the atmospheric depth at which the energy deposit is maximum $\left(\frac{dE}{dX}\right)_{max}$, X_0 is the first interaction point and λ_r is the interaction length characteristic of the electromagnetic cascade. The four Gaisser-Hillas parameters are not reconstructed if the shower track is too small or the shower maximum X_{max} is not inside the FOV of the telescopes. Integrating f_{GH} provides a measurement of the calorimetric energy E_{cal}, which is given by

$$E_{cal} = \int_0^\infty f_{GH}(X)dX. \tag{5.16}$$

The total energy is estimated by correcting for the invisible energy carried away by neutrinos and high-energy muons. The invisible energy is estimated using experimental data above 3×10^{18} eV, for which the SD array is fully efficient [191]. Hence the total energy of the primary cosmic-ray is given by

$$E_{FD} = E_{cal} \cdot f_{invis} \tag{5.17}$$

where f_{invis} is the correction factor for the invisible energy [192, 193, 194]. The correction factor is 1.21 for 10^{17} eV and 1.15 for $10^{18.4}$ eV.

The statistical uncertainties on the energy scale come from the fit parameters, the geometrical and atmospheric uncertainties. For the systematic uncertainties [191], the FD calibration contributes with about 9.9%, the fluorescence yield $\sim$ 3.6%, the atmosphere $\sim$ 3.4 - 6.2%, the FD profile reconstruction $\sim$ 6.5 - 5.6%, the invisible energy $\sim$ 3.0 - 1.5%, the statistical error of the SD calibration fit $\sim$ 0.7 - 1.8% and the stability of the energy scale $\sim$ 5.0%. The systematic uncertainties sum up to a total of $\sim$ 14.0%. For the X_{max}, the systematic uncertainty for ultra-high energies is of about $^{+10}_{-7}$g/cm^2.

An example of the camera event view and the geometry fit for a proton shower with $E = 5.304 \times 10^{18}$ eV and $\theta = 38^o$ recorded by Coihueco telescope mirror 5 is shown in Figures 5.5 and 5.6. The reconstruction yields a shower distance of 5.32 ± 0.3 km from Coihueco.

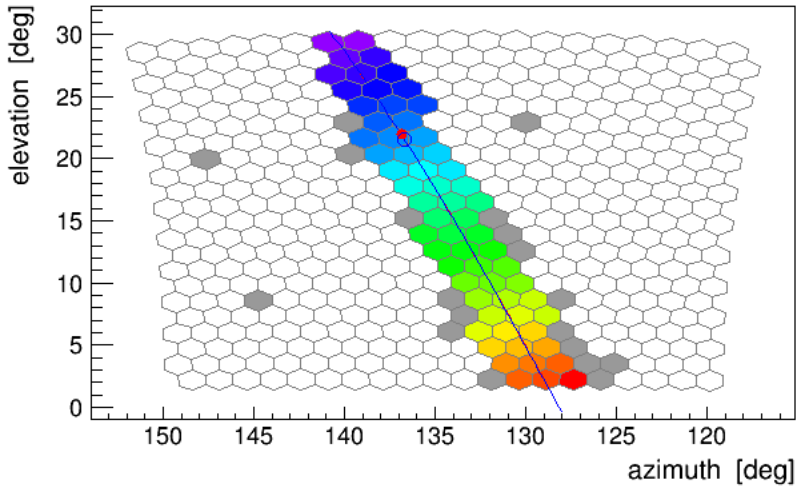

FIGURE 5.5: Proton shower recorded by Coihueco telescope mirror 5. The relative arrival time of the fluorescence light is coded in the colour of the pixel from blue (early) to red (late).

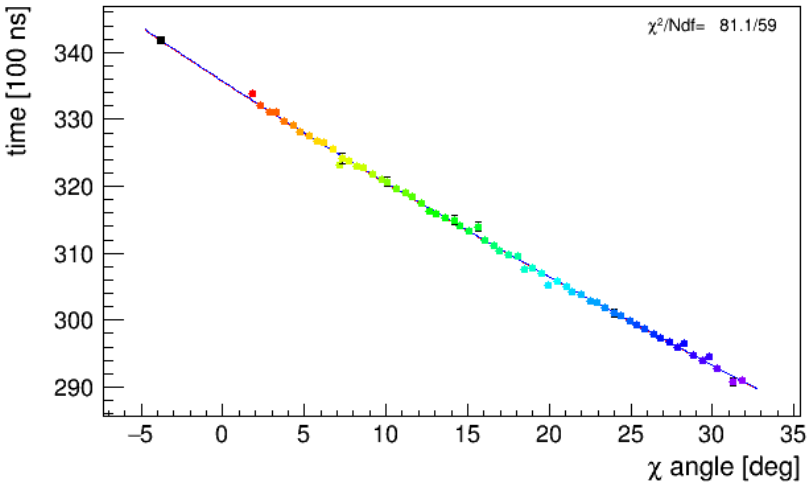

FIGURE 5.6: Event display of a single proton shower event. The coded colours correspond to the timing information from early (blue) to late (red). The black point represents the used surface detector.

Figure 5.7 shows the number of collected photons at the aperture as a function of time is converted into an energy-deposit profile as a function of the atmospheric depth (see Figure 5.8). The Gaisser-Hillas fit yields a value of 743 $\pm$ 9 g/cm^2.

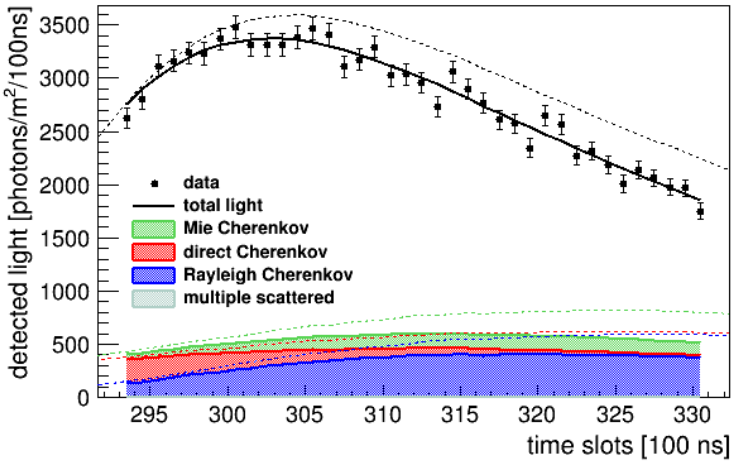

FIGURE 5.7: Collected UV photons at telescope aperture per time bin of 100 ns including the fractions identified as being due to direct and multiple scattered Cherenkov light. The fitted light curve is marked as black line. The night-sky background light is subtracted.

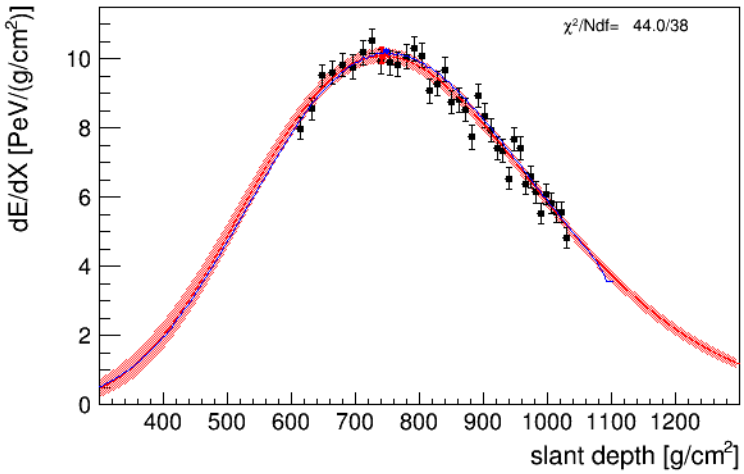

FIGURE 5.8: Longitudinal shower profile of the recorded event together with Gaisser-Hillas-fit.

Air Shower Simulations

This chapter describes the Monte Carlo simulations of cosmic-ray induced air showers produced with CORSIKA program and its extension for the radio emission CoREAS, which are used to investigate the shower observables measured by AMIGA, fluorescence detectors and AERA. Moreover, these observables are combined for mass composition studies. From the simulated signal in the detectors the muon density, the primary energy, the radiation energy and the fluorescence energy were reconstructed as described in Chapter 5. The muon density was reconstructed at different distances from the shower axis and combined with the different energy estimators to investigate which distance and energy estimator feature the best mass separation. The mass composition analyses using the different detection-method responses were carried out in two phases: i) AMIGA and Fluorescence analyses and ii) AMIGA and AERA analyses.

6.1 Simulation setup

The Monte Carlo simulations used in this thesis consist of 500 showers for proton and 500 showers for iron as primaries for QGSJETII-04 [76] and EPOS-LHC [195] hadronic models and 1500 showers for proton and 1500 showers for iron for Sibyll 2.3 [79], zenith angle θ = 38°, azimuth angle ϕ from 0° to 60°, uniformly distributed over the full energy range from 3 $\times$ $10^{17.5}$ to 10^{19} eV (see Figure 6.1). The chosen zenith angle corresponds to the median of the solid angle from the SD analysis for the zenith angle distribution between 0° and 50°. The use of different hadronic interaction models allows us to understand qualitatively the dependence of the air-shower observables on the characteristics of the hadronic particle production. Comparing the different models, the remaining open issues in hadronic interactions are the pion-air interactions and nuclear effects [196]. All showers were simulated with CORSIKA [197] and CoREAS [189] with a thinning threshold $\epsilon_{\text{th}} = E/E_0$ of E_0 = 10^6 eV. The Earth's magnetic field is set to a constant value of B_x = 19.79 μT and B_z = -14.15 μT for all events. The US standard atmosphere is used as atmospheric model. The observation level was adjusted to 100 m below the mean altitude of the AERA array to avoid artefacts that can occur in the simulation of the radio emission when the shower stops at the detector height (on average 1452 m a.s.l. corresponding to 870 g cm^{-2} atmospheric depth). All showers were simulated with radio cores distributed over the AMIGA Unitary Cell.

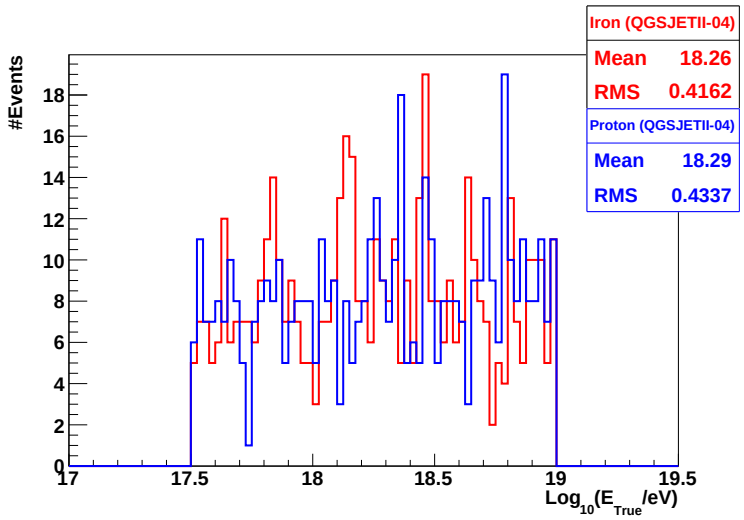

FIGURE 6.1: Energy distribution of the simulated showers induced by proton and iron in logarithmic scale.

The showers simulated with CORSIKA and CoREAS were used as input in the analysis software framework Offline [177], which is designed to reconstruct the air-shower properties from measured and simulated showers. For the analyses regarding AMIGA and fluorescence detectors, the Offline release Holt (v3r3, revision 31361) was used and for AMIGA and AERA, the release Fschlueter (trunk, revision 31522) was utilized. The reason for using different Offline versions lies in the fact that in revision 31522 there is another model for the two-dimensional lateral distribution function for radio (named GeoCeLDF, previously explained in section 5.3) which increases the reconstructed radiation-energy resolution. The pipeline regarding the simulation and reconstruction modules for simulated showers is reported in Appendix A.1.1 (for AMIGA and Fluorescence analyses), and Appendix A.1.2 (for AMIGA and AERA analyses).

The detectors were simulated in the 750 m *infill* array of the Observatory which comprises AMIGA MD counters at each of the 61 surface detectors (each muon counter consists of 3 modules. Each module consists of 64 plastic scintillator strips and a PMT multi-pixel electronic acquisition which is triggered by the surface detectors) spaced 750 m from each other, 24 radio stations equipped with LPDA antennas on a grid with 150 m antenna separation, 125 stations of butterfly antennas with 250 m, 375 m and 750 m spacing and three fluorescence telescopes with 30° to 56° elevation angle located next to the 3° to 30° elevation angle fluorescence telescopes with elevation angle 3° to 30° installed at Cerro Coihueco (see Figure 6.2).

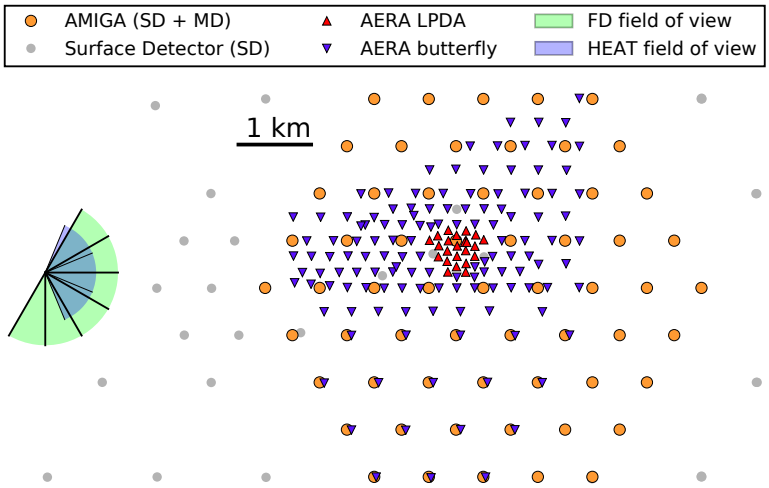

FIGURE 6.2: Schematic overview of the Auger Engineering Radio Array, a part of the surface detector array and AMIGA. The Coihueco site of the fluorescence detector and the HEAT extension are also indicated with their fields of view.

The simulated AMIGA MD counters have a total area of 30 m^2 and are buried at 2.3 m below the ground. An illustration of one of the simulated AMIGA MD counters is shown in Figure 6.3.

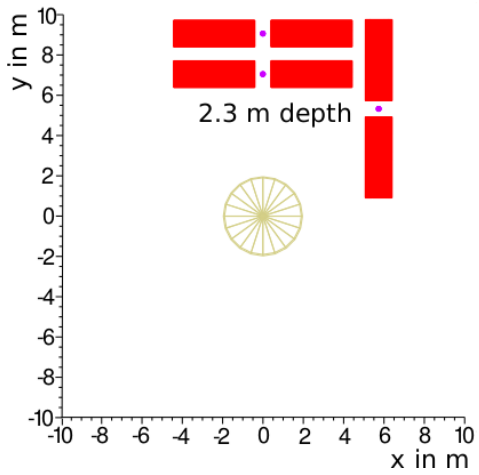

FIGURE 6.3: Illustration of the AMIGA counter design used for the simulation.

The reconstructed arrival directions of the simulated events are shown in Figure 6.4 and a map of the air shower cores is displayed in Figure 6.5. The shower core is reconstructed by fitting a plane shower front model to the signal arrival times in the surface detectors.

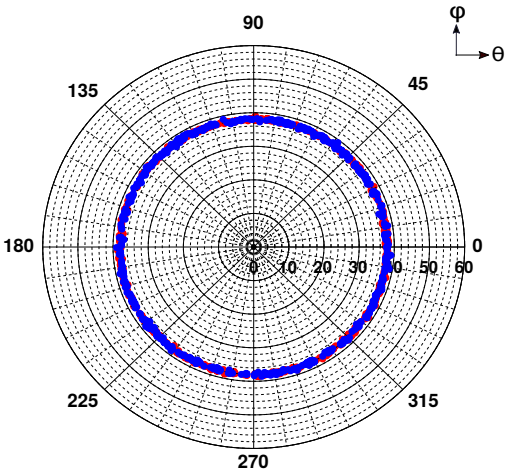

FIGURE 6.4: Skyplot of the arrival directions of proton (blue) and iron (red)-induced air showers simulated with QGSJETII-04 hadronic interaction model. The showers were simulated with a fixed zenith angle of 38°.

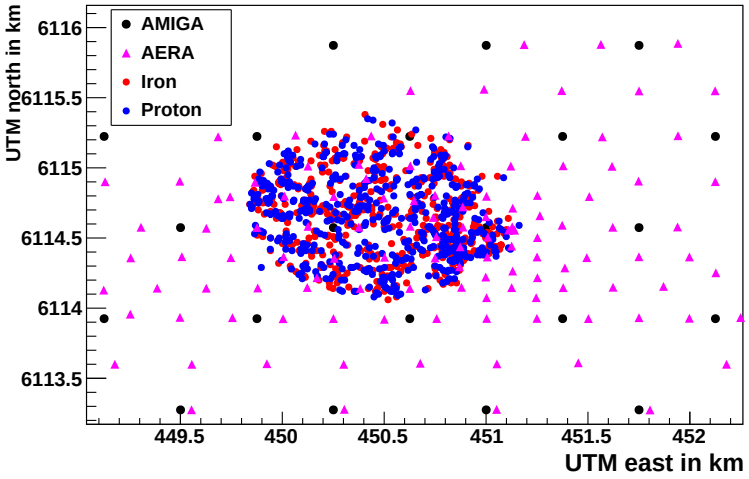

FIGURE 6.5: Map of the shower cores reconstructed with the surface detectors for proton (blue) and iron (red)-induced air showers.

Since MD, AERA and FD are exclusively sensitive to the muonic and electromagnetic component respectively, we can analyse the muon density at a certain distance from the shower axis using AMIGA MD counters, the radiation energy radiated by the electromagnetic component of the air shower using AERA stations, and the fluorescence energy emitted by the nitrogen in the atmosphere using Coihueco and HEAT telescopes. The obtained results are described in the following sections.

6.2 MD analysis

6.2.1 Reconstruction of the Muon Lateral Distribution

The muon density registered by the AMIGA MD counters was estimated using the MLDF described in section 5.2. The distributions of the muon density reconstructed at all r_{ref} from the shower axis for QGSJETII-04, EPOS-LHC and Sibyll 2.3 are shown in Figures 6.6, 6.7 and 6.8.

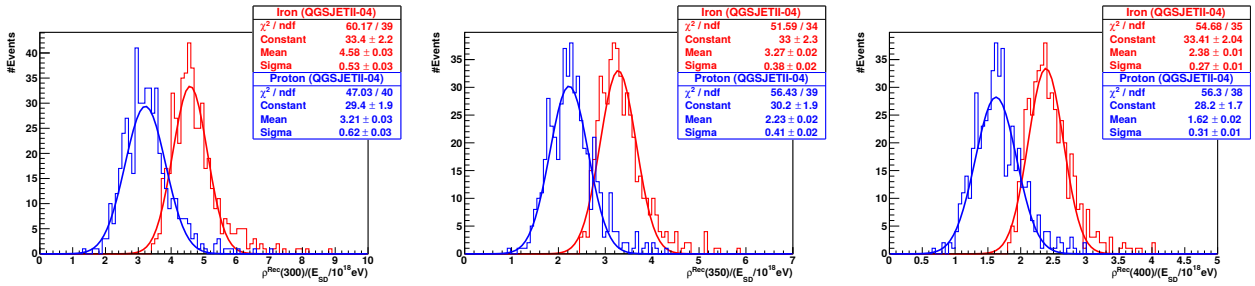

(A) 300 m

(B) 350 m

(C) 400 m

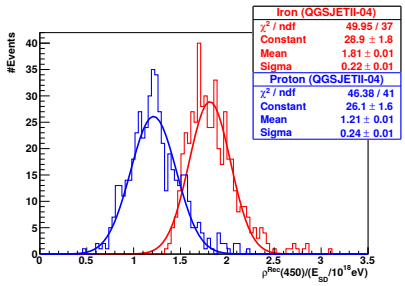

(D) 450 m

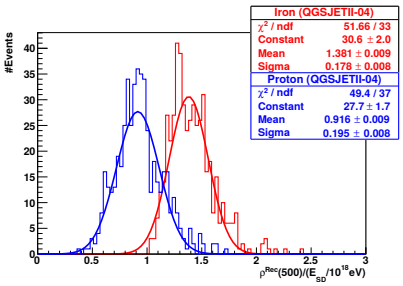

(E) 500 m

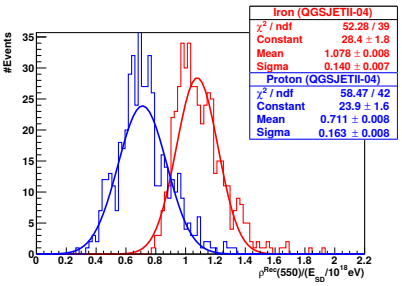

(F) 550 m

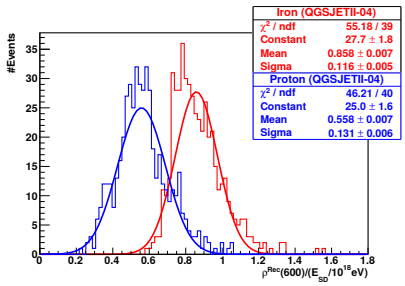

(G) 600 m

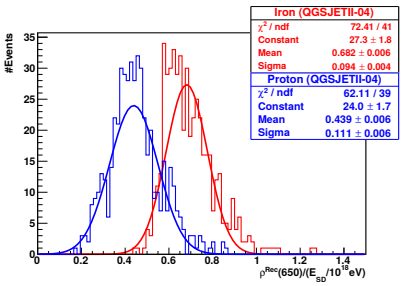

(H) 650 m

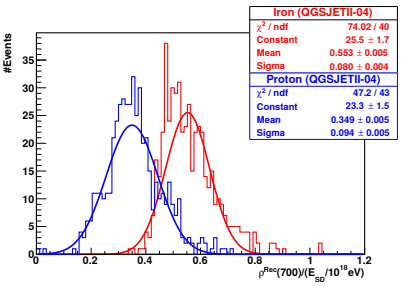

(I) 700 m

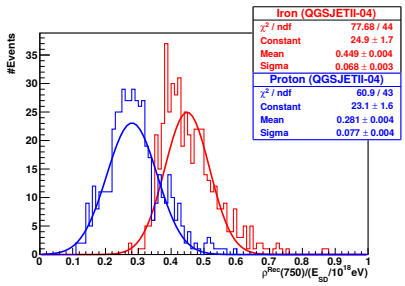

(J) 750 m

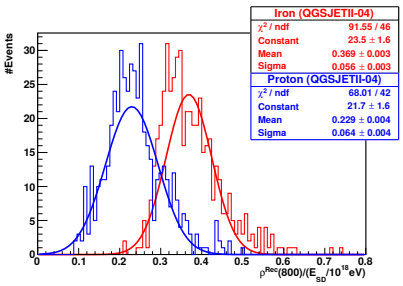

(K) 800 m

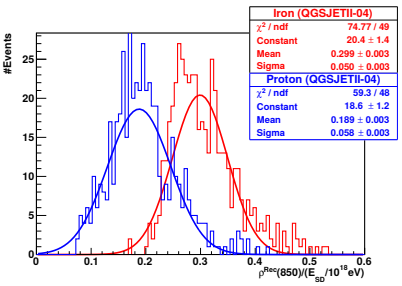

(L) 850 m

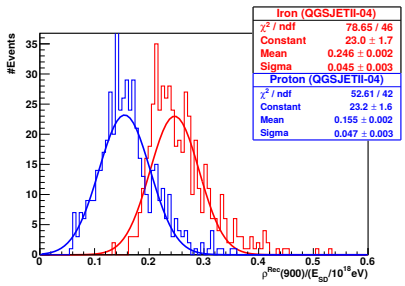

(M) 900 m

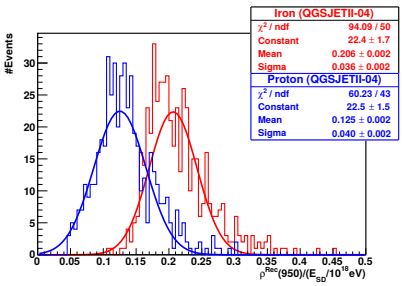

(N) 950 m

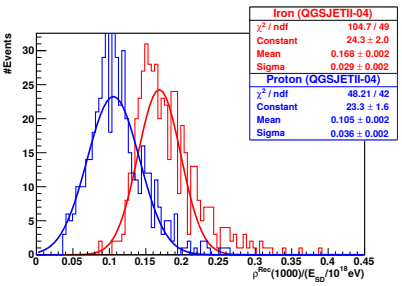

(O) 1000 m

FIGURE 6.6: Muon density reconstructed at r_{ref} =300, 350, 400, 450, 500, 550, 600, 650, 700, 750, 800, 850, 900, 950, and 1000 m from the shower axis divided by the normalized SD energy for proton (blue) and iron (red) showers simulated with QGSJETII-04 hadronic interaction model.

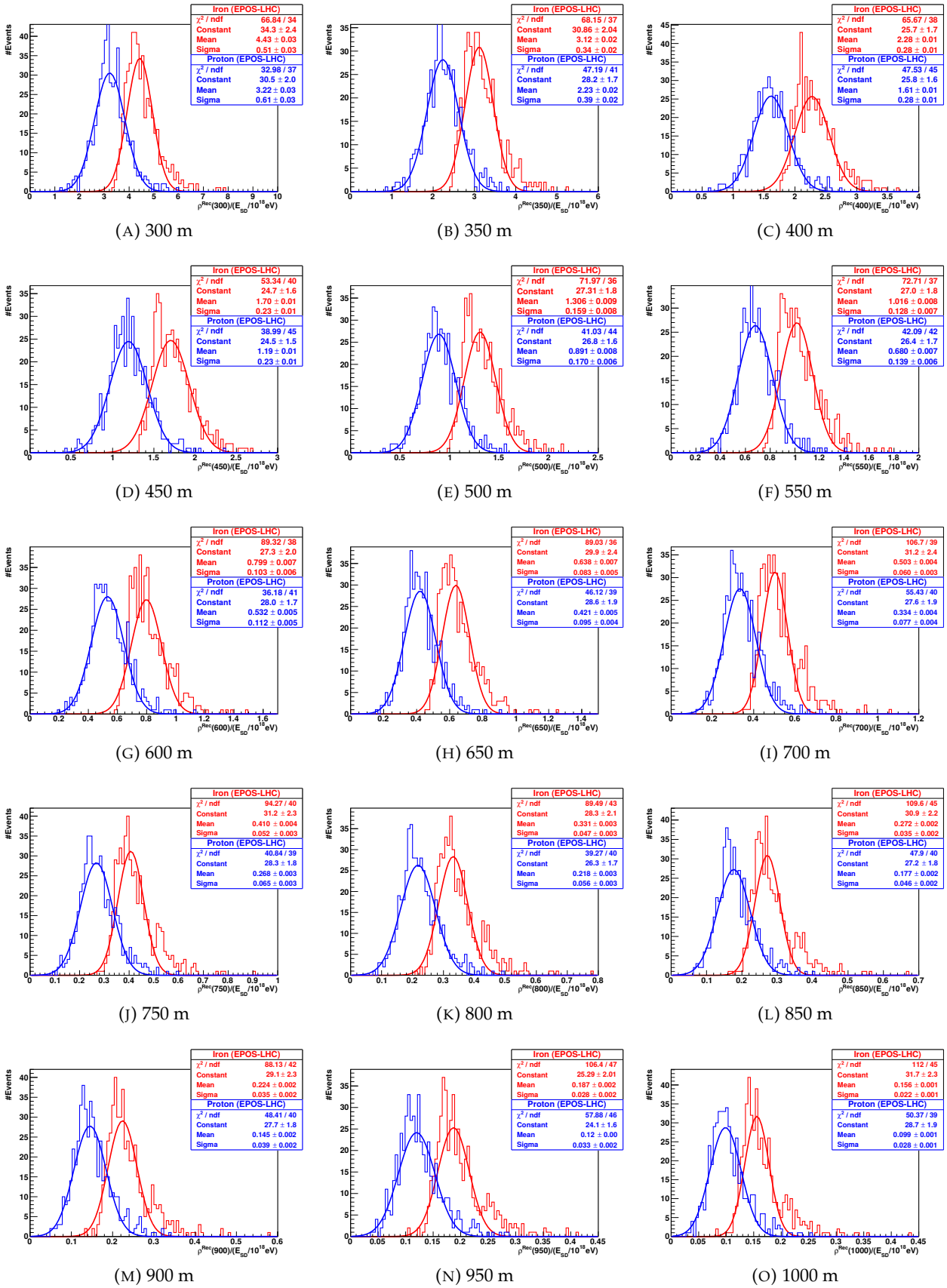

(A) 300 m (B) 350 m (C) 400 m

(D) 450 m (E) 500 m (F) 550 m

(G) 600 m (H) 650 m (I) 700 m

(J) 750 m (K) 800 m (L) 850 m

(M) 900 m (N) 950 m (O) 1000 m

FIGURE 6.7: Muon density reconstructed at r_{ref} =300, 350, 400, 450, 500, 550, 600, 650, 700, 750, 800, 850, 900, 950, and 1000 m from the shower axis divided by the normalized SD energy for proton (blue) and iron (red) showers simulated with EPOS-LHC hadronic interaction model.

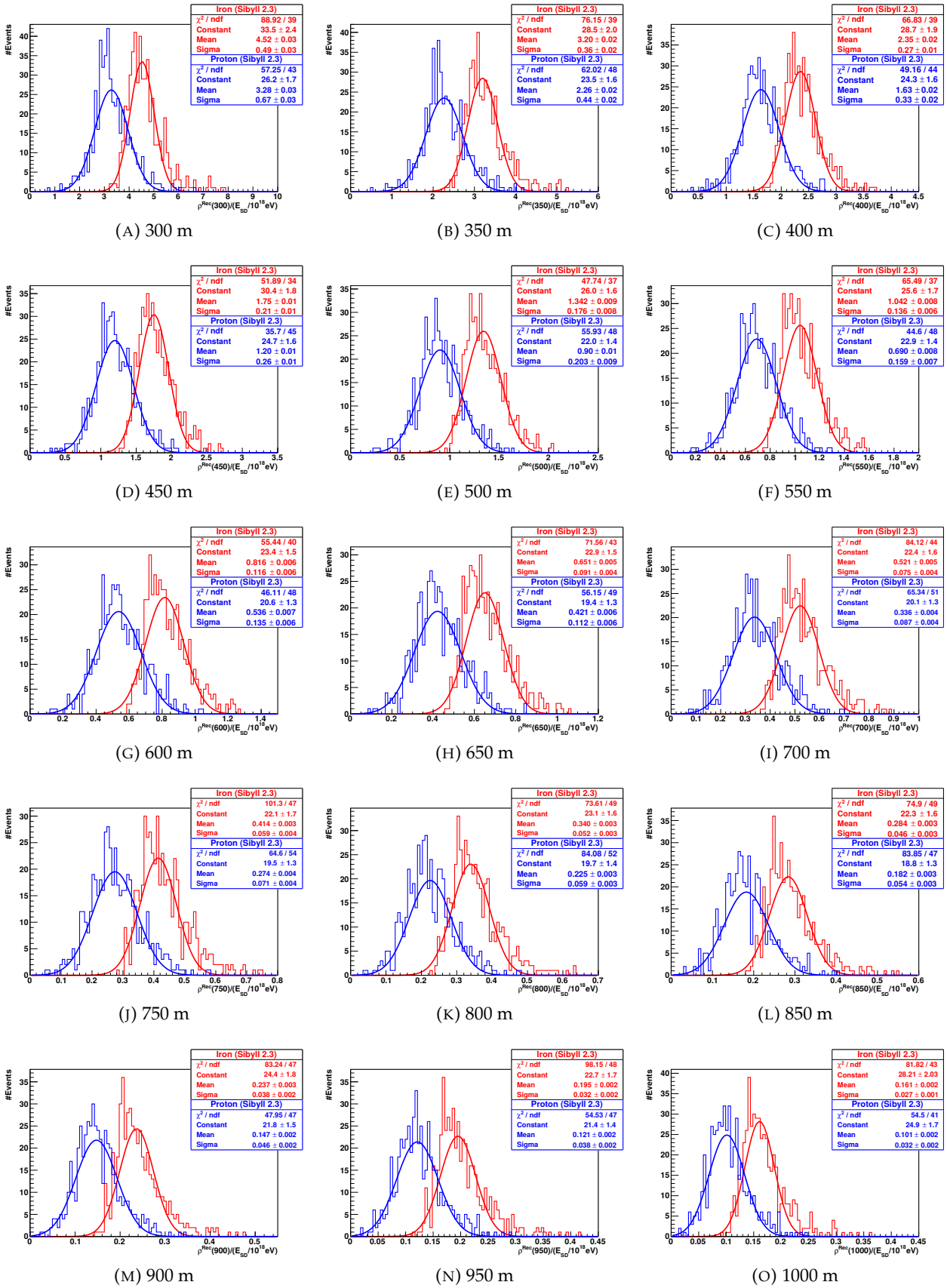

(A) 300 m (B) 350 m (C) 400 m

(D) 450 m (E) 500 m (F) 550 m

(G) 600 m (H) 650 m (I) 700 m

(J) 750 m (K) 800 m (L) 850 m

(M) 900 m (N) 950 m (O) 1000 m

FIGURE 6.8: Muon density reconstructed at r_{ref} =300, 350, 400, 450, 500, 550, 600, 650, 700, 750, 800, 850, 900, 950, and 1000 m from the shower axis divided by the normalized SD energy for proton (blue) and iron (red) showers simulated with Sibyll 2.3 hadronic interaction model.

The mean value of the muon density reconstructed ($\rho_{\mu}^{\mathrm{Rec}}(r_{\mathrm{ref}})$) at different distances from the shower axis is shown in Figure 6.9. Showers initiated by heavier primaries develop earlier and have a larger muon content than proton showers. Since muons are produced close to the shower axis and interact weakly with matter, they can travel long distances to reach the detector without being deflected from their propagation direction. Therefore, the muon density is higher for distances closer to the shower axis. Furthermore, the uncertainty of the reconstructed muon density is increased for distances closer to the shower axis as the muon density is divided by the energy reconstructed with the surface detectors (SD energy).

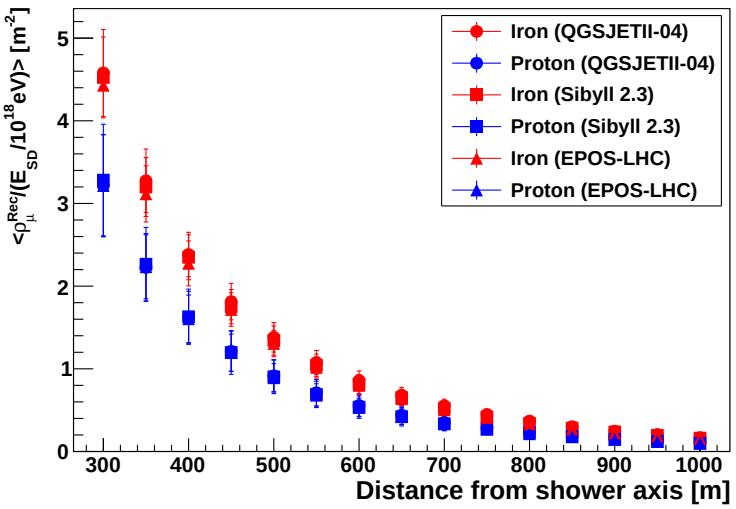

FIGURE 6.9: Mean muon density reconstructed for different distances from the shower axis normalized by the SD energy for proton and iron-induced air showers.

The mass discrimination power of $\rho_{\mu}^{\mathrm{Rec}}(r_{\mathrm{ref}})$ depends strongly on the uncertainty of the reconstruction method. Thus to study the uncertainty introduced by the reconstruction method we define [198]

$$\epsilon = \frac{\rho_{\mu}^{\mathrm{Rec}}(r_{\mathrm{ref}})}{\rho_{\mu}^{\mathrm{True}}(r_{\mathrm{ref}})} - 1, \tag{6.1}$$

where $\rho_{\mu}^{\mathrm{Rec}}(r_{\mathrm{ref}})$ is the reconstructed muon density for all r_{ref} and $\rho_{\mu}^{\mathrm{True}}(r_{\mathrm{ref}})$ is the true average muon density. $\rho_{\mu}^{\mathrm{True}}(r_{\mathrm{ref}})$ was determined by sampling muons in a 4.2 m wide ring (in the ground plane) at the different r_{ref} from the shower axis. Since the detection threshold of the AMIGA MD counters corresponds to approximate 1 GeV, only muons above this energy are considered for the true muon density. The true muon density was determined for each simulated air shower, assuming no significant azimuthal asymmetries being present.

In Figure 6.10 an example histogram of the ϵ distribution for the muon density reconstructed at 500 m from the shower axis is shown for showers induced by proton and iron with energies from 3×10^{17} to 10^{19} eV for the QGSJETII-04 hadronic interaction model. The reconstructed muon density is underestimated by $(22.6 \pm 0.4)\%$ for iron showers and $(31.4 \pm 0.4)\%$ for proton showers. Proton showers show a larger offset to the true muon density than iron showers which implies they are subject to larger shower-to-shower fluctuations.

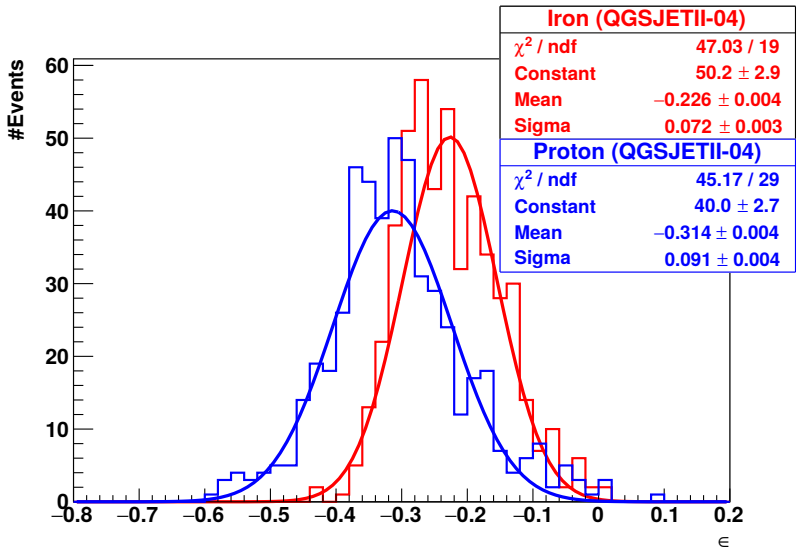

FIGURE 6.10: ϵ distribution for the muon density reconstructed at 500 m from the shower axis for showers initiated by proton (blue) and iron (red) as primaries for the QGSJETII-04 hadronic interaction model.

Figure 6.11 shows $\sigma(\epsilon)$ (relative error of $\rho_{\mu}^{\mathrm{Rec}}(r_{\mathrm{ref}})$) obtained as the RMS of the distributions of ϵ, as a function of the distance from the shower axis for QGSJETII-04, Sibyll 2.3 and EPOS-LHC. With increasing distance to the shower axis, the uncertainty of the reconstructed muon density keeps more or less stable. The relative uncertainty is lower than 11% for all distances and hadronic interaction models, showing a good correlation between the true muon density and the muon density reconstructed at all distances from the shower axis. The relative error for iron as primary is smaller than for protons because proton showers feature larger shower-to-shower fluctuations.

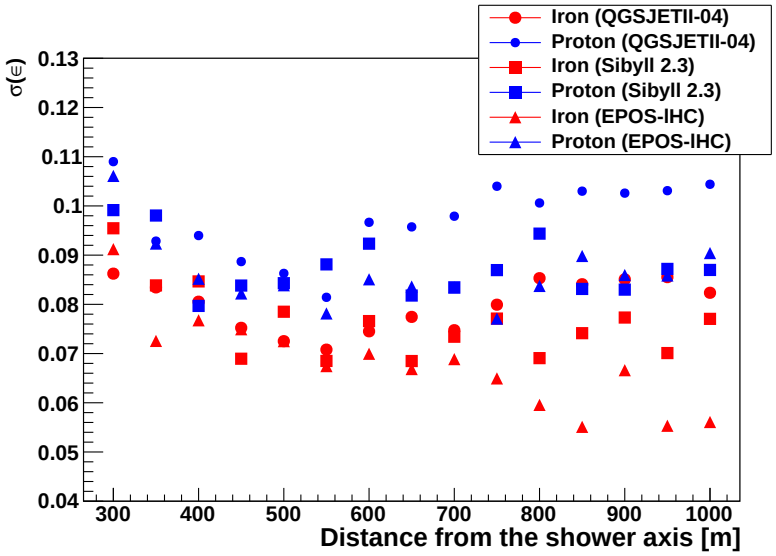

FIGURE 6.11: Relative error of the muon density reconstructed at distances from 300 to 1000 m from the shower axis for showers induced by proton and iron for QGSJETII-04, Sibyll 2.3 and EPOS-LHC.

The relative error of the muon density reconstructed at 500 m from the shower axis as a function of the primary cosmic-ray energy in logarithmic scale is shown in Figure 6.12. As expected, the relative error decreases with energy, since the number of muons in the air showers increase almost linearly with primary energy ($\propto E^{0.9}$), and therefore, the number of triggered muon detectors and the total number of muons in each detector also increase.

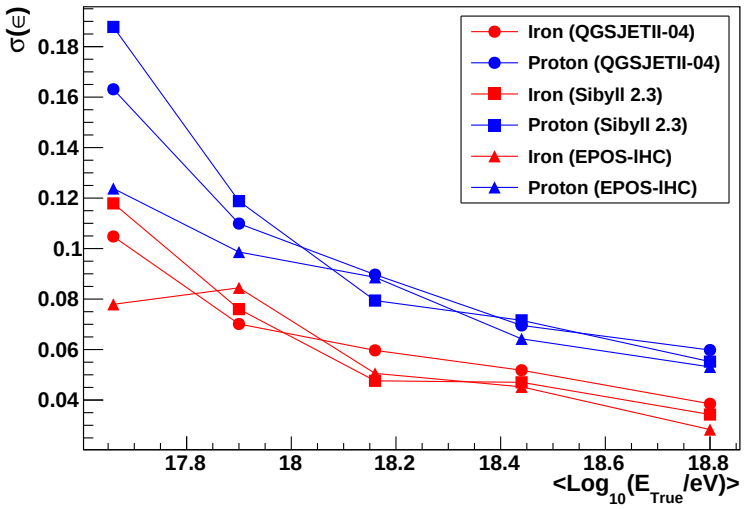

FIGURE 6.12: Relative error of the muon density reconstructed at 500 m from the shower axis for proton and iron as primaries for QGSJETII-04, Sibyll 2.3 and EPOS-LHC as a function of the primary cosmic-ray energy in logarithmic scale.

6.3 Energy Reconstruction with Surface Detectors

Figure 6.13 shows the energy reconstructed with the surface detectors as a function of the true primary cosmic-ray energy for the hadronic interaction interaction models QGSJETII-04, EPOS-LHC and Sibyll 2.3. The reconstructed primary energy has a linear dependence on the primary cosmic-ray energy.

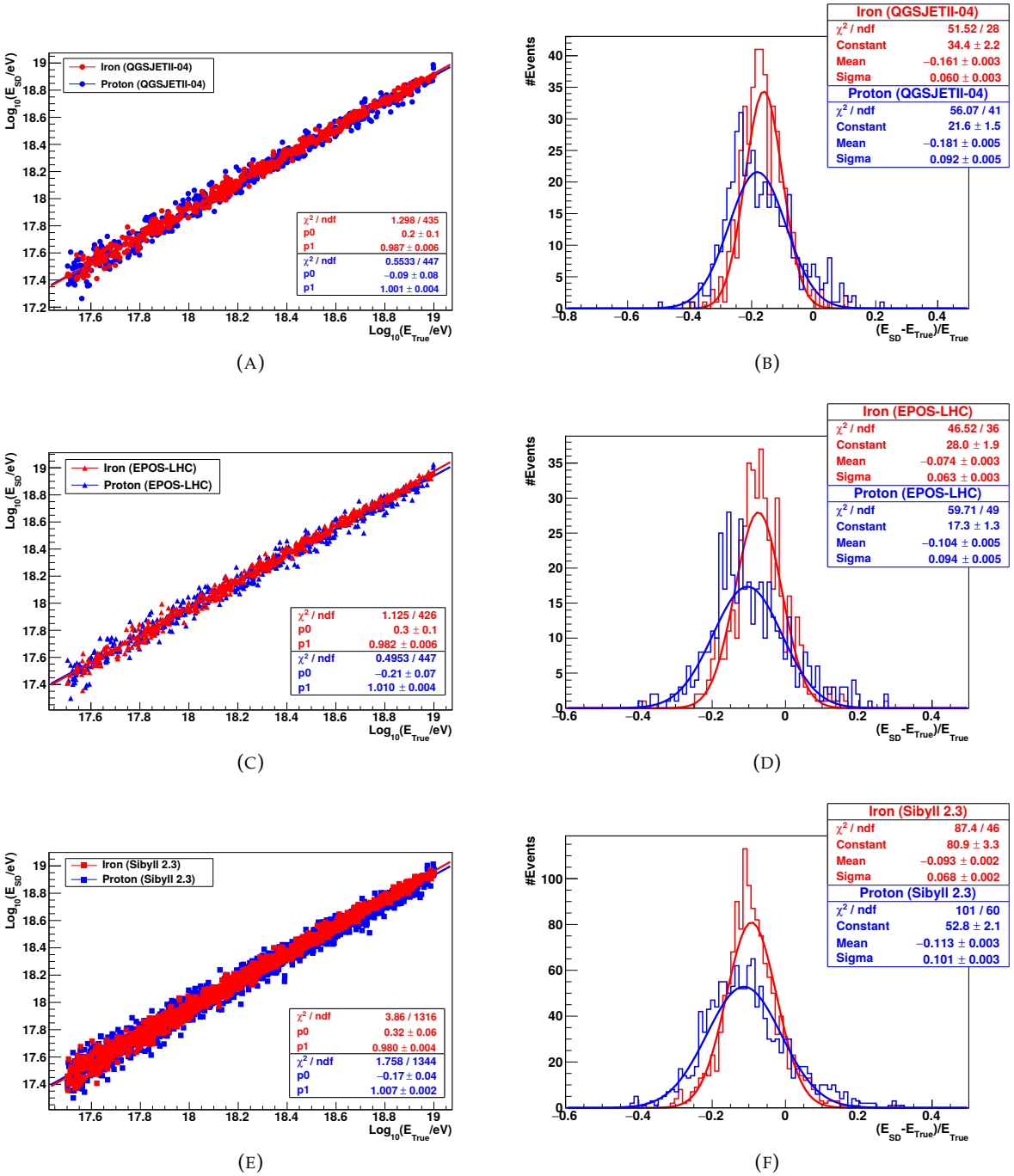

FIGURE 6.13: Reconstruction of the primary cosmic-ray energy from the SD signal. Left: Primary energy reconstructed with the surface detectors (E_{SD}) as a function of the true primary cosmic-ray energy for the hadronic interaction models QGSJETII-04, EPOS-LHC and Sibyll 2.3. Right: E_{SD} reconstruction uncertainty. The E_{SD} is underestimated for both proton and iron-induced air showers due to the deficit of muons in the hadronic interaction models. Showers initiated by proton feature less muons than iron showers of the same energy. Since the surface detectors are sensitive to the muonic component of the shower, the signal from proton showers is smaller than from iron ones.

The primary energy reconstructed with SD is underestimated for proton and iron-induced showers for all three hadronic interaction models. The SD is sensitive to the muonic component of the shower and since there is a muon deficit in the hadronic interaction models in comparison to experimental measurements [199], the reconstructed SD energy is influenced by this discrepancy. The bias in the energy reconstruction is slightly larger for proton than iron showers and it depends on the hadronic interaction model. This offset indicates a mass dependent reconstruction bias on the primary cosmic ray energy. Furthermore, showers induced by proton feature less muon content than iron showers of the same energy. The relative difference between the reconstructed and true energy is larger for proton by 2% for QGSJETII-04, 3% for EPOS-LHC and 2% for Sibyll 2.3. Moreover, QGSJETII-04 is the hadronic model that features the largest bias in the energy reconstruction and EPOS-LHC shows the smallest one.

6.3.1 Radiation Energy

The radiation energy originates from the radiation emitted by the electromagnetic component of the air shower. Thus the radiation energy correlates best with the electromagnetic cascade energy instead of the full shower energy, in which there is energy carried away by neutrinos and high energy muons that is not significant for the radio emission. The electromagnetic cascade energy can be inferred assuming a specific cosmic-ray composition and hadronic interaction model.

In what follows the true radiation energy is calculated for the set of CORSIKA simulations described above (proton and iron-induced air-showers with a fixed zenith angle of 38°, uniformly distributed over the energy range from 3×10^{17} eV to 10^{19} eV, and QGSJETII-04 hadronic model) using the model developed by Glaser et al. [170] to study the radiation energy released by extensive air showers in the frequency range of MHz. Moreover, a correlation of the true radiation energy with the electromagnetic air shower energy is made and it is analysed at the Auger Observatory level.

The radiation energy is the sum of the radiation energy of the geomagnetic emission and the radiation energy of the charge-excess emission [200]. However, before correlating the radiation energy with the electromagnetic cascade energy, the radiation of the geomagnetic emission has to be corrected for geometry. This radiation depends on the magnitude of the geomagnetic field B_{Earth} and the angle α between the shower axis and the geomagnetic field, scaling with $\sin^2\alpha$. On the other hand, the radiation energy of the charge-excess emission does not depend on the Earth's magnetic field.

Using a parametrization function from Glaser et al. [170] (Eq. 6.3) for the radiation energy corrected for $\sin\alpha$ as well as the atmospheric density at shower maximum correlated with the electromagnetic cascade energy, we can analyse the residuals of the relation between the corrected radiation energy (S_{RD}) and the electromagnetic cascade energy (E_{em}) as a function of the atmospheric density at shower maximum ($\rho_{X_{\text{max}}}$). The atmospheric density was determined by using the US standard atmospheric model.

The correction for the radiation energy is given by

$$S_{\mathrm{RD}} = \frac{E_{\mathrm{rad}}}{a(\rho_{\mathrm{X_{max}}})^2 + (1 - a(\rho_{\mathrm{X_{max}}})^2)\sin^2\alpha}, \tag{6.2}$$

where $a(\rho_{\mathrm{X_{max}}})$ is the parametrization of the charge-excess fraction [170]. Fitting a power-law function of the form

$$S_{\mathrm{RD}} = A \times 10^7 \mathrm{eV} \left(\frac{E_{\mathrm{em}}}{10^{18}\,\mathrm{eV}} \right)^B \tag{6.3}$$

where A=1.683 $\pm$ 0.004 and B=2.006 $\pm$ 0.001, one finds that S_{RD} scales quadratically with the electromagnetic cascade energy E_{em} as expected for coherent emission.

The amount of radiation energy increases with slant depth as the shower develops in the atmosphere. The relation between the corrected radiation energy S_{RD} and the electromagnetic cascade energy of the air shower depends on the density at shower maximum ($\rho_{\mathrm{X_{max}}}$) as shown in Figure 6.14. There is more radiation energy in a region where the atmospheric density is low. Thus, showers that develop earlier in the atmosphere have a slightly larger radiation energy than showers of the same energy that develop deeper in the atmosphere as the air density increases with increasing atmospheric depth.

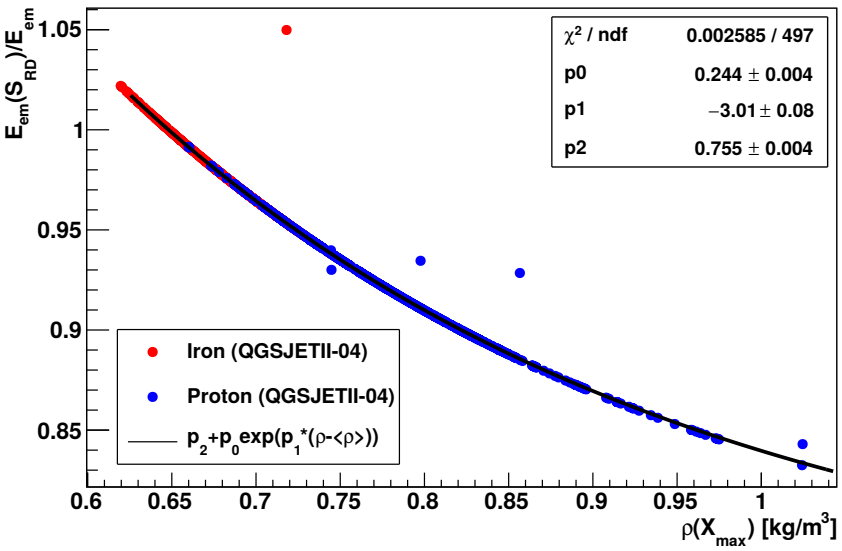

FIGURE 6.14: Correlation between S_{RD} and electromagnetic cascade energy (E_{em}) of proton and iron induced air-showers and QGSJETII-04 hadronic interaction model plotted as a function of the atmospheric density at shower maximum ($\rho_{\mathrm{X_{max}}}$).

As the radiation energy increases with decreasing atmospheric density, a second correction term is applied to S_{RD}:

$$S^{\rho}_{RD} = \frac{E_{rad}}{a(\rho_{X_{max}})^2 + (1 - a(\rho_{X_{max}})^2)\sin^2\alpha} \frac{1}{(1 - p_0 + p_0 \exp[p_1(\rho_{X_{max}} - \langle\rho\rangle)])^2}, \quad (6.4)$$

where $\langle\rho\rangle$=0.65 kg/m^3, p_0 and p_1 are parameters from a combined chi-square fit of S^{ρ}_{RD} as a function of the electromagnetic cascade energy. Their values are p_0 = -29.47 $\pm$ 0.009 and p_1 = -2.95 $\pm$ 0.06 m^3/kg.

Sometimes the X_{max} information is not accessible in a measurement or it presents large experimental uncertainties. As most of the variation of $\rho_{X_{max}}$ is due to the zenith angle of the incident shower, the radiation energy can be corrected only taking into account the zenith angle. For all showers the density at the position of the shower maximum $\rho_\theta = \rho(\theta, \langle X_{max}\rangle)$ was calculated assuming an average $\langle X_{max}\rangle$=669 g/cm^2. Thus parametrizing the variation of the charge excess fraction (Eq. 6.5) using the zenith angle we have Eq. 6.6

$$a(\rho_{X_{max}}) = 0.43(e^{1.11 m^3/kg(\rho_{X_{max}} - \langle\rho\rangle)}) - 0.24, \quad (6.5)$$

where $\langle\rho\rangle$ = 0.65 kg/m^3 is the atmospheric density at shower maximum for an average zenith angle of 45^o [170].

$$a(\rho_\theta) = 0.45(e^{1.14 m^3/kg(\rho_\theta - \langle\rho\rangle)}) - 0.24, \quad (6.6)$$

and then the corrected radiation energy (Eq. 6.4) can be defined as

$$S^{\rho_\theta}_{RD} = \frac{E_{rad}}{a(\rho_\theta)^2 + (1 - a(\rho_\theta)^2)\sin^2\alpha} \frac{1}{(1 - p_0 + p_0 \exp[p_1(\rho_\theta - \langle\rho\rangle)])^2}. \quad (6.7)$$

Figure 6.15 shows the corrected radiation energy $S^{\rho_\theta}_{RD}$ correlated with the electromagnetic cascade energy for air showers induced by proton and iron and QGSJETII-04 hadronic interaction model.

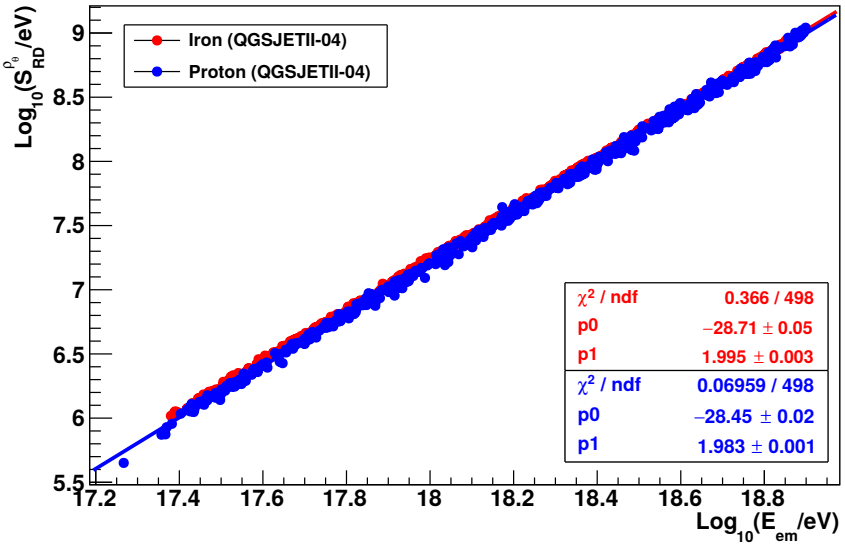

FIGURE 6.15: Correlation between $S^{\rho_\theta}_{\mathrm{RD}}$ and the electromagnetic cascade energy (E_{em}) of air showers induced by proton (blue) and iron (red) and QGSJETII-04 hadronic interaction model. The solid lines correspond to a power-law fit.

The slope parameter p_1 deviates from 2, which is because the average X_{max} increases linearly with the logarithm of the cosmic-ray energy [201]. Therefore, for the same zenith angle, the higher the shower energy the deeper the shower penetrates in the atmosphere, and consequently the smaller is the radiation energy. As we do not correct $S^{\rho_\theta}_{\mathrm{RD}}$ for an X_{max} dependence, the slope parameter p_1 shows a value slightly smaller than 2.

Clipping effect

If the radiation energy is detected by an observer located at a given altitude above sea level the shower may not be completely developed when it reaches the ground (such as the Pierre Auger Observatory), i. e., part of the shower that could contribute to the radiation energy is clipped.

The clipping effect depends on the atmospheric depth between the observer and the shower maximum X_{max}, and is defined as following (Eq. 6.8) [170]

$$DX_{\mathrm{max}} = \int_{h_0}^{\infty} \frac{\rho(h)}{\cos\theta} dh - X_{\mathrm{max}} = \int_{h_0}^{h(X_{\mathrm{max}})} \frac{\rho(h)}{\cos\theta} dh - X_{\mathrm{max}}, \tag{6.8}$$

where h_0 is the observer's altitude, θ is the zenith angle and $\rho(h)$ is the atmospheric density at a given height h above sea level.

Parametrizing the radiation energy fraction which is radiated as a function of DX_{max} we have

$$\frac{E_{\rm rad}(DX_{\rm max})}{E_{\rm rad}} = 1 - \exp(-8.7\,{\rm cm}^2/{\rm kg}(DX_{\rm max} + 0.29\,{\rm kg/cm}^2)^{1.89}). \quad (6.9)$$

The clipping effect is very important because the radiation energy needs to be corrected to estimate the primary cosmic-ray energy. As the $X_{\rm max}$ information is not always accessible or can present large experimental uncertainties, Glaser et al. (2016) [170] made an alternative parametrization for the clipping effect using the zenith angle and the primary cosmic-ray energy. The atmospheric depth between the observer and the $X_{\rm max}$ is proportional to the secant of the zenith angle with a dependence on the second order of the primary cosmic-ray energy as the mean value of $X_{\rm max}$ increases proportionally to the logarithm of the mass.

Thus the parametrization functions for showers induced by proton and iron as primaries used in this thesis are shown in Eqs. 6.10 and 6.11 as

$$E^{\rm p}_{\rm rad,1564\,m} = E_{\rm rad}\left(1 - \exp\left(-8.27\left(\frac{\sec\theta \cdot \log_{10}(10^{18})}{\log_{10}E_{\rm True}}\right)\right) - 0.71\right), \quad (6.10)$$

$$E^{\rm Fe}_{\rm rad,1564\,m} = E_{\rm rad}\left(1 - \exp\left(-7.17\left(\frac{\sec\theta \cdot \log_{10}(10^{18})}{\log_{10}E_{\rm True}}\right)\right) - 0.8\right). \quad (6.11)$$

Figure 6.16 shows the radiation-energy fraction ($E_{\rm rad,1564m}/E_{\rm rad}$) for proton and iron-induced showers with zenith angle of 38° and QGSJETII-04 hadronic interaction model. Since iron showers have a smaller $X_{\rm max}$ than proton showers, the fraction of clipped radiation energy is also smaller. The resulted radiation-energy fraction is compatible with [170] for the range between 1.2 and 1.3 in the x axis.

Radiation energy reconstruction

In Offline reconstruction the radiation energy is obtained by spatially integrating the two-dimensional lateral distribution function GeoCeLDF (as previously mentioned in section 5.3). Various quality cuts were applied to improve the radiation energy results.

1) A minimum number of 5 radio stations with signal and $S^2/N^2 \geq 10$ were considered to have one event reconstructed;

2) Events with unsuccessful reconstruction of the radio lateral distribution function (GeoCeLDF) were not taken into account since the radiation energy ($E_{\rm rad}$) is not reconstructed in that case. However, there are events that even having a successful GeoCeLDF reconstruction, present high uncertainty in the radiation energy value. Therefore we demanded the uncertainty on the radiation energy to be smaller than 100% of its value;

3) The radiation energy ($E_{\rm rad}$) depends on the geomagnetic angle α, which corresponds to the angle between the Earth's magnetic field and the shower axis,

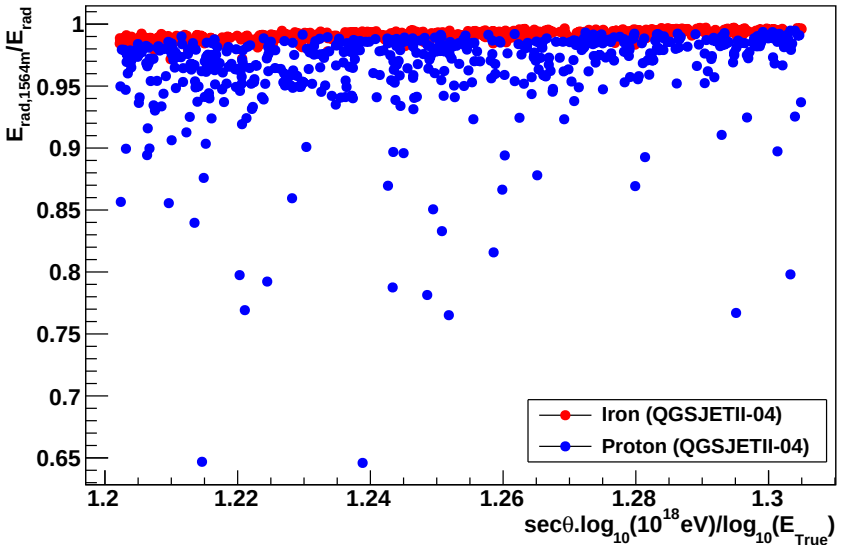

FIGURE 6.16: Fraction of radiation energy which is radiated up to the height of the Pierre Auger Observatory (1564 m a.s.l.) as a function of the zenith angle and the primary cosmic-ray energy for proton (blue) and iron (red)-induced showers and QGSJETII-04 hadronic interaction model.

and has to be corrected for this influence. On the other hand, these corrections lead to large uncertainties for small geomagnetic angles. Therefore, we used $\alpha \geq 10^{o}$, which corresponds to the domain of the geomagnetic emission over the Askaryan effect;

4) For the GeoCeLDF fit a chi-square probability higher than 0.0004 was applied.

The radiation energy is then corrected for the zenith-angle dependence and clipping effect using Eqs. 6.10 and 6.11 in 6.7. Figure 6.17 shows the radiation energy as a function of the true primary cosmic-ray energy for proton and iron-induced air showers for QGSJETII-04, EPOS-LHC and Sibyll 2.3. The events were fitted with a power-law function (Eq. 6.12) based on a maximum-likelihood approach accounting for the estimated uncertainties and detection efficiencies in the reconstruction of $S_{RD}^{\rho_\theta}$ as

$$S_{RD}^{\rho_\theta} = p_0 \left(\frac{E_{True}}{10^{18}\,eV} \right)^{p_1}. \tag{6.12}$$

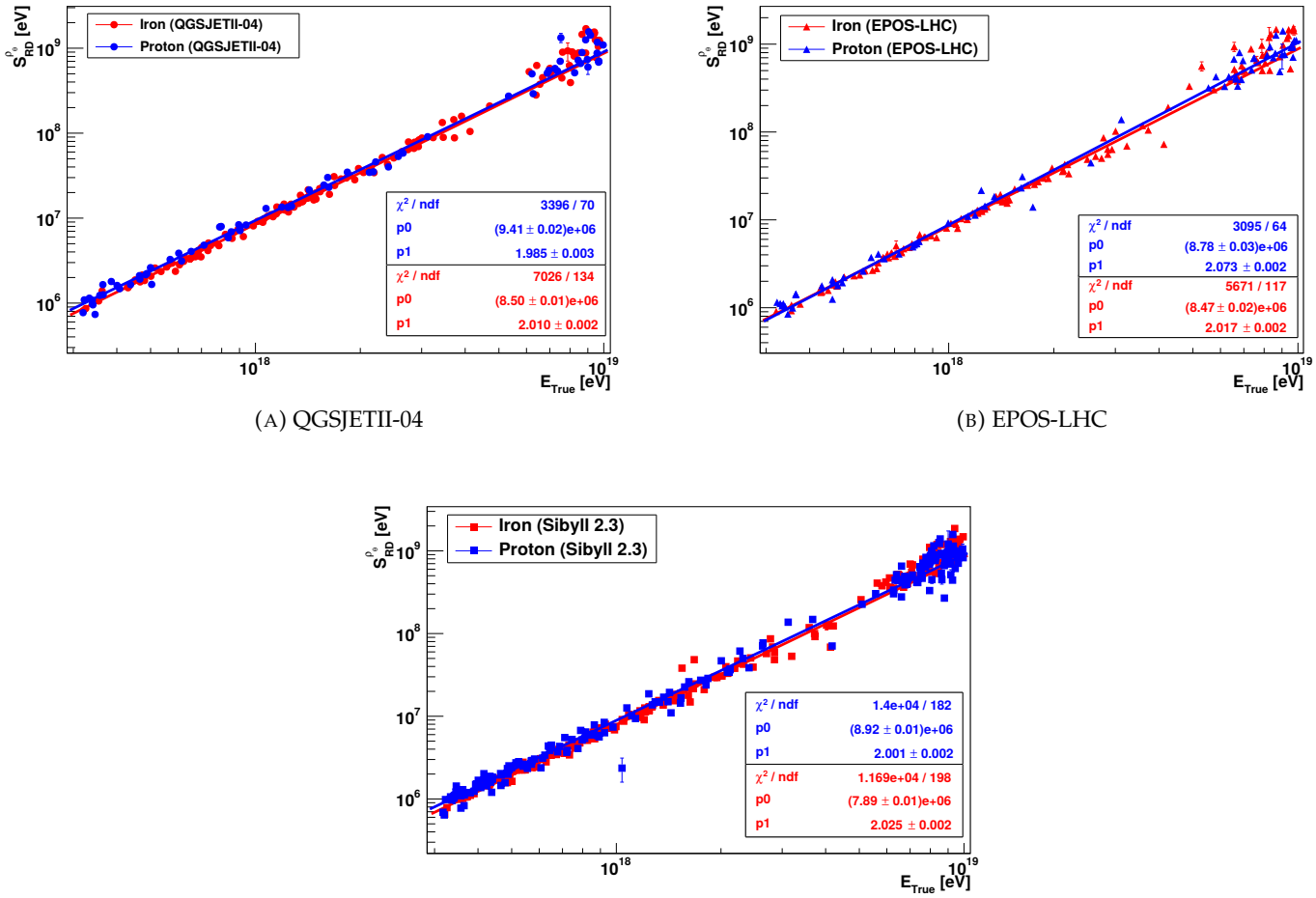

(A) QGSJETII-04

(B) EPOS-LHC

(C) Sibyll 2.3

FIGURE 6.17: Radiation energy corrected for the zenith-angle dependence and clipping effect as a function of the true primary cosmic-ray energy for proton (blue) and iron (red)-induced air showers with zenith angle of 38° and hadronic interaction models QGSJETII-04, EPOS-LHC and Sibyll 2.3. The solid lines correspond to the power-law fit.

The radiation energy increases with the true primary energy with an average index of 1.997 ± 0.002 for QGSJETII-04, 2.045 ± 0.002 for EPOS-LHC and 2.013 ± 0.002 for Sibyll 2.3. The derived parameters p_0 and p_1 from the fit are used to reconstruct the primary cosmic ray energy E_{RD} (Eq. 6.13)

$$E_{RD} = 10^{18}\text{eV} \left(\frac{S_{RD}^{\rho_\theta}}{p_0} \right)^{1/p_1} \tag{6.13}$$

which will be further combined with the muon density to estimate mass composition of primary cosmic rays. The E_{RD} reconstruction uncertainty is shown in Figure 6.18.

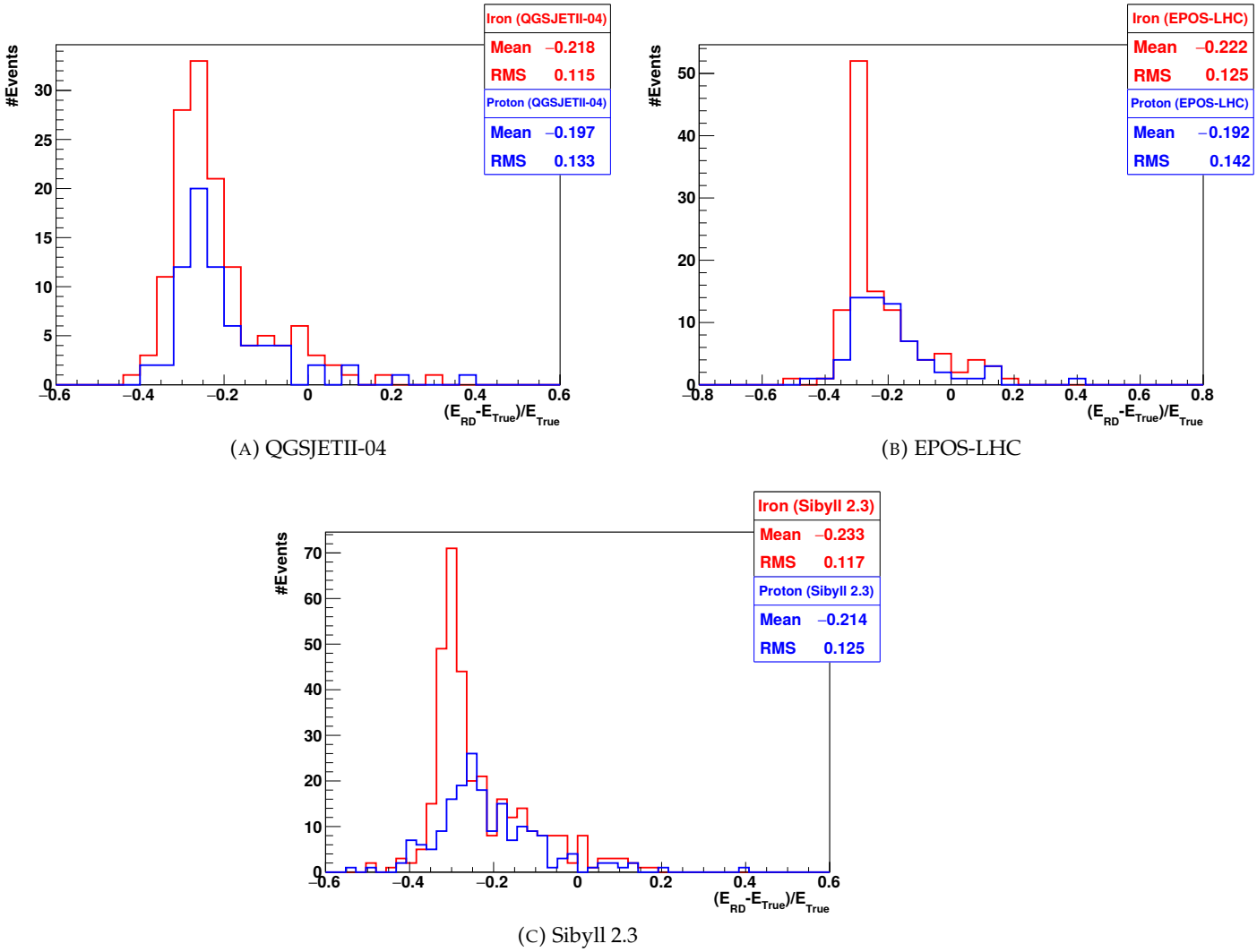

(A) QGSJETII-04

(B) EPOS-LHC

(C) Sibyll 2.3

FIGURE 6.18: E_{RD} uncertainty for the hadronic interaction models QGSJETII-04, EPOS-LHC and Sibyll 2.3.

The reconstructed primary energy estimated using the radiation energy measured by AERA is underestimated for proton and iron showers by about 21% for all the used hadronic interaction models. The uncertainty difference between proton and iron showers is about 2% which is not statistically significant. This statistical uncertainty is a combination of the uncertainties of the measurement and the reconstruction of the radiation energy. It is not only the radiation energy that is underestimated in the reconstruction, but also the energy fluence in the radio detectors from which the radiation energy is calculated [202]. The reconstructed energy fluence in the antennas features an average bias of 11%, while the reconstructed radiation energy shows an average bias of 10%. A description of the reconstruction steps to investigate the underestimation of the energy fluence can be found in [202].

6.4 FD analysis

To get high quality of the fluorescence detector analyses some cuts were applied.

The applied quality cuts can be classified in three categories: general, geometric and profile cuts. The general cuts correspond to the basic properties that the reconstructed events must have, as the fact that the event must be hybrid. The geometric cuts refer to the reconstructed shower geometry, such as the zenith angle must be lower than 55°. On the other hand, the profile cuts are related to the reconstructed shower profile, such as possible holes in the measured shower profile can not be very large.

General cuts

The applied general cuts are:

1) Events must be hybrid (events reconstructed by both SD and FD);

2) Event with no pixel saturation. The pixel saturates when the recorded light signal is larger than the dynamic range of the FD electronics. This may be the case for showers that fall directly onto the telescope;

3) The uncertainty on the reconstructed fluorescence energy ($\sigma(E_{\mathrm{FD}})/E_{\mathrm{FD}}$) of the event should be smaller than 20%;

4) The fluorescence energy should have at most 50% of Cherenkov radiation. The Cherenkov light contaminates the fluorescence signal [190]. When there is too much Cherenkov radiation in the FD measurements, the X_{max} and energy reconstruction can be influenced.

Geometric cuts

The geometric cuts refer to cuts applied in the zenith angle (which must be lower than 55°) and cuts in the distance between the shower core and the closest surface detector to this core (which must be lower than 800 m so that the active detection area is within the surface-detector array). As the showers were simulated inside the *infill* array, where the spacing among the surface detectors is 750 m, being the

shower axis inside the unitary cell and with a fixed zenith angle of 38°, no geometric cut was applied.

Profile cuts

The applied profile cuts are:

6) X_{max} reconstructed should be in the FOV (xMaxInFOV). Moreover, it is important that the reconstructed X_{max} does not lie at the border of the FOV but at a certain distance away from the border, so X_{max} should be at least 20 g/cm^2 distant from the FOV borders;

7) The X_{max} reconstructed uncertainty (xMaxError) should be less than 40 g/cm^2;

8) Possible holes in the shower profile without data have to be smaller than 30% of the total profile. The possible sources of holes are: i) the existence of clouds between the detector and the air shower, which taint the measured light profile. This source exists only for measured data since there is no cloud in simulations and ii) gaps between the FOV of different telescopes. This source is possible for both simulated and measured data;

9) The reduced χ^2/NDF of the Gaisser-Hillas fit has to be smaller than 2.5. This cut lets pass only events with a relative high fit quality.

Figure 6.19 shows the fluorescence light detected by the telescopes at Coihueco and HEAT (separately and simultaneously) as a function of the primary cosmic-ray energy for the hadronic interaction models QGSJETII-04, EPOS-LHC and Sibyll 2.3. The reconstructed fluorescence energy has a linear dependence with the primary cosmic ray energy. The fluorescence light is emitted by the nitrogen molecules in the atmosphere, which are mostly excited by electrons from the electromagnetic component of the air shower. Since proton showers produce larger electromagnetic size than iron showers of the same energy [203], there is more fluorescence light in showers induced by proton than iron.

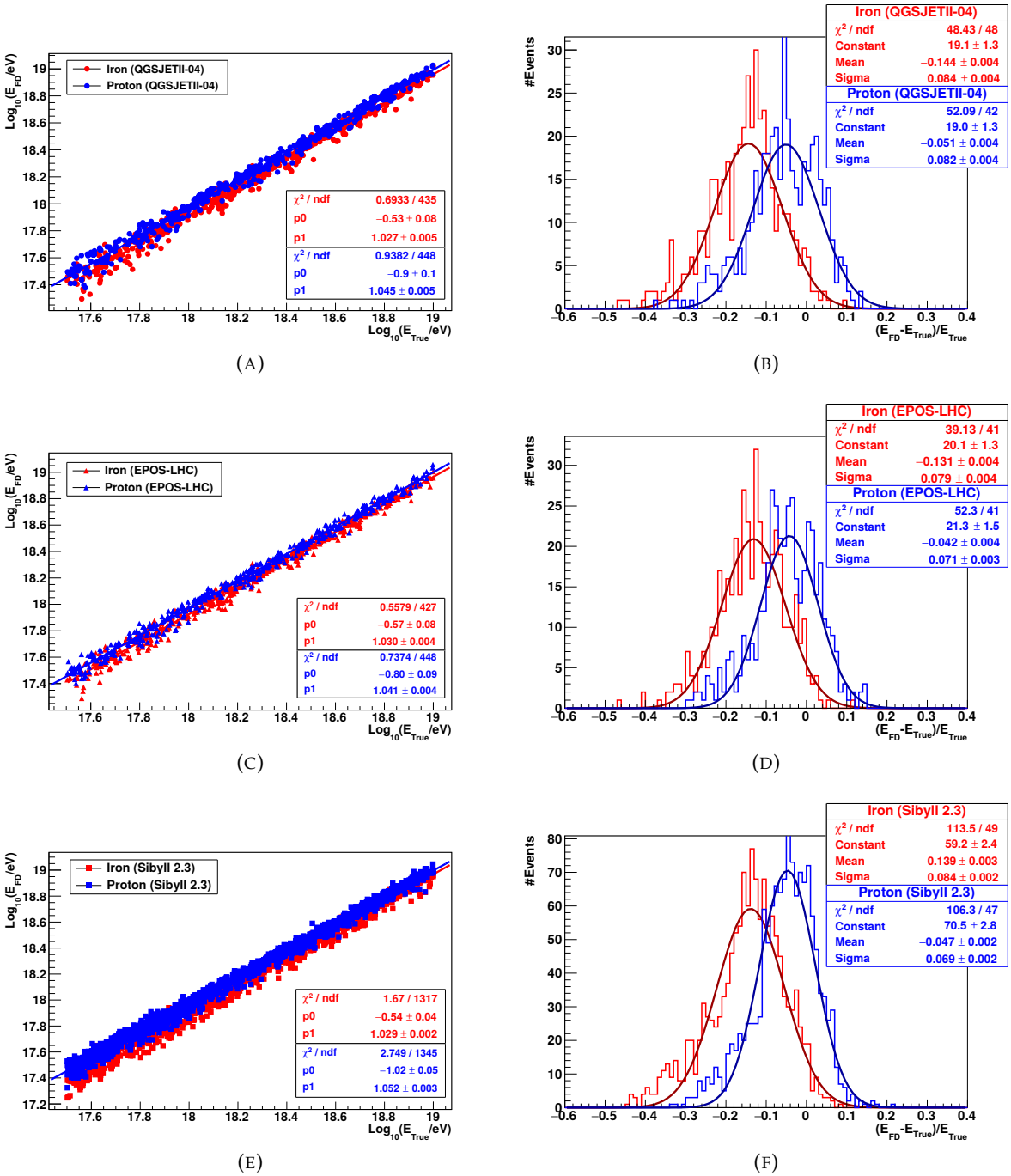

(A) (B) (C) (D) (E) (F)

FIGURE 6.19: Fluorescence energy (E_{FD}) as a function of the primary cosmic-ray energy (left) and E_{FD} uncertainty (right) for the hadronic interaction models QGSJETII-04, EPOS-LHC and Sibyll 2.3.

Quality cuts	QGSJETII-04		Sibyll 2.3		EPOS-LHC	
	Iron	Proton	Iron	Proton	Iron	Proton
SD+MD+FD						
FD energy successfully reconstructed	499	491	1493	1472	496	490
$\Delta E_{FD}/E_{FD} \leq 0.2$	498	491	1486	1467	495	490
$xMaxInFOV = 20$	492	490	1475	1462	487	483
$xMaxError < 40$ g/cm^2	488	490	1469	1462	485	483
maxDepthHole <= 30%	477	477	1448	1439	471	470
$\geq$ 50% *Cherenkov radiation*	477	477	1448	1439	471	470
Gaisser-Hillas fit $\chi^2/NDF < 2.5$	**456**	**447**	**1356**	**1339**	**456**	**437**
SD+MD+RD						
Radiation energy successfully reconstructed	390	379	1160	1075	396	377
α *(geomagnetic angle)* $\geq 10^o$	390	377	1158	1073	396	376
RDS with signal ≥ 5	282	238	819	647	286	244
GeoCeLDF: χ^2 *prob* $>$ 4e-4	**136**	**72**	**341**	**187**	**119**	**66**

TABLE 6.1: Number of events after each quality cut for SD, FD and RD analysis for proton and iron showers with hadronic interaction models QGSJETII-04, Sibyll 2.3 and EPOS-LHC.

Table 6.1 shows the number of events for proton and iron showers for the hadronic interaction models QGSJETII-04, Sibyll 2.3 and EPOS-LHC after each applied quality cut.

Figures 6.20 and 6.21 show an example event simulated for a proton and iron-induced air shower detected simultaneously by SD, MD, FD and RD detectors. In both figures, the index **(A)** shows the event map of the surface and radio detectors. The coloured circles are surface detectors which measured the event, whereas the grey circles are surface detectors which measured a signal below the threshold. The size of the circles is proportional to the measured intensity of the signal. The signal time is colour coded from blue (early) to green (late). The coloured crosses are the RD stations that measured the event and grey and black crosses are the remaining RD antennas. The star represents the reconstructed shower core and the black line the shower axis; **(B)** Two-dimensional lateral distribution function of the radiation energy fluence. The energy density distribution is not symmetric due to the interference of both the geomagnetic and the charge-excess emission mechanisms. The brown star denotes the shower core reconstructed with surface detectors and the blue one represents the shower core from RD reconstruction; **(C)** Fit of the lateral distribution function on the surface detector signal of the measured event as a

function of the distance to the shower core; **(D)** Fit of the lateral distribution function of the muon density in units of m^{-2}. The muon detectors that measured the event are included in the plot; and **(E)** Energy-deposit profile as a function of the atmospheric depth with the Gaisser-Hillas fit in red. The red dot marks the position of shower maximum X_{max} and the red-shaded area represents the fit uncertainties. The events were detected by Coihueco and/or HEAT telescopes.

6.5 Correlation Analysis

To evaluate the correlation among the muon density reconstructed, ρ_{μ}^{Rec}, at all those r_{ref} from the shower axis and the SD energy (E_{SD}), FD energy (E_{FD}) and RD energy (E_{RD}), we used the Pearson correlation coefficient, which is a measure of the linear dependence between two variables. It has a value between +1 and -1 inclusive, where 1 is a total positive linear correlation, 0 is a non linear correlation, and -1 is a total negative linear correlation.

The muon density reconstructed at 500 m from the shower axis as a function of the true cosmic-ray energy (E_{True}), the true calorimetric energy (E_{True}^{cal} - which is a measure of the shower electromagnetic energy), E_{SD}, E_{FD} and E_{RD} for proton and iron showers for QGSJETII-04, EPOS-LHC and Sibyll 2.3 are shown in Figures 6.22, 6.23 and 6.24. The $\rho_{\mu}^{Rec}(r_{ref})$ has a linear dependence with the all energy estimators. For all correlations among the muon density reconstructed and all energy estimators we performed a power-law fit given by

$$\rho_{\mu}^{Rec}(r_{ref}) = p_0 \cdot E^{p_1}. \tag{6.14}$$

The fit method is based on a maximum-likelihood approach accounting for the estimated uncertainties in the respective $\rho_{\mu}^{Rec}(r_{ref})$ and E_{SD}, E_{FD} and E_{RD} reconstructions.

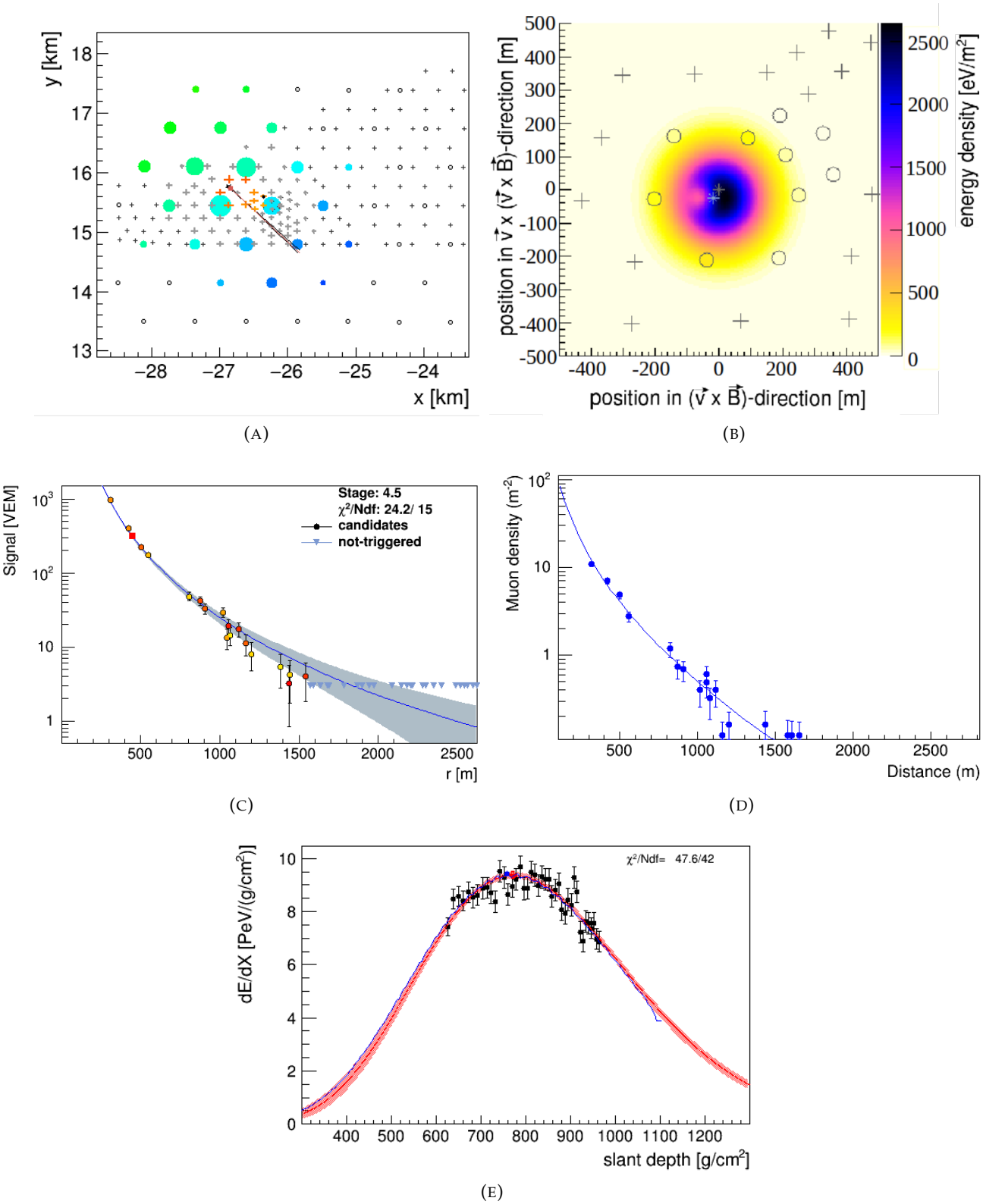

(A) (B)

(C) (D)

(E)

FIGURE 6.20: Example of a simulated event for a proton-induced air shower with $E = 5 \times 10^{18}$ eV and 38° zenith angle. The event was detected by 22 surface detectors, 10 RD stations and observed by Coihueco mirrors 4 and 5. In **(E)** the curve reaches its maximum at around (769.97 $\pm$ 7.45) g/cm^2.

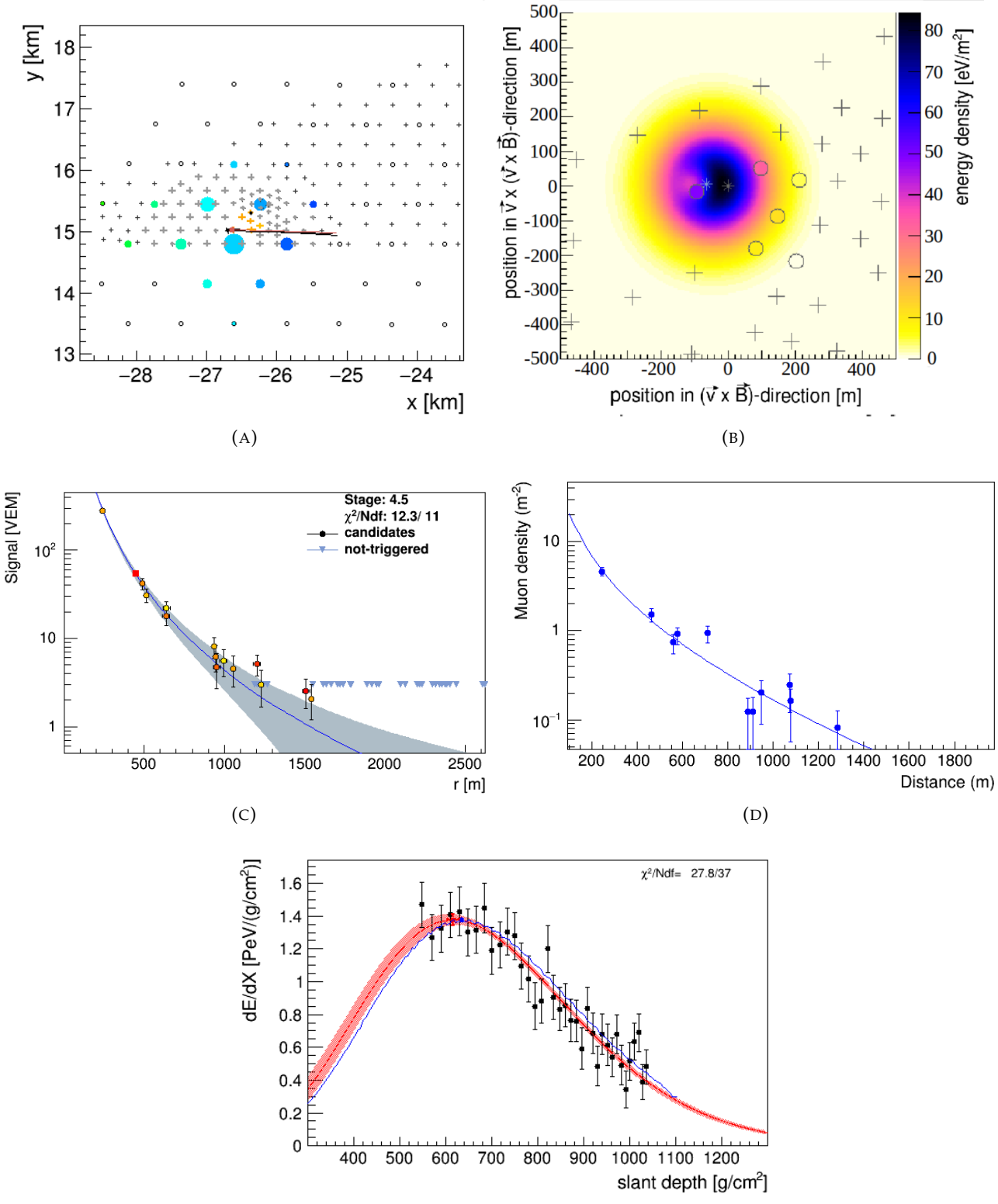

(A) (B)

(C) (D)

(E)

FIGURE 6.21: Example of a simulated event for an iron-induced air shower with $E = 8.24 \times 10^{17}$ eV and 38º zenith angle. The event was detected by 14 surface detectors, 6 RD stations and observed by Coihueco mirror 4. In **(E)** the curve reaches its maximum at around (657.51 ± 7.18) g/cm^2.

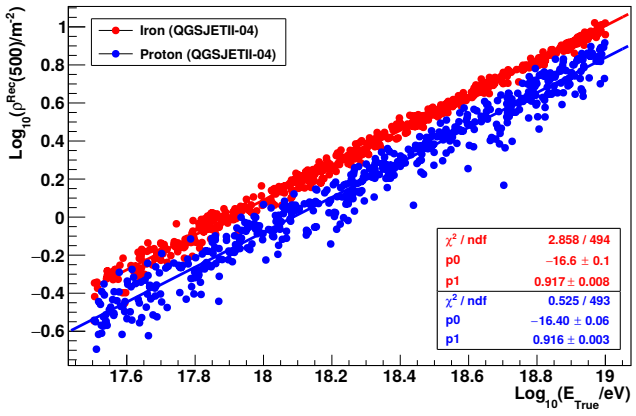

(A) $\rho_{\mu}^{\text{Rec}}(500)$ vs E_{True}

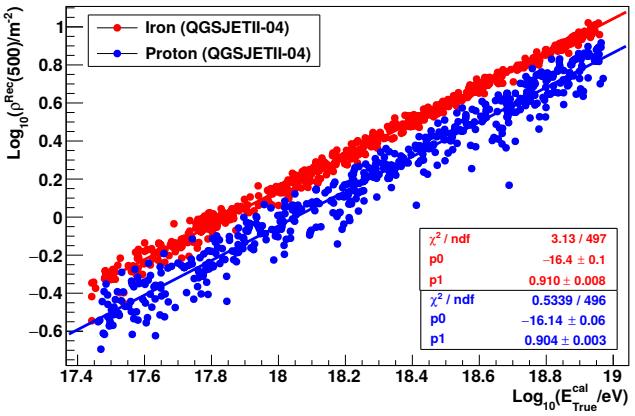

(B) $\rho_{\mu}^{\text{Rec}}(500)$ vs $E_{\text{True}}^{\text{cal}}$

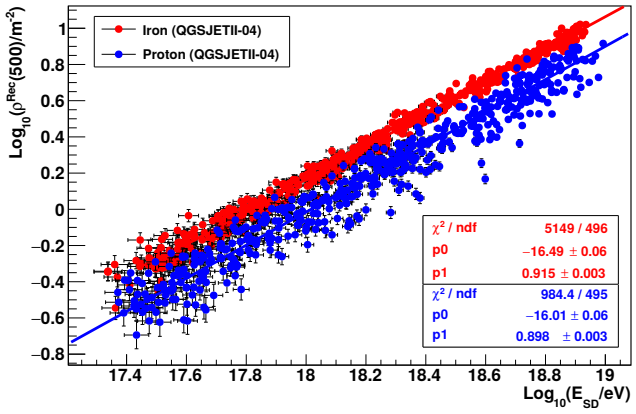

(C) $\rho_{\mu}^{\text{Rec}}(500)$ vs E_{SD}

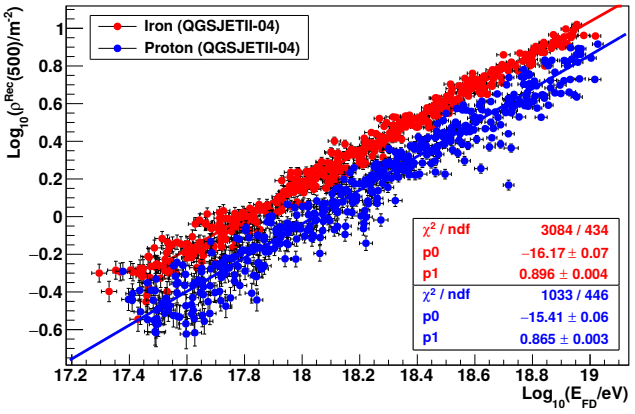

(D) $\rho_{\mu}^{\text{Rec}}(500)$ vs E_{FD}

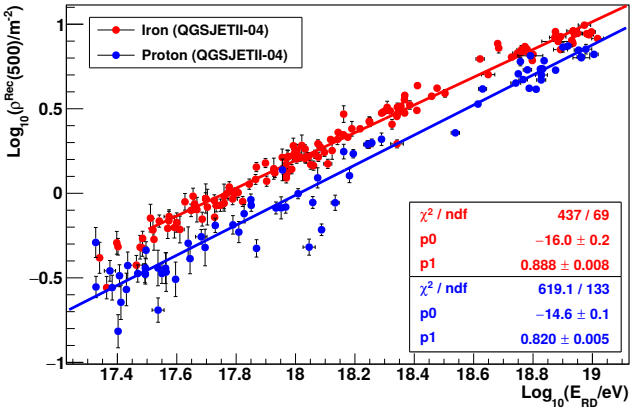

(E) $\rho_{\mu}^{\text{Rec}}(500)$ vs E_{RD}

FIGURE 6.22: Muon density reconstructed at 500 m from the shower axis as a function of the true primary energy, true calorimetric energy, SD energy, FD energy and RD energy for proton (blue) and iron (red) showers for the QGSJETII-04 hadronic interaction model.

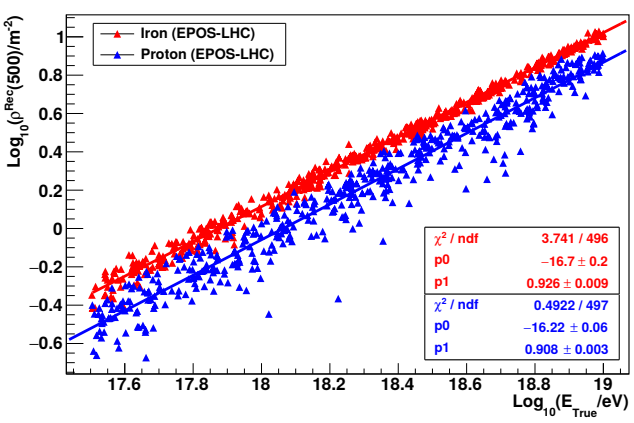

(A) $\rho_{\mu}^{\text{Rec}}(500)$ vs E_{True}

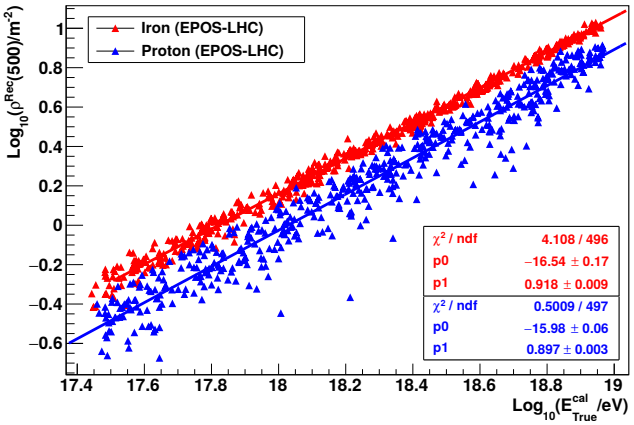

(B) $\rho_{\mu}^{\text{Rec}}(500)$ vs $E_{\text{True}}^{\text{cal}}$

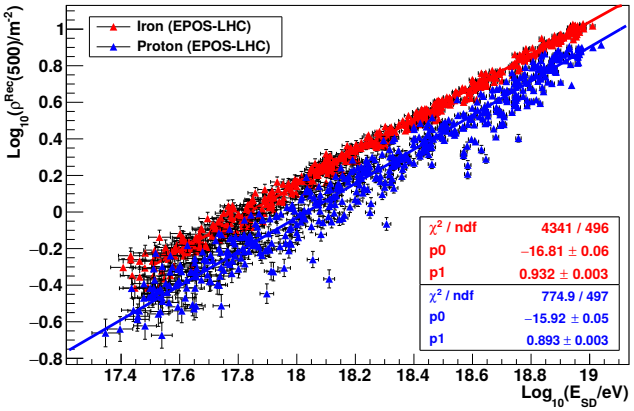

(C) $\rho_{\mu}^{\text{Rec}}(500)$ vs E_{SD}

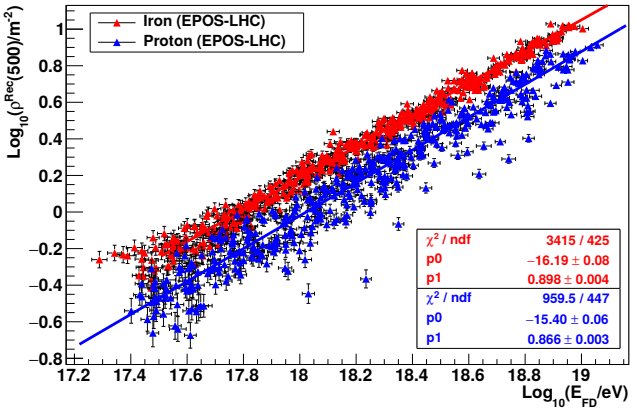

(D) $\rho_{\mu}^{\text{Rec}}(500)$ vs E_{FD}

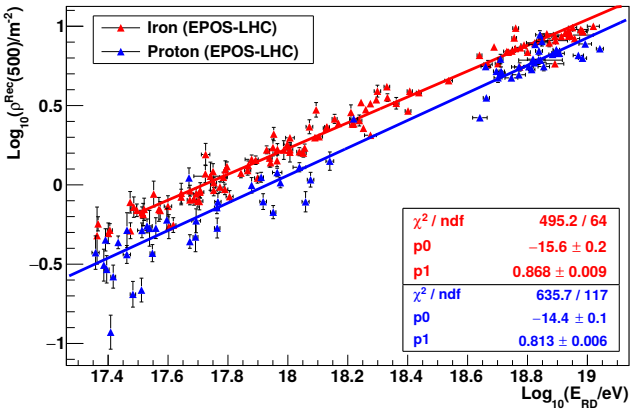

(E) $\rho_{\mu}^{\text{Rec}}(500)$ vs E_{RD}

FIGURE 6.23: Muon density reconstructed at 500 m from the shower axis as a function of the true primary energy, true calorimetric energy, SD energy, FD energy and RD energy for proton (blue) and iron (red) showers for the EPOS-LHC hadronic interaction model.

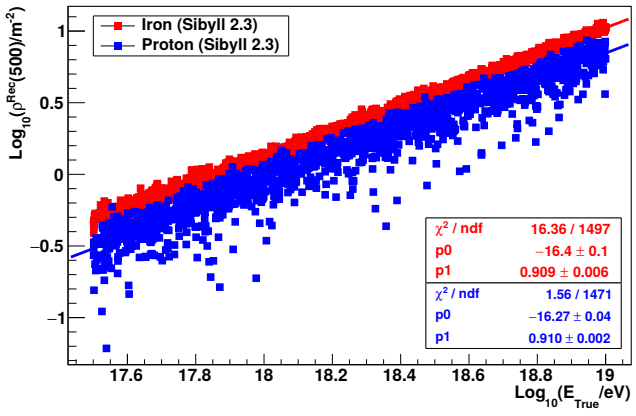

(A) $\rho_{\mu}^{\mathrm{Rec}}(500)$ vs E_{True}

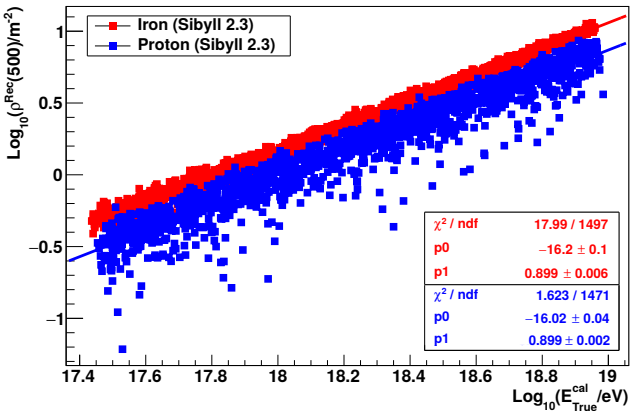

(B) $\rho_{\mu}^{\mathrm{Rec}}(500)$ vs $E_{\mathrm{True}}^{\mathrm{cal}}$

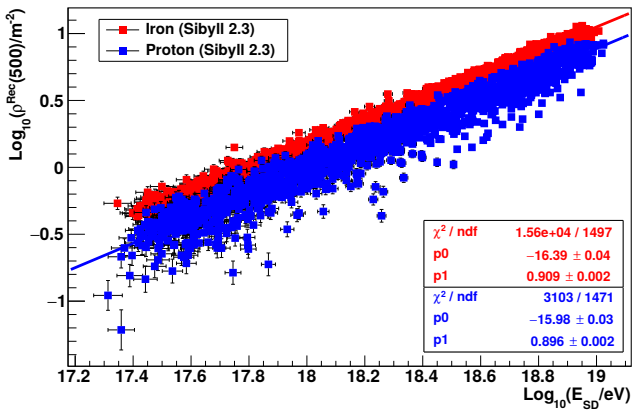

(C) $\rho_{\mu}^{\mathrm{Rec}}(500)$ vs E_{SD}

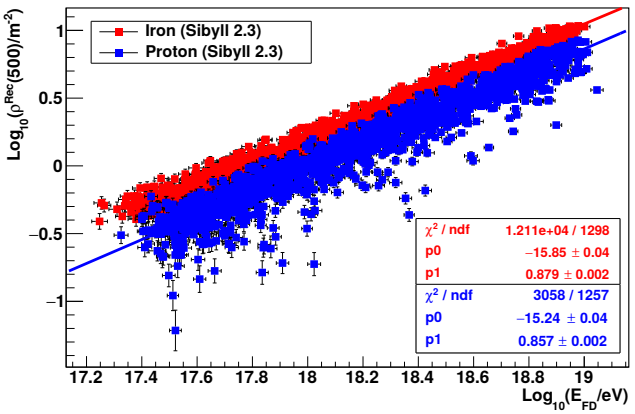

(D) $\rho_{\mu}^{\mathrm{Rec}}(500)$ vs E_{FD}

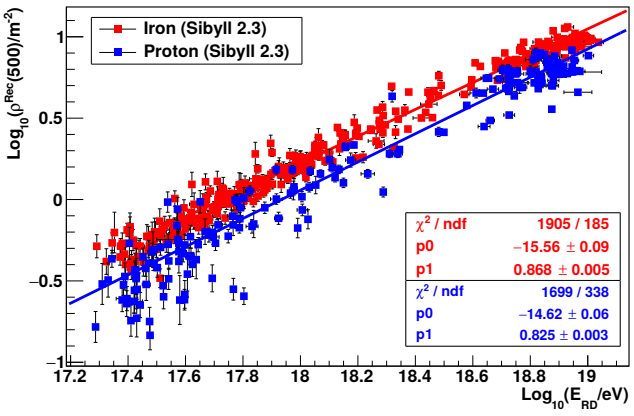

(E) $\rho_{\mu}^{\mathrm{Rec}}(500)$ vs E_{RD}

FIGURE 6.24: Muon density reconstructed at 500 m from the shower axis as a function of the true primary energy, true calorimetric energy, SD energy, FD energy and RD energy for proton (blue) and iron (red) showers for the Sibyll 2.3 hadronic interaction model.

Figure 6.25 shows the Pearson coefficient for the reconstructed muon density correlated to the true cosmic-ray energy, SD energy, FD energy and RD energy for proton and iron showers for QGSJETII-04 as a function of the different distances from the shower axis. As a result, we have a correlation coefficient close to 1 for all distances from the shower axis and energy parameters motivating the combination of the reconstructed muon density with different energy estimators. The same result was obtained for EPOS-LHC and Sibyll 2.3 hadronic interaction models.

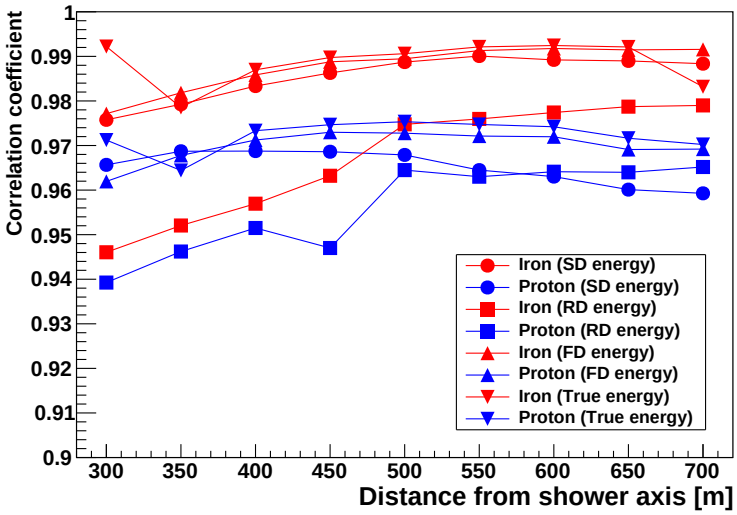

FIGURE 6.25: Pearson coefficient correlating the reconstructed muon density at all r_{ref} from the shower axis to the true primary cosmic ray energy, SD energy, RD energy and FD energy for proton and iron showers for QGSJETII-04 hadronic interaction model.

6.5.1 Mass-discrimination power

The muon density at a given distance from the shower axis has been used as a parameter for composition analyses at a given energy. Therefore, the mass-discrimination factor between proton and iron showers is analysed using the reconstructed muon density at all r_{ref} from the shower axis taking into account the true cosmic-ray energy, true calorimetric energy, SD energy, FD energy and RD energy. The aim of using different distances and energy parameter is to evaluate which distance and energy parameter provide the best mass separation.

The mass-discrimination power was calculated using the expression of the merit factor (MF) [198]

$$MF = \frac{|\langle q_{\text{p}}\rangle - \langle q_{\text{Fe}}\rangle|}{\sqrt{\sigma^2(q_{\text{p}}) + \sigma^2(q_{\text{Fe}})}}, \tag{6.15}$$

where q_A is the parameter for nucleus A, $\langle q_A \rangle$ is the mean value and $\sigma(q_A)$ the standard deviation for the distribution of q_A. In our work, q_A corresponds to $\rho_\mu(r_{\text{ref}})$ divided by all energy estimators (E_{True}, $E^{\text{cal}}_{\text{True}}$, E_{SD}, E_{RD}, E_{FD}). From the definition of the MF, we see that the larger its value, the greater is the discrimination power of the parameter q.

To investigate which distance gives the best mass separation, it is important that we have the same events reconstructed for all distances, but since the quality cuts applied for SD and FD analyses do not lose much events in comparison to the RD cuts, we decided to first use only the dataset with the reconstructed muon density, the SD energy and FD energy so we can have better statistics.

Figures 6.26, 6.27 and 6.28 show the distributions for the muon density reconstructed at 500 m from the shower axis divided by the true cosmic-ray energy, the true calorimetric energy, the SD energy and the FD energy for the hadronic interaction models QGSJETII-04, EPOS-LHC and Sibyll 2.3. All energy estimators were normalized to 10^{18} eV and raised to a given power p_1 from the power-law fit in Figures 6.22, 6.23 and 6.24. The p_1 value used in the following distributions corresponds to the mean value between p_1 for proton and iron-induced showers for all three models (see Table 6.2).

Energy Estimators	**QGSJETII-04**	**EPOS-LHC**	**Sibyll 2.3**
	p_1	p_1	p_1
E_{True}	0.917	0.917	0.910
$E^{\text{cal}}_{\text{True}}$	0.907	0.907	0.899
E_{SD}	0.907	0.912	0.903
E_{FD}	0.881	0.882	0.868
E_{RD}	0.854	0.840	0.841

TABLE 6.2: p_1 mean value from a power-law fit for the $\rho^{\text{Rec}}_\mu(r_{\text{ref}})$ as a function of the different energy estimators (E_{True}, $E^{\text{cal}}_{\text{True}}$, E_{SD}, E_{FD} and E_{RD}) for proton and iron-induced air showers with the hadronic interaction models QGSJETII-04, EPOS-LHC and Sibyll 2.3.

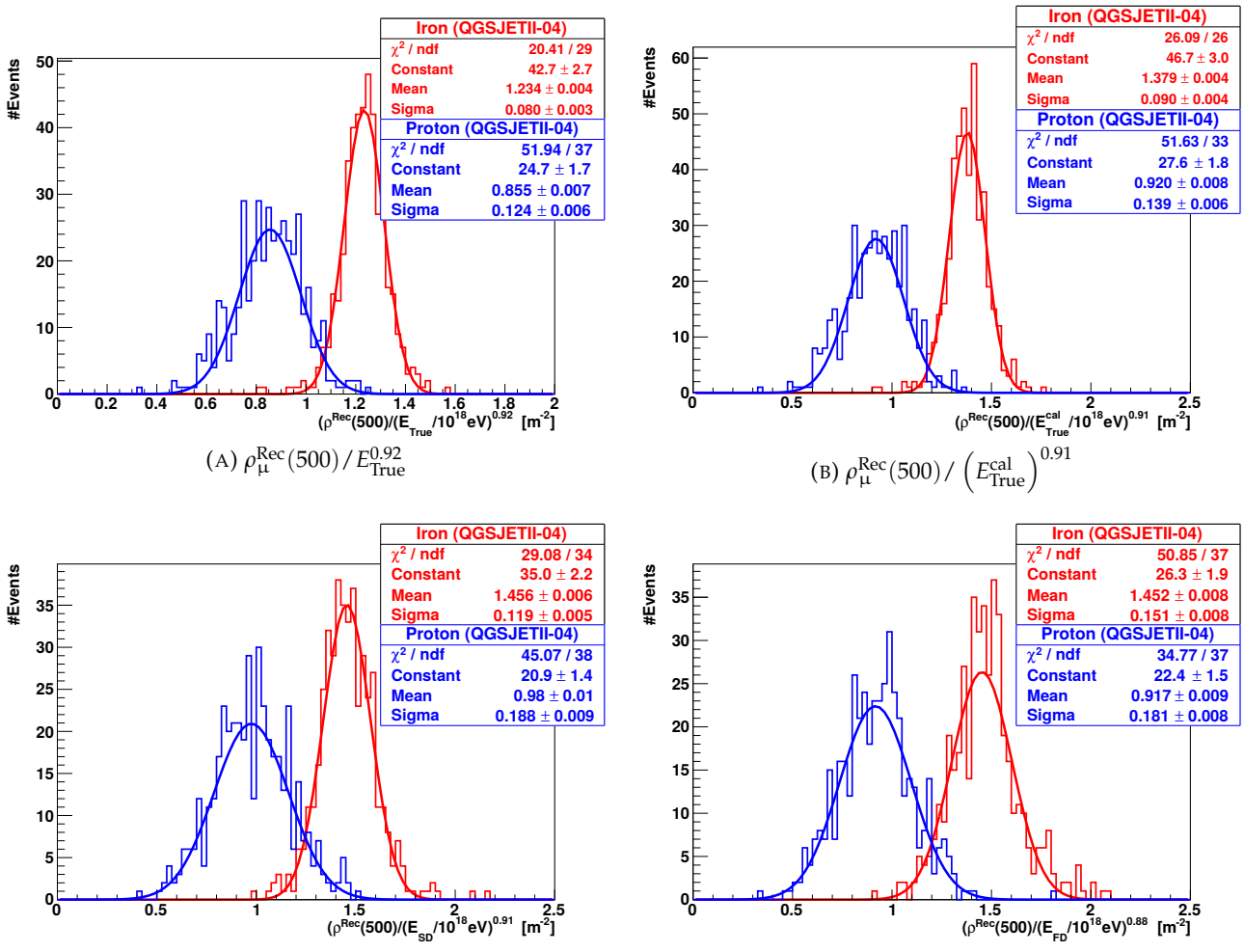

(A) $\rho_{\mu}^{\mathrm{Rec}}(500)\,/\,E_{\mathrm{True}}^{0.92}$

(B) $\rho_{\mu}^{\mathrm{Rec}}(500)\,/\,\left(E_{\mathrm{True}}^{\mathrm{cal}}\right)^{0.91}$

(C) $\rho_{\mu}^{\mathrm{Rec}}(500)\,/\,E_{\mathrm{SD}}^{0.91}$

(D) $\rho_{\mu}^{\mathrm{Rec}}(500)\,/\,E_{\mathrm{FD}}^{0.88}$

FIGURE 6.26: Muon density reconstructed at 500 m from the shower axis divided by the true cosmic-ray energy, true calorimetric energy, SD energy and FD energy for proton (blue) and iron (red) showers for the QGSJETII-04 hadronic interaction model.

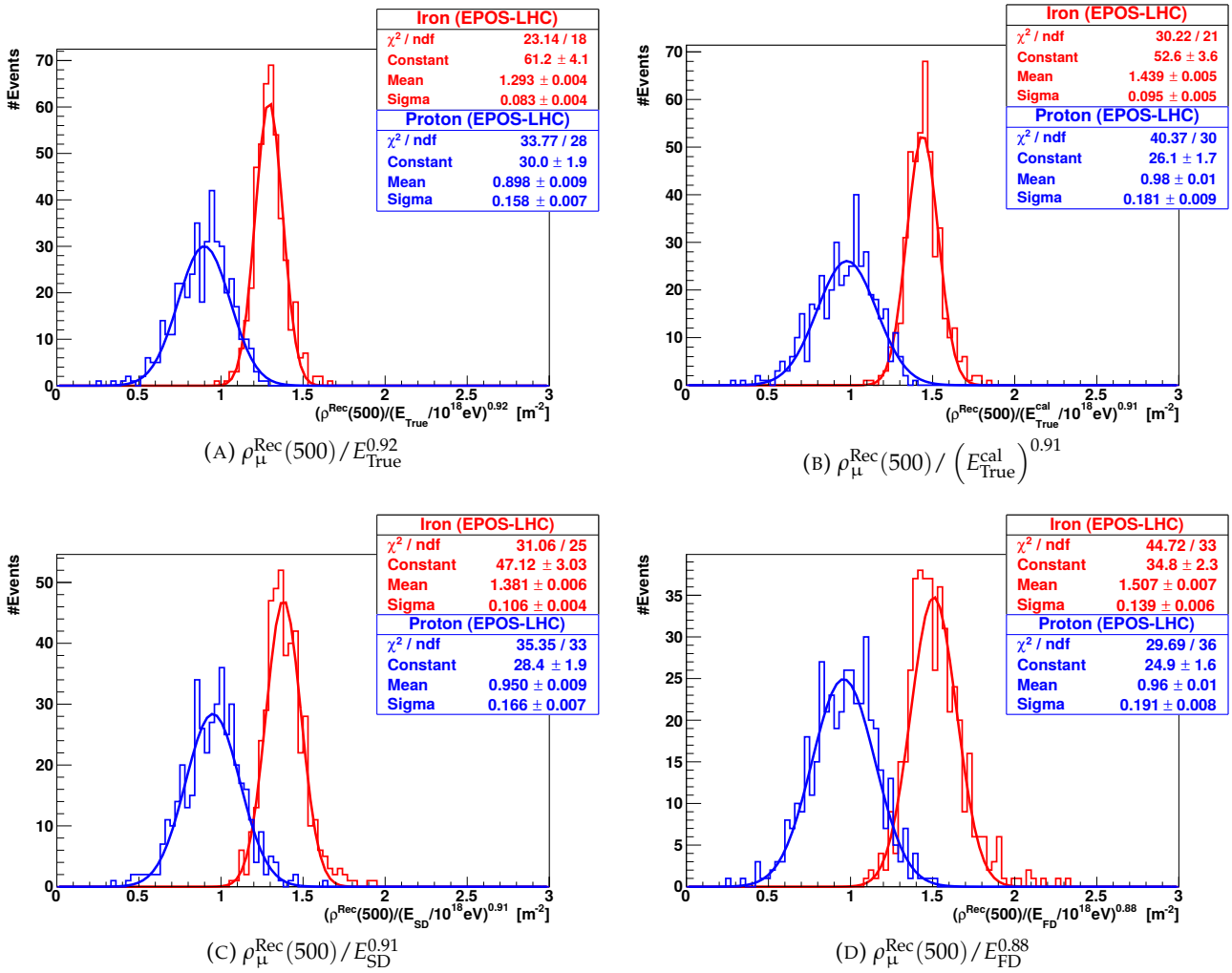

(A) $\rho_{\mu}^{\mathrm{Rec}}(500) / E_{\mathrm{True}}^{0.92}$

(B) $\rho_{\mu}^{\mathrm{Rec}}(500) / \left(E_{\mathrm{True}}^{\mathrm{cal}}\right)^{0.91}$

(C) $\rho_{\mu}^{\mathrm{Rec}}(500) / E_{\mathrm{SD}}^{0.91}$

(D) $\rho_{\mu}^{\mathrm{Rec}}(500) / E_{\mathrm{FD}}^{0.88}$

FIGURE 6.27: Muon density reconstructed at 500 m from the shower axis divided by the true cosmic-ray energy, true calorimetric energy, SD energy and FD energy for proton (blue) and iron (red) showers for the EPOS-LHC hadronic interaction model.

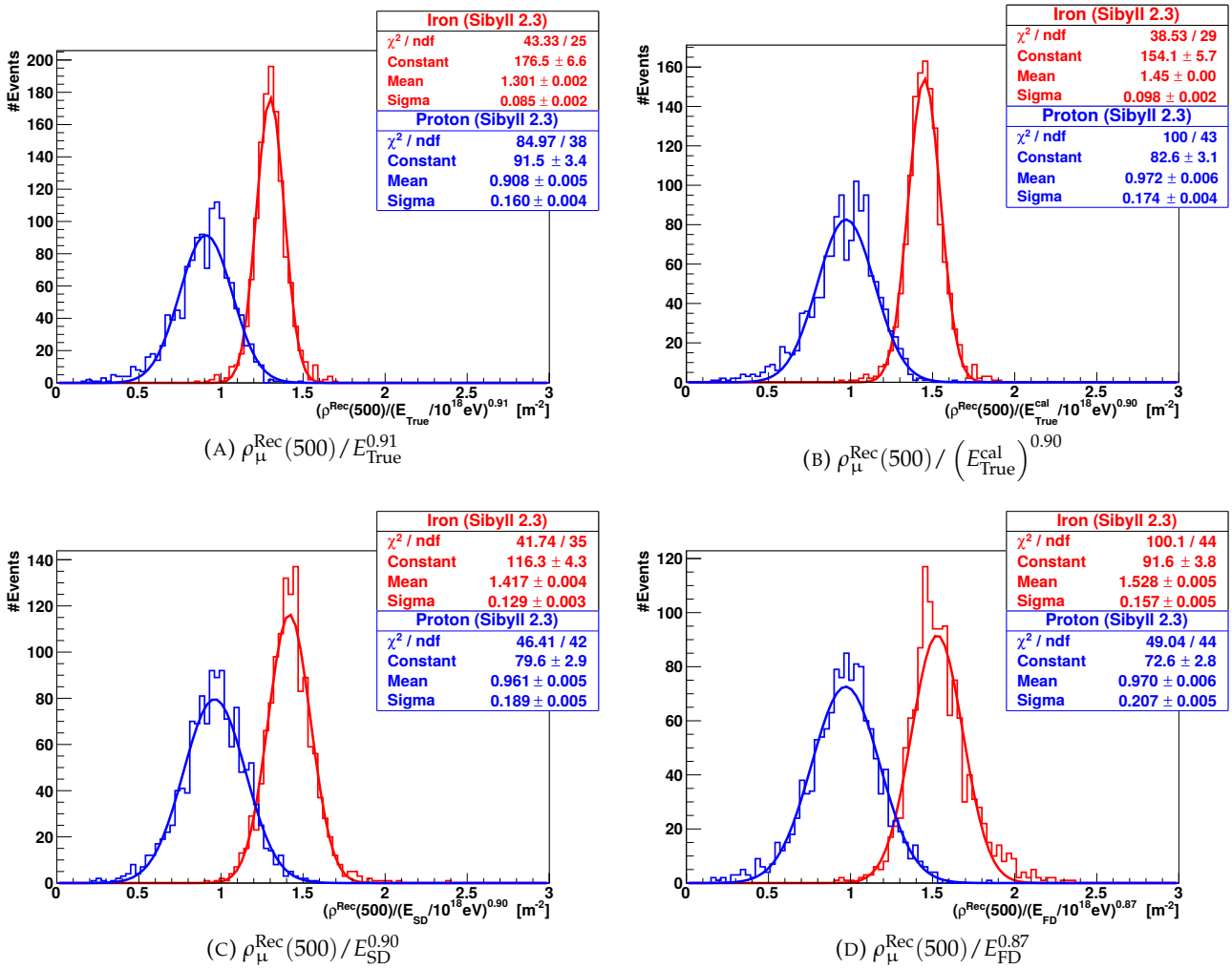

(A) $\rho_{\mu}^{\mathrm{Rec}}(500)\,/\,E_{\mathrm{True}}^{0.91}$

(B) $\rho_{\mu}^{\mathrm{Rec}}(500)\,/\,\left(E_{\mathrm{True}}^{\mathrm{cal}}\right)^{0.90}$

(C) $\rho_{\mu}^{\mathrm{Rec}}(500)\,/\,E_{\mathrm{SD}}^{0.90}$

(D) $\rho_{\mu}^{\mathrm{Rec}}(500)\,/\,E_{\mathrm{FD}}^{0.87}$

FIGURE 6.28: Muon density reconstructed at 500 m from the shower axis divided by the true cosmic-ray energy, true calorimetric energy, SD energy and FD energy for proton (blue) and iron (red) showers for the Sibyll 2.3 hadronic interaction model.

In Figures 6.29, 6.30 and 6.31 the merit factor is shown for the muon density reconstructed at all r_{ref} from the shower axis divided by the true cosmic-ray energy, true calorimetric energy, SD energy, and FD energy for the hadronic interaction models QGSJETII-04, Sibyll 2.3 and EPOS-LHC. In these figures the merit factor error was estimated using the *bootstrap* method which is a resampling technique proposed by Bradley Efron in 1979, used in different statistical situations [204]. The technique is based on obtaining a new dataset by random resampling with replacement of the original dataset. It is frequently used to estimate the variance of a statistical dataset, as well as constructing confidence intervals or performing hypothesis tests on parameters of interest. Therefore the original dataset of events was randomly resampled 10000 times. Thus, calculating 10000 times the merit factor (for $\rho_{\mu}^{Rec}(r_{ref})/E_{True}$, $\rho_{\mu}^{Rec}(r_{ref})/E_{True}^{cal}$, $\rho_{\mu}^{Rec}(r_{ref})/E_{SD}$ and $\rho_{\mu}^{Rec}(r_{ref})/E_{FD}$) and analysing the frequency distribution of the merit factor sets we used the standard deviation of the merit factor distributions as an estimator of the merit factor uncertainty (see Tables 6.3, 6.4 and 6.5).

r_{ref}	$\rho_{\mu}^{Rec}(r_{ref})/E_{True}^{0.92}$		$\rho_{\mu}^{Rec}(r_{ref})/\left(E_{True}^{cal}\right)^{0.91}$		$\rho_{\mu}^{Rec}(r_{ref})/E_{SD}^{0.91}$		$\rho_{\mu}^{Rec}(r_{ref})/E_{FD}^{0.88}$	
	MF	Uncertainty	MF	Uncertainty	MF	Uncertainty	MF	Uncertainty
300 m	1.76	0.11	1.95	0.12	1.89	0.12	1.83	0.10
350 m	2.08	0.13	2.14	0.12	1.95	0.13	2.08	0.10
400 m	2.27	0.12	2.40	0.13	2.15	0.13	2.19	0.11
450 m	2.43	0.13	2.64	0.14	2.19	0.15	2.22	0.13
500 m	2.56	0.13	2.77	0.14	2.16	0.12	2.27	0.15
550 m	2.38	0.12	2.56	0.12	2.04	0.12	2.33	0.13
600 m	2.29	0.11	2.40	0.13	2.04	0.13	2.31	0.13
650 m	2.28	0.12	2.32	0.11	2.00	0.17	2.26	0.12
700 m	2.18	0.10	2.23	0.11	1.86	0.13	2.17	0.12
750 m	2.01	0.12	2.16	0.12	1.74	0.12	2.15	0.12
800 m	1.93	0.13	2.14	0.13	1.72	0.10	2.03	0.12
850 m	1.95	0.13	2.06	0.14	1.60	0.11	2.07	0.12
900 m	1.84	0.13	2.06	0.13	1.63	0.10	1.98	0.12
950 m	1.77	0.11	1.96	0.13	1.59	0.09	1.91	0.12
1000 m	1.73	0.12	1.83	0.12	1.57	0.09	1.84	0.11

TABLE 6.3: Merit factor and its uncertainty for $\rho_{\mu}^{Rec}(r_{ref})/E_{True}^{0.92}$, $\rho_{\mu}^{Rec}(r_{ref})/\left(E_{True}^{cal}\right)^{0.91}$, $\rho_{\mu}^{Rec}(r_{ref})/E_{SD}^{0.91}$ and $\rho_{\mu}^{Rec}(r_{ref})/E_{FD}^{0.88}$ distributions for proton and iron-induced air showers with the QGSJETII-04 hadronic interaction model.

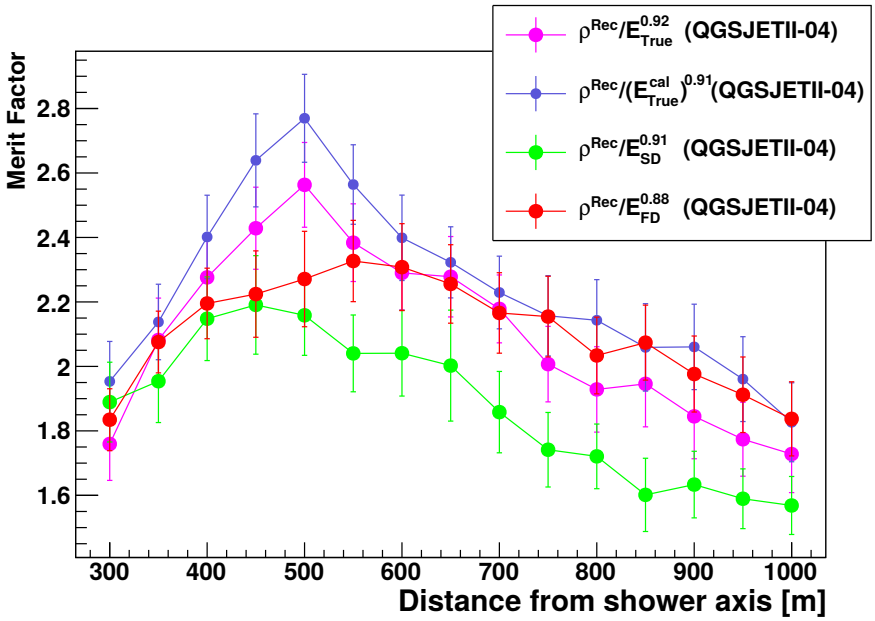

FIGURE 6.29: Mass discrimination power as function of the distance from the shower axis for the reconstructed muon density divided by the true cosmic-ray energy, true calorimetric energy, SD energy and FD energy for the QGSJETII-04 hadronic interaction model.

r_{ref}	$\rho_\mu^{Rec}(r_{ref})/E_{True}^{0.92}$		$\rho_\mu^{Rec}(r_{ref})/\left(E_{True}^{cal}\right)^{0.91}$		$\rho_\mu^{Rec}(r_{ref})/E_{SD}^{0.91}$		$\rho_\mu^{Rec}(r_{ref})/E_{FD}^{0.88}$	
	MF	Uncertainty	MF	Uncertainty	MF	Uncertainty	MF	Uncertainty
300 m	1.74	0.10	1.79	0.10	1.82	0.11	1.72	0.10
350 m	1.90	0.10	2.03	0.12	1.97	0.13	1.97	0.11
400 m	2.09	0.12	2.18	0.11	2.13	0.12	2.15	0.11
450 m	2.14	0.11	2.29	0.11	2.13	0.12	2.15	0.12
500 m	2.21	0.11	2.25	0.14	2.19	0.12	2.32	0.12
550 m	2.17	0.10	2.35	0.12	2.12	0.10	2.24	0.12
600 m	2.10	0.11	2.24	0.11	2.06	0.11	2.25	0.12
650 m	2.01	0.11	2.19	0.11	1.88	0.11	2.16	0.12
700 m	2.10	0.10	2.14	0.11	1.95	0.11	2.16	0.12
750 m	2.00	0.10	2.11	0.11	1.79	0.10	2.08	0.12
800 m	2.01	0.11	2.03	0.10	1.77	0.11	2.07	0.11
850 m	1.84	0.10	1.95	0.10	1.69	0.10	2.12	0.11
900 m	1.86	0.10	1.91	0.10	1.69	0.11	2.08	0.11
950 m	1.79	0.10	1.89	0.10	1.66	0.11	1.96	0.10
1000 m	1.72	0.10	1.81	0.11	1.60	0.11	1.83	0.12

TABLE 6.4: Merit factor (MF) and its uncertainty for $\rho_\mu^{Rec}(r_{ref})/E_{True}^{0.92}$, $\rho_\mu^{Rec}(r_{ref})/\left(E_{True}^{cal}\right)^{0.91}$, $\rho_\mu^{Rec}(r_{ref})/E_{SD}^{0.91}$ and $\rho_\mu^{Rec}(r_{ref})/E_{FD}^{0.88}$ distributions for proton and iron-induced air showers with the EPOS-LHC hadronic interaction model.

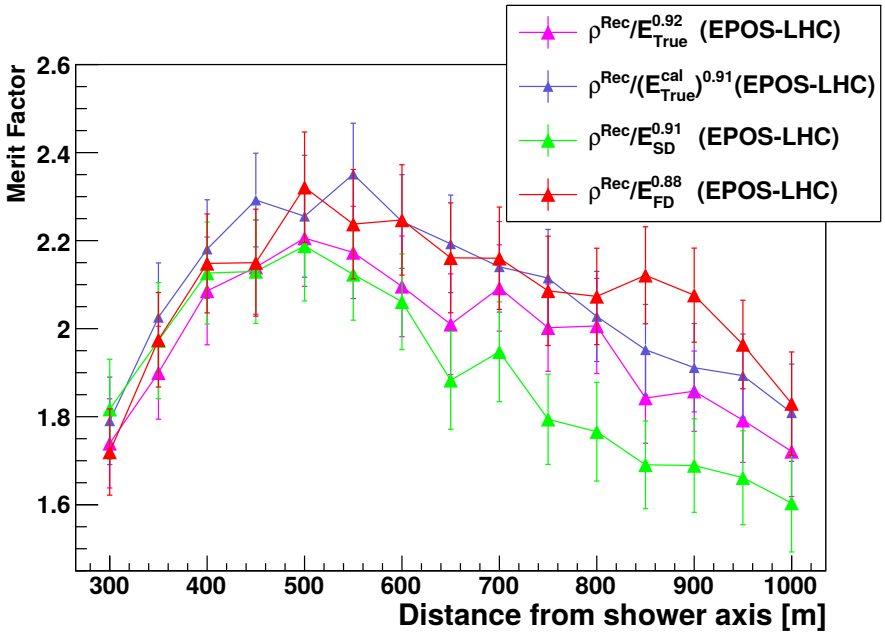

FIGURE 6.30: Mass discrimination power as function of the distance from the shower axis for the reconstructed muon density divided by the true cosmic-ray energy, true calorimetric energy, SD energy and FD energy for the EPOS-LHC hadronic interaction model.

$r_{\|mathrmref}$	$\rho_\mu^{Rec}(r_{ref})/E_{True}^{0.91}$		$\rho_\mu^{Rec}(r_{ref})/E_{True}^{Cal\ 0.90}$		$\rho_\mu^{Rec}(r_{ref})/E_{SD}^{0.90}$		$\rho_\mu^{Rec}(r_{ref})/E_{FD}^{0.87}$	
	MF	Uncertainty	MF	Uncertainty	MF	Uncertainty	MF	Uncertainty
300 m	1.59	0.05	1.73	0.05	1.67	0.05	1.76	0.06
350 m	1.78	0.05	1.97	0.06	1.86	0.05	1.89	0.06
400 m	1.98	0.05	2.14	0.06	1.95	0.05	2.05	0.06
450 m	2.15	0.06	2.26	0.07	2.03	0.06	2.13	0.06
500 m	2.16	0.06	2.39	0.07	1.99	0.05	2.15	0.06
550 m	2.25	0.07	2.34	0.06	2.01	0.06	2.19	0.06
600 m	2.17	0.06	2.32	0.06	1.94	0.05	2.15	0.06
650 m	2.11	0.06	2.20	0.06	1.88	0.05	2.17	0.06
700 m	2.01	0.06	2.11	0.06	1.81	0.05	2.11	0.06
750 m	1.95	0.05	2.06	0.05	1.75	0.05	2.01	0.06
800 m	1.84	0.05	1.99	0.05	1.70	0.05	1.98	0.06
850 m	1.80	0.05	1.96	0.06	1.67	0.05	1.87	0.05
900 m	1.74	0.05	1.87	0.05	1.61	0.05	1.83	0.05
950 m	1.71	0.05	1.81	0.05	1.57	0.05	1.80	0.05
1000 m	1.63	0.05	1.74	0.05	1.53	0.05	1.74	0.05

TABLE 6.5: Merit factor (MF) and its uncertainty for $\rho_\mu^{Rec}(r_{ref})/E_{True}^{0.91}$, $\rho_\mu^{Rec}(r_{ref})/E_{True}^{Cal\ 0.90}$, $\rho_\mu^{Rec}(r_{ref})/E_{SD}^{0.90}$ and $\rho_\mu^{Rec}(r_{ref})/E_{FD}^{0.87}$ distributions for proton and iron-induced air showers with the Sibyll 2.3 hadronic interaction model.

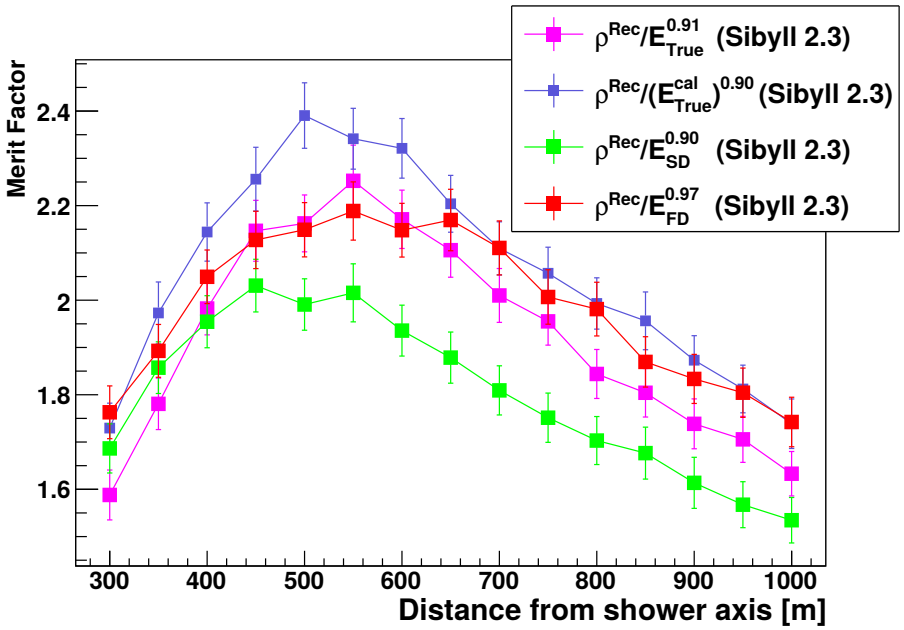

FIGURE 6.31: Mass discrimination power as function of the distance from the shower axis for the reconstructed muon density divided by the true cosmic-ray energy, true calorimetric energy, SD energy and FD energy for the Sibyll 2.3 hadronic interaction model.

The merit factor is maximized in the range of distances between 400 and 550 m from the shower axis, so we can use the 500 m distance as the reference distance to study mass composition of cosmic rays. Moreover, the uncertainties in the muon density reconstruction method for 500 m are very reduced (< 9%). The muon density divided by the fluorescence energy features a better mass separation between iron and proton showers than the SD energy. This was expected as the fluorescence energy is proportional to the true calorimetric electromagnetic energy of the shower which also features a better mass separation than the true cosmic ray energy. In general the combination of muonic and electromagnetic component of the extensive air shower shows a great potential for mass composition studies.

Since we have few events after the RD quality cuts and assuming that 500 m is an optimum distance to reconstruct the muon density to study mass composition of primary cosmic rays, we studied the merit factor taking into account the radiation energy only at the distance of 500 m from the shower axis. Figure 6.32 shows $\rho_{\mu}^{\mathrm{Rec}}(500)/E_{\mathrm{SD}}^{p_1}$ and $\rho_{\mu}^{\mathrm{Rec}}(500)/E_{\mathrm{RD}}^{p_1}$ for proton (blue) and iron (red)-induced air showers for the hadronic interaction models QGSJETII-04, EPOS-LHC and Sibyll 2.3. The respective merit-factor values and their statistical uncertainties (obtained via *bootstrap* method) are shown in Table 6.6. In general there is no additional mass separation when we divide the muon density reconstructed by the radiation energy in comparison to the SD energy for all three hadronic interaction models. Nevertheless, both air shower observables are good estimators of the primary mass composition. Moreover, the radio reconstruction was not optimized for the event dataset

used in this thesis. It was only optimized for AERA24, and not for the large array with mixed spacings and antenna types. Therefore, the radiation energy reconstructed from the radio footprint needs to be enhanced. In comparison to FD energy, the muon density combined with the FD energy features the best mass separation but due to the low duty cycle of the telescopes, we have only a few measured events. Hence it is worth using the muon density combined with the SD or RD energy to study primary mass composition.

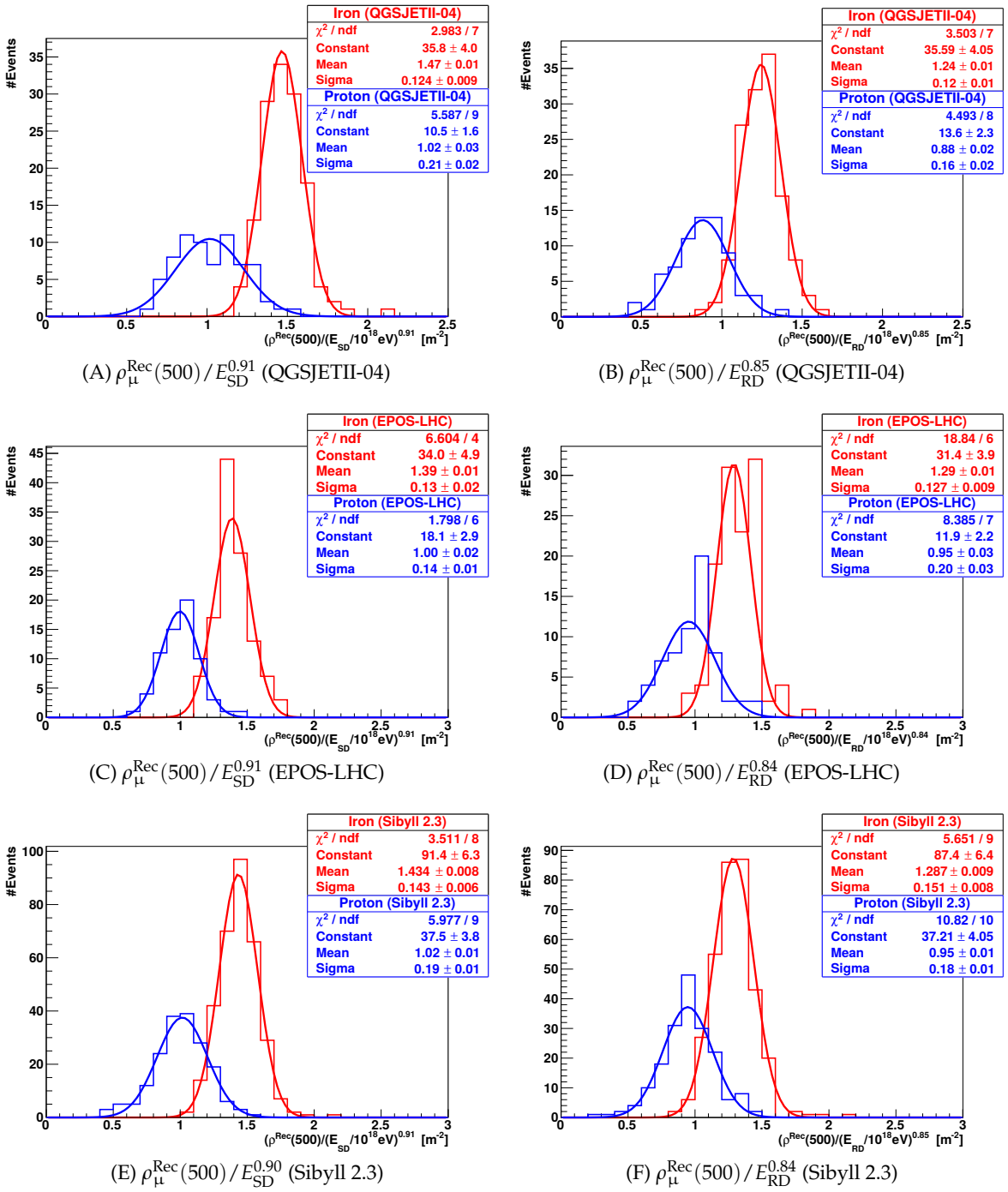

(A) $\rho_{\mu}^{\mathrm{Rec}}(500)/E_{\mathrm{SD}}^{0.91}$ (QGSJETII-04)

(B) $\rho_{\mu}^{\mathrm{Rec}}(500)/E_{\mathrm{RD}}^{0.85}$ (QGSJETII-04)

(C) $\rho_{\mu}^{\mathrm{Rec}}(500)/E_{\mathrm{SD}}^{0.91}$ (EPOS-LHC)

(D) $\rho_{\mu}^{\mathrm{Rec}}(500)/E_{\mathrm{RD}}^{0.84}$ (EPOS-LHC)

(E) $\rho_{\mu}^{\mathrm{Rec}}(500)/E_{\mathrm{SD}}^{0.90}$ (Sibyll 2.3)

(F) $\rho_{\mu}^{\mathrm{Rec}}(500)/E_{\mathrm{RD}}^{0.84}$ (Sibyll 2.3)

FIGURE 6.32: Muon density reconstructed at 500 m from the shower axis divided by the SD energy and RD energy for proton (blue) and iron (red) showers for the hadronic interaction models QGSJETII-04, Sibyll 2.3 and EPOS-LHC.

Hadronic Model	$\rho_\mu^{\mathrm{Rec}}(500)/E_{\mathrm{SD}}^{p_1}$		$\rho_\mu^{\mathrm{Rec}}(500)/E_{\mathrm{RD}}^{p_1}$	
	MF	Uncertainty	MF	Uncertainty
QGSJETII-04	1.82	0.27	1.76	0.25
EPOS-LHC	1.99	0.40	1.45	0.23
Sibyll 2.3	1.77	0.30	1.43	0.23

TABLE 6.6: Merit factor (MF) and its uncertainty for $\rho_\mu^{\mathrm{Rec}}(500)/E_{\mathrm{SD}}^{p_1}$ and $\rho_\mu^{\mathrm{Rec}}(500)/E_{\mathrm{RD}}^{p_1}$ distributions for proton and iron-induced air showers with the hadronic interaction models QGSJETII-04, EPOS-LHC and Sibyll 2.3.

6.6 Maximum atmospheric shower depth (X_{max})

The maximum shower depth (X_{max}) is proportional to the logarithm of the mass A of the primary particle. However, due to the fluctuations of the properties of the first hadronic interactions in the shower development, the primary mass can not be measured in an event-by-event basis but can be statistically inferred from the X_{max} distribution of an ensemble of air showers.

The X_{max} parameter provides the atmospheric depth the shower traversed before the maximum particle density is reached. This parameter is calculated from the measurement of the amount of fluorescence light deposited in the atmosphere and the corresponding position of the atmospheric shower.

Figure 6.33 shows the X_{max} distribution for proton and iron-induced showers and hadronic interaction models QGSJETII-04, EPOS-LHC and Sibyll 2.3.

From these figures, we can see that showers induced by heavier primaries develop earlier and faster in the atmosphere than lighter primaries. Moreover the difference among the X_{max} values for the different hadronic interaction models vary between 0.4 and 2.4% for proton showers and between 2.0 and 3.4% for iron showers. In general, the X_{max} parameter strongly depends on the primary mass but not significantly on the used hadronic interaction model.

Since the muon density reconstructed at 500 m from the shower axis features an optimal mass separation in comparison to other distances, we compared the mass discrimination power of the parameters $\rho_\mu^{\mathrm{Rec}}(500)/E_{\mathrm{SD}}^{p_1}$ and $\rho_\mu^{\mathrm{Rec}}(500)/E_{\mathrm{FD}}^{p_1}$ with the slope parameter (β_μ) of the MLDF and X_{max}. The parameter distributions for proton and iron-induced showers simulated with QGSJETII-04, EPOS-LHC and Sibyll 2.3 are shown in Figures 6.34, 6.35 and 6.36. The mass discrimination values are shown in Table 6.7. As already described in section 6.5.1, we estimated the merit-factor uncertainty by using the *bootstrap* method in which we randomly resampled 10000 distributions with replacement of the original dataset for $\rho_\mu^{\mathrm{Rec}}(500)/E_{\mathrm{SD}}^{p_1}$, $\rho_\mu^{\mathrm{Rec}}(500)/E_{\mathrm{FD}}^{p_1}$, β_μ and X_{max}.

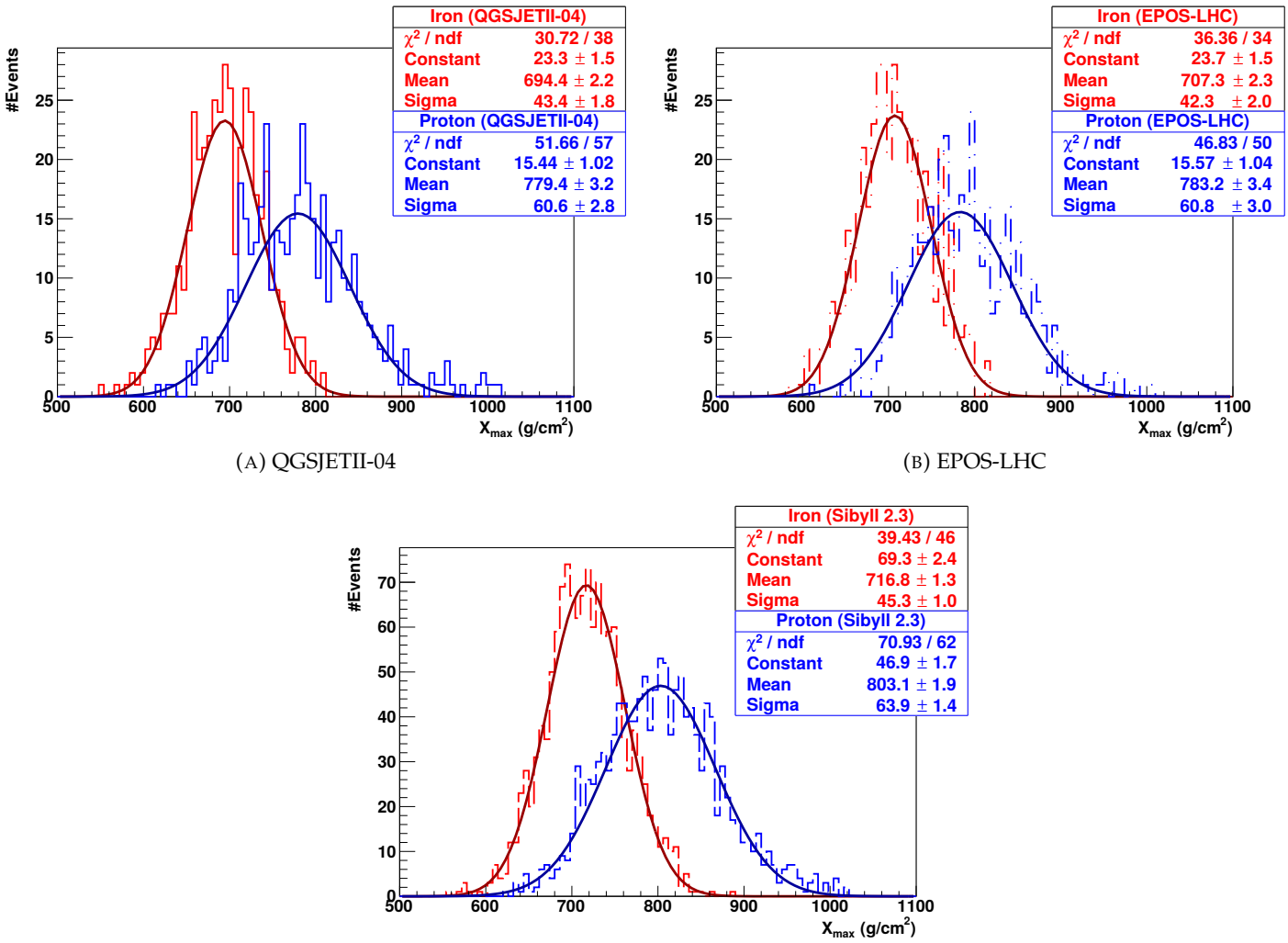

(A) QGSJETII-04

(B) EPOS-LHC

(C) Sibyll 2.3

FIGURE 6.33: X_{max} distribution for proton and iron-induced showers and hadronic interaction models QGSJETII-04, EPOS-LHC and Sibyll 2.3.

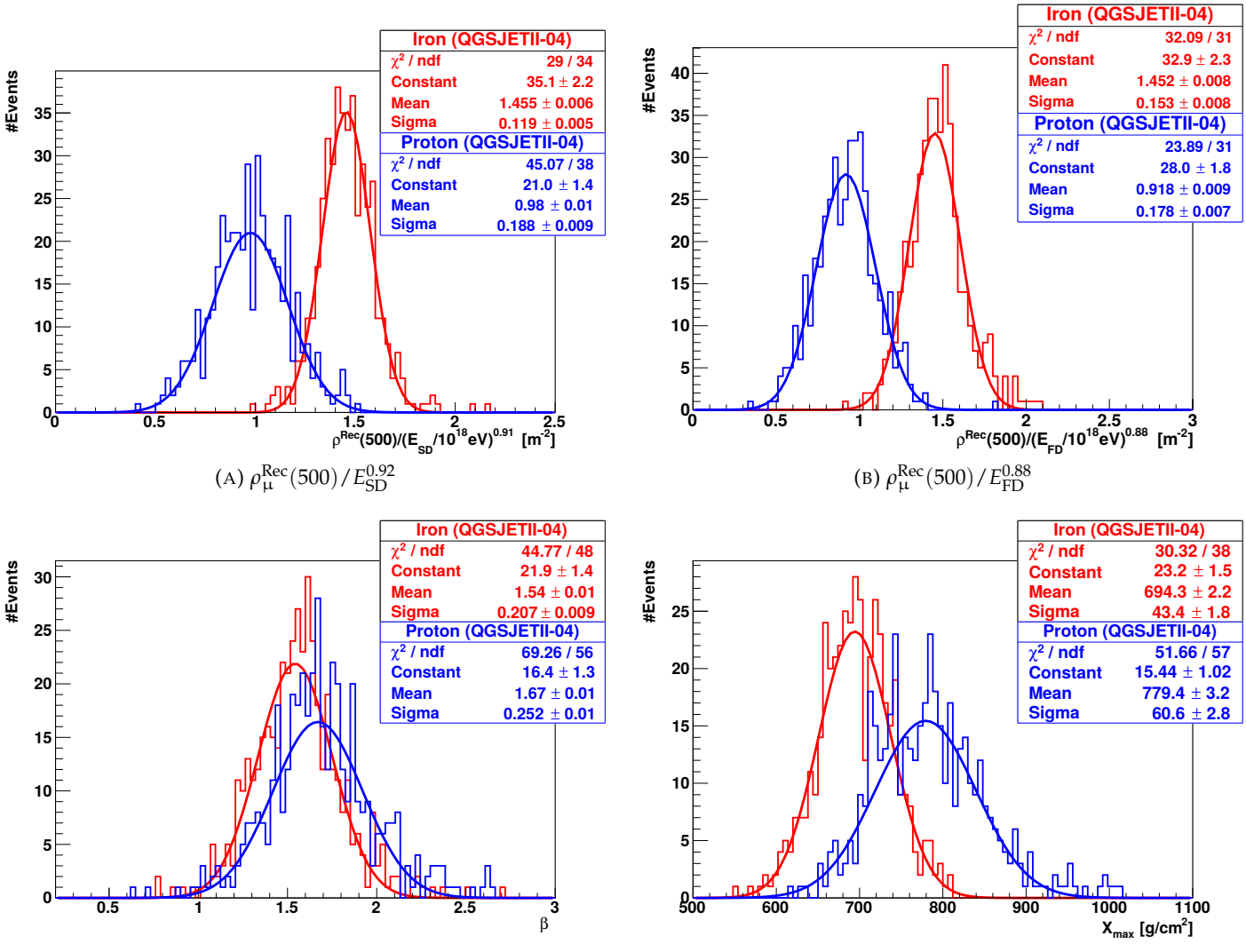

(A) $\rho_{\mu}^{\mathrm{Rec}}(500)/E_{\mathrm{SD}}^{0.92}$

(B) $\rho_{\mu}^{\mathrm{Rec}}(500)/E_{\mathrm{FD}}^{0.88}$

(C) β_{μ}

(D) X_{max}

FIGURE 6.34: Mass discrimination power for the muon density reconstructed at 500 m from the shower axis divided by the SD energy ($\rho_{\mu}^{\mathrm{Rec}}(500)/E_{\mathrm{SD}}^{0.92}$) and FD energy ($\rho_{\mu}^{\mathrm{Rec}}(500)/E_{\mathrm{FD}}^{0.88}$), slope parameter ($\beta_{\mu}$) of the MLDF and X_{max} for QGSJETII-04 hadronic interaction model.

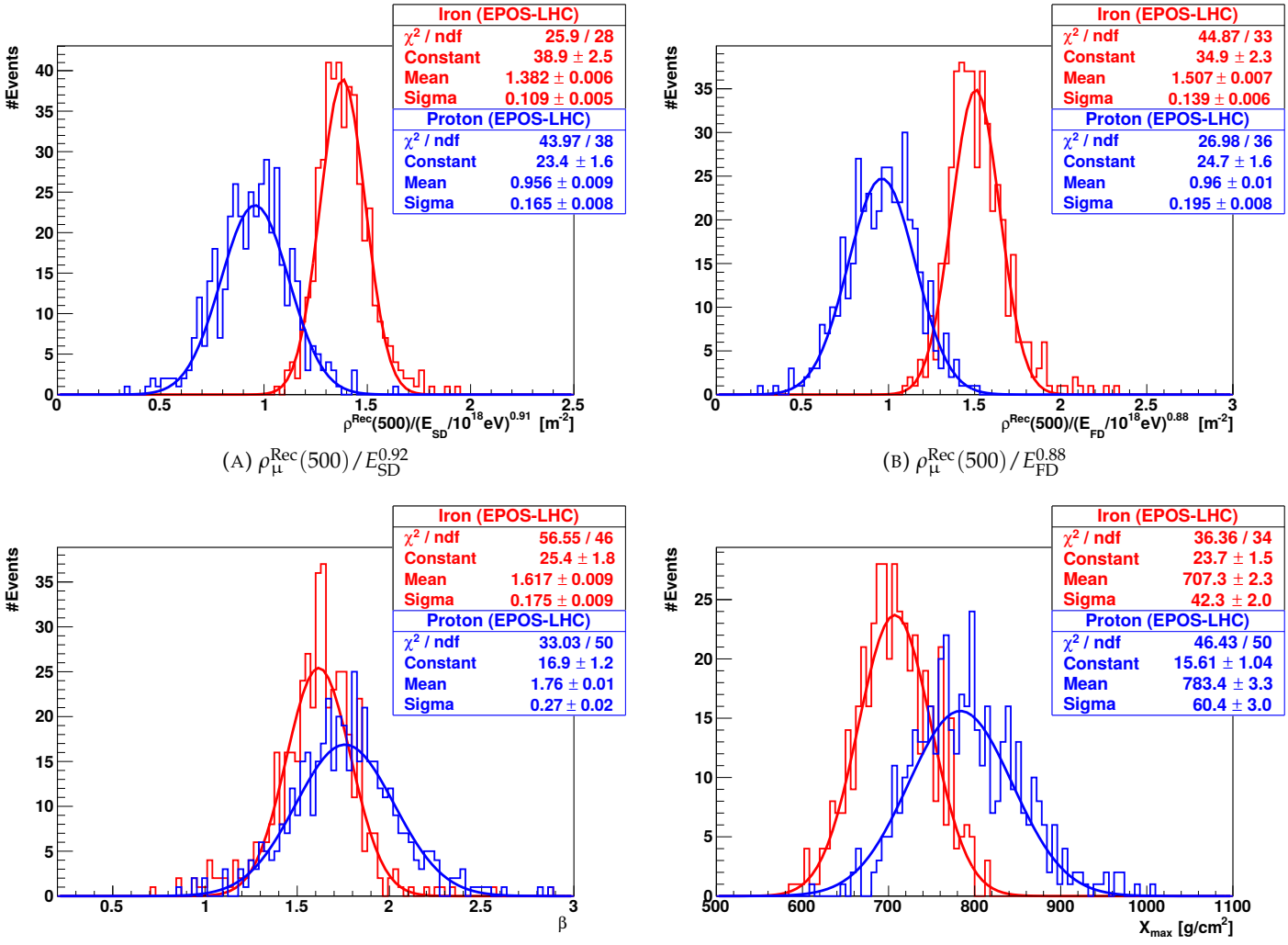

(A) $\rho_{\mu}^{\mathrm{Rec}}(500)/E_{\mathrm{SD}}^{0.92}$

(B) $\rho_{\mu}^{\mathrm{Rec}}(500)/E_{\mathrm{FD}}^{0.88}$

(C) β_{μ}

(D) X_{max}

FIGURE 6.35: Mass discrimination power for the muon density reconstructed at 500 m from the shower axis divided by the SD energy ($\rho_{\mu}^{\mathrm{Rec}}(500)/E_{\mathrm{SD}}^{0.92}$) and FD energy ($\rho_{\mu}^{\mathrm{Rec}}(500)/E_{\mathrm{FD}}^{0.88}$), slope parameter ($\beta_{\mu}$) of the MLDF and X_{max} for EPOS-LHC hadronic interaction model.

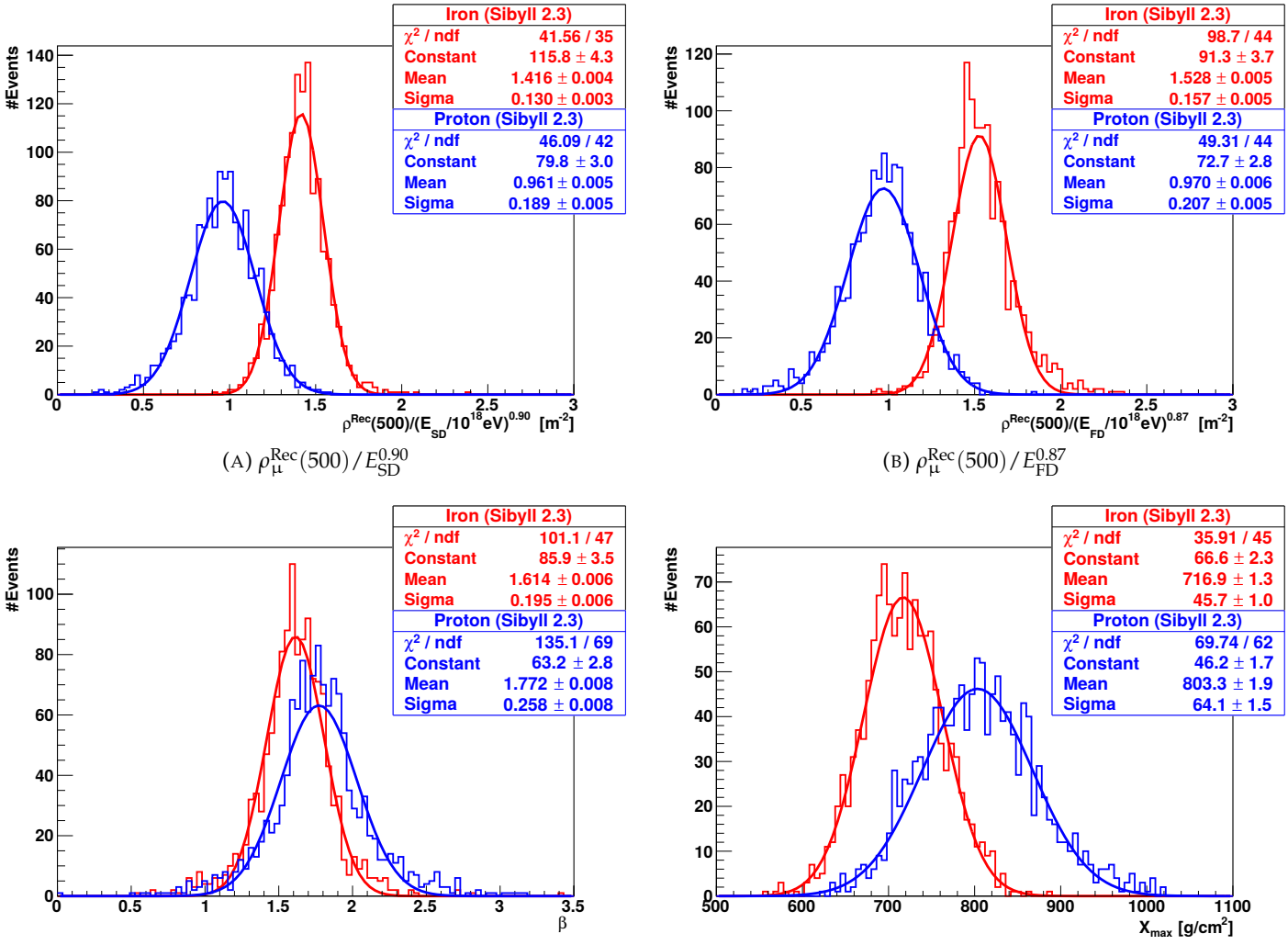

(A) $\rho_{\mu}^{\mathrm{Rec}}(500)/E_{\mathrm{SD}}^{0.90}$

(B) $\rho_{\mu}^{\mathrm{Rec}}(500)/E_{\mathrm{FD}}^{0.87}$

(C) β_{μ}

(D) X_{max}

FIGURE 6.36: Mass discrimination power for the muon density reconstructed at 500 m from the shower axis divided by the SD energy ($\rho_{\mu}^{\mathrm{Rec}}(500)/E_{\mathrm{SD}}^{0.90}$) and FD energy ($\rho_{\mu}^{\mathrm{Rec}}(500)/E_{\mathrm{FD}}$), slope parameter ($\beta_{\mu}$) of the MLDF and X_{max} for Sibyll 2.3 hadronic interaction model.

Mass Estimators	QGSJETII-04		EPOS-LHC		Sibyll 2.3	
	MF	Uncertainty	MF	Uncertainty	MF	Uncertainty
$\rho_{\mu}^{\mathrm{Rec}}(500)/E_{\mathrm{SD}}^{p_1}$	2.16	0.13	2.15	0.13	1.99	0.06
$\rho_{\mu}^{\mathrm{Rec}}(500)/E_{\mathrm{FD}}^{p_1}$	2.27	0.12	2.28	0.12	2.14	0.06
β_{μ}	0.39	0.08	0.44	0.08	0.5	0.04
X_{max}	1.14	0.09	1.03	0.10	1.10	0.04

TABLE 6.7: Merit Factor (MF) and its uncertainty for $\rho_{\mu}^{\mathrm{Rec}}(500)/E_{\mathrm{SD}}^{p_1}$, $\rho_{\mu}^{\mathrm{Rec}}(500)/E_{\mathrm{FD}}^{p_1}$, β_{μ} and X_{max} for showers simulated with proton and iron as primaries and hadronic interaction models QGSJETII-04, EPOS-LHC and Sibyll 2.3.

From the figures and table above, the muon density reconstructed at 500 m from the shower axis divided by the SD and FD energy features a better mass separation than X_{max}, and the MLDF slope parameter β_{μ} is not sensitive to the chemical composition of cosmic rays. Moreover, we also investigated the behaviour of the discrimination power as a function of the true primary cosmic-ray energy. Thus, we divided the simulated energy range (3.16×10^{17} - $10^{18.8}$ eV) into seven bins of energy. However, as there are much more events (consequently more statistics) for the Sibyll 2.3 hadronic interaction model than in the others, we only analysed the mass-discrimination power (for the parameters $\rho_{\mu}^{\mathrm{Rec}}(500)/E_{\mathrm{SD}}^{p_1}$, $\rho_{\mu}^{\mathrm{Rec}}(500)/E_{\mathrm{FD}}^{p_1}$ and X_{max}) as a function of the primary energy in logarithmic scale for the Sibyll 2.3 model (see Figure 6.37). The merit factor uncertainty was estimated by using the *bootstrap* method. As a result, $\rho_{\mu}^{\mathrm{Rec}}(500)/E_{\mathrm{SD}}^{0.90}$ and $\rho_{\mu}^{\mathrm{Rec}}(500)/E_{\mathrm{FD}}^{0.87}$ slightly increase with increasing primary energy, while X_{max} keeps approximately constant within uncertainties with increasing logarithmic energy. The distributions of the mass-composition estimators for each logarithmic energy bin from $10^{17.5}$ eV to $10^{18.8}$ eV are shown in Figures 6.38, 6.39 and 6.40. From Figures 6.38 and 6.39, the standard deviation of the proton and iron distributions slightly decreases with increasing logarithmic energy, while the mean values keep approximately constant. Since the mass-discrimination power (Eq. 6.8) increases with decreasing standard deviation, the less this deviation the higher the merit factor for a constant mean value. This explains the increasing of the mass-discrimination power of Figure 6.37 with increasing primary energy. On the other hand, despite the uncertainty of the X_{max} distributions decreases with increasing logarithmic energy in Figure 6.40, the difference between the proton and iron mean values also decreases. This makes the mass-discrimination power for X_{max} constant with increasing logarithmic energy in Figure 6.37.

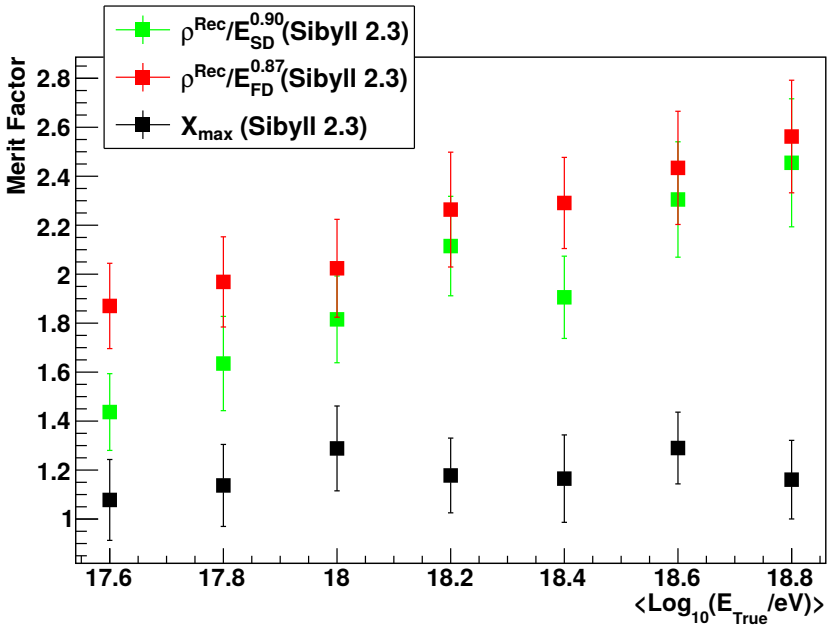

FIGURE 6.37: Mass discrimination power $\rho_{\mu}^{\mathrm{Rec}}(500)/E_{\mathrm{SD}}^{0.90}$, $\rho_{\mu}^{\mathrm{Rec}}(500)/E_{\mathrm{FD}}^{0.87}$ and X_{max} as a function of the true primary cosmic-ray energy for proton and iron-induced showers and Sibyll 2.3 hadronic interaction model.

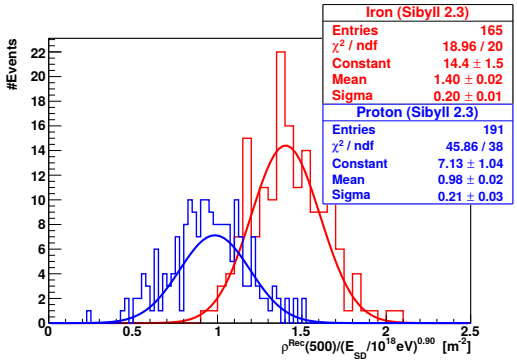

(A) $10^{17.5} \leq \mathrm{Log}_{10}(\mathrm{E_{True}}/\mathrm{eV}) < 10^{17.7}$

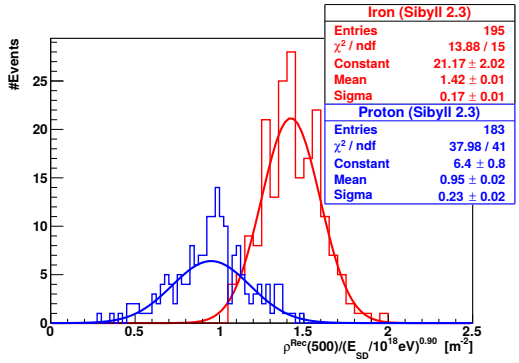

(B) $10^{17.7} \leq \mathrm{Log}_{10}(\mathrm{E_{True}}/\mathrm{eV}) < 10^{17.9}$

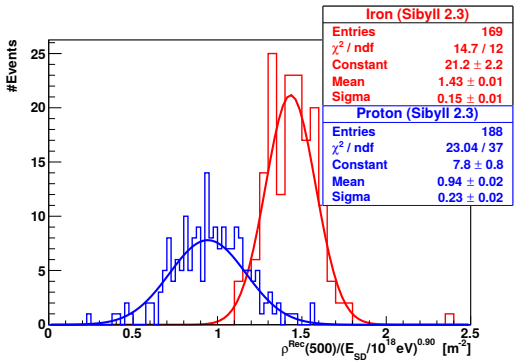

(C) $10^{17.9} \leq \mathrm{Log}_{10}(\mathrm{E_{True}}/\mathrm{eV}) < 10^{18.1}$

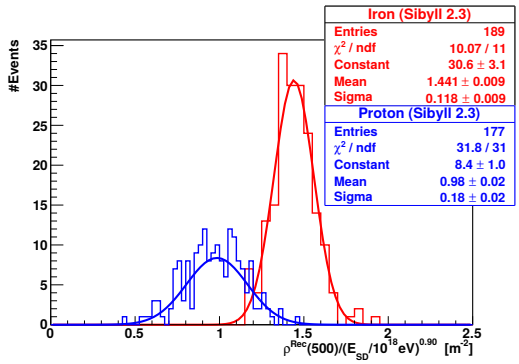

(D) $10^{18.1} \leq \mathrm{Log}_{10}(\mathrm{E_{True}}/\mathrm{eV}) < 10^{18.3}$

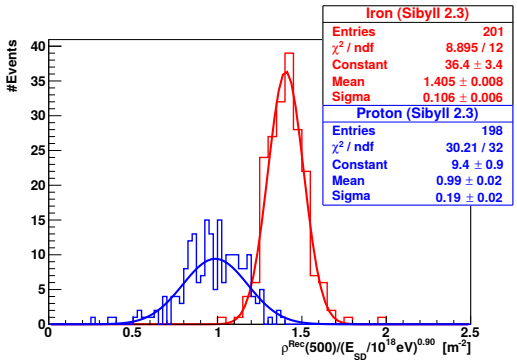

(E) $10^{18.3} \leq \mathrm{Log}_{10}(\mathrm{E_{True}}/\mathrm{eV}) < 10^{18.5}$

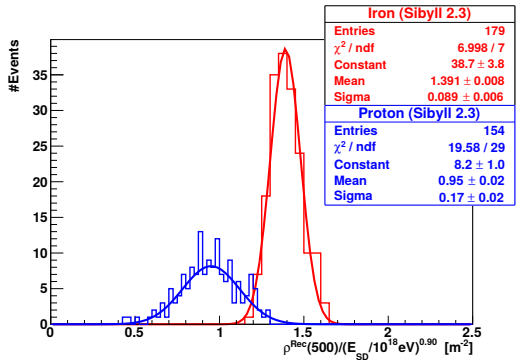

(F) $10^{18.5} \leq \mathrm{Log}_{10}(\mathrm{E_{True}}/\mathrm{eV}) < 10^{18.7}$

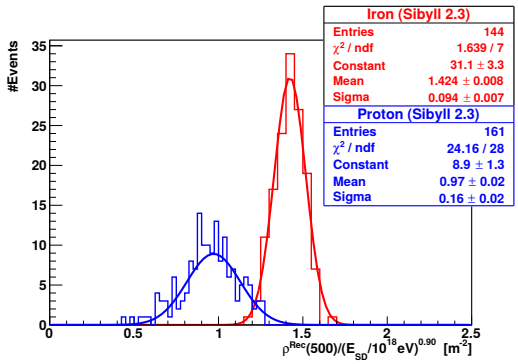

(G) $10^{18.7} \leq \mathrm{Log}_{10}(\mathrm{E_{True}}/\mathrm{eV}) < 10^{18.9}$

FIGURE 6.38: $\rho_{\mu}^{\mathrm{Rec}}(500)/E_{\mathrm{SD}}^{0.90}$ distributions for proton (blue) and iron (red) showers for Sibyll 2.3 hadronic interaction model for different energy bins in logarithmic scale.

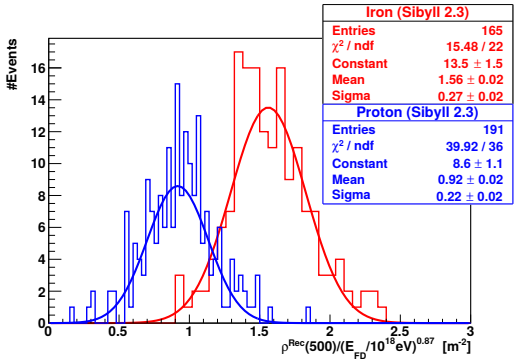

(A) $10^{17.5} \leq \mathrm{Log}_{10}(\mathrm{E_{True}}/\mathrm{eV}) < 10^{17.7}$

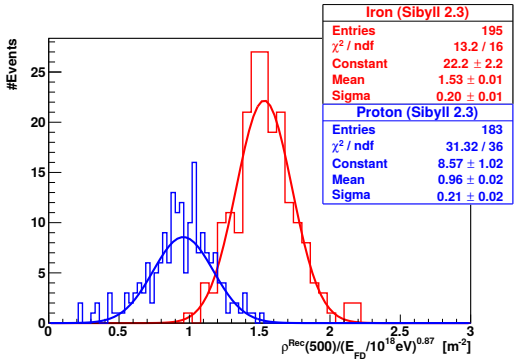

(B) $10^{17.7} \leq \mathrm{Log}_{10}(\mathrm{E_{True}}/\mathrm{eV}) < 10^{17.9}$

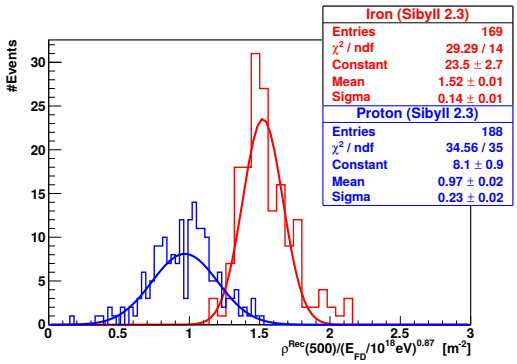

(C) $10^{17.9} \leq \mathrm{Log}_{10}(\mathrm{E_{True}}/\mathrm{eV}) < 10^{18.1}$

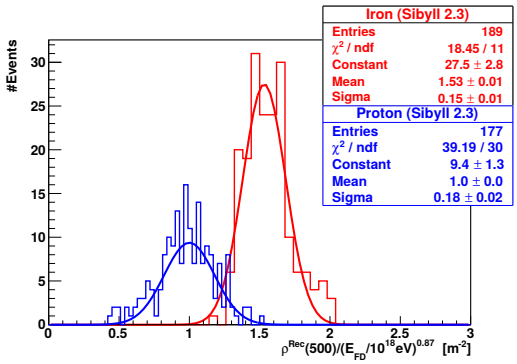

(D) $10^{18.1} \leq \mathrm{Log}_{10}(\mathrm{E_{True}}/\mathrm{eV}) < 10^{18.3}$

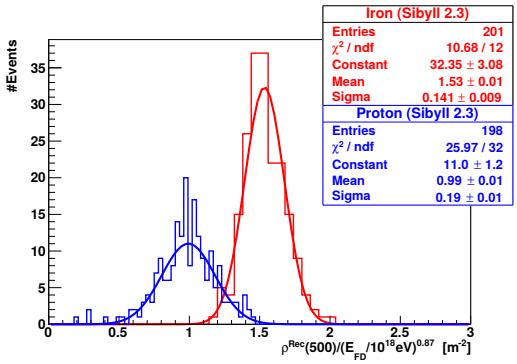

(E) $10^{18.3} \leq \mathrm{Log}_{10}(\mathrm{E_{True}}/\mathrm{eV}) < 10^{18.5}$

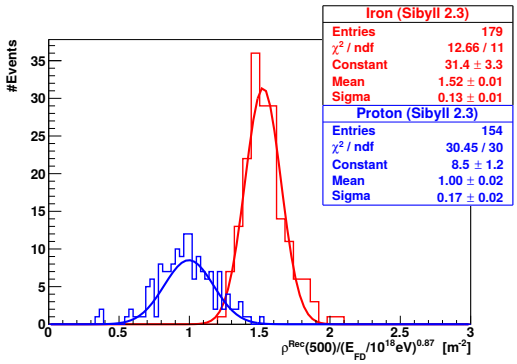

(F) $10^{18.5} \leq \mathrm{Log}_{10}(\mathrm{E_{True}}/\mathrm{eV}) < 10^{18.7}$

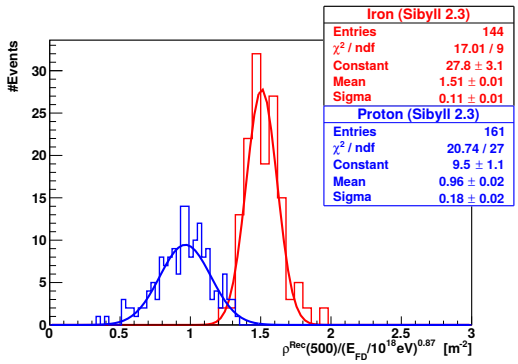

(G) $10^{18.7} \leq \mathrm{Log}_{10}(\mathrm{E_{True}}/\mathrm{eV}) < 10^{18.9}$

FIGURE 6.39: $\rho_{\mu}^{\mathrm{Rec}}(500)/E_{\mathrm{FD}}^{0.87}$ distributions for proton (blue) and iron (red) showers for Sibyll 2.3 hadronic interaction model for different energy bins in logarithmic scale.

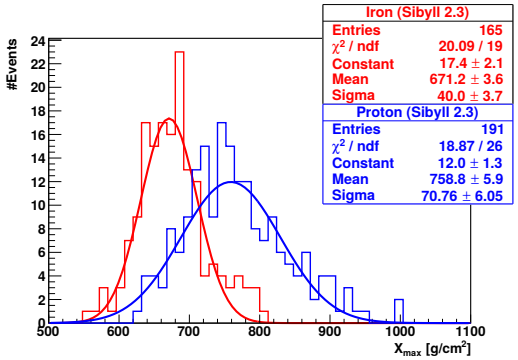

(A) $10^{17.5} \leq \mathrm{Log}_{10}(\mathrm{E}_{\mathrm{True}}/\mathrm{eV}) < 10^{17.7}$

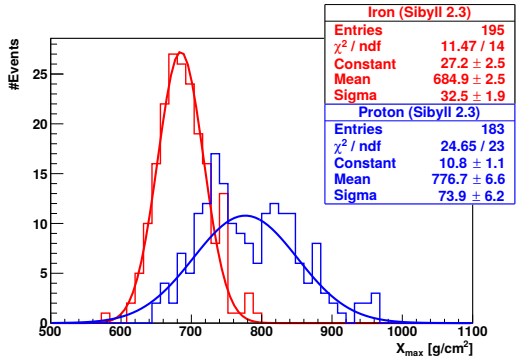

(B) $10^{17.7} \leq \mathrm{Log}_{10}(\mathrm{E}_{\mathrm{True}}/\mathrm{eV}) < 10^{17.9}$

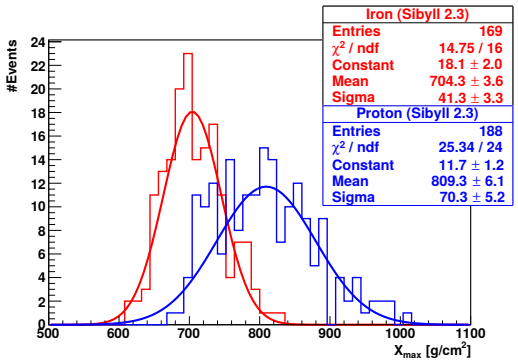

(C) $10^{17.9} \leq \mathrm{Log}_{10}(\mathrm{E}_{\mathrm{True}}/\mathrm{eV}) < 10^{18.1}$

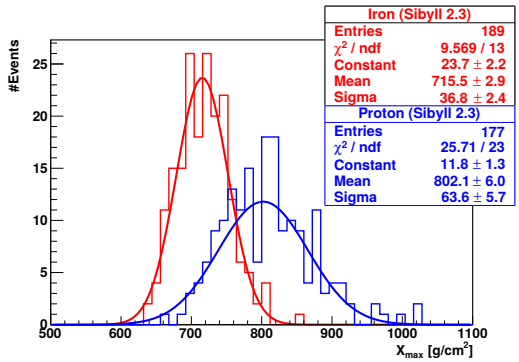

(D) $10^{18.1} \leq \mathrm{Log}_{10}(\mathrm{E}_{\mathrm{True}}/\mathrm{eV}) < 10^{18.3}$

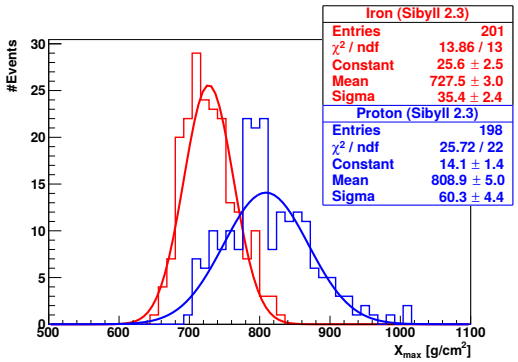

(E) $10^{18.3} \leq \mathrm{Log}_{10}(\mathrm{E}_{\mathrm{True}}/\mathrm{eV}) < 10^{18.5}$

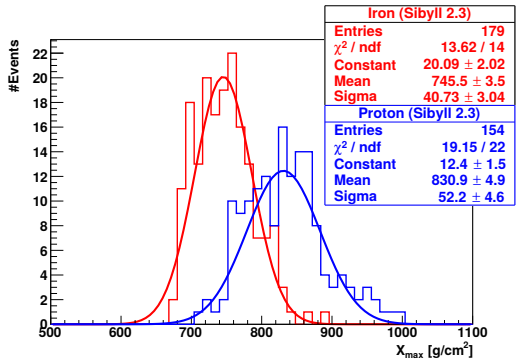

(F) $10^{18.5} \leq \mathrm{Log}_{10}(\mathrm{E}_{\mathrm{True}}/\mathrm{eV}) < 10^{18.7}$

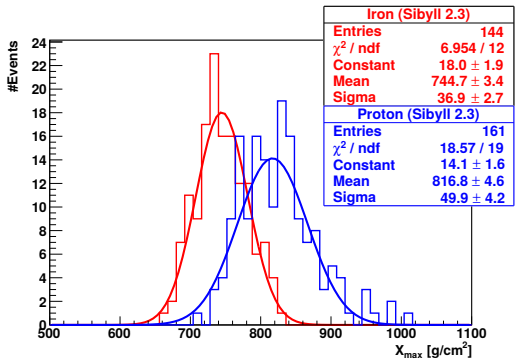

(G) $10^{18.7} \leq \mathrm{Log}_{10}(\mathrm{E}/\mathrm{eV}) < 10^{18.9}$

FIGURE 6.40: X_{max} distributions for proton (blue) and iron (red) showers for Sibyll 2.3 hadronic interaction model for different energy bins in logarithmic scale.

Data Analyses

The combination of the muon density reconstructed at 500 m from the shower axis with the different primary-energy parameters features a large mass separation within measurement uncertainties, as shown in the simulation studies in the previous chapter. This chapter provides an overview of the hybrid data recorded by the AMIGA (SD+MD), AERA (RD), and Fluorescence (FD) detectors independently from each other, and triple-hybrid events detected simultaneously by SD+MD+RD and SD+MD+FD. Moreover, fourfold-hybrid events (SD+MD+FD+RD) were also investigated. The data were measured in the period from 19/10/2015 to 17/10/2016, in which all muon counters were calibrated. The muon detectors are triggered by the surface detectors, so for all MD events, the SD data is also available. Moreover, AERA is triggered by SD, FD and self-triggered. However, in the following analysis only the events triggered by SD are used. The recorded data were analysed with the Offline software (release Fschlueter (trunk, revision 31522)). The module sequence used for the event reconstruction measured by the fourfold-hybrid detector (SD, MD, FD and RD) can be seen in Appendix A.2.

For the analysis we applied the same quality cuts derived in Section 6.4. Moreover, some quality cuts for the surface detector were applied, which require that the SD energy is higher than 3×10^{17} eV and the reconstructed zenith angle is lower than 55^{o}. After applying the selection criteria, we have a total of 304 SD+MD reconstructed events, 61 SD+MD+FD events, 82 SD+MD+RD events, and only two fourfold-hybrid events (SD+MD+ FD+RD) after the calibration of the muon detectors. As soon as more statistics of data is available, we can perform more accurate mass-composition measurements for the triple-hybrid datasets as well as fourfold-hybrid dataset.

The arrival directions and a map of the shower core of the reconstructed events are shown in Figure 7.1 (with the exception of the two four-fold hybrid events). The zenith and azimuth angles are reconstructed from the SD signal. The reconstructed shower cores are approximately uniformly distributed over the Unitary Cell, which excludes a locational detection bias.

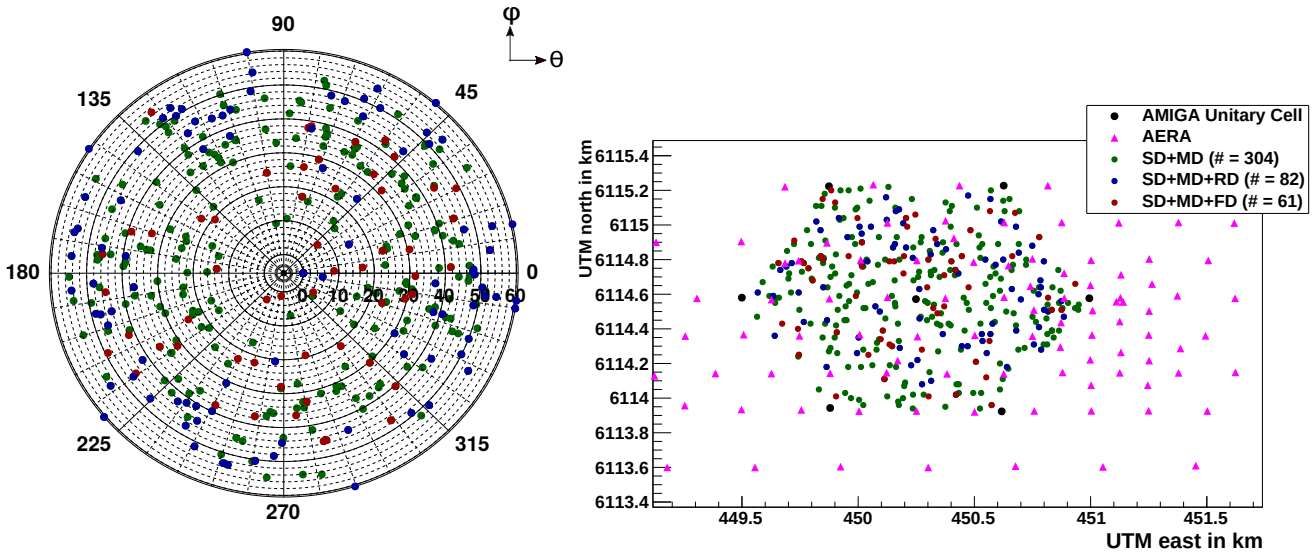

FIGURE 7.1: Left: Skyplot of cosmic-ray air shower arrival directions. The arrival direction was reconstructed by the surface detectors. Right: Spatial distribution of the reconstructed event shower cores within the AMIGA Unitary Cell (black circles). The radio stations are marked as pink triangles.

Figure 7.2 shows the energy (left panel) and zenith-angle (right panel) distributions for the reconstructed events. The primary energy is taken from SD reconstruction. The energy distribution reflects the reduced particle flux for higher energies. However, it is worth saying that the number of RD events decreases slower with increasing logarithmic energy, which indicates that RD measurements have larger detection efficiency at higher energies than AMIGA (the energy distribution for RD events is not shown in the figure). AMIGA has full detection efficiency at energies around 3.16×10^{17} eV. The highest energetic event measured in coincidence by RD and AMIGA detectors features a reconstructed primary energy of $(2.505 \pm 0.08) \times 10^{18}$ eV, while the highest energetic event detected in coincidence by FD and AMIGA has a primary energy of $(1.41 \pm 0.07) \times 10^{18}$ eV. Moreover, the AERA detection efficiency decreases significantly towards smaller zenith angles due to the smaller lateral distribution of the radio signal. Therefore, the lower the zenith angle, the smaller the energy of the events reconstructed with the RD detector.

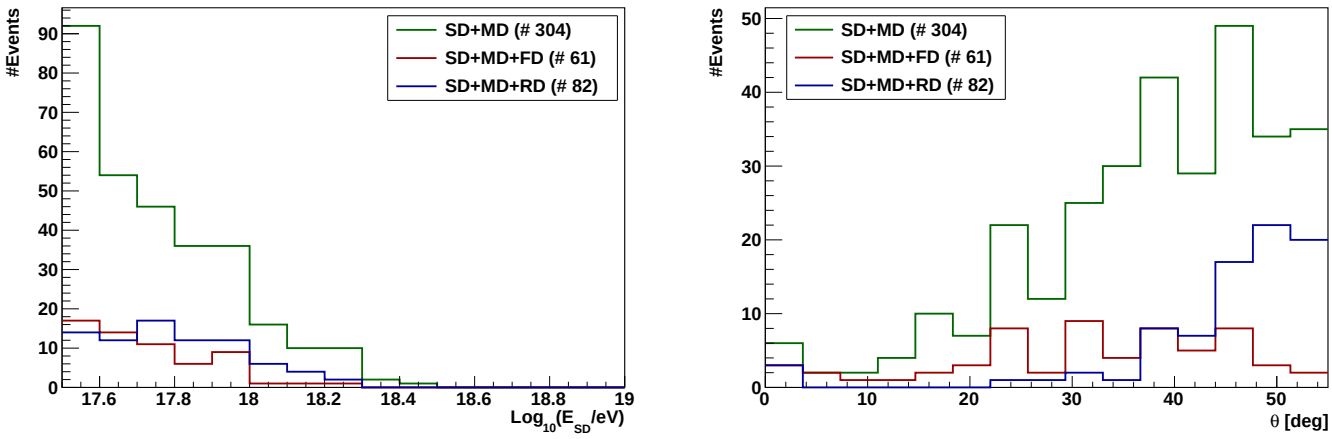

FIGURE 7.2: Left: Energy distribution of the events reconstructed with SD+MD, SD+MD+FD and SD+MD+RD. The number of reconstructed events decreases with the increasing logarithm of the energy in accordance with the primary cosmic-ray flux. Right: Zenith-angle distribution of the events reconstructed with SD+MD, SD+MD+FD and SD+MD+RD. The number of reconstructed events increases with increasing zenith angle.

The fourfold hybrid measurements offer the possibility of measuring the cosmic-ray properties using different independent detection methods and to cross-calibrate the different detector responses. An example of a four-fold hybrid event is shown in Figure 7.3. The event (Auger-ID: 153434861501) was detected on 10/12/2015 with a reconstructed primary energy of $(8.22 \pm 0.77 \pm 0.81) \times 10^{17}$ eV and zenith and azimuth angles of $(\theta,\phi) = (49.9 \pm 0.4, 286.0 \pm 0.4)^{o}$. The event was measured by nine surface detectors, four MD, eight RD stations and two fluorescence telescopes of Coihueco, which is the closest telescope to the *infill* array. The shower maximum $X_{\max}$ was reconstructed as (801 ± 16) g/cm^2 from the fluorescence signal.

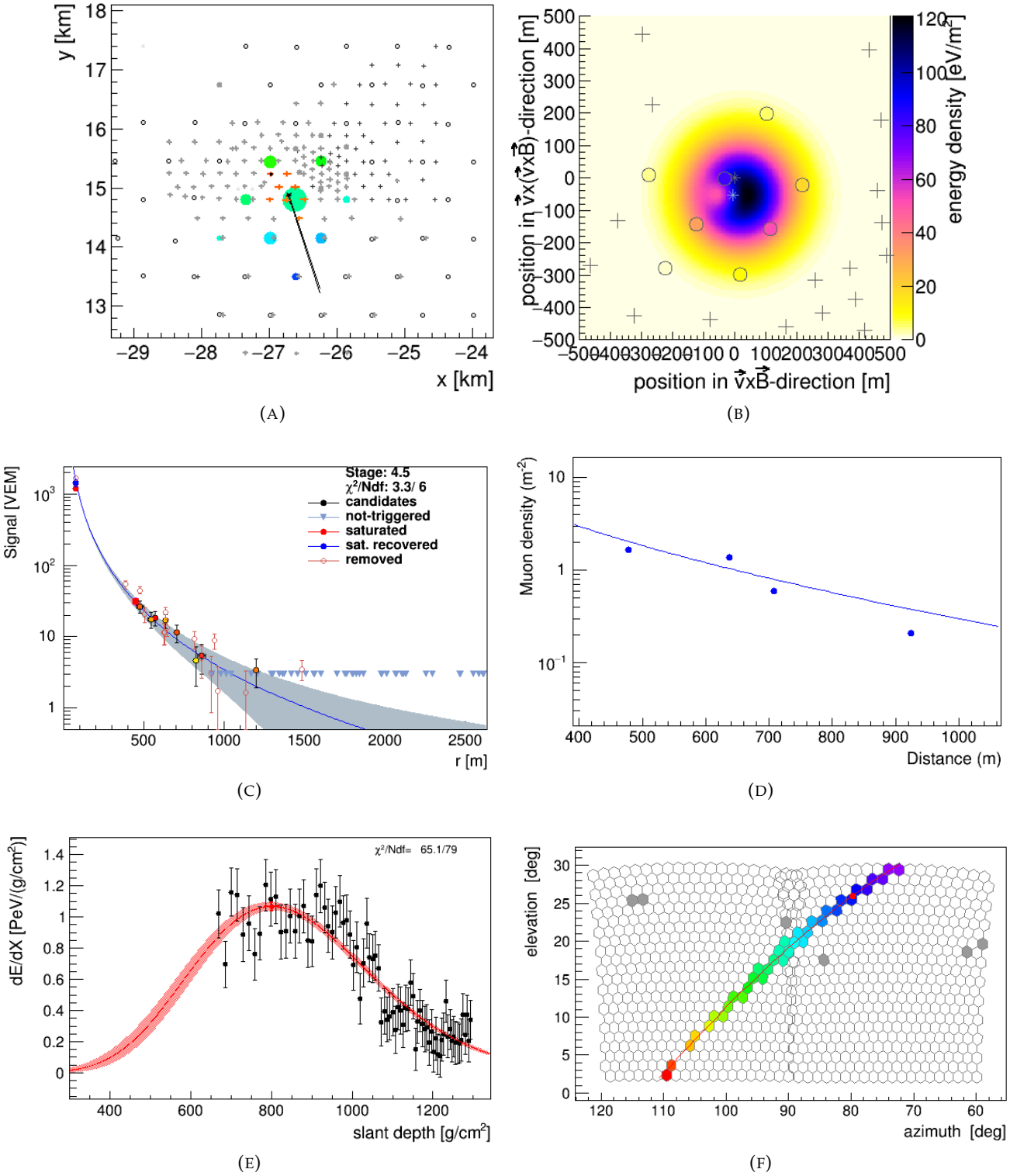

(A) (B) (C) (D) (E) (F)

FIGURE 7.3: Example of a reconstructed fourfold-hybrid event detected simultaneously by the SD, MD, FD and RD detectors The event map with the nine SD and eight RD active detectors is shown in **(A)**. The two-dimensional lateral distribution function of the radiation energy fluence is shown in **(B)**. The fittings of the lateral distribution function on the surface and muon detector signals are shown in **(C)** and **(D)**. The angular distribution of the observed fluorescence light by Coihueco mirrors 3 and 4 is depicted in **(E)**. The reconstructed longitudinal profile of the released shower energy in the atmosphere is shown in **(F)**.

For mass-composition investigation, we analysed the muon density reconstructed at 500 m from the shower axis divided by the SD, FD and RD energy separately as following.

7.1 AMIGA analysis

The muon density is reconstructed at 500 m from the shower axis by fitting a lateral distribution function to the muon signal detected by the AMIGA counters. The reconstructed muon density was analysed as a function of the primary energy reconstructed with SD detectors (see Figure 7.4 (left panel)) to investigate the energy dependence, and then compared with simulation predictions. We parametrized the muon density correlation with the SD energy using a first-order polynomial function (in the same way as for simulation studies presented in the previous chapter) which shows an energy dependence with an exponent equivalent to 1.004. This value is a bit higher than the slope of the muon density predicted for proton and iron showers simulated with the hadronic interaction models QGSJETII-04, EPOS-LHC and Sibyll 2.3, which give a slope between 0.89 and 0.92. Moreover, we also analysed the angular dependence for the muon density (see Figure 7.4 (right panel)), which shows no significant dependence on the zenith angle.

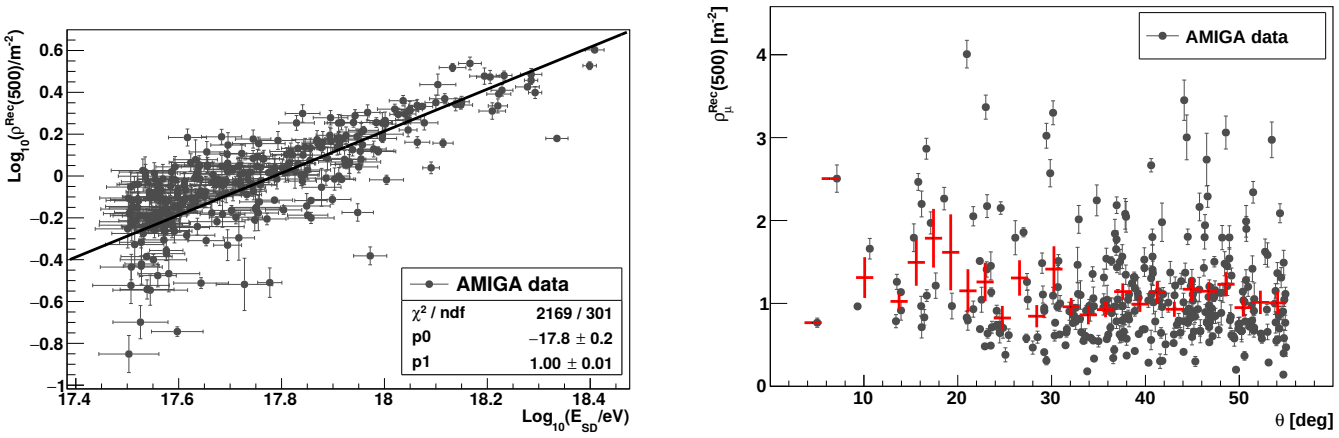

FIGURE 7.4: Left: Muon density reconstructed at 500 m from the shower axis as a function of the cosmic-ray energy reconstructed with the SD detectors. The reconstructed muon density increases with energy with a slope of 1.004, which is a bit higher ($\sim$ 9%) than the slope predicted in simulations. Right: The reconstructed muon density as a function of the zenith angle. The red croses correspond to the mean value of the muon density. The zenith angle is divided into 26 bins. As there are very few events for zenith angles smaller than 30^o, the fluctuation of the mean values is higher than in the region between 30^o and 50^o where most of the events are. So, in general, there is no significant angular dependence for the muon density.

Figure 7.5 shows the muon density distribution for the time period from 10/2015 to 10/2016 (left panel) and the muon density uncertainty for each event with respect to the mean density value (right panel).

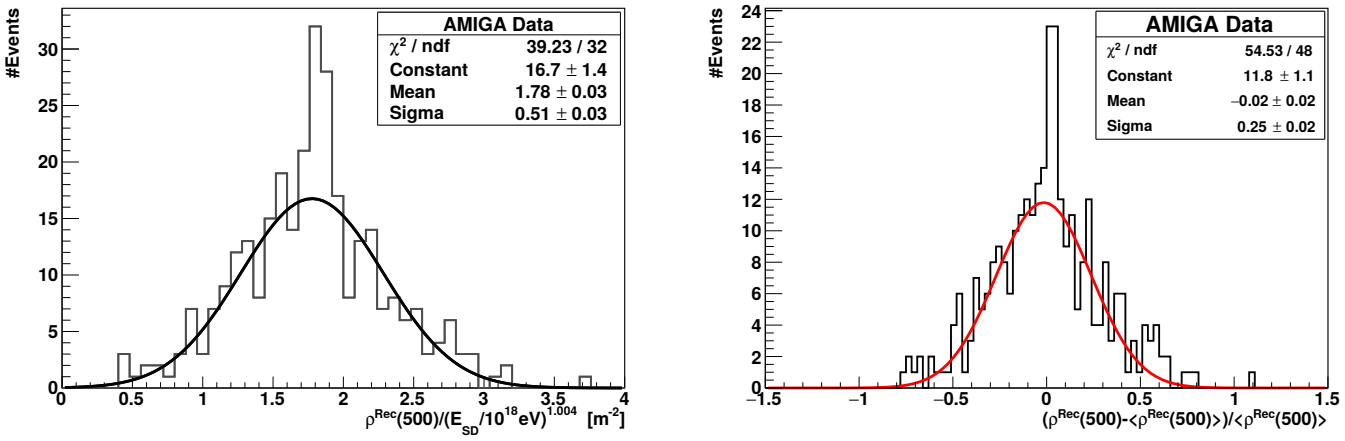

FIGURE 7.5: Left: Muon density distribution normalized to 1 EeV for the period from 10/2015 to 10/2016. Right: Muon density uncertainty with respect to the mean value of the muon density distribution which is of 1.78 muons/m^2. Most of the events show an uncertainty of about 1.5% lower than the mean value.

Figure 7.6 shows the cosmic-ray observable $\rho^{\mu\mathrm{Rec}}/E_{\mathrm{SD}}^{p_1}$ (p_1 is the slope of the first-order polynomial fit) distribution (left panel) and as a function of the primary energy estimated with the SD detectors (E_{SD}) (right panel) for measured and simulated data to investigate mass sensitivity.

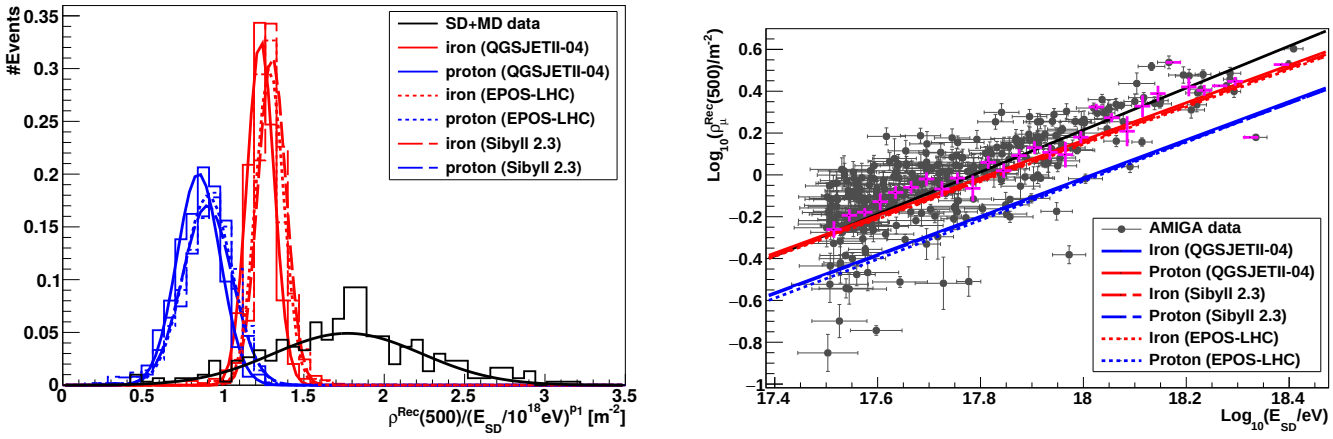

FIGURE 7.6: Left: Distribution of the muon density divided by the primary cosmic-ray energy normalized to 1 EeV. The simulated and measured distributions are fitted with a gaussian function. Right: Cosmic-ray observable $\rho_{\mu}^{\mathrm{Rec}}(500)/E_{\mathrm{SD}}^{p_1}$ as a function of the primary cosmic-ray energy estimated with the SD detectors. Theoretical curves for iron (red lines) and proton (blue lines) showers simulated with QGSJETII-04 (solid lines), EPOS-LHC (dotted lines) and Sibyll 2.3 (dashed lines) are shown for comparison. The pink crosses correspond to the mean value of the muon density and its uncertainty for 30 bins of energy.

The Auger Observatory has already shown evidences that the currently used hadronic interaction models predict less muons than observed in data [205], i. e., the models exhibit a deficit in the prediction of the muon content of extensive air showers. Hence, we investigated how larger the average muon density is for data in comparison to the simulations. Since the SD energy is influenced by the muon content of the shower, in Figure 7.6 we divided the muon density (for simulations) by the true cosmic-ray energy instead of the SD energy in order to estimate more accurately how much larger the average muon density is for data. Therefore, taking into account the average muon density for data and simulations, we found that the muon density in data is larger than: *i)* QGSJETII-04 model by 44% for iron and 109% for proton predictions; *ii)* EPOS-LHC model by 36% for iron and 99% for proton predictions; and *iii)* Sibyll 2.3 model by 37% for iron and 96% for proton predictions.

Given that the observed distribution of the depth of the shower maximum in the logarithmic energy range from $10^{17.5}$ to $10^{18.2}$ eV is not compatible with an iron dominated composition [206], we conclude that the observed muon density is not well reproduced by models tuned to fit accelerator data. To quantify the discrepancy between the predicted and observed properties of the cosmic-ray air showers, a new method was introduced to test hadronic interaction models that

does not rely on the absolute energy calibration [199]. So, a multiplicative rescaling parameter of the hadronic component of the shower was found [199], that rescales only the contribution to the ground signal of inherently hadronic origin, which consists mostly of muons. The hadronic rescaling for EPOS-LHC comprising a mixed composition (50% iron and 50% proton) is of about 1.33 ± 0.16, while for QGSJETII-04 it is 1.61 ± 0.21. Thus, applying this correction parameter to the hadronic interactions in the simulations and comparing to data (Figure 7.7), we get a result compatible with the evolution of $\langle X_{\rm max} \rangle$ as a function of the primary energy [206], which shows a general trend for a light mass composition with increasing energy for data comparison to QGSJETII-04 hadronic interaction model. However, EPOS-LHC predicts a change from heavy to mixed composition with increasing logarithmic energy. Moreover, we can not derive exactly the absolute scale for the mass sensitive observables $\rho_{\mu}^{\rm Rec}(500)/E^{p_1}$ (with E = $E_{\rm SD}$, $E_{\rm RD}$ and $E_{\rm FD}$) for a pure proton and iron simulations since the rescaling parameter was calculated for a mixed composition. The difference between the predicted theoretical curves for QGSJETII-04 and EPOS-LHC slightly decreases with increasing logarithmic energy. However, the reason for the large distance between the curves needs further investigation.

Furthermore, it is worth taking into account that the primary energy reconstructed from the surface detectors features a bias on the primary mass, since the SD signal is primarily produced by the shower muonic component which is underestimated in simulations.

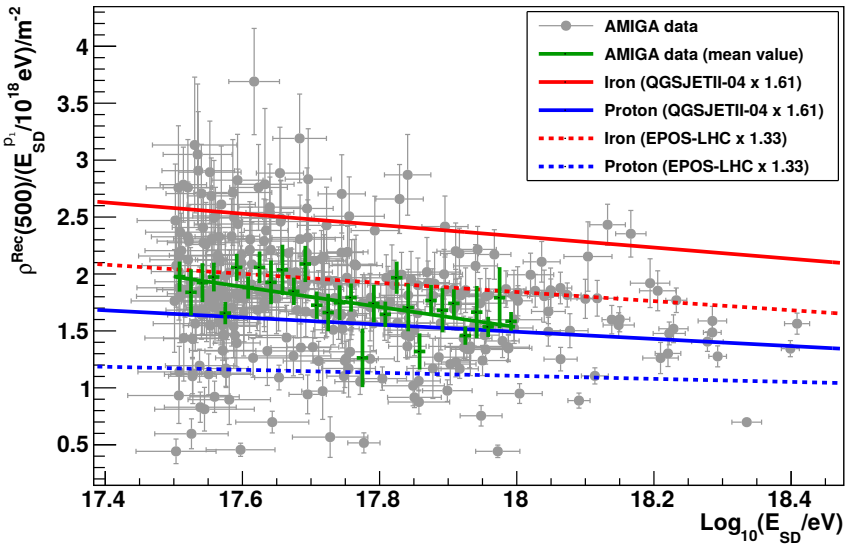

FIGURE 7.7: Evolution of the shower observable $\rho_{\mu}^{\rm Rec}(500)/E_{\rm SD}^{p_1}$ as a function of the primary energy estimated with the SD detectors for data in comparison to iron (red lines) and proton (blue lines)-induced showers simulated with QGSJETII-04 (solid lines), EPOS-LHC (dotted lines) corrected by a multiplicative rescaling of the hadronic component of the shower. The green crosses correspond to the mean value of the muon density and its standard deviation for 30 bins of energy. The green line is a linear fit of the mean value of the muon density.

The analyses of hybrid data comprising the AMIGA and AERA, and that of AMIGA and FD combination are shown in the following sections.

7.2 AMIGA+AERA analysis

The combining analyses of AMIGA and AERA were performed similarly to the AMIGA analyses reported in the previous section. The radiation energy was reconstructed by fitting the energy fluence (energy deposit per area) measured with AERA antennas with a two-dimensional lateral distribution function (GeoCeLDF). This energy was corrected for the zenith-angle dependence and clipping effect. Figure 7.8 shows the corrected radiation energy $S_{\mathrm{RD}}^{\rho_\theta}$ as a function of the primary energy measured with the surface detectors E_{SD}. The radiation-energy dependence on the primary energy was parametrized using a calibration function which follows the same method used for the calibration of the hybrid events measured with the surface and fluorescence detectors of the Pierre Auger Observatory []. The calibration function (Eq. 6.12) is obtained by maximizing a likelihood function, which takes into account uncertainties of the measurements and detector efficiencies. The result of the calibration fit is $p_0 = (14.8 \pm 0.3) \times 10^6$ eV and $p_1 = 2.10 \pm 0.03$. The resulting slope p_1 implies that the radiation energy emitted by the electromagnetic component of the shower increases quadratically with the primary cosmic-ray energy as already predicted from the simulation study previously performed in this thesis. For a 1-EeV shower perpendicular to the magnetic field axis, on average 14.8 MeV is deposited in radio emission in the frequency range from 30 to 80 MHz.

The fitting parameters p_0 and p_1 are used in Eq. 6.13 to obtain E_{RD} which is the primary energy estimated using the total energy emitted by the air shower as a radio pulse.

To investigate the mass sensitivity of the shower observable $\rho_\mu^{\mathrm{Rec}}(500)/E_{\mathrm{RD}}^{p_1}$, we parametrized the dependence of the muon density reconstructed at 500 m from the shower axis as a function of the RD energy, which is shown on the left panel of Figure 7.9. The data is fitted with a power-law function. The reconstructed muon density increases less than linear with increasing primary energy E_{RD}. The measured data is correlated with proton and iron showers simulated with the hadronic interaction models QGSJETII-04, EPOS-LHC and Sibyll 2.3 for comparison. Data describes the same energy evolution as simulations. The right panel of Figure 7.9 shows the histograms of the shower observable $\rho_\mu^{\mathrm{Rec}}(500)/E_{\mathrm{RD}}^{p_1}$ for measured data and simulations. A Gaussian fit to the data results in an average $\rho_\mu^{\mathrm{Rec}}(500)/E_{\mathrm{RD}}^{0.90}$ of about 1.5 ± 0.5 and σ of about 0.4 ± 0.9.

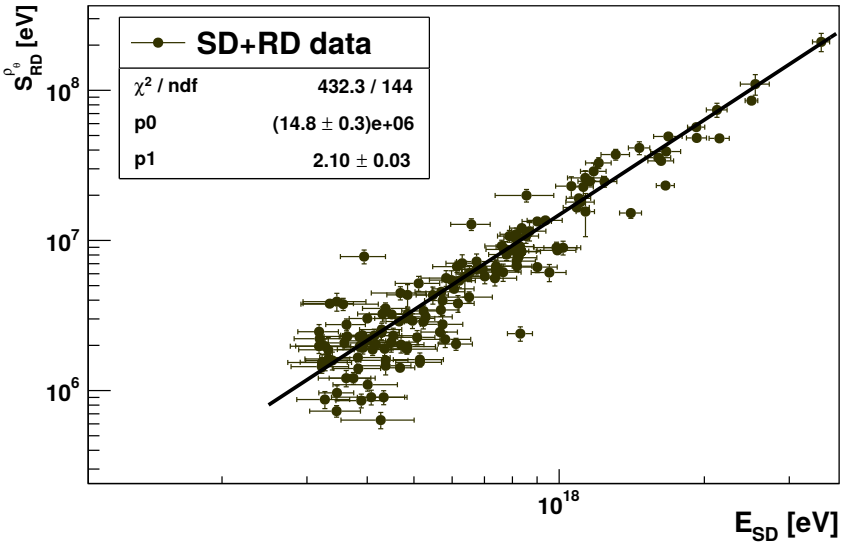

FIGURE 7.8: Radiation energy $S^{\rho_\theta}_{RD}$ corrected for the zenith-angle dependence and clipping effect as a function of the primary cosmic ray measured with the surface detectors. The data is fitted with a power-law function based on a maximum-likelihood approach which takes into account the reconstruction uncertainties of $S^{\rho_\theta}_{RD}$ and E_{SD}.

The muon density correlated with the RD energy shows a composition dominated by heavy elements that is not compatible with the observed distribution of the depth of the shower maximum (as shown in the previous section). So the observed muon density is not well reproduced by the shower simulations. Hence, applying the multiplicative rescaling factor for QGSJETII-04 and EPOS-LHC simulations to correct the muon deficit problem, the data shows a trend towards a lighter composition with increasing logarithmic energy (see Figure 7.10) as in [206]. The validation of the shower observable $\rho^{Rec}_{\mu}(500)\,/\,E^{p_1}_{RD}$ shows its larger potential to study mass composition of cosmic rays.

7.3 AMIGA+FD analysis

Although all muon detectors were calibrated from 20th of October, 2015 to 10th of October, 2016, the fluorescence energy (FD energy) was correctly calibrated only until October 2015. Hence for the analysis of the muon density combined with the FD energy for the full calibration period of the AMIGA muon detectors, we investigated how discrepant the non-properly calibrated FD energy is from the calibrated energy. Figure 7.11 shows the histograms for the logarithm of the calibrated and improperly calibrated FD energy. The average of the non-properly calibrated FD energy is 9.0% larger than the calibrated energy, while its uncertainty is smaller than the uncertainty of the calibrated energy by a factor of only 1.4%. Thus, there is no need to apply any correction factor for the non-properly calibrated FD energy.

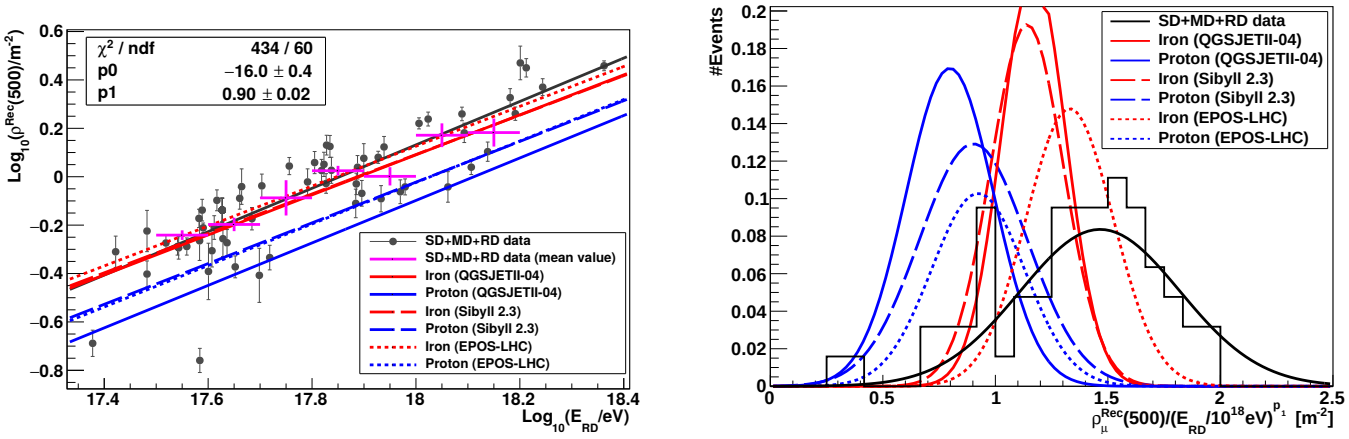

FIGURE 7.9: Left: Muon density reconstructed at 500 m from the shower axis as a function of the primary energy estimated with the radiation energy emitted by the electromagnetic component of the shower measured by the RD antennas. The data was fitted to a power-law function which accounts for the estimated uncertainties in the reconstruction of $\rho_\mu^{\mathrm{Rec}}(500)$ and E_{RD}. The fit method shows a linear correlation between both variables. Theoretical curves for iron (red lines) and proton (blue lines) showers simulated with QGSJETII-04 (solid lines), EPOS-LHC (dotted lines), and Sibyll 2.3 (dashed lines) are shown for comparisons. The pink crosses correspond to the mean value of the muon density and its standard deviation for seven bins of energy. Right: Distributions of the shower observable $\rho_\mu^{\mathrm{Rec}}(500)/E_{\mathrm{RD}}^{p_1}$ for measured data and simulations. The distributions were fitted with a Gaussian function.

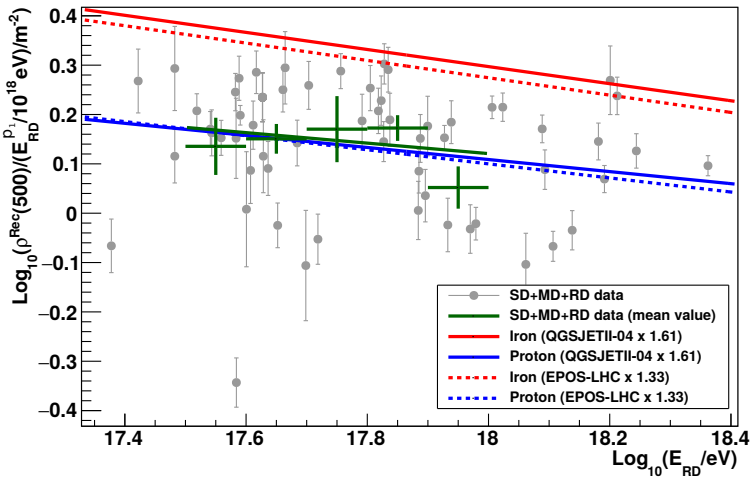

FIGURE 7.10: Mass-sensitive observable $\rho_\mu^{\mathrm{Rec}}(500)/E_{\mathrm{RD}}^{p_1}$ as a function of the RD energy (both in logarithm scales). The linear fit shows a trend towards a lighter composition (proton dominated composition) with increasing logarithmic energy.

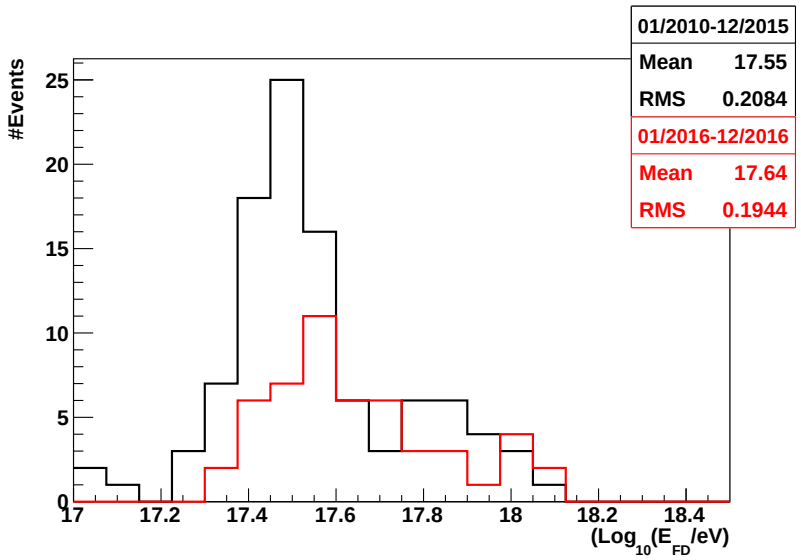

FIGURE 7.11: Histograms of the calibrated (black line) and non-properly calibrated (red line) FD energy in logarithmic scale. The calibration period is from January 2010 to December 2015 and the non-properly calibration period (used in this thesis) is from January to December 2016.

For composition analysis, we parametrized the relation between the muon density reconstructed at 500 m from the shower axis and the FD energy. Figure 7.12 (left panel) shows the muon density as a function of the FD energy in logarithm scale for measured data together with the theoretical curves for proton and iron showers simulated with the models QGSJETII-04, EPOS-LHC and Sibyll 2.3. The linear fit method takes into account the uncertainties in the respective reconstruction of $\rho_{\mu}^{\mathrm{Rec}}(500)$ and E_{FD}. The slope of the measured muon density $p_1 = 1.02 \pm 0.03$ carries information about possible changes in the average logarithmic mass. The simulation predictions for proton and iron showers give a slope between 0.85 and 0.90 as the number of muons increases less than linear with increasing primary energy. On the right panel of Figure 7.12, we have the mass-sensitive observable $\rho_{\mu}^{\mathrm{Rec}}(500)/(E_{\mathrm{FD}})^{p_1}$ normalized at 1 EeV. As a result, most of the measured events show a composition dominated by heavier elements that is in disagreement with the $\langle X_{\mathrm{max}} \rangle$ measurements for this energy range as previously mentioned. However, this heavier-dominated composition can be explained by the underestimation of the number of muons in simulations. Thus, we corrected the simulations by applying the hadronic rescaling parameters for QGSJETII-04 and EPOS-LHC models. The result is shown in Figure 7.13 and agrees with the AMIGA and AERA combined analysis with a trend towards a lighter composition with increasing logarithmic energy.

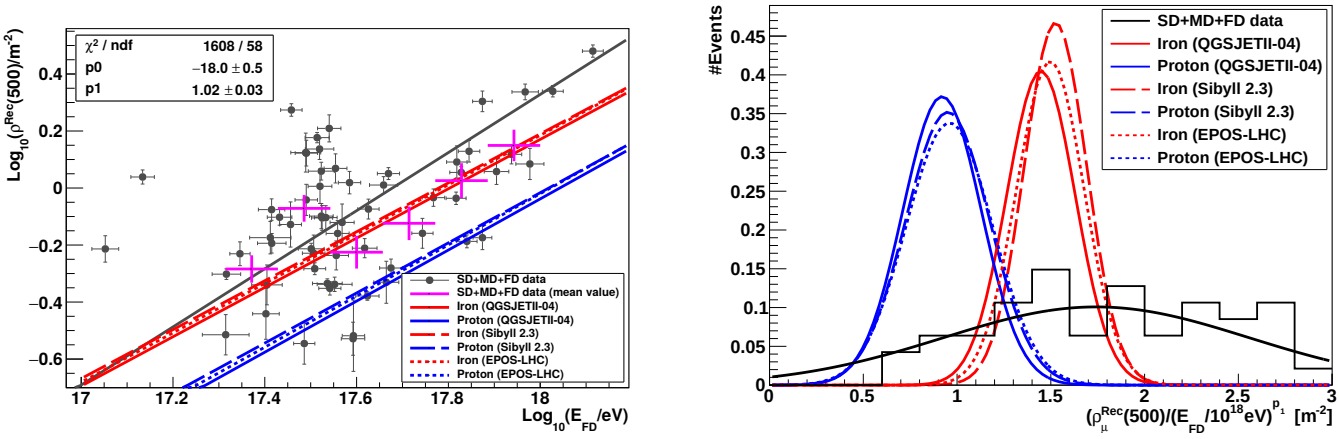

FIGURE 7.12: Left: Measured muon density as a function of the primary cosmic-ray energy measured with FD telescopes (both in logarithmic scales). The fit of the correlation is $\rho_{\mu}^{\mathrm{Rec}}(500) = p_0 \cdot E^{p_1}$ with E_{FD} in high-quality hybrid data. Blue and red lines are the theoretical curves for proton and iron simulated showers. Right: Histograms of shower observable $\rho_{\mu}^{\mathrm{Rec}}(500)/E_{\mathrm{FD}}^{p_1}$ distributions for measured data and simulations.

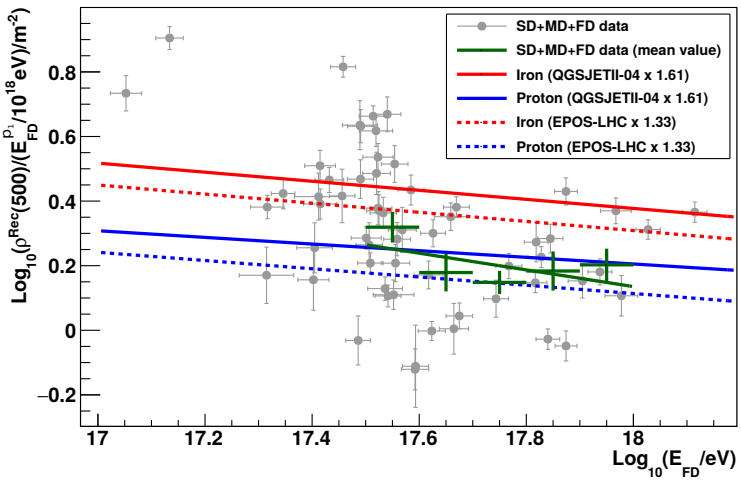

FIGURE 7.13: Mass-sensitive observable $\rho_{\mu}^{\mathrm{Rec}}(500)/E_{\mathrm{FD}}^{p_1}$ as a function of the FD energy (both in logarithm scales). The linear fit shows a trend towards a lighter composition (proton-dominated composition) with increasing logarithmic energy.

Furthermore, for the same measured events by AMIGA and FD telescopes we analysed the X_{max} as a function of the FD energy and its distribution in comparison with the theoretical curves for proton and iron showers (Figure 7.14). On the left panel of this figure, the linear fit shows a trend towards a lighter composition for the energy range between 3.16×10^{17} and 10^{18} eV. Moreover, the corresponding result of the Gaussian fit for the measured X_{max} distribution (right panel) shows an average value of (736.1 ± 69.7) g/cm^2 and an uncertainty of (61.91 ± 57.99) g/cm^2.

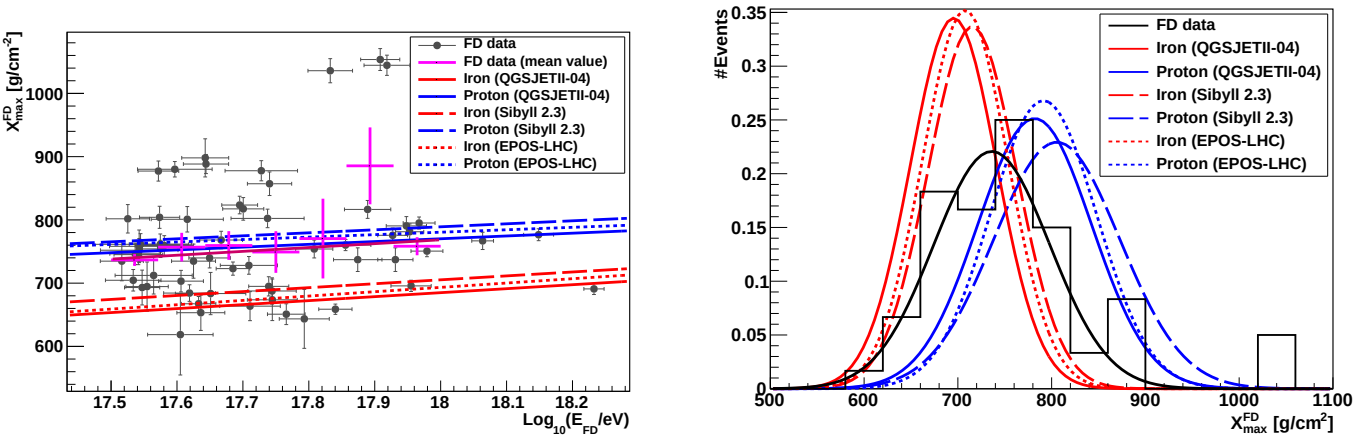

FIGURE 7.14: Left: Measured shower maximum X_{max} as a function of the FD energy. Theoretical curves for proton and iron showers are shown for comparison. The pink crosses are the mean values of the measured X_{max} in seven bins of energy. Right: Histogram of the measured X_{max} distribution and theoretical curves from simulations. The distributions are fitted with a gaussian function.

In summary, despite a few high-quality statistics for the combined analysis of AMIGA and AERA, and also of AMIGA and fluorescence telescopes, the validation of the shower observables $\rho_\mu^{Rec}(500)/E^{p_1}$ (with $E = E_{SD}$, E_{RD} and E_{FD}) showed their large potential in investigating the mass composition of primary cosmic rays. In the future, with more AMIGA detectors deployed, there will be more high-quality events detected in coincidence with AMIGA and AERA, AMIGA and FD telescopes, as well as fourfold-hybrid events detected in coincidence by SD, MD, RD, and FD detectors. In one year of data analyses, only two high-quality events were detected simultaneously by SD, MD, RD, and FD detectors. This is insufficient to correlate $\rho_\mu^{Rec}(500)/E_{RD}$ with X_{max} on an event-by-event basis.

The mass-composition study carried out in this thesis comprises vertical showers with zenith angle below 55°. However, it can be extended to inclined showers with zenith angles exceeding 60°. Since the AMIGA Muon Detectors are not sensitive to inclined showers, the muon content of air showers can be measured by the surface detectors by reconstructing the shower-size parameter N_{19}, which estimates the total number of muons at ground level [207]. This parameter is estimated via a maximum-likelihood fit of the predicted muon density to the measured signals. The

electromagnetic component is completely absorbed by the atmosphere in inclined showers, but not the radio pulses. Thus, we can detect the pure muon component with surface detectors and the electromagnetic component (via radio pulses) by the radio antennas. Moreover, the electromagnetic component can also be studied using the calorimetric energy measured by fluorescence telescopes. A combined analysis of SD and FD to study mass composition of inclined showers with energies above 4×10^{18} eV has already been performed in [207]. Therefore, the combined muonic and electromagnetic analysis performed in this thesis can be extended to higher energies and zenith angles, as well as to every cosmic-ray experiment which makes use of WCD or scintillation detectors, radio antennas and fluorescence telescopes, such as TA [9], TAIGA [208], and ICE-TOP [209, 210].

Summary and Conclusion

In this thesis the chemical composition of cosmic rays with energy above 10^{17} eV was investigated using multi-parametric measurements of a super-hybrid detector array, i. e., data from SD, FD, AMIGA and AERA were coherently reconstructed and compared to detailed simulations to better optimize mass separation of cosmic rays in the region of the energy spectrum where the transition from Galactic to extra-galactic cosmic rays occurs. Moreover, it is the first time all four different cosmic-ray detection techniques are combined to perform multi-detector cross-calibrations for composition analyses. The primary mass estimation is performed by combining the muon signal with the fluorescence energy emitted by the atmospheric nitrogen and the radio emission from the electromagnetic component of high-energy extensive air showers. The measurements of the Auger Observatory have widely advanced our understanding about cosmic rays of ultra-high energies. The Pierre Auger Collaboration has recently observed a large-scale anisotropy in the arrival directions of cosmic rays with energies above 8×10^{18} eV [211]. The direction and magnitude of the anisotropy support the hypothesis that the high-energy cosmic rays are extra-galactic in origin. However, it is difficult to locate the sources of cosmic rays, as they interact with the magnetic fields in our Galaxy and the intergalactic medium in their way from the sources to the Earth. The origin and nature of the ultra-high energy cosmic rays can be deciphered by combining the studies of anisotropy, composition and features in the energy spectrum. Therefore, the method for composition analysis performed in this thesis can be extended to the whole range of zenith angles improving the accuracy of composition measurements.

In this work we simulated 500 showers for proton and 500 showers for iron as primaries with a fixed zenith angle of 38°, uniformly distributed over the energy range from 3.16×10^{17} to 10^{19} eV using the hadronic interaction models QGSJETII-04 and EPOS-LHC, and 1500 showers for proton and 1500 showers for iron using Sibyll 2.3. All showers were simulated with CORSIKA and CoREAS. The CORSIKA files were used as an input in the Offline software framework where AMIGA, AERA and Fluorescence modules were combined. AMIGA MD, AERA and FD are exclusively sensitive to the muonic and electromagnetic components of the cosmic-ray shower. With AMIGA MD we detected the muon density reconstructed at different distances from the shower axis (300, 350, 400, 450, 500, 550, 600, 650, 700, 750, 800, 850, 900, 950, and 1000 m), with AERA we obtained the radiation energy emitted by the electromagnetic component (positrons and electrons) from the shower, and with the fluorescence detectors we obtained the fluorescence light produced from the de-excitation of atmospheric nitrogen molecules excited by the

charged particles of the shower (mostly electrons).

The muon density was successfully reconstructed for all distances from the shower axis as well as the fluorescence energy and radiation energy, which has a quadratic dependence on the cosmic-ray energy reconstructed by the SD detectors. Unfortunately, due to the several quality cuts applied in the analysis, we did not end with great statistics for the fourfold hybrid analysis (SD, MD, FD and RD) for a mass-composition separation study. Hence, we divided our dataset (SD+MD+FD+RD) without any quality cuts into two sub-datasets: *i)* SD+MD+FD dataset with only FD quality cuts, and *ii)* SD+MD+RD dataset with only RD quality cuts.

Having all parameters successfully reconstructed, we determined the mass-discri- mination power between proton and iron showers dividing the muon density reconstructed at different distances by the true cosmic-ray energy, true calorimetric energy, SD energy, RD energy, and FD energy. The aim of using different energy parameters was to investigate whether we could have an additional mass separation when we combined the muon density at a certain reference distance from the shower axis with the energy emitted by the electromagnetic component of the air shower. The investigation of which reference distance from the shower axis features the best mass separation was performed using the SD+MD+FD dataset as we have more events. In the following, we also analysed which energy estimator combined with the muon density provides the best mass separation. As a result, the mass-discrimination power depends on the distance from the shower axis, and is maximized for distances between 400 and 550 m from the shower axis. We have shown that 500 m is an optimal reference distance to be used in the analyses. The reconstructed muon density divided by the FD energy shows a better mass separation in comparison to other energy estimators, but due to the low duty cycle of the fluorescence detectors (10%), we have very few recorded measured events. In principle, this can be solved by using the RD energy or SD energy to study mass composition of cosmic rays [202].

Furthermore, the muon density reconstructed at 500 m from the shower axis divided by the SD and FD energies was compared to the shower maximum X_{max} to investigate which mass-sensitive observable features a better mass separation. As a result, the combined muon density with different primary-energy estimators gives a better mass separation by a factor of about 100% than X_{max} for all three hadronic models within statistical uncertainties. Moreover, the observables $\rho_{\mu}^{\mathrm{Rec}}(500)/E_{\mathrm{SD}}^{p_1}$ and $\rho_{\mu}^{\mathrm{Rec}}(500)/E_{\mathrm{FD}}^{p_1}$ increase with the logarithm of the primary energy while the X_{max} keeps constant with increasing logarithmic energy. Hence, the combined muonic and electromagnetic components of the shower are important to optimize and potentialize the mass separation of primary cosmic rays.

Beyond the simulation studies, we analysed events measured simultaneously and separately by SD, MD, FD and RD for a data period of 302 days when the muon detectors were properly calibrated, yielding a high-quality data set of 304 events measured by AMIGA, 61 coincident events measured by AMIGA and FD, 82 events by AMIGA and AERA and only two events by AMIGA, AERA and FD (with FD properly calibrated). The measured muon density reconstructed at 500 m from the shower axis as a function of the measured primary energy reconstructed with the

SD, RD and FD detectors describes a similar shower evolution as simulations, validating their capability as mass sensitive observables. The combined muon density with different primary-energy estimators shows a trend towards a light composition for the energy range between 3.16×10^{17} and 10^{18} eV in agreement with the evolution of X_{max} measured with HEAT and Coihueco telescopes as a function of the primary energy [206].

The combined analysis of the muonic (via AMIGA MD) and electromagnetic (via AERA and fluorescence detectors) components of the shower carried out in this thesis comprises cosmic-ray showers with zenith angles below 55º. However, this study can be extended to higher zenith angles. Inclined showers are characterized by the dominance of secondary muons at the ground, as the electromagnetic component is largely absorbed in the atmosphere [212]. However, the atmosphere is essentially transparent for radio emission [170]. Hence, the pure muonic content can be measured by the surface detectors, while the electromagnetic component can be measured by AERA via radio-pulse detection and by fluorescence telescopes via fluorescence light emitted by nitrogen molecules that are excited by mostly secondary electromagnetic particles. Moreover, the upgrade of the Auger Observatory, named AugerPrime, will provide important direct measurements of the muon content of the shower, which can be correlated with the AMIGA muon-detector measurements to verify and fine-tune the methods to extract the muon information of the shower. Thus the combined method of the muon signal (SSD) with calorimetric (FD) and radio emission (AERA) energy can be extended to ultra-high energies as the AugerPrime will extend the composition sensitivity of the measurements into the flux suppression region. Understanding the origin of the flux suppression will provide important constraints on the astrophysical sources, allowing us to precisely determine the fluxes of neutrinos and gamma-rays at ultra-high energies. In general, these combined analyses can be implemented in other high-energy cosmic-ray experiments whose detection systems comprise muon detectors, radio antennas and fluorescence telescopes.

Bibliography

[1] V. F. Hess. «Über Beobachtungen der durchdringenden Strahlung bei sieben Freiballonfahrten». In: *Physik. Zeitschr.* 13 (1912), pp. 1084–1091.

[2] The Pierre Auger Collaboration et al. «The Pierre Auger Cosmic Ray Observatory». In: *Nuclear Instruments and Methods in Physics Research Section A: Accelerators, Spectrometers, Detectors and Associated Equipment* 798 (2015), pp. 172 –213. ISSN: 0168-9002. DOI: https://doi.org/10.1016/j.nima.2015.06.058. URL: http://www.sciencedirect.com/science/article/pii/S0168900215008086.

[3] A. Aab et al. «The Pierre Auger Observatory: Contributions to the 33rd ICRC, Rio de janeiro, Brazil». In: *ArXiv e-prints* (July 2013). arXiv: 1307.5059 [astro-ph.HE].

[4] J. Abraham et al. «Measurement of the energy spectrum of cosmic rays above 10^{18} eV using the Pierre Auger Observatory». In: *Physics Letters B* 685.4 (2010), pp. 239 –246. ISSN: 0370-2693. DOI: https://doi.org/10.1016/j.physletb.2010.02.013. URL: http://www.sciencedirect.com/science/article/pii/S0370269310001875.

[5] K. Greisen. «End to the Cosmic-Ray Spectrum?» In: *Physical Review Letters* 16 (17 1966), pp. 748–750. DOI: 10.1103/PhysRevLett.16.748. URL: https://link.aps.org/doi/10.1103/PhysRevLett.16.748.

[6] A. A. Penzias and R. W. Wilson. «A Measurement of excess antenna temperature at 4080-Mc/s». In: *Astrophysical Journal* 142 (1965), pp. 419–421. DOI: 10.1086/148307.

[7] D. Harari. «Ultra-high energy cosmic rays». In: *Physics of the Dark Universe* 4 (2014). DARK TAUP2013, pp. 23 –30. ISSN: 2212-6864. DOI: https://doi.org/10.1016/j.dark.2014.04.003. URL: http://www.sciencedirect.com/science/article/pii/S2212686414000120.

[8] R. U. Abbasi et al. «A Study of the composition of ultrahigh energy cosmic rays using the High Resolution Fly's Eye». In: *Astrophysical Journal* 622 (2005), pp. 910–926. DOI: 10.1086/427931. arXiv: astro-ph/0407622 [astro-ph].

[9] D. Ikeda. «Recent Results and Future Prospects From the Telescope Array Experiment». In: *Nuclear and Particle Physics Proceedings* 291-293 (2017). "New eyes on the Universe" CRIS 2016 Cosmic Rays International Seminars Proceedings of the Cosmic Rays International Seminars, pp. 74 –81. ISSN: 2405-6014. DOI: https://doi.org/10.1016/j.nuclphysbps.2017.06.016. URL: http://www.sciencedirect.com/science/article/pii/S2405601417303954.

[10] J. P. Lundquist. «Study of UHECR Composition Using Telescope Array's Middle Drum Detector and Surface Array in Hybrid Mode». In: *PoS* 34th ICRC, The Hague, The Netherlands (2015), p. 441.

[11] K. H. Kampert and M. Unger. «Measurements of the cosmic ray composition with air shower experiments». In: *Astroparticle Physics* 35 (May 2012), pp. 660–678. DOI: 10.1016/j.astropartphys.2012.02.004. arXiv: 1201.0018 [astro-ph.HE].

[12] R. Ulrich, R. Engel, and M. Unger. «Hadronic multiparticle production at ultrahigh energies and extensive air showers». In: *Physical Review* 83.5, 054026 (Mar. 2011), p. 054026. DOI: 10.1103/PhysRevD.83.054026. arXiv: 1010.4310 [hep-ph].

[13] T. Pierog and K. Werner. «Muon Production in Extended Air Shower Simulations». In: *Physical Review Letters* 101.17, 171101 (Oct. 2008), p. 171101. DOI: 10.1103/PhysRevLett.101.171101. eprint: astro-ph/0611311.

[14] T. Huege. «Radio detection of cosmic ray air showers in the digital era». In: *Physics Reports* 620 (2016). Radio detection of cosmic ray air showers in the digital era, pp. 1 –52. ISSN: 0370-1573. DOI: https://doi.org/10.1016/j.physrep.2016.02.001. URL: http://www.sciencedirect.com/science/article/pii/S0370157316000636.

[15] K. H. Kampert. «Cosmic Rays from the Knee to the Ankle Status and Prospects». In: *Nuclear Physics B Proceedings Supplements* 165 (Mar. 2007), pp. 294–306. DOI: 10.1016/j.nuclphysbps.2006.11.048. eprint: astro-ph/0611884.

[16] V. Verzi, D. Ivanov, and Y. Tsunesada. «Measurement of Energy Spectrum of Ultra-High Energy Cosmic Rays». In: *ArXiv e-prints* (May 2017). arXiv: 1705.09111 [astro-ph.HE].

[17] K. Rawlins and T. Feusels. «Latest Results on Cosmic Ray Spectrum and Composition from Three Years of IceTop and IceCube». In: *PoS* 34th ICRC, The Hague, The Netherlands (2015), p. 334.

[18] S. Knurenko et al. «The Spectrum of Cosmic Rays in the Energy Range 10^{16} - 10^{18} eV According to the Small Cherenkov Array in Yakutsk». In: *PoS* 34th ICRC, The Hague, The Netherlands (2015).

[19] W. D. Apel et al. «The spectrum of high-energy cosmic rays measured with KASCADE-Grande». In: *Astroparticle Physics* 36 (2012), pp. 183–194. DOI: 10.1016/j.astropartphys.2012.05.023.

[20] R. U. Abbasi et al. «First Observation of the Greisen-Zatsepin-Kuzmin Suppression». In: *Physical Review Letters* 100 (10 2008), p. 101101. DOI: 10.1103/PhysRevLett.100.101101. URL: https://link.aps.org/doi/10.1103/PhysRevLett.100.101101.

[21] Dmitri I. «TA Spectrum Summary». In: *PoS* 34th ICRC, The Hague, The Netherlands (2015), p. 349.

[22] I. Valiño. «The flux of ultra-high energy cosmic rays after ten years of operation of the Pierre Auger Observatory». In: *PoS* 34th ICRC, The Hague, The Netherlands (2015), p. 271.

[23] W.D. Apel et al. «The spectrum of high-energy cosmic rays measured with KASCADE-Grande». In: *Astroparticle Physics* 36.1 (2012), pp. 183 –194. ISSN: 0927-6505. DOI: https://doi.org/10.1016/j.astropartphys.2012.05.023. URL: http://www.sciencedirect.com/science/article/pii/S0927650512001284.

[24] M. Nagano and A. A. Watson. «Observations and implications of the ultrahigh-energy cosmic rays». In: *Reviews of Modern Physics* 72 (3 2000), pp. 689–732. DOI: 10.1103/RevModPhys.72.689. URL: https://link.aps.org/doi/10.1103/RevModPhys.72.689.

[25] V. S. Ptuskin et al. «Diffusion and Drift of Very High Energy Cosmic Rays in Galactic Magnetic Field». In: *22th International Cosmic Ray Conference* 2 (Aug. 1991), p. 201.

[26] The KASCADE-Grande Collaboration et al. «KASCADE-Grande measurements of energy spectra for elemental groups of cosmic rays». In: *ArXiv e-prints* (June 2013). arXiv: 1306.6283 [astro-ph.HE].

[27] D. J. Bird et al. «The cosmic-ray energy spectrum observed by the Fly's Eye». In: *Physical Review* 424 (Mar. 1994), pp. 491–502. DOI: 10.1086/173906.

[28] V. Berezinsky, A. Gazizov, and S. Grigorieva. «On astrophysical solution to ultrahigh energy cosmic rays». In: *Physical Review D* 74 (4 2006), p. 043005. DOI: 10.1103/PhysRevD.74.043005. URL: https://link.aps.org/doi/10.1103/PhysRevD.74.043005.

[29] G. T. Zatsepin and V. A. Kuz'min. «Upper Limit of the Spectrum of Cosmic Rays». In: *Soviet Journal of Experimental and Theoretical Physics Letters* 4 (Aug. 1966), p. 78.

[30] J. W. Cronin. «The highest-energy cosmic rays». In: *Nuclear Physics B Proceedings Supplements* 138 (Jan. 2005), pp. 465–491. DOI: 10.1016/j.nuclphysbps.2004.11.107. eprint: astro-ph/0402487.

[31] S. Sarkar. «New physics from ultrahigh-energy cosmic rays». In: *Acta Physica Polonica* B35 (2004), pp. 351–364. arXiv: hep-ph/0312223 [hep-ph].

[32] A. Letessier-Selvon. «Highlights from the Pierre Auger Observatory». In: *Brazilian Journal of Physics* 44 (Oct. 2014), pp. 560–570. DOI: 10.1007/s13538-014-0218-6. arXiv: 1310.4620 [astro-ph.HE].

[33] H. Sagawa. «Telescope Array extension». In: *Nuclear and Particle Physics Proceedings* 279-281 (2016). Proceedings of the 9th Cosmic Ray International Seminar, pp. 145 – 152. ISSN: 2405-6014. DOI: https://doi.org/10.1016/j.nuclphysbps.2016.10.021. URL: http://www.sciencedirect.com/science/article/pii/S2405601416302024.

[34] B. Rouillé d'Orfeuil et al. «Anisotropy expectations for ultra-high-energy cosmic rays with future high-statistics experiments». In: *Astronomy Astrophysics* 567, A81 (July 2014), A81. DOI: 10.1051/0004-6361/201423462. arXiv: 1401.1119 [astro-ph.HE].

[35] K. Kotera and A. V. Olinto. «The Astrophysics of Ultrahigh-Energy Cosmic Rays». In: *Annual Review of Astronomy and Astrophysics* 49 (Sept. 2011), pp. 119–153. DOI: 10.1146/annurev-astro-081710-102620. arXiv: 1101.4256 [astro-ph.HE].

[36] J. L. Han et al. «Pulsar Rotation Measures and the Large-Scale Structure of the Galactic Magnetic Field». In: *Monthly Notices of the Royal Astronomical Society* 642 (May 2006), pp. 868–881. DOI: 10.1086/501444. eprint: astro-ph/0601357.

[37] J. L. Han, R. N. Manchester, and G. J. Qiao. «Pulsar rotation measures and the magnetic structure of our Galaxy». In: *Monthly Notices of the Royal Astronomical Society* 306.2 (1999), pp. 371–380. DOI: 10.1046/j.1365-8711.1999.02544.x. eprint: /oup/backfile/content_public/journal/mnras/306/2/10.1046_j.1365-8711.1999.02544.x/1/306-2-371.pdf. URL: +http://dx.doi.org/10.1046/j.1365-8711.1999.02544.x.

[38] A. Waelkens et al. «Simulating polarized Galactic synchrotron emission at all frequencies, the Hammurabi code». In: *Astronomy Astrophysics* 495 (2009), p. 697. DOI: 10.1051/0004-6361:200810564. arXiv: 0807.2262 [astro-ph].

[39] M. Kachelrieß, P. D. Serpico, and M. Teshima. «The Galactic magnetic field as spectrograph for ultra-high energy cosmic rays». In: *Astroparticle Physics* 26 (Jan. 2007), pp. 378–386. DOI: 10.1016/j.astropartphys.2006.08.004. eprint: astro-ph/0510444.

[40] H. Takami and K. Sato. «Toward Unravelling the Structural Distribution of Ultra-High-Energy Cosmic Ray Sources». In: *Astrophysical Journal* 678.2 (2008), p. 606. URL: http://stacks.iop.org/0004-637X/678/i=2/a=606.

[41] R. M. Kulsrud and E. G. Zweibel. «On the origin of cosmic magnetic fields». In: *Reports on Progress in Physics* 71.4 (2008), p. 046901. URL: http://stacks.iop.org/0034-4885/71/i=4/a=046901.

[42] L. M. Widrow. «Origin of galactic and extragalactic magnetic fields». In: *Reviews of Modern Physics* 74 (3 2002), pp. 775–823. DOI: 10.1103/RevModPhys.74.775. URL: https://link.aps.org/doi/10.1103/RevModPhys.74.775.

[43] G. T. Birk et al. «The role of Kelvin-Helmholtz modes in superwinds of primeval galaxies for the magnetization of the intergalactic medium». In: *Anstronomy and Astrophysics* 353 (Jan. 2000), pp. 108–116.

[44] S. Bertone, F. Stoehr, and S. D. M. White. «Semi-analytic simulations of galactic winds: volume filling factor, ejection of metals and parameter study». In: *Monthly Notices of the Royal Astronomical Society* 359 (June 2005), pp. 1201–1216. DOI: 10.1111/j.1365-2966.2005.08772.x. eprint: astro-ph/0402044.

[45] S. Bertone, C. Vogt, and T. Enßlin. «Magnetic field seeding by galactic winds». In: *Monthly Notices of the Royal Astronomical Society* 370 (July 2006), pp. 319–330. DOI: 10.1111/j.1365-2966.2006.10474.x. eprint: astro-ph/0604462.

[46] P. P. Kronberg, H. Lesch, and U. Hopp. «Magnetization of the Intergalactic Medium by Primeval Galaxies». In: *Astrophysical Journal* 511 (Jan. 1999), pp. 56–64. DOI: 10.1086/306662.

[47] E. Fermi. «On the Origin of the Cosmic Radiation». In: *Physical Review* 75 (8 1949), pp. 1169–1174. DOI: 10.1103/PhysRev.75.1169. URL: https://link.aps.org/doi/10.1103/PhysRev.75.1169.

[48] P. Bhattacharjee. «Origin and propagation of extremely high energy cosmic rays». In: *Physics Reports* 327 (Mar. 2000), pp. 109–247. DOI: 10.1016/S0370-1573(99)00101-5. eprint: astro-ph/9811011.

[49] K. C. Wali. «Introduction to Grand Unified Theories». In: *Gravitation, Gauge Theories and the Early Universe*. Ed. by B. R. Iyer, N. Mukunda, and C. V. Vishveshwara. Dordrecht: Springer Netherlands, 1989, pp. 237–280. ISBN: 978-94-009-2577-9. DOI: 10.1007/978-94-009-2577-9_12. URL: https://doi.org/10.1007/978-94-009-2577-9_12.

[50] V. Berezinsky, M. Kachelrieß, and A. Vilenkin. «Ultrahigh Energy Cosmic Rays without Greisen-Zatsepin-Kuzmin Cutoff». In: *Physical Review Letters* 79 (22 1997), pp. 4302–4305. DOI: 10.1103/PhysRevLett.79.4302. URL: https://link.aps.org/doi/10.1103/PhysRevLett.79.4302.

[51] T. Stanev. «Ultra high energy cosmic rays: A review». In: *ArXiv e-prints* (Nov. 2010). arXiv: 1011.1872 [astro-ph.HE].

[52] K. V. Ptitsyna and S. V. Troitsky. «PHYSICS OF OUR DAYS Physical conditions in potential accelerators of ultra-high-energy cosmic rays: updated Hillas plot and radiation-loss constraints». In: *Physics Uspekhi* 53 (Oct. 2010), pp. 691–701. DOI: 10.3367/UFNe.0180.201007c.0723. arXiv: 0808.0367.

[53] M. Bustamante et al. «High-energy cosmic-ray acceleration». In: (2010). URL: https://cds.cern.ch/record/1249755.

[54] R. D. Blandford and J. P. Ostriker. «Particle acceleration by astrophysical shocks». In: *Physics Reports* 221 (Apr. 1978), pp. L29–L32. DOI: 10.1086/182658.

[55] M. T. Dova. «Ultra-High Energy Cosmic Rays». In: *ArXiv e-prints* (Apr. 2016). arXiv: 1604.07584 [astro-ph.HE].

[56] A. M. Hillas. «The Origin of Ultra-High-Energy Cosmic Rays». In: *Annual Review of Astronomy and Astrophysics* 22 (1984), pp. 425–444. DOI: 10.1146/annurev.aa.22.090184.002233.

[57] L. Alfredo Anchordoqui. «Ultrahigh Energy Cosmic Rays: Facts, Myths, and Legends». In: *ArXiv e-prints* (Apr. 2011). arXiv: 1104.0509 [hep-ph].

[58] B. M. Peterson. *An Introduction to Active Galactic Nuclei*. Cambridge University Press, 1997. DOI: 10.1017/CBO9781139170901.

[59] V. Beckmann and C. R. Shrader. «The AGN phenomenon: open issues». In: 2013. arXiv: 1302.1397 [astro-ph.HE]. URL: http://inspirehep.net/record/1217833/files/arXiv:1302.1397.pdf.

[60] N. K. Glendenning. *Compact stars: Nuclear physics, particle physics, and general relativity*. Springer-Verlag New York, 1997.

[61] T. K. Gaisser. *Cosmic rays and particle physics*. 1990. ISBN: 9780521339315. URL: http://www.cambridge.org/uk/catalogue/catalogue.asp?isbn=0521326672.

[62] H. P. Dembinski. «Measurement of the flux of ultra high energy cosmic rays using data from very inclined air showers at the Pierre Auger Observatory». PhD thesis. Aachen, Tech. Hochsch., 2009. URL: http://web.physik.rwth-aachen.de/~hebbeker/theses/dembinski_phd.pdf.

[63] A. A. Watson. «Catching the highest energy cosmic rays». In: *Astronomy Geophysics* 50.2 (2009), pp. 2.20–2.27. DOI: 10.1111/j.1468-4004.2009.50220.x. eprint: /oup/backfile/content_public/journal/astrogeo/50/2/10.1111/j.1468-4004.2009.50220.x/2/50-2-2.20.pdf. URL: http://dx.doi.org/10.1111/j.1468-4004.2009.50220.x.

[64] A. Haungs et al. «KCDC - The KASCADE Cosmic-ray Data Centre». In: *Journal of Physics: Conference Series* 632.1 (2015), p. 012011. DOI: 10.1088/1742-6596/632/1/012011. arXiv: 1504.06696 [astro-ph.IM].

[65] M. T. Dova. «Phenomenology of Cosmic Ray Air Showers». In: *New Worlds in Astroparticle Physics: Proceedings of the Fifth International Workshop*. Ed. by A. M. Mourão et al. Feb. 2006, pp. 95–109. DOI: 10.1142/9789812774439_0005. eprint: astro-ph/0505583.

[66] R. R. Daniel and S. A. Stephens. «Cosmic-ray-produced electrons and gamma rays in the atmosphere». In: *Reviews of Geophysics* 12.2 (1974), pp. 233–258. ISSN: 1944-9208. DOI: 10.1029/RG012i002p00233. URL: http://dx.doi.org/10.1029/RG012i002p00233.

[67] K. P. Beuermann and G. Wibberenz. «Secondary spectra of electrons and photons in the atmosphere». In: *Canadian Journal of Physics* 46.10 (1968), S1034–S1037. DOI: 10.1139/p68-411. eprint: https://doi.org/10.1139/p68-411. URL: https://doi.org/10.1139/p68-411.

[68] R. Engel, D. Heck, and T. Pierog. «Extensive Air Showers and Hadronic Interactions at High Energy». In: *Annual Review of Nuclear and Particle Science* 61.1 (2011), pp. 467–489. DOI: 10.1146/annurev.nucl.012809.104544. eprint: https://doi.org/10.1146/annurev.nucl.012809.104544. URL: https://doi.org/10.1146/annurev.nucl.012809.104544.

[69] J. Matthews. «A Heitler model of extensive air showers». In: *Astroparticle Physics* 22.5 (2005), pp. 387 –397. ISSN: 0927-6505. DOI: https://doi.org/10.1016/j.astropartphys.2004.09.003. URL: http://www.sciencedirect.com/science/article/pii/S0927650504001598.

[70] S. W. Li and J. F. Beacom. «Spallation Backgrounds in Super-Kamiokande Are Made in Muon-Induced Showers». In: *Physical Review* D91.10 (2015), p. 105005. DOI: 10.1103/PhysRevD.91.105005. arXiv: 1503.04823 [hep-ph].

[71] H. Montanus. «An extended Heitler-Matthews model for the full hadronic cascade in cosmic air showers». In: (2013). arXiv: 1311.0642 [astro-ph.HE].

[72] J. Alvarez-Muñiz et al. «Hybrid simulations of extensive air showers». In: *Physical Review* 66.3, 033011 (Aug. 2002), p. 033011. DOI: 10.1103/PhysRevD.66.033011. eprint: astro-ph/0205302.

[73] J. Blümer, R. Engel, and J. R. Hörandel. «Cosmic rays from the knee to the highest energies». In: *Progress in Particle and Nuclear Physics* 63 (Oct. 2009), pp. 293–338. DOI: 10.1016/j.ppnp.2009.05.002. arXiv: 0904.0725 [astro-ph.HE].

[74] S. Ostapchenko. «Cosmic Ray Interaction Models: an Overview». In: *European Physical Journal Web of Conferences*. Vol. 120. European Physical Journal Web of Conferences. July 2016, p. 04003. DOI: 10.1051/epjconf/201612004003.

[75] S. Ostapchenko. «QGSJET-II: Towards reliable description of very high energy hadronic interactions». In: *Nuclear Physics B - Proceedings Supplements* 151 (2006), pp. 143–146. DOI: 10.1016/j.nuclphysbps.2005.07.026. arXiv: hep-ph/0412332 [hep-ph].

[76] S. Ostapchenko. «Monte Carlo treatment of hadronic interactions in enhanced Pomeron scheme: QGSJET-II model». In: *Physical Review D* 83 (1 2011), p. 014018. DOI: 10.1103/PhysRevD.83.014018. URL: https://link.aps.org/doi/10.1103/PhysRevD.83.014018.

[77] K. Werner. «The hadronic interaction model EPOS». In: *Nuclear Physics B - Proceedings Supplements* 175-176 (2008). Proceedings of the XIV International Symposium on Very High Energy Cosmic Ray Interactions, pp. 81 –87. ISSN: 0920-5632. DOI: https://doi.org/10.1016/j.nuclphysbps.2007.10.012. URL: http://www.sciencedirect.com/science/article/pii/S0920563207007736.

[78] T. Pierog et al. «EPOS LHC: Test of collective hadronization with data measured at the CERN Large Hadron Collider». In: *Physical Review C* 92 (3 2015), p. 034906. DOI: 10.1103/PhysRevC.92.034906. URL: https://link.aps.org/doi/10.1103/PhysRevC.92.034906.

[79] F. Riehn et al. «A new version of the event generator Sibyll». In: *ArXiv e-prints* (Oct. 2015). arXiv: 1510.00568 [hep-ph].

[80] A. Aab et al. «Depth of maximum of air-shower profiles at the Pierre Auger Observatory. I. Measurements at energies above $10^{17.8}$eV». In: *Physical Review D* D90.12 (2014), p. 122005. DOI: 10.1103/PhysRevD.90.122005. arXiv: 1409.4809 [astro-ph.HE].

[81] F. G. Schröder. «Radio detection of cosmic-ray air showers and high-energy neutrinos». In: *Progress in Particle and Nuclear Physics* 93 (2017), pp. 1 –68. ISSN: 0146-6410. DOI: https://doi.org/10.1016/j.ppnp.2016.12.002. URL: http://www.sciencedirect.com/science/article/pii/S0146641016300758.

[82] M. Aglietta et al. «The cosmic ray primary composition in the 'knee' region through the EAS electromagnetic and muon measurements at EAS-TOP». In: *Astroparticle Physics* 21 (2004), pp. 583–596. DOI: 10.1016/j.astropartphys.2004.04.005.

[83] T. Antoni et al. «The Cosmic ray experiment KASCADE». In: *Nuclear Instruments and Methods* A513 (2003), pp. 490–510. DOI: 10.1016/S0168-9002(03)02076-X.

[84] W. D. Apel et al. «The KASCADE-Grande experiment». In: *Nuclear Instruments and Methods in Physics Research Section A: Accelerators, Spectrometers, Detectors and Associated Equipment* 620.2 (2010), pp. 202 –216. ISSN: 0168-9002. DOI: https://doi.org/10.1016/j.nima.2010.03.147. URL: http://www.sciencedirect.com/science/article/pii/S0168900210007734.

[85] N. Hayashida et al. «The anisotropy of cosmic ray arrival directions around 10^{18} eV». In: *Astroparticle Physics* 10 (May 1999), pp. 303–311. DOI: 10.1016/S0927-6505(98)00064-4. eprint: astro-ph/9807045.

[86] T. Abu-Zayyad et al. «The prototype high-resolution Fly's Eye cosmic ray detector». In: *Nuclear Instruments and Methods in Physics Research Section A: Accelerators, Spectrometers, Detectors and Associated Equipment* 450.2 (2000), pp. 253 –269. ISSN: 0168-9002. DOI: https://doi.org/10.1016/S0168-9002(00)00307-7. URL: http://www.sciencedirect.com/science/article/pii/S0168900200003077.

[87] Y. Tameda. «Telescope Array Experiment». In: *Nuclear Physics B - Proceedings Supplements* 196 (2009). Proceedings of the XV International Symposium on Very High Energy Cosmic Ray Interactions (ISVHECRI 2008), pp. 74 –79. ISSN: 0920-5632. DOI: https://doi.org/10.1016/j.nuclphysbps.2009.09.011. URL: http://www.sciencedirect.com/science/article/pii/S0920563209006471.

[88] J. Abraham et al. «Properties and performance of the prototype instrument for the Pierre Auger Observatory». In: *Nucl. Instrum. Meth.* A523 (2004), pp. 50–95. DOI: 10.1016/j.nima.2003.12.012.

[89] G. A. Askar'yan. «Excess negative charge of an electron-photon shower and its coherent radio emission». In: *Soviet Physics JETP* 14.2 (1962). [Zh. Eksp. Teor. Fiz.41,616(1961)], pp. 441–443.

[90] F. D. Kahn and I. Lerche. «Radiation from Cosmic Ray Air Showers». In: *Proceedings of the Royal Society of London Series A* 289 (Jan. 1966), pp. 206–213. DOI: 10.1098/rspa.1966.0007.

[91] J. V. Jelley et al. «Radio pulses from extensive air showers». In: *Il Nuovo Cimento A (1971-1996)* 46.4 (2016), p. 649. ISSN: 1826-9869. DOI: 10.1007/BF02857512. URL: https://doi.org/10.1007/BF02857512.

[92] The Pierre Auger Collaboration et al. «The Pierre Auger Observatory: Contributions to the 33rd International Cosmic Ray Conference (ICRC 2013)». In: *ArXiv e-prints* (July 2013). arXiv: 1307.5059 [astro-ph.HE].

[93] H. Schoorlemmer. «Tuning in on cosmic rays. Polarization of radio signals from air showers as a probe of emission mechanisms». PhD thesis. Nijmegen U., 2012. URL: http://inspirehep.net/record/1186117/files/thesis_HarmSchoorlemmer.pdf.

[94] K. D. de Vries, O. Scholten, and K. Werner. «Macroscopic geo-magnetic radiation model; polarization effects and finite volume calculations». In: *Nuclear Instruments and Methods in Physics Research Section A: Accelerators, Spectrometers, Detectors and Associated Equipment* 662 (2012). 4th International workshop on Acoustic and Radio EeV Neutrino detection Activities, S175 –S178. ISSN: 0168-9002. DOI: https://doi.org/10.1016/j.nima.2010.10.127. URL: http://www.sciencedirect.com/science/article/pii/S0168900210024125.

[95] A. Aab et al. «Probing the radio emission from air showers with polarization measurements». In: *Physical Review* 89.5, 052002 (Mar. 2014), p. 052002. DOI: 10.1103/PhysRevD.89.052002. arXiv: 1402.3677 [astro-ph.HE].

[96] S. Buitink et al. «Method for high precision reconstruction of air shower X_{max} using two-dimensional radio intensity profiles». In: *Physical Review D* 90.8, 082003 (Oct. 2014), p. 082003. DOI: 10.1103/PhysRevD.90.082003. arXiv: 1408.7001 [astro-ph.IM].

[97] A. Nelles et al. «A parameterization for the radio emission of air showers as predicted by CoREAS simulations and applied to LOFAR measurements». In: *Astroparticle Physics* 60 (Jan. 2015), pp. 13–24. DOI: 10.1016/j.astropartphys.2014.05.001. arXiv: 1402.2872 [astro-ph.HE].

[98] A. Nelles et al. «The radio emission pattern of air showers as measured with LOFARa tool for the reconstruction of the energy and the shower maximum». In: *Journal of Cosmology and Astroparticle Physics* 5, 018 (May 2015), p. 018. DOI: 10.1088/1475-7516/2015/05/018. arXiv: 1411.7868 [astro-ph.HE].

[99] A. Corstanje et al. «The shape of the radio wavefront of extensive air showers as measured with LOFAR». In: *Astroparticle Physics* 61 (Feb. 2015), pp. 22–31. DOI: 10.1016/j.astropartphys.2014.06.001. arXiv: 1404.3907 [astro-ph.HE].

[100] W. D. Apel et al. «The wavefront of the radio signal emitted by cosmic ray air showers». In: *JCAP* 9, 025 (Sept. 2014), p. 025. DOI: 10.1088/1475-7516/2014/09/025. arXiv: 1404.3283 [hep-ex].

[101] S. Grebe and Pierre Auger Collaboration. «Spectral index analysis of the data from the Auger Engineering Radio Array». In: *American Institute of Physics Conference Series*. Ed. by R. Lahmann et al. Vol. 1535. American Institute of Physics Conference Series. May 2013, pp. 73–77. DOI: 10.1063/1.4807524.

[102] J. Schulz. «Status and Prospects of the Auger Engineering Radio Array». In: *PoS* 34th ICRC, The Hague, The Netherlands (2015), p. 615.

[103] M. Aglietta et al. «Self-triggering Radio Antennas for Extensive Air Shower Detection». In: *23rd International Cosmic Ray Conference* 4 (1993), p. 258.

[104] I. Kravchenko et al. «Performance and simulation of the RICE detector». In: *Astroparticle Physics* 19 (2003), pp. 15–36. DOI: 10.1016/S0927-6505(02)00194-9. arXiv: astro-ph/0112372 [astro-ph].

[105] I. Kravchenko et al. «Rice limits on the diffuse ultrahigh energy neutrino flux». In: *Physical Review* D73 (2006), p. 082002. DOI: 10.1103/PhysRevD.73.082002. arXiv: astro-ph/0601148 [astro-ph].

[106] I. Kravchenko et al. «Limits on the ultra-high energy electron neutrino flux from the RICE experiment». In: *Astroparticle Physics* 20 (2003), pp. 195–213. DOI: 10.1016/S0927-6505(03)00181-6. arXiv: astro-ph/0206371 [astro-ph].

[107] F. Halzen, E. Zas, and T. Stanev. «Radiodetection of cosmic neutrinos. A numerical, real time analysis». In: *Physics Letters B* 257 (Mar. 1991), pp. 432–436. DOI: 10.1016/0370-2693(91)91920-Q.

[108] C. Allen et al. «Status of the RICE Experiment». In: *Astrophysics From Antarctica*. Ed. by G. Novak and R. Landsberg. Vol. 141. Astronomical Society of the Pacific Conference Series. 1998, p. 234.

[109] D. Saltzberg et al. «Observation of the Askaryan Effect: Coherent Microwave Cherenkov Emission from Charge Asymmetry in High-Energy Particle Cascades». In: *Physical Review Letters* 86 (Mar. 2001), pp. 2802–2805. DOI: 10.1103/PhysRevLett.86.2802. eprint: hep-ex/0011001.

[110] S. W. Barwick et al. «Constraints on Cosmic Neutrino Fluxes from the Antarctic Impulsive Transient Antenna Experiment». In: *Physical Review Letters* 96.17, 171101 (May 2006), p. 171101. DOI: 10.1103/PhysRevLett.96.171101. eprint: astro-ph/0512265.

[111] C. Grupen et al. «Radio detection of cosmic rays with LOPES (LOPES Collaboration)». en. In: *Brazilian Journal of Physics* 36 (Dec. 2006), pp. 1157 –1164. ISSN: 0103-9733. URL: http://www.scielo.br/scielo.php?script=sci_arttext&pid=S0103-97332006000700008&nrm=iso.

[112] T. Huege and the LOPES Collaboration. «Radio detection of cosmic ray air showers with the LOPES experiment». In: *Journal of Physics: Conference Series* 110.6 (2008), p. 062012. URL: http://stacks.iop.org/1742-6596/110/i=6/a=062012.

[113] D. T. Machado and the CODALEMA Collaboration. «Latest results of the CODALEMA experiment: cosmic rays radio detection in a self trigger mode». In: *Journal of Physics: Conference Series* 409.1 (2013), p. 012074. URL: http://stacks.iop.org/1742-6596/409/i=1/a=012074.

[114] D. Ardouin et al. «CODALEMA: A COSMIC RAY AIR SHOWER RADIO DETECTION EXPERIMENT». In: *International Journal of Modern Physics A* 21.supp01 (2006), pp. 192–196. DOI: 10.1142/S0217751X0603360X. eprint: http://www.worldscientific.com/doi/pdf/10.1142/S0217751X0603360X. URL: http://www.worldscientific.com/doi/abs/10.1142/S0217751X0603360X.

[115] C. Glaser. «Results and Perspectives of the Auger Engineering Radio Array». In: *European Physical Journal Web of Conferences*. Vol. 135. European Physical Journal Web of Conferences. Mar. 2017, p. 01006. DOI: 10.1051/epjconf/201713501006. arXiv: 1609.01513 [astro-ph.HE].

[116] B. K. Lubsandorzhiev. «The Tunka experiment: From small "toy" experiments to multi-TeV gamma-ray observatory». In: *Physics of Particles and Nuclei* 46.2 (2015), pp. 190–196. ISSN: 1531-8559. DOI: 10.1134/S1063779615020136. URL: https://doi.org/10.1134/S1063779615020136.

[117] F. G. Schröder et al. «Tunka-Rex: a Radio Extension of the Tunka Experiment». In: *Journal of Physics Conference Series*. Vol. 409. Journal of Physics Conference Series. Feb. 2013, p. 012076. DOI: 10.1088/1742-6596/409/1/012076. arXiv: 1301.2555 [astro-ph.IM].

[118] T. Huege and D. Besson. «Radio-wave detection of ultra-high-energy neutrinos and cosmic rays». In: *Progress of Theoretical and Experimental Physics* 2017.12 (2017), 12A106. DOI: 10.1093/ptep/ptx009. eprint: /oup/backfile/content_public/journal/ptep/2017/12/10.1093_ptep_ptx009/6/ptx009.pdf. URL: +http://dx.doi.org/10.1093/ptep/ptx009.

[119] H. S. Ahn et al. «Measurements of the Relative Abundances of High-energy Cosmic-ray Nuclei in the TeV/Nucleon Region». In: *Astrophysical Journal* 715.2 (2010), p. 1400. URL: http://stacks.iop.org/0004-637X/715/i=2/a=1400.

[120] A. P. Garyaka et al. «Rigidity-dependent cosmic ray energy spectra in the knee region obtained with the GAMMA experiment». In: *Astroparticle Physics* 28 (Oct. 2007), pp. 169–181. DOI: 10.1016/j.astropartphys.2007.04.004. arXiv: 0704.3200.

[121] I. Anatoly. «The Yakutsk array experiment: Main results and future directions». In: *EPJ Web Conf.* 53 (2013), p. 04003. DOI: 10.1051/epjconf/20135304003.

[122] T. Antoni et al. «KASCADE measurements of energy spectra for elemental groups of cosmic rays: Results and open problems». In: *Astroparticle Physics* 24 (Sept. 2005), pp. 1–25. DOI: 10.1016/j.astropartphys.2005.04.001. eprint: astro-ph/0505413.

[123] M. A. K. Glasmacher et al. «The cosmic ray energy spectrum between 10^{14} eV and 10^{16} eV». In: *Astroparticle Physics* 10 (1999), pp. 291–302. DOI: 10.1016/S0927-6505(98)00070-X.

[124] M. Aglietta et al. «The cosmic ray primary composition between 10^{15} and 10^{16} eV from Extensive Air Showers electromagnetic and TeV muon data». In: *Astroparticle Physics* 20 (2004), pp. 641–652. DOI: 10.1016/j.astropartphys.2003.10.004. arXiv: astro-ph/0305325 [astro-ph].

[125] A. Chiavassa. «Cosmic rays measurements around the knee of the primary spectrum». In: *European Physical Journal Web of Conferences*. Vol. 52. European Physical Journal Web of Conferences. June 2013, p. 04001. DOI: 10.1051/epjconf/20125204001.

[126] P. Doll et al. «Muon tracking detector for the air shower experiment KASCADE». In: *Nuclear Instruments and Methods in Physics Research Section A: Accelerators, Spectrometers, Detectors and Associated Equipment* 488.3 (2002), pp. 517 –535. ISSN: 0168-9002. DOI: https://doi.org/10.1016/S0168-9002(02)00560-0. URL: http://www.sciencedirect.com/science/article/pii/S0168900202005600.

[127] Y. Hayashi et al. «A large area muon tracking detector for ultra-high energy cosmic ray astrophysics: The GRAPES-3 experiment». In: *Nuclear Instruments and Methods* A545 (2005), pp. 643–657. DOI: 10.1016/j.nima.2005.02.020.

[128] W. D. Apel et al. «Muon production height studies with the air shower experiment KASCADE-Grande». In: *Astroparticle Physics* 34 (Jan. 2011), pp. 476–485. DOI: 10.1016/j.astropartphys.2010.10.016.

[129] The Pierre Auger Collaboration et al. «The Pierre Auger Observatory II: Studies of Cosmic Ray Composition and Hadronic Interaction models». In: *ArXiv e-prints* (July 2011). arXiv: 1107.4804 [astro-ph.HE].

[130] D. García-Gámez. «Measurement of atmospheric production depths of muons with the pierre auger observatory». In: *European Physical Journal Web of Conferences*. Vol. 53. European Physical Journal Web of Conferences. June 2013, p. 04008. DOI: 10.1051/epjconf/20135304008.

[131] The Pierre Auger Collaboration et al. «The Pierre Auger Observatory: Contributions to the 35th International Cosmic Ray Conference (ICRC 2017)». In: *ArXiv e-prints* (Aug. 2017). arXiv: 1708.06592 [astro-ph.HE].

[132] L. Collica. «Measurement of the muon production depths at the Pierre Auger Observatory». In: *The European Physical Journal Plus* 131.9 (2016), p. 301. ISSN: 2190-5444. DOI: 10.1140/epjp/i2016-16301-6. URL: https://doi.org/10.1140/epjp/i2016-16301-6.

[133] M. Mallamaci. «Maximum Muon Production Depth and its fluctuations above 15 EeV at the Pierre Auger Observatory: mass composition and constraints on hadronic interaction models». PhD thesis. University of Milan, 2017.

[134] S. Andringa et al. «The muonic longitudinal shower profiles at production». In: *Astroparticle Physics* 35 (July 2012), pp. 821–827. DOI: 10.1016/j.astropartphys.2012.03.010. arXiv: 1111.1424 [hep-ph].

[135] M. T. Dova et al. «Time asymmetries in extensive air showers: A novel method to identify UHECR species». In: *Astroparticle Physics* 31 (May 2009), pp. 312–319. DOI: 10.1016/j.astropartphys.2009.03.001. arXiv: 0903.1755 [astro-ph.IM].

[136] A. Aab et al. «Azimuthal asymmetry in the risetime of the surface detector signals of the Pierre Auger Observatory». In: *Physical Review D* 93.7, 072006 (Apr. 2016), p. 072006. DOI: 10.1103/PhysRevD.93.072006. arXiv: 1604.00978 [astro-ph.HE].

[137] A. Karle. «Design and performance of the angle integrating Cherenkov array AIROBICC». In: *Astroparticle Physics* 3 (1995), pp. 321–347. DOI: 10.1016/0927-6505(95)00009-6.

[138] J. W. Fowler et al. «A measurement of the cosmic ray spectrum and composition at the knee». In: *Astroparticle Physics* 15 (Mar. 2001), pp. 49–64. DOI: 10.1016/S0927-6505(00)00139-0. eprint: astro-ph/0003190.

[139] N. M. Budnev et al. «The Cosmic Ray Mass Composition in the Energy Range 10^{15} - 10^{18} eV measured with the Tunka Array: Results and Perspectives». In: *Nucl. Phys. Proc. Suppl.* 190 (2009), pp. 247–252. DOI: 10.1016/j.nuclphysbps.2009.03.095. arXiv: 0902.3156 [astro-ph.HE].

[140] B. A. Antokhonov et al. «A new 1-km**2 EAS Cherenkov array in the Tunka valley». In: *Nucl. Instrum. Meth.* A639 (2011), pp. 42–45. DOI: 10.1016/j.nima.2010.09.142.

[141] S.P. Knurenko et al. «Recent results from the Yakutsk experiment: The development of EAS and the energy spectrum and primary particle mass composition in the energy region of 1015–1019 eV». In: *Nuclear Physics B - Proceedings Supplements* 175-176 (2008). Proceedings of the XIV International Symposium on Very High Energy Cosmic Ray Interactions, pp. 201 –206. ISSN: 0920-5632. DOI: https://doi.org/10.1016/j.nuclphysbps.2007.10.035. URL: http://www.sciencedirect.com/science/article/pii/S0920563207007967.

[142] P. K. F. Grieder. *Extensive Air Showers: High Energy Phenomena and Astrophysical Aspects - A Tutorial, Reference Manual and Data Book*. Berlin, Heidelberg: Springer, 2010. URL: https://cds.cern.ch/record/1339647.

[143] V. V. Prosin et al. «Results and perspectives of cosmic ray mass composition studies with EAS arrays in the Tunka Valley». In: *Journal of Physics: Conference Series* 718.5 (2016), p. 052031. URL: http://stacks.iop.org/1742-6596/718/i=5/a=052031.

[144] S. Mollerach and E. Roulet. «Progress in high-energy cosmic ray physics». In: *Progress in Particle and Nuclear Physics* 98 (2018), pp. 85–118. DOI: 10.1016/j.ppnp.2017.10.002. arXiv: 1710.11155 [astro-ph.HE].

[145] R. M. Baltrusaitis et al. «THE UTAH FLY'S EYE DETECTOR». In: *Nucl. Instrum. Meth.* A240 (1985), pp. 410–428. DOI: 10.1016/0168-9002(85)90658-8.

[146] G. L. Cassiday et al. «Measurements of cosmic-ray air shower development at energies above 10^{17} eV». In: *Astrophysical Journal* 356 (June 1990), pp. 669–674. DOI: 10.1086/168873.

[147] R. U. Abbasi et al. «A Study of the Composition of Ultra-High-Energy Cosmic Rays Using the High-Resolution Fly's Eye». In: *Astrophysical Journal* 622.2 (2005), p. 910. URL: http://stacks.iop.org/0004-637X/622/i=2/a=910.

[148] T. K. Gaisser and A. M. Hillas. «Reliability of the method of constant intensity cuts for reconstructing the average development of vertical showers». In: *Proceedings of 15th ICRC, Plovidv, Bulgaria* 8 (1977), pp. 353–357.

[149] M. Unger et al. «Reconstruction of longitudinal profiles of ultra-high energy cosmic ray showers from fluorescence and Cherenkov light measurements». In: *Nuclear Instruments and Methods in Physics Research A* 588 (Apr. 2008), pp. 433–441. DOI: 10.1016/j.nima.2008.01.100. arXiv: 0801.4309.

[150] T. Abu-Zayyad et al. «A measurement of the average longitudinal development profile of cosmic ray air showers between 10^{17} and 10^{18} eV». In: *Astroparticle Physics* 16.1 (2001), pp. 1 –11. ISSN: 0927-6505. DOI: https://doi.org/10.1016/S0927-6505(00)00170-5. URL: http://www.sciencedirect.com/science/article/pii/S0927650500001705.

[151] T. Fujii. «The Mass Composition of Ultra-high Energy Cosmic Rays Measured by New Fluorescence Detectors in the Telescope Array Experiment». In: *Physics Procedia* 61 (2015). 13th International Conference on Topics in Astroparticle and Underground Physics, TAUP 2013, pp. 418 –424. ISSN: 1875-3892. DOI: https://doi.org/10.1016/j.phpro.2014.12.092. URL: http://www.sciencedirect.com/science/article/pii/S1875389214007056.

[152] D. J. Bird et al. «Evidence for correlated changes in the spectrum and composition of cosmic rays at extremely high-energies». In: *Physical Review Letters* 71 (1993), pp. 3401–3404. DOI: 10.1103/PhysRevLett.71.3401.

[153] M. Unger for the Pierre Auger Collaboration. «Highlights from the Pierre Auger Observatory (ICRC17)». In: *ArXiv e-prints* (Oct. 2017). arXiv: 1710.09478 [astro-ph.HE].

[154] S. P. Knurenko and A. Sabourov. «The depth of maximum shower development and its fluctuations: cosmic ray mass composition at $E_0 \geq 10^{17}$ eV». In: *Astrophysics and Space Sciences Transactions* 7 (July 2011), pp. 251–255. DOI: 10.5194/astra-7-251-2011. arXiv: 1010.1185 [astro-ph.HE].

[155] S. P. Knurenko and A. Sabourov. «Study of cosmic rays at the Yakutsk EAS array: energy spectrum and mass composition». In: *Nuclear Physics B - Proceedings Supplements* 212-213 (2011). Proceedings of the Cosmic Ray International Seminars (CRIS 2010), pp. 241 –251. ISSN: 0920-5632. DOI: https://doi.org/10.1016/j.nuclphysbps.2011.03.033. URL: http://www.sciencedirect.com/science/article/pii/S0920563211000661.

[156] T. Abu-Zayyad et al. «Measurement of the Cosmic-Ray Energy Spectrum and Composition from 1017 to 1018.3 eV Using a Hybrid Technique». In: *Astrophysical Journal* 557.2 (2001), p. 686. URL: http://stacks.iop.org/0004-637X/557/i=2/a=686.

[157] R. U. Abbasi et al. «Publisher's Note: Indications of Proton-Dominated Cosmic-Ray Composition above 1.6 EeV [Physical Review Letters 104, 161101 (2010)]». In: *Physical Review Letters* 104 (19 2010), p. 199902. DOI: 10.1103/PhysRevLett.104.199902. URL: https://link.aps.org/doi/10.1103/PhysRevLett.104.199902.

[158] C. C. H. Jui and Telescope Array Collaboration. «Cosmic Ray in the Northern Hemisphere: Results from the Telescope Array Experiment». In: *Journal of Physics Conference Series*. Vol. 404. Journal of Physics Conference Series. Dec. 2012, p. 012037. DOI: 10.1088/1742-6596/404/1/012037. arXiv: 1110.0133 [astro-ph.IM].

[159] M. Amenomori et al. «Cosmic-ray energy spectrum around the knee obtained by the Tibet experiment and future prospects». In: *Adv. Space Res.* 47 (2011), pp. 629–639. DOI: 10.1016/j.asr.2010.08.029.

[160] R. C. Shellard and Pierre Auger Collaboration. «First Results from the Pierre Auger Observatory». In: *Brazilian Journal of Physics* 36 (Dec. 2006), pp. 1184–1193. DOI: 10.1590/S0103-97332006000700012. eprint: astro-ph/0609060.

[161] T. Waldenmaier, J. Blümer, and H. Klages. «Spectral resolved measurement of the nitrogen fluorescence emissions in air induced by electrons». In: *Astroparticle Physics* 29 (Apr. 2008), pp. 205–222. DOI: 10.1016/j.astropartphys.2008.01.004. arXiv: 0709.1494.

[162] M. Plum. «Measurement of the chemical composition of ultra high energy cosmic rays with the HEAT telescopes of the Pierre Auger Observatory». PhD thesis. RWTH Aachen U., 2016. URL: https://web.physik.rwth-aachen.de/~hebbeker/theses/plum_phd.pdf.

[163] The Pierre Auger Collaboration et al. «The Fluorescence Detector of the Pierre Auger Observatory». In: *ArXiv e-prints* (July 2009). arXiv: 0907.4282 [astro-ph.IM].

[164] E. Varela and the Pierre Auger Collaboration. «The low-energy extensions of the Pierre Auger Observatory». In: *Journal of Physics: Conference Series* 468.1 (2013), p. 012013. URL: http://stacks.iop.org/1742-6596/468/i=1/a=012013.

[165] A. Aab et al. «Prototype muon detectors for the AMIGA component of the Pierre Auger Observatory». In: *Journal of Instrumentation* 11 (Feb. 2016), P02012. DOI: 10.1088/1748-0221/11/02/P02012. arXiv: 1605.01625 [physics.ins-det].

[166] B. Wundheiler. «The AMIGA Muon Counters of the Pierre Auger Observatory: Performance and Studies of the Lateral Distribution Function». In: *PoS* 34th ICRC, The Hague, The Netherlands (2015), p. 324.

[167] T. Hermann-Josef Mathes. «The HEAT telescopes of the Pierre Auger Observatory: Status and first data». In: *Proceedings, 32nd International Cosmic Ray Conference (ICRC 2011): Beijing, China, August 11-18, 2011*. Vol. 3. 2011, p. 153. DOI: 10.7529/ICRC2011/V03/0761. URL: http://inspirehep.net/record/924989/files/924989.pdf.

[168] P. Abreu et al. «Antennas for the detection of radio emission pulses from cosmic-ray induced air showers at the Pierre Auger Observatory». In: *Journal of Instrumentation* 7 (Oct. 2012), P10011. DOI: 10.1088/1748-0221/7/10/P10011. arXiv: 1209.3840 [astro-ph.IM].

[169] D. Charrier. «Antenna development for astroparticle and radioastronomy experiments». In: *Nuclear Instruments and Methods in Physics Research Section A: Accelerators, Spectrometers, Detectors and Associated Equipment* 662 (2012). 4th International workshop on Acoustic and Radio EeV Neutrino detection Activities, S142 –S145. ISSN: 0168-9002. DOI: https://doi.org/10.1016/j.nima.2010.10.141. URL: http://www.sciencedirect.com/science/article/pii/S0168900210024265.

[170] C. Glaser et al. «Simulation of radiation energy release in air showers». In: *JCAP* 9, 024 (Sept. 2016), p. 024. DOI: 10.1088/1475-7516/2016/09/024. arXiv: 1606.01641 [astro-ph.HE].

[171] E. M., Holt for the Pierre Auger Collaboration. «The Auger Engineering Radio Array and multi-hybrid cosmic ray detection». In: *Journal of Physics Conference Series*. Vol. 718. Journal of Physics Conference Series. 2016, p. 052019. DOI: 10.1088/1742-6596/718/5/052019. arXiv: {1704.07240} [astro-ph.HE].

[172] Q. Dorosti Hasankiadeh. «Advanced Reconstruction Strategies for the Auger Engineering Radio Array». In: *ArXiv e-prints* (May 2017). arXiv: 1705.06230 [astro-ph.IM].

[173] The Pierre Auger Collaboration et al. «The Pierre Auger Observatory: Contributions to the 34th International Cosmic Ray Conference (ICRC 2015)». In: *ArXiv e-prints* (Sept. 2015). arXiv: 1509.03732 [astro-ph.HE].

[174] R. Engel. «Upgrade of the Pierre Auger Observatory (AugerPrime)». In: *PoS* 34th ICRC, The Hague, The Netherlands (2015), p. 686.

[175] D. Martello et al. «The Pierre Auger Observatory Upgrade». In: *Pos*. Vol. 301. 2017. URL: http://repozitorij.ung.si/IzpisGradiva.php?lang=eng&id=3827.

[176] T. Suomijärvi. «New electronics for the surface detectors of the Pierre Auger Observatory». In: *The Pierre Auger Observatory: Contributions to the 35th International Cosmic Ray Conference (ICRC 2017)*. 2017, pp. 155–160. URL: http://inspirehep.net/record/1618431/files/1617990_155-160.pdf.

[177] S. Argirò et al. «The offline software framework of the Pierre Auger Observatory». In: *Nuclear Instruments and Methods in Physics Research A* 580 (Oct. 2007), pp. 1485–1496. DOI: 10.1016/j.nima.2007.07.010. arXiv: 0707.1652.

[178] P. Abreu et al. «Advanced functionality for radio analysis in the Offline software framework of the Pierre Auger Observatory». In: *Nuclear Instruments and Methods in Physics Research A* 635 (Apr. 2011), pp. 92–102. DOI: 10.1016/j.nima.2011.01.049. arXiv: 1101.4473 [astro-ph.IM].

[179] R. Brun and F. Rademakers. «ROOT - An Object Oriented Data Analysis Framework». In: *AIHENP'96 Workshop, Lausane*. Vol. 389. 1996, pp. 81–86.

[180] Maris, I. C. «Measurement of the Ultra High Energy Cosmic Ray Flux using Data of the Pierre Auger Observatory». PhD thesis. Universität Karlsruhe (TH), 2008. URL: https://publikationen.bibliothek.kit.edu/1000010441/697773.

[181] Koichi Kamata and Jun Nishimura. «The Lateral and the Angular Structure Functions of Electron Showers». In: *Progress of Theoretical Physics Supplement* 6 (1958), pp. 93–155. DOI: 10.1143/PTPS.6.93. eprint: /oup/backfile/content_public/journal/ptps/6/10.1143/ptps.6.93/2/6-93.pdf. URL: +http://dx.doi.org/10.1143/PTPS.6.93.

[182] J. van Buren et al. «Muon Size Spectrum measured by KASCADE-Grande». In: *International Cosmic Ray Conference* 6 (2005), p. 301.

[183] O. Scholten, K. D. de Vries, and K. Werner. «Coherent radiation from extensive air showers». In: *Nuclear Instruments and Methods in Physics Research Section A: Accelerators, Spectrometers, Detectors and Associated Equipment* 662 (2012). 4th International workshop on Acoustic and Radio EeV Neutrino detection Activities, S80 –S84. ISSN: 0168-9002. DOI: https://doi.org/10.1016/j.nima.2010.11.125. URL: http://www.sciencedirect.com/science/article/pii/S0168900210026720.

[184] C. Glaser. «The Energy Content of Extensive Air Showers in the Radio Frequency Range of 30-80 MHz». In: *PoS* 34th ICRC, The Hague, The Netherlands (2015), p. 364.

[185] A. Aab et al. «Energy estimation of cosmic rays with the Engineering Radio Array of the Pierre Auger Observatory». In: *Physical Review D* 93.12, 122005 (June 2016), p. 122005. DOI: 10.1103/PhysRevD.93.122005. arXiv: 1508.04267 [astro-ph.HE].

[186] A. Aab et al. «Measurement of the Radiation Energy in the Radio Signal of Extensive Air Showers as a Universal Estimator of Cosmic-Ray Energy». In: *Physical Review Letters* 116.24, 241101 (June 2016), p. 241101. DOI: 10.1103/PhysRevLett.116.241101. arXiv: 1605.02564 [astro-ph.HE].

[187] A. Nelles et al. «A parameterization for the radio emission of air showers as predicted by CoREAS simulations and applied to LOFAR measurements». In: *Astroparticle Physics* 60 (2015), pp. 13–24. DOI: 10.1016/j.astropartphys.2014.05.001. arXiv: 1402.2872 [astro-ph.HE].

[188] C. Glaser et al. «An analytic description of the radio emission of air showers based on its emission mechanisms». In: *ArXiv e-prints* (June 2018). arXiv: 1806.03620 [astro-ph.HE].

[189] T. Huege, M. Ludwig, and C. W. James. «Simulating radio emission from air showers with CoREAS». In: *AIP Conference Proceedings* 1535.1 (2013), pp. 128–132. DOI: 10.1063/1.4807534. eprint: https://aip.scitation.org/doi/pdf/10.1063/1.4807534. URL: https://aip.scitation.org/doi/abs/10.1063/1.4807534.

[190] B. R. Dawson. «The importance of atmospheric monitoring at the Pierre Auger Observatory». In: *European Physical Journal Web of Conferences*. Vol. 144. Jan. 2017, p. 01001. DOI: 10.1051/epjconf/201714401001.

[191] V. Verzi. «The Energy Scale of the Pierre Auger Observatory». In: *Proceedings, 33rd International Cosmic Ray Conference (ICRC2013): Rio de Janeiro, Brazil, July 2-9, 2013*, p. 0928. URL: http://www.cbpf.br/%7Eicrc2013/papers/icrc2013-0928.pdf.

[192] H. M. J. Barbosa et al. «Determination of the calorimetric energy in extensive air showers». In: *Astroparticle Physics* 22 (Nov. 2004), pp. 159–166. DOI: 10.1016/j.astropartphys.2004.06.007. eprint: astro-ph/0310234.

[193] A. G. Mariazzi. «A new method for determining the primary energy from the calorimetric energy of showers observed in hybrid mode on a shower-by-shower basis». In: *Proceedings, 32nd International Cosmic Ray Conference (ICRC 2011): Beijing, China, August 11-18, 2011*. Vol. 2. 2011, p. 161. DOI: 10.7529/ICRC2011/V02/0950.

[194] M. J. Tueros. «Estimate of the non-calorimetric energy of showers observed with the fluorescence and surface detectors of the Pierre Auger Observatory». In: *Proceedings, 33rd International Cosmic Ray Conference (ICRC2013): Rio de Janeiro, Brazil, July 2-9, 2013*, p. 0705. URL: http://www.cbpf.br/%7Eicrc2013/papers/icrc2013-0705.pdf.

[195] T. Pierog et al. «EPOS LHC: test of collective hadronization with LHC data». In: *ArXiv e-prints* (June 2013). arXiv: 1306.0121 [hep-ph].

[196] T. Pierog. «Open issues in hadronic interactions for air showers». In: *EPJ Web of Conferences* 145 (2017), p. 18002. DOI: 10.1051/epjconf/201614518002.

[197] D. Heck et al. *CORSIKA: a Monte Carlo code to simulate extensive air showers.* Forschungszentrum Karlsruhe GmbH, Karlsruhe, Germany, Feb. 1998. URL: https://publikationen.bibliothek.kit.edu/270043064/3813660.

[198] A. D. Supanitsky et al. «Underground muon counters as a tool for composition analyses». In: *Astroparticle Physics* 29 (July 2008), pp. 461–470. DOI: 10.1016/j.astropartphys.2008.05.003. arXiv: 0804.1068.

[199] A. Aab et al. «Testing Hadronic Interactions at Ultrahigh Energies with Air Showers Measured by the Pierre Auger Observatory». In: *Physical Review Letters* 117.19, 192001 (Nov. 2016), p. 192001. DOI: 10.1103/PhysRevLett.117.192001. arXiv: 1610.08509 [hep-ex].

[200] D. Kostunin et al. «Reconstruction of air-shower parameters for large-scale radio detectors using the lateral distribution». In: *Astroparticle Physics* 74 (Feb. 2016), pp. 79–86. DOI: 10.1016/j.astropartphys.2015.10.004. arXiv: 1504.05083 [astro-ph.HE].

[201] The Pierre Auger Collaboration et al. «The Pierre Auger Observatory: Contributions to the 34th ICRC, The Hague, The Netherlands». In: *ArXiv e-prints* (Sept. 2015). arXiv: 1509.03732 [astro-ph.HE].

[202] E. M. Holt. «Combined Detection of Muons and Radio Emission of Cosmic-Ray Air Showers». PhD thesis. Karlsruhe Institut for Technology (KIT) and National University of San Martín (UNSAM), 2018.

[203] H. Rebel. «What Do We Learn About Hadronic Interactions at Very High Energies From Extensive Air Shower Observations?» In: *Nuclei Far from Stability and Astrophysics*. Ed. by Dorin N. Poenaru, Heinigerd Rebel, and Jürgen Wentz. Dordrecht: Springer Netherlands, 2001, pp. 397–407. ISBN: 978-94-010-0708-5. DOI: 10.1007/978-94-010-0708-5_34. URL: https://doi.org/10.1007/978-94-010-0708-5_34.

[204] M. B. Brown. «Book reviews : Efron B, Tibshirani TJ 1993: An introduction to the bootstrap. London: Chapman and Hall. 436pp. ISBN 0 412 04231 2». In: *Statistical Methods in Medical Research* 4.1 (1995), pp. 91–92. DOI: 10.1177/096228029500400108. eprint: https://doi.org/10.1177/096228029500400108. URL: https://doi.org/10.1177/096228029500400108.

[205] A. A. Petrukhin, A. G. Bogdanov, and R. P. Kokoulin. «Muon problem in UHECR investigations». In: *Journal of Physics: Conference Series* 409.1 (2013), p. 012103. URL: http://stacks.iop.org/1742-6596/409/i=1/a=012103.

[206] The Pierre Auger Collaboration et al. «Inferences on Mass Composition and Tests of Hadronic Interactions from 0.3 to 100 EeV using the water-Cherenkov Detectors of the Pierre Auger Observatory». In: *ArXiv e-prints* (Oct. 2017). arXiv: 1710.07249 [astro-ph.HE].

[207] I. Valiño. «A measurement of the muon number in showers using inclined events recorded at the Pierre Auger Observatory». In: *Proceedings, 33rd International Cosmic Ray Conference (ICRC2013): Rio de Janeiro, Brazil, July 2-9, 2013*, p. 0635. URL: http://www.cbpf.br/%7Eicrc2013/papers/icrc2013-0635.pdf.

[208] N. Budnev et al. «The TAIGA experiment: From cosmic-ray to gamma-ray astronomy in the Tunka valley». In: *Nuclear Instruments and Methods in Physics Research Section A: Accelerators, Spectrometers, Detectors and Associated Equipment* 845 (2017). Proceedings of the Vienna Conference on Instrumentation 2016, pp. 330 –333. ISSN: 0168-9002. DOI: https://doi.org/10.1016/j.nima.2016.06.041. URL: http://www.sciencedirect.com/science/article/pii/S0168900216305836.

[209] R. Abbasi et al. «IceTop: The surface component of IceCube. The IceCube Collaboration». In: *Nuclear Instruments and Methods in Physics Research A* 700 (Feb. 2013), pp. 188–220. DOI: 10.1016/j.nima.2012.10.067. arXiv: 1207.6326 [astro-ph.IM].

[210] A. Balagopal V. et al. «Search for PeVatrons at the Galactic Center using a radio air-shower array at the South Pole». In: *European Physical Journal C* 78, 111 (Feb. 2018), p. 111. DOI: 10.1140/epjc/s10052-018-5537-2. arXiv: 1712.09042 [astro-ph.IM].

[211] Pierre Auger Collaboration et al. «Observation of a large-scale anisotropy in the arrival directions of cosmic rays above 8×10^{18} eV». In: *Science* 357 (Sept. 2017), pp. 1266–1270. DOI: 10.1126/science.aan4338. arXiv: 1709.07321 [astro-ph.HE].

[212] A. Schulz. «The measurement of the energy spectrum of cosmic rays above $3x10^{17}$ eV with the Pierre Auger Observatory». In: *Proceedings, 33rd International Cosmic Ray Conference (ICRC2013): Rio de Janeiro, Brazil, July 2-9, 2013*, p. 0769. URL: http://www.cbpf.br/%7Eicrc2013/papers/icrc2013-0769.pdf.

Analysis pipeline for combined SD, AMIGA, FD, RD

The Offline release Holt (v3r3, revision 31361) was used to run the analysis pipelines for AMIGA and fluorescence simulation analysis and the release Fschlueter (trunk, revision 31522) for AMIGA and AERA analysis. For data reconstruction analysis, the Offline release (trunk, revision 31522) was used.

A.1 Air-shower Simulations

A.1.1 AMIGA and Fluorescence analysis

Module Sequence

```
<loop numTimes="unbounded" pushEventToStack="yes">

<module>  EventFileReaderOG                  </module>

<loop numTimes="1" pushEventToStack="yes">

<!- - SD, MD and FD simulation - ->

<try>
<module>  RdStationAssociator                </module>
<module>  EventGeneratorOG                   </module>

<loop numTimes="unbounded" pushEventToStack="no">

<module>  CachedXShowerRegeneratorAG         </module>
<module>  G4XTankSimulatorAG                 </module>
</loop>
<module>  SdSimulationCalibrationFillerOG    </module>
<module>  SdPMTSimulatorOG                   </module>
<module>  SdFilterFADCSimulatorMTU           </module>
<module>  SdBaselineSimulatorOG              </module>
<module>  TankTriggerSimulatorOG             </module>
<module>  TankGPSSimulatorOG                 </module>
```

A.1.2 AMIGA and AERA analysis

Module Sequence

```
<module>  UnderGrdInjectorAG                </module>
<module>  EdepSimulatorAG                   </module>
<module>  MdCounterSimulatorAG              </module>
<module>  FdSimEventCheckerOG               </module>
<module>  ShowerLightSimulatorKG            </module>
<module>  LightAtDiaphragmSimulatorKG       </module>
<module>  ShowerPhotonGeneratorOG           </module>
<module>  TelescopeSimulatorKG              </module>
<module>  FdBackgroundSimulatorOG           </module>
<module>  FdElectronicsSimulatorOG          </module>
<module>  FdTriggerSimulatorOG              </module>
<module>  CentralTriggerSimulatorXb         </module>
<module>  CentralTriggerEventBuilderOG      </module>
<module>  EventBuilderOG                    </module>
<module>  EventCheckerOG                    </module>
<module>  SdCalibratorOG                    </module>

<!– SD, MD and FD reconstruction –>

  <try>
<module>  FdCalibratorOG                    </module>
<module>  FdEyeMergerKG                     </module>
<module>  FdPulseFinderOG                   </module>
<module>  PixelSelectorOG                   </module>
<module>  FdSDPFinderOG                     </module>
<module>  FdAxisFinderOG                    </module>
<module>  HybridGeometryFinderOG            </module>
<module>  HybridGeometryFinderWG            </module>
<module>  FdApertureLightKG                 </module>
<module>  FdEnergyDepositFinderKG           </module>
  </try>
<module>  SdEventSelectorOG                 </module>
<module>  SdMonteCarloEventSelectorOG       </module>
<module>  SdPlaneFitOG                      </module>
<module>  LDFFinderKG                       </module>
<module>  SdEventPosteriorSelectorOG        </module>
  <try>
<module>  MdMuonCounterAG                   </module>
<module>  MdModuleRejectorAG                </module>
<module>  MdEventSelectorAG                 </module>
<module>  MdBiasCorrecterAG                 </module>
<module>  MdLDFFinderAG                     </module>
  </try>
<module>  RecDataWriterNG                   </module>
</try>
  </loop>
</loop>
```

```
<loop numTimes="unbounded" pushEventToStack="yes">

<module>  EventFileReaderOG                  </module>

<loop numTimes="1" pushEventToStack="yes">

<!- - SD, MD and RD simulation - ->

<module>  RdStationAssociator                </module>
<module>  EventGeneratorOG                   </module>

<loop numTimes="unbounded" pushEventToStack="no">

<module>  CachedXShowerRegeneratorAG         </module>
<module>  G4XTankSimulatorAG                 </module>
</loop>
<module>  SdSimulationCalibrationFillerOG    </module>
<module>  SdPMTSimulatorOG                   </module>
<module>  SdFilterFADCSimulatorMTU           </module>
<module>  SdBaselineSimulatorOG              </module>
<module>  TankTriggerSimulatorOG             </module>
<module>  TankGPSSimulatorOG                 </module>
<module>  UnderGrdInjectorAG                 </module>
<module>  EdepSimulatorAG                    </module>
<module>  MdCounterSimulatorAG               </module>
<module>  CentralTriggerSimulatorXb          </module>
<module>  CentralTriggerEventBuilderOG       </module>
<module>  EventBuilderOG                     </module>
<module>  EventCheckerOG                     </module>
<module>  SdCalibratorOG                     </module>

<!- - SD and MD reconstruction - ->

<module>  SdEventSelectorOG                  </module>
<module>  SdMonteCarloEventSelectorOG        </module>
<module>  SdPlaneFitOG                       </module>
```

```
<module>  LDFFinderKG                              </module>
<module>  SdEventPosteriorSelectorOG               </module>

<try>
<module>  MdMuonCounterAG                         </module>
<module>  MdModuleRejectorAG                      </module>
<module>  MdEventSelectorAG                       </module>
<module>  MdBiasCorrecterAG                       </module>
<module>  MdLDFFinderAG                           </module>
</try>

<!- - RD simulation - ->

<module>  RdAntennaStationToChannelConverter      </module>
<module>  RdChannelResponseIncorporator           </module>
<module>  RdChannelResampler                      </module>
<module>  RdChannelTimeSeriesClipper              </module>
<module>  RdChannelVoltageToADCConverter          </module>
<module>  RdChannelNoiseImporter                  </module>

<!- - RD reconstruction - ->

  <try>
<module>  RdEventInitializer                      </module>
<module>  RdStationRejector                       </module>
<module>  RdChannelADCToVoltageConverter          </module>
<module>  RdChannelSelector                       </module>
<module>  RdChannelPedestalRemover                </module>
<module>  RdChannelResponseIncorporator           </module>
<module>  RdChannelBeaconSuppressor               </module>
<module>  RdChannelTimeSeriesTaperer              </module>
<module>  RdChannelBandstopFilter                 </module>
<module>  RdChannelUpsampler                      </module>
<module>  RdAntennaChannelToStationConverter      </module>
<module>  RdStationSignalReconstructor            </module>
<module>  RdStationEFieldVectorCalculator         </module>

<loop numTimes="unbounded" pushEventToStack="no">

<module>  RdTopDownStationSelector                </module>
<module>  RdPlaneFit                              </module>
 </loop>
<module>  RdClusterFinder                         </module>
<module>  RdPlaneFit                              </module>
<module>  RdLDFMultiFitter                        </module>
<module>  RdGeoCeLDFFitter                        </module>
  </try>
<module>  RecDataWriterNG                         </module>
 </loop>
</loop>
```

A.2 Data Reconstruction

Module Sequence

```
<loop numTimes="unbounded">

<module>  EventFileReaderOG                </module>
<module>  RdEventPreSelector               </module>
<module>  EventCheckerOG                   </module>

<!- - SD pre-selection - ->

<module>  SdPMTQualityCheckerKG            </module>
<module>  TriggerTimeCorrection            </module>
<module>  SdCalibratorOG                   </module>
<module>  SdStationPositionCorrection      </module>
<module>  SdBadStationRejectorKG           </module>
<module>  SdSignalRecoveryKLT              </module>
<module>  SdEventSelectorOG                </module>

<!- - SD reconstruction - ->

<module>  SdPaneFitOG                      </module>
<module>  LDFFinderKG                      </module>
<module>  EnergyCalculationPG              </module>
<module>  DLECorrectionGG                  </module>
<module>  SdEventPosteriorSelectorOG       </module>

  <try>
<module>  SdHorizontalReconstructor        </module>
  </try>

<!- - RD reconstruction - ->

<module>  RdEventInitializer               </module>
<module>  RdStationRejector                </module>
<module>  RdChannelADCToVoltageConverter   </module>
<module>  RdChannelSelector                </module>
<module>  RdChannelPedestalRemover         </module>
<module>  RdChannelResponseIncorporator    </module>
```

```
<module>  RdChannelBeaconSuppressor              </module>
<module>  RdChannelTimeSeriesTaperer             </module>
<module>  RdChannelBandstopFilter                </module>
<module>  RdChannelUpsampler                     </module>
<module>  RdAntennaChannelToStationConverter     </module>
<module>  RdStationSignalReconstructor           </module>
<module>  RdStationEFieldVectorCalculator        </module>

<loop numTimes="unbounded">

<module>  RdTopDownStationSelector               </module>
<module>  RdPlaneFit                             </module>
 </loop>
<module>  RdClusterFinder                        </module>
<module>  RdPlaneFit                             </module>
<module>  RdEventPostSelector                    </module>
<module>  RdLDFMultiFitter                       </module>
<module>  RdGeoCeLDFFitter                       </module>

<!- - MD reconstruction - ->

<try>
<module>  MdMuonCounterAG                        </module>
<module>  MdModuleRejectorAG                     </module>
<module>  MdEventSelectorAG                      </module>
<module>  MdBiasCorrecterAG                      </module>
<module>  MdLDFFinderAG                          </module>
</try>

<!- - FD hybrid reconstruction - ->

<try>
<module>  FdCalibratorOG                         </module>
<module>  FdEyeMergerKG                          </module>
<module>  FdPulseFinderOG                        </module>
<module>  FdSDPFinderOG                          </module>
<module>  FdAxisFinderOG                         </module>
<module>  HybridGeometryFinderOG                 </module>
<module>  HybridGeometryFinderWG                 </module>
<module>  FdApertureLightKG                      </module>
<module>  FdEnergyDepositFinderKG                </module>
</try>

<module>  RdStationTimeSeriesWindowCutter        </module>
<module>  RdStationTimeSeriesTaperer             </module>
<module>  RecDataWriterNG                        </module>
</loop>
```